

# Sheffield Hallam University

*Effect of heat treatment and mechanical deformation on the structure and properties of iron-manganese alloys (10-40% Mn).*

HOLDEN, Alan.

Available from the Sheffield Hallam University Research Archive (SHURA) at:

<http://shura.shu.ac.uk/19809/>

## A Sheffield Hallam University thesis

This thesis is protected by copyright which belongs to the author.

The content must not be changed in any way or sold commercially in any format or medium without the formal permission of the author.

When referring to this work, full bibliographic details including the author, title, awarding institution and date of the thesis must be given.

Please visit <http://shura.shu.ac.uk/19809/> and <http://shura.shu.ac.uk/information.html> for further details about copyright and re-use permissions.

7904060019



**Sheffield City Polytechnic  
Eric Mensforth Library**

# REFERENCE ONLY

This book must not be taken from the Library

PL/26

R5193

**Fines are charged at 50p per hour**

12 SEP 2005  
5pm

ProQuest Number: 10697111

All rights reserved

INFORMATION TO ALL USERS

The quality of this reproduction is dependent upon the quality of the copy submitted.

In the unlikely event that the author did not send a complete manuscript and there are missing pages, these will be noted. Also, if material had to be removed, a note will indicate the deletion.



ProQuest 10697111

Published by ProQuest LLC (2017). Copyright of the Dissertation is held by the Author.

All rights reserved.

This work is protected against unauthorized copying under Title 17, United States Code  
Microform Edition © ProQuest LLC.

ProQuest LLC.  
789 East Eisenhower Parkway  
P.O. Box 1346  
Ann Arbor, MI 48106 – 1346

EFFECT OF HEAT TREATMENT AND MECHANICAL

DEFORMATION ON THE STRUCTURE

AND PROPERTIES OF

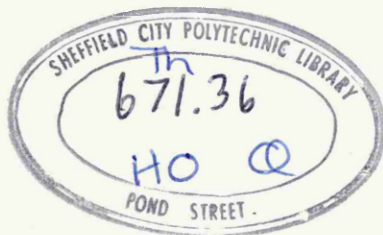
IRON-MANGANESE ALLOYS (10-40% Mn)

by

ALAN HOLDEN

Department of Metallurgy,  
Sheffield Polytechnic,  
Pond Street,  
Sheffield.

December, 1969.



7904060-01

This thesis is submitted for the degree of Master of Philosophy to the Council for National Academic Awards.

As far as the author is aware the work is original except where reference is made to author(s) of books, papers or periodicals. No part of this work has been submitted to another body for the purpose of obtaining a higher degree.

The work was carried out at the Sheffield Polytechnic under the supervision of Dr. E.R. Petty during the period October 1966 - December 1969.

During this time the following courses were attended:

- (1) Short course on electron microscopy by Dr. P.L. James, Sheffield Polytechnic.
- (2) Martensite conference held at the Sheffield Polytechnic.
- (3) "Crystallography of martensite transformations" by R. Wood, Sheffield Polytechnic.
- (4) Manchester Conference, "The mechanism of phase transformations in crystalline solids", international symposium held by The Institute of Metals, 1968.
- (5) "The structure and properties of Fe - Mn alloys" by J.D. Bolton and A. Holden, Sheffield Polytechnic.
- (6) Quantitative metallography by Dr. R. Stratton et al. Sheffield Polytechnic.

# I N D E X

	<u>Page</u>
1. Introduction	2
2. Review of literature	4
2.1. General introduction to martensitic structures	4
2.2. Theories of martensite transformation mechanism	4
2.2.1. The crystallography of the martensite transformation	8
2.2.1.1. Military and civilian transformations	8
2.2.1.2. Lattice correspondence	9
2.2.1.3. Formal theories of crystallography	12
2.3. Morphology	14
2.3.1. Massive structures	16
2.3.2. Epsilon-martensite	21
2.3.3. Twinned martensites	28
2.4. Thermodynamics of martensite transformations	31
2.4.1. Magnetic effect in the martensite transformation	39
2.5. Kinetics of the martensite transformation	42
2.5.1. Athermal reactions	43
2.5.2. Isothermal reactions	44
2.5.3. Autocatalytic effects	45
2.5.4. Thermal stabilisation	45
2.5.5. Nucleation of martensite	46
2.5.6. Heterogeneous nucleation	48
2.6. Effect of applied strain on the martensite transformation	52
2.7. Strengthening mechanisms in martensite	57

3.0.	Strengthening mechanisms in non-martensitic or partially martensitic structures	64
3.1.	Strengthening mechanism of grain boundaries	65
3.2.	Strengthening effect of alloying elements	69
3.2.1.	Order or Fisher hardening	69
3.2.2.	Frictional hardening mechanisms	70
3.2.3.	Influence of solutes on stacking fault energy	73
3.2.4.	Dislocation locking by solute atoms	74
3.2.5.	Effect of precipitates	76
3.3.	The influence of temperature	78
3.3.1.	Brittle fracture	81
4.0.	The structures of alloys in the Fe - Mn system	85
4.1.	The effect of stress on the formation of epsilon phase	90
4.2.	Mechanical properties of iron-manganese alloys	94
4.3.	Iron-manganese-carbon alloys	96
5.0.	Experimental details	99
5.1.	Preparation of alloys	99
5.2.	Testing techniques	101
5.2.1.	Mechanical tests	101
5.2.1.1.	Tensile tests	101
5.2.2.	Impact tests	102
5.3.	Metallography	103
5.3.1.	Optical techniques	103
5.3.2.	X-ray diffraction	104
5.4.	Ageing of air cooled alloys	108

<u>Index - Cont'd.</u>	<u>Page</u>
5.5. Cold rolling	109
6.0. Results	110
6.1. Mechanical tests	110
6.1.1. True-stress v True-strain curves	111
6.2. Metallography	111
6.2.1. Optical microscopy	111
6.2.2. X-ray diffraction	114
6.2.2.1. Forged bar samples air cooled from 950°C.	114
6.2.2.2. Tapered tensile specimens	115
6.2.2.3. Cold rolling experiment	116
6.3. Ageing experiments	117
6.4. Cold rolling	118
7.0. Discussion	118
7.1. Properties of alloys examined	119
7.1.1. Phases present after standard heat treatment	119
7.1.2. Effect of temperature on properties	120
7.1.3. Diffractometer study of sections cut from tapered test pieces	123
7.1.4. Effect of deformation by cold rolling	124
7.2. Transformation thermodynamics	125
7.2.1. Thermodynamics of the $\gamma \rightarrow \alpha$ transformation	125
7.2.2. Thermodynamics of the $\gamma \rightarrow \epsilon$ transformation	129
7.2.3. Effect of mechanical energy	130
8.0. Conclusions	131
9.0. Future work	132
9.1. Elements favouring solid solution	132
9.2. Carbide dispersions	134

<u>Index - Cont'd.</u>	<u>Page</u>
9.3. Transformation strengthening	134
9.4. Age hardening	135
10.0. References	137
 Acknowledgements	 221
 <u>Appendices</u>	
A.1.0. Analysis of alloys used in experiments	222
A.2.0. Typical diffractometer traces	223
A.3.0. Computer programme for diffractometer analysis	225
A.4.0. Statistical survey of light and dark bands	228

## F I G U R E I N D E X

		<u>Page</u>
Figure 1	Equilibrium diagram of the system Fe-Mn	146
Figure 2	Transformation characteristics of Fe-Mn alloys	146
Figure 3	Transformation characteristics of Fe-Ni alloys	147
Figure 4	The shape deformation produced by a martensite plate	147
Figure 5	The lattice correspondence for martensite formation in steels	148
Figure 6(a)	Geometric representation of homogeneous deformation	149
Figure 6(b)	Geometric representation of an undistorted plane	150
Figure 6(c)	Section through $X_2X_3$ plane of figure 6(b)	151
Figure 6(d)	Shows the lattice invariant shear S required to distort the first ellipsoid to shape ellipsoid	152
Figure 7	Examples of invariant plane strain	153
Figure 8	The crystallographic features of a martensitic reaction	154
Figure 9	Diagram showing second shear compensated by (a) slip and (b) twinning	155
Figure 10	Massive ferrite in Fe-4% Ni alloy (Mag X 1500)	156
Figure 11	Surface shears on prepolished specimen of Fe-15% Ni alloy (Mag X 1000)	156
Figure 12	Transformation temperatures of an Fe-10% Ni alloy as a function of austenitising temperature	157
Figure 13	Transformation temperature v. cooling rate	157

<u>Figure Index - Cont'd.</u>	<u>Page</u>
Figure 14      Lattice re-arrangement and relief formation as a result of the $\gamma \rightarrow \epsilon$ transformation	158
Figure 15      Dilatometric curves of a steel with 0.05W/o C + 12.75 w/o Mn	159
Figure 16      Schematic representation of the free energy as a function of temperature for a high temperature phase $\gamma$ , the phase stable at low temperature $\alpha$ and the product of martensitic change $\alpha'$ .	159
Figure 17      Schematic free energy composition diagrams	160
Figure 18      Separation of $\Delta F^{\alpha \rightarrow \gamma}$ into magnetic and non-magnetic terms	160
Figure 19      TTT diagram for isothermal martensite reaction in an Fe-Ni-Mn alloy	161
Figure 20(a)   Martensite embryo	161
Figure 20(b)   Knapp and Dehlinger's model of the martensite embryo	162
Figure 20(c)   Overall free energy ( $\Delta W$ )	162
Figure 21      Effect of applied stress on the martensite) reaction )	163
Figure 22      Strain energy to start martensite reaction at various temperatures	163
Figure 23      Available undercooling for martensite reaction	163
Figure 24      Effect of testing temperature and degree of deformation on martensite formation during compression (70% Fe, 30% Ni)	164
Figure 25      True stress-true strain in 18% Cr - 13% Ni with alloy additions	164
Figure 26      Stacking fault energy increment per at.% in 18% Cr - 10% Ni base alloy as a function of atomic number	164
Figure 27      Comparison of hardening effects of interstitials (carbon and nitrogen) in solution in ferrite and in iron-nickel-carbon martensite	165
Figure 28      Tensile properties of silver as a function of temperature	165

<u>Figure Index - Cont'd.</u>		<u>Page</u>
Figure 29	Stress-strain curves for molybdenum at various temperatures	166
Figure 30	General influence of temperature on Petch analysis	166
Figure 31	Dependence of $K_y$ on temperature for iron containing 0.001% carbon and nitrogen after various quenching and ageing treatments.	167
Figure 32	A Griffith crack	167
Figure 33	Effect of grain size on the yield and fracture stress of a polycrystalline metal	168
Figure 34	Structures found in Fe-Mn-C alloys	169
Figure 35	Effect of plastic deformation on the amount of $\epsilon$ -phase and $\alpha$ solid solution in manganese alloys.	169
Figure 36	Effect of $\gamma \rightleftharpoons \epsilon$ phase transitions on the amount of $\epsilon$ -phase in the alloy G 19	170
Figure 37	Effect of $\gamma \rightleftharpoons \epsilon$ phase transitions on the probability of stacking faults in G 19	170
Figure 38	Tensile strength of carbon-manganese steels quenched from 1000°C into water	170
Figure 39	Tensile elongation of carbon-manganese steels quenched from 1000°C into water	171
Figure 40	Gradual formation of martensitic phases by shears of the austenite (111) planes	171
Figure 41	Alteration of crystal lattice on phase transformations in manganese containing steels	172
Figure 42	Tapered tensile test piece	173
Figure 43	Apparatus for tensile testing at elevated temperatures	174
Figure 44	Cold chamber for Hounsfield machine	174
Figure 45	Mechanical properties v. percentage manganese	175

<u>Figure Index - Cont'd.</u>	<u>Page</u>
Figure 46(a) Hounsfield balanced	176
(b) impact curves	176
(c) for	177
(d) alloy series	177
(e)	178
Figure 47(a) True-stress v. True-strain	179
(b) curves for alloy	180
(c) series at	181
(d) various temperatures	182
Figure 48(a) Properties	183
(b) v.	184
(c) temperature	185
(d)	186
Figure 49 Fe-12.5% Mn alloy air cooled from gamma region (1150°C for 24 hours + 950°C for 1½ hours)	187
Figure 50 Fe-18.5% Mn alloy air cooled from gamma region (1150°C for 24 hours + 950°C for 1½ hours)	187
Figure 51 Fe-37.0% Mn alloy air cooled from gamma region (1150°C for 24 hours + 950°C for 1½ hours)	188
Figure 52 Percentage phase v. composition based on point counting (annealed at 950°C for 1½ hours air cooled)	189
Figure 53 Number of intersections with epsilon phase v. composition (annealed at 1150°C for 24 hours + 950°C for 1½ hours air cooled)	190
Figure 54 Number of intersections with gamma phase v. composition (annealed at 1150°C for 24 hours + 950°C for 1½ hours air cooled)	190
Figure 55 Unallocated area in Fe - 15.6% Mn alloy (annealed at 1150°C for 24 hours + 950°C for 1½ hours air cooled) X 2000	191
Figure 56 Estimate of phases present based on point counting v. composition (annealed at 1150°C for 24 hours + 950°C for 1½ hours)	192

<u>Figure Index - Cont'd.</u>	<u>Page</u>
Figure 57      Effect of etching time on percentage epsilon phase determined by point counting (reagent used was saturated Sodium thio-sulphate + Potassium metabisulphite)	193
Figure 58(a)   Percentage phase v. composition based on diffractometer measurements (annealed at 950°C for 1½ hours air cooled)	194
Figure 58(b)   Percentage phase v. composition based on diffractometer measurements (annealed at 1150°C for 24 hours + 950°C for 1½ hours)	194
Figure 59      Percentage phase v. strain based on diffractometer measurements	195
Figure 60(a)   Percentage phase based on diffractometer measurements v. percentage reduction in thickness by cold rolling (Fe - 15.6% Mn alloy)	196
Figure 60(b)   Percentage phase based on diffractometer measurements v. percentage reduction in thickness by cold rolling (Fe - 23.0% Mn alloy)	197
Figure 60(c)   Percentage phase based on diffractometer measurements v. percentage reduction in thickness by cold rolling (Fe - 28.25% Mn alloy)	198
Figure 61      Fe - 15.6% Mn alloy after 20% reduction in thickness by cold rolling (magnification X 500)	199
Figure 62(a)   Ageing curves	200
(b) for alloy	201
(c) series	202
(d) air cooled	203
(e) from 1050°C	204
(f)	205
Figures 62(g-i) Ageing curves for Fe-Mn alloys air cooled from 1050°C	206
Figure 63      Change in hardness ( $\Delta H_v$ ) v. percentage reduction in thickness by cold rolling	207
Figure 64 $M_s$ temperature v. composition for Fe-Mn system	208

<u>Figure Index - Cont'd.</u>	<u>Page</u>
Figure 65(a) Work hardening coefficient v. strain at a temperature of 173°K	209
Figure 65(b) Work hardening coefficient v. strain at a temperature of 293°K	210
Figure 65(c) Work hardening coefficient v. strain at a temperature of 573°K	211
Figure 66 Estimated free energy change for the martensitic transformations in the iron- manganese system	212
Figure 67 Free energy change for gamma to alpha transformation in iron	213
Figure 68 Hypothetical iron-manganese diagram	214
Figure 69 Free energy v. temperature curves for cold working of the gamma phase	215
Figure 70 Free energy v. temperature curves for cold working of epsilon phase	215
A.2.0./Figure 2.1. Typical trace for alpha + epsilon structure. Fe-12.86% Mn alloy	223
A.2.0./Figure 2.2. Typical trace for epsilon + gamma structure. Fe-20.30% Mn alloy	224
A.4.0./Figure 4.1. Knoop hardness distribution light areas. Fe-12.50% Mn alloy	233
A.4.0./Figure 4.2. Knoop hardness distribution dark areas. Fe-12.50% Mn alloy	233
A.4.0./Figure 4.3. Knoop hardness distribution light areas. Fe-18.50% Mn alloy	234
A.4.0./Figure 4.4. Knoop hardness distribution dark areas. Fe-18.5% Mn alloy	234
A.4.0./Figure 4.5. Knoop hardness distribution for light areas. Fe-37.00% Mn alloy	235
A.4.0./Figure 4.6. Knoop hardness distribution for dark areas. Fe-37.00% Mn alloy	235

T A B L E I N D E X

		<u>Page</u>
Table 1	Variation of stacking fault energy per at-% solute	216
Table 2	Amount of phases present after quenching powder samples of Fe-18.5% Mn alloy	216
Table 3	Amounts of phases present after tempering at 450°C following water quench from 1050°C (Fe-18.5% Mn)	217
Table 4	Amount of phases present after tempering at 240°C following water quenching from 1050°C (Fe-18.5% Mn)	217
Table 5	Amount of phases present in an 18.5% Mn alloy after quenching, cold working and annealing	218
Table 6	Chemical composition % of steels used by Yershova et al.	218
Table 7	Steels used by Lysak and Vauk	218
Table 8	G values for (200) $\alpha$ (200) $\gamma$ and (10.1) $\epsilon$ reflections	219
Table 9	Calculated free energy change for $\gamma \rightarrow \epsilon$ transformation	219
Table 10	Calculated free energy change for $\gamma \rightarrow \alpha'$ transformation	220

Effect of heat treatment and mechanical deformation on the structure and properties of iron-manganese alloys (10-40% Mn)

SUMMARY

Alloys in the lower part of the range under investigation have been reported as being brittle by some authors while others find them to be as ductile as steels of the same tensile strength and suggested that the brittleness was due to high carbon and phosphorus contents. With this possibility in mind, the impurity content of the alloys used in this investigation was kept to as low a level as was practicable.

The investigation has shown that although duplex structures composed of alpha plus epsilon martensite are the strongest of the series they experienced a ductile to brittle transition under impact conditions at about room temperature (20°C). With the appearance of the gamma phase in the structure at room temperature the ductility of the material improved with some loss in strength. Deformation during cold rolling was seen to aid the transformation of gamma → epsilon → alpha martensite. The ductile epsilon plus gamma structures would seem to be capable of forming the basis for high strength precipitation hardenable alloys.

## 1.0. Introduction

The equilibrium diagram of the iron-manganese system is of the open gamma field type. It is of the same general type as the iron-nickel system apart from complications resulting from the occurrence of four different modifications of manganese (figure 1). Iron is freely soluble in alpha manganese and beta manganese and forms a complete range of solid solutions with f.c.c. gamma manganese. Not only do the systems Fe-Mn and Fe-Ni resemble one another closely with regard to the general form of the equilibrium diagram but also in the way the metastable phases are formed during the gamma to alpha transformation (figures 2 and 3). In both alloy systems the alpha and gamma phases in equilibrium vary greatly in composition from one another and if transformation is to take place under equilibrium conditions, considerable diffusion must take place. This means that diffusionless transformations are favoured. Alloys which transform in this manner are strengthened by solid solution hardening on which is superimposed the structural strengthening resulting from the martensite reaction.

In view of the fact that alloys of the Fe-Ni system already form the basis of high strength alloys it was thought feasible that the Fe-Mn system might provide similar basis alloys. This should be of commercial significance in view of the high cost of nickel and its single source of supply. Conflicting reports about the properties of Fe-Mn alloys were found in the literature; they being variously described as "extremely brittle"<sup>(125)</sup> or "more ductile than steels of the

same tensile strength".<sup>(126)</sup> It was thought that impurities might account for the differing reports so it was decided to use alloys with a low impurity content in any preliminary investigations.

This particular investigation is concerned with alloys in the range 10-40% Mn, alloys up to 10% Mn forming the basis of another study.

It was decided initially to investigate the properties of these alloys in the normalised condition as this state is the one most easily achieved commercially. It is reported, however, that widely differing rates of cooling have little effect upon the structures formed.<sup>(82)</sup>

For the alloys to be of any use commercially they must combine strength with ductility at likely service temperatures. With this in mind a limited number of tests were carried out at both low and elevated temperatures.

The effect of deformation on properties and micro-structure were also investigated as being of both theoretical and practical interest. It is considered that mechanical deformation assists the driving force for transformation from  $\gamma \rightarrow \epsilon \rightarrow \infty$  thus the decrease in free energy is seen to be composed of the algebraic sum of mechanical and thermal energies. From the practical point of view it is, of course, necessary that the alloys be capable of forming to shape by conventional techniques.

This initial investigation was designed to cover as wide a field as possible with a view to the selection of particular alloys for further investigation and development.

## 2.0. Review of Literature

In view of the fact that two types of Martensite occur in alloys of the Fe - Mn Binary system, before discussing the alloys themselves a review of martensitic transformations is appropriate.

### 2.1. General Introduction to Martensitic Structures

From early times it has been known that rapidly cooled steels are much harder than those which have been slowly cooled. If a specimen of plain carbon steel is first austenitised, then rapidly quenched, a hard brittle structure is produced. The structure as formed is described as acicular or needlelike although in fact most martensite crystals are lenticular in shape whose cross sections may appear as needles.

The martensite transformation is a diffusionless process and martensite forms without interchange in the positions of neighbouring atoms. In the absence of an interstitial solute martensite is cubic, in ferrous systems, the tetragonal nature of iron-carbon and iron-nitrogen martensite being due to distortion of the cubic structure by the interstitial atoms.

### 2.2. Theories of Martensite Transformation Mechanism

The observation of a surface relief or shape deformation produced by the formation of a martensite plate suggested to earlier investigators of this phenomenon that the parent to martensite transition involved a homogeneous distortion, as in mechanical twinning. From the observed displacement of straight reference scratches cut on the polished surface of

the parent phase, on transformation, it is possible to deduce the shape deformation involved. Straight scratches in the parent phase are transformed to straight scratches in the martensite (see figure 4). The martensite plates appear to be tilted about their junction plane with the austenite, i.e. the habit or interface plane, and this plane is thus unrotated as a result of the shape deformation. The continuity of the scratches at the interface also suggests that the habit plane is not significantly distorted.

The first suggestion of a transformation mechanism was made by Bain in 1924<sup>(1)</sup>. He suggested that the body-centred tetragonal lattice could be obtained from the face centred lattice by approximately 20% compression along the 'z' axis and approximately 12% expansion along the 'x' and 'y' axes of the martensite, (see figure 5). Any simple distortion of this nature is now known as Bain strain or Bain distortion. This distortion involves a minimum number of atomic movements. However, it was found that the magnitude of the principal strains of the Bain distortion were inconsistent with the surface relief observations which suggested that the martensite habit plane is essentially undistorted.

Greninger and Troiano in 1949<sup>(2)</sup> proposed a phenomenological two shear theory in an attempt to predict the observed crystallographic features of the transformation: the habit plane, parent/product orientation relationship, and shape deformation. This attempt was not entirely successful because the shape deformation was assumed to be a simple shear on the habit plane, neglecting the normal component of the shape strain due to the volume change accompanying the

f.c.c. - b.c.t. transformation.

The difficulties that the most obvious lattice distortion is inconsistent with an undistorted habit plane and that the apparent homogeneous shape strain does not generate the martensite lattice from the austenite lattice were overcome by later theories. Bowles and Mackenzie<sup>(3)</sup> in Australia, and Wechsler, Lieberman and Read<sup>(136)</sup> in America, independently proposed a two shear theory which successfully predicted the observed crystallographic features of a number of martensite transformations. The theory is phenomenological and involves a Bain distortion occurring simultaneously with an inhomogeneous shear.

In the case of Fe - C, Fe - Ni, and Fe - Ni - C, martensites with a  $\{259\}_\gamma$  habit the observed crystallographic features have been quite well predicted when it is supposed that slip or twinning takes place on  $\{112\}_\alpha$ , suggesting the theories to be essentially correct.

The theory of martensite transformation has advanced almost independently in two complementary directions: in the field of thermodynamics and kinetics on the one hand and geometry and crystallography on the other. These directions have yet to be brought together as a coherent whole. The thermodynamic and kinetic aspects have been reviewed by Kaufman and Cohen<sup>(4)</sup> and Walker and Borland<sup>(5)</sup>, while the geometrical and crystallographic theories have been reviewed by Bilby and Christian<sup>(6)</sup>.

The general ideas of homogeneous nucleation and growth have been applied to martensitic reaction in steels,

usually with the assumption that the original embryos and succeeding nuclei are small discs or spheroids. The conclusions cannot be reconciled with the existence of an  $M_s$  temperature and rapid rates of reaction at 4°K.

The crystallographic theory takes account only of the geometrical relationships between the initial and final structures in a transformation, saying nothing about the detailed motion of the atoms which bring this relationship about. It was suggested by Bowles and Barrett<sup>(7)</sup> that because of geometrical similarities with the case of the iron-martensite transformation certain nucleation and growth transformations such as the precipitation of CuBe from the  $\alpha$  solid solution might conform to the same basic geometry and this has since proved to be the case<sup>(8)</sup>.

Experimental work in this field has been directed towards determining the extent of the applicability of the geometrical theory and towards modifications which would make it more comprehensive. For example, it has been found that the theory fits experimental evidence, with reasonable agreement, in the following cases:-

- (i) The fast diffusionless transformation in iron and iron-nickel alloys<sup>(9)</sup>.
- (ii) The relatively slow transformation in Au Cd<sup>(10)</sup>.
- (iii) The precipitation reaction in Cu-Be alloys<sup>(8)</sup>.
- (iv) The order-disorder transformation in Cu Au<sup>(11)</sup>.

The theory has also been used to predict the indices of the plane interfaces formed during annealing between grains of  $\alpha$  and  $\beta$  brass, and during precipitation of

$\text{Fe}_4\text{N}$  and  $\text{Fe}_3\text{P}$  from  $\infty$  iron<sup>(12)</sup>.

Although developed specifically to deal with those phase changes in which a single phase transforms into another single phase product, the theory has been applied with partial success to the transformation of austenite to bainite in the Fe-C system<sup>(14)</sup>. The product phase, bainite, consists of cementite  $\text{Fe}_3\text{C}$  dispersed in a matrix of ferrite.

### 2.2.1. The Crystallography of Martensite Transformations

#### 2.2.1.1. Military and Civilian Transformations

The common feature of the above is that the formal theory of martensite crystallography seems to be applicable to all of them and provides some information about the way in which the new phase grows. Frank<sup>(13)</sup> termed them 'military transformations' in order to describe the disciplined manner in which rearrangement of the atomic configuration takes place. In this nomenclature nucleation and growth transformations are regarded as 'civilian', the atoms moving independently of one another in an apparently random manner. Bainitic transformations are mixed in character in that some of the atoms species involved in the transformation move in a disciplined manner while others move through greater distances in a random manner.

The most orderly transformation in the military category is the martensitic type in which no atom changes place with any of its neighbours during the growth of the new phase. This condition may be relaxed in two different ways. In the first of these, each atom may be supposed to be sufficiently mobile to move a small number of atomic

distances during growth, but not to move distances of the order of the dimensions of the growing crystal. This would seem to be the situation in some ordering reactions and massive transformations described elsewhere in the review. The other way of relaxing the martensite conditions is to suppose that some of the atoms present in the parent phase can move long distances during the growth of the other phase, whilst others are immobile. The complete transformation may then involve the diffusion of the mobile component(s) to form phases of differing composition, together with a military type rearrangement of the atomic configuration of the remaining component(s). This is thought to be characteristic of bainite formation in steels, and reactions of this general type are called bainitic.

#### 2.2.1.2. Lattice Correspondence

The theory of martensite crystallography is based on the postulate of local lattice correspondence between parent and product phase, any misfit at the boundary being corrected periodically. The lattice correspondence is related to the experimentally observed changes in the transformed region. From a knowledge of the relationship between parent and product lattices and their lattice parameters it is possible to predict the orientation relations between the lattices, habit plane of the plates, and to specify the change of shape in the transformed region. There are usually several alternatives to the geometric problem, the correct selection is made to fit the observed facts.

We have already noted that the macroscopic change of

shape may be observed by the tilting of an originally polished flat surface, or by the deviation of reference lines scribed on it before transformation (figure 4). The line AB is unrotated by the deformation, which means that no line in the habit plane ABML can be rotated by more than a few minutes of arc. In addition the reference line remains continuous indicating that lines in the habit plane must be unchanged within a few per cent. From these observations it is concluded that the habit plane remains approximately invariant. An invariant plane strain may be considered to be a combination of simple shear and uniaxial expansion (see figure 7) or contraction normal to the interface. The homogeneous deformation involved in the transformation may be represented by deformation of a unit sphere into a triaxial ellipsoid. The deformation involved is separated into two parts, a pure strain plus a rotation (see Figure 6a). For a pure strain three mutually perpendicular axes, the principal axes, are unrotated but change lengths in the ratios  $\eta_1$ ,  $\eta_2$  and  $\eta_3$  where the extensions  $\eta_i - 1$  are the principal strains. If all these strains are all positive or all negative there can be no question of either plane or line being undistorted. It is possible to obtain unextended planes only when one of the principal strains is zero and the other two are of opposite sign. Figure 6b shows how the undistorted plane A' C' is generated from plane AC in the parent phase. For the two planes to correspond a rotation through angle  $\phi$  is necessary.

In the martensite transformation, the lattice correspondence fixes the pure lattice deformation. However, since

the lattice parameters of parent and product are fixed it is not possible to relate the lattices by a deformation in which one of the principal strains is zero. This means that generally the two structures do not have a plane of matching on a microscopic scale, although the habit plane is a plane of matching in the macroscopic sense. This means that in the case of iron-carbon martensite application of the pure strain to the f.c.c. lattice will not produce the product lattice. The difficulty may be overcome by making a distinction between shape deformation, which is a homogeneous deformation on a scale large in comparison to the lattice dimensions, and lattice deformation, which is inhomogeneous. A shape transformation can be achieved either by a lattice deformation, which changes the shape of a unit cell (figure 8b), or a lattice invariant deformation, which produces no basic change in the unit cell (figure 8c). The invariant plane strain involved in the martensite transformation is achieved by combining the two types of lattice deformation shown in figure 9a or by combining two different types of lattice deformation (figure 9b). The lattice deformation is homogeneous over a few unit cells, any misfit which occurs being periodically corrected by the presence of interface dislocations or by a second lattice deformation.

There are two slightly different approaches to the crystallography of the martensite transformation, which have been shown to be mathematically equivalent. The lattice deformation is factorised into two parts, a shape deformation and an invisible deformation so called because the

macroscopic effects are annulled by the lattice invariant deformation. Where the two different lattice deformations are involved, they have a common factor which gives the deformation observed whilst the other factors are opposite in the sense that they produce zero net effect. The foregoing may be summarised in the form of an equation.

$$\text{Lattice} = \text{Shape} \times \text{Invisible} \dots \dots \dots (1)$$

which formulates the Bowles, Mackenzie approach.

A slightly different approach due to Wechsler, Lieberman and Read is to obtain the required shape deformation by combining lattice and lattice invariant deformations, which may be expressed in equation form as

$$\text{Shape} = \text{Lattice} \times \text{Lattice invariant}(S) \dots (2)$$

If both sides of the equation are multiplied by the invisible term (considered to annul the lattice invariant term) equation (1) is obtained and the two approaches may be considered mathematically equivalent.

### 2.2.1.3. Formal Theories of Crystallography

Although matrix algebra and vector notation are widely used in the representation of martensitic transformations, it is possible to regard the notation employed as a form of shorthand. It should be remembered, however, that matrices do not obey the commutative rules i.e.  $C = BA$  is not necessarily equivalent to  $C' = AB$ .

From the known structures of the phases involved a pure strain  $P$  is chosen which will convert one lattice into the other. The total lattice deformation, which brings the unit cells into a particular relative orientation, may be

represented by  $D = RP$  (figure 6a) where  $R$  is the pure rotation to be determined. If we consider the approach of equation (2), the lattice invariant deformation may be represented by the symbol  $S$ . In most published work,  $S$  is considered to be simple shear along a known plane and direction but of unknown magnitude.

Consider a deformation  $F = SP$  which differs from the total shape change by a rotation  $R$ . As the deformation  $P$  must leave one plane undistorted i.e. one of its principal deformations  $\eta_i$  must be unity (figure 6b). If  $F$  is known the principal deformation and axes may be obtained. As the deformation  $F$  contains a parameter representing an unknown amount of shear making one of the principal deformations equal to unity ( $E'F'$  in figure 6d), this leads in the mathematical treatment to two different values of shear. These two values of shear are supposed to give products having volume fractions  $(1 - f)$  and  $f$  in the martensite plate.  $F$  then becomes the average deformation  $F = (1-f)P_1 + fP_2$ , which in order to preserve a low energy state are twins of each other. If  $S$  is now regarded as the equivalent average shear obtained by applying the twinning shear to a fraction  $f$  of the orientation produced by  $P_1$ , we may write  $F = SP_1$ . The condition imposed on  $F$  leads to a quadratic equation for the relative amounts of the two twin orientations. Once the principal axes of  $F$  are known the habit plane is one of two undistorted planes produced by  $F$ . For a complete description, a rotation  $R$  is calculated which will return one of these planes to its original orientation and the total shape

deformation.

$$E = RSP \dots \dots \dots (3)$$

The stated lattice deformation is

$$D = RP \dots \dots \dots (4)$$

The choice of which undistorted plane is made invariant together with the choice of the amount of shear mean that in the general case there are four non-equivalent solutions to the crystallographic problem. Some of these solutions may be crystallographic variants of each other but for steel a unique solution is obtained.

The above outline is of the approach used by Wechsler et al. in 1953. Bullough and Bilby in 1956 reversed the deformations P and S for convenience in computation showing that the order is unimportant.

The only arbitrary step in the treatment is the choice of the elements of S, which are generally assumed to represent either a simple shear on a twinning plane in a twinning direction of the product, or on a slip plane and in a slip direction. The simplest assumption about S leads to very good agreement between theory and experiment in some martensite transformations but not in others. In order to adjust the theoretical prediction to the observed data the elements of S may be varied or the condition that the total shape deformation shall be an invariant plane strain is relaxed.

### 2.3. Morphology

The most familiar martensitic product formed in steels consists of irregular plates which in three dimensions are

approximately lens shaped. This type of structure is usually described as acicular, and is also to be found in many non-ferrous alloys which undergo martensitic type transformation. The lenticular shape is attributed to the constraints imposed by the matrix on the growth of a plate. When the constraints are absent, as when a product region traverses a single crystal, the habit plane interface is planar as predicted by the crystallographic theory. As yet this experiment has only been possible in alloys in which the polycrystalline morphology is banded rather than acicular<sup>(10,15,16)</sup>. Planar interfaces crossing single crystals have also been observed in the special case of the coherent martensite transformation in cobalt and its alloys<sup>(17-19)</sup>.

The microstructures of transformed indium-thallium<sup>(15)</sup>, and certain uranium alloys<sup>(21)</sup> show a banded appearance. The parallel sided main bands are able to form because of the small shape deformation and because of the crystallography in the sense that opposite shape deformations may share a common habit plane. Within the main bands are to be found twinned regions of the product known as sub bands. The transition occurs over a small temperature range, coherence between parent and product phase being maintained on the evidence of the completely reversible nature of the process. This is not true of acicular martensites in which some reaction intervenes on the reverse transformation which has to be renucleated e.g. the tempering reaction intervenes on the reverse transformation in the Fe - C system.

### 2.3.1. Massive Structures

The term massive was first used by Greninger<sup>(22)</sup> to describe a microconstituent in a Cu-9.3% Al. alloy quenched from 1020°C. The massive structure however, is not unique to non-ferrous systems, and microstructures containing massive  $\alpha$  have been found in fairly pure iron<sup>(23)</sup>, iron-carbon<sup>(24)</sup>, iron-nitrogen<sup>(24)</sup>, iron-nickel<sup>(24-27)</sup>, iron-chromium<sup>(25)</sup>, iron-silicon<sup>(25)</sup> and iron-manganese alloys<sup>(28)</sup>.

All microstructures containing a massive constituent do not form by the same transformation mechanism. Two extremes have been recognised, those formed by short range diffusion across an incoherent, or semi-coherent interface with no resulting shape change, and those produced by martensitic processes involving shear. In the case of short-range diffusion<sup>(27)</sup> the massive grains grow by the movement of incoherent grain boundaries which are not restricted or impeded by the boundaries of the parent grains through which they move (see figure 10). The surface of specimens of iron-nickel alloy transformed to massive alpha by short-range diffusion have been examined but no evidence of surface shears or other irregularities have been found<sup>(23,29)</sup>. At the other extreme, the massive transformations may be represented by the martensitic transformation which takes place in alloys containing between 10 and 29.5% Ni<sup>(29)</sup>. Over a wide range of cooling rates the gamma phase transforms to alpha of the same composition. Figure 11 shows the surface shears on a prepolished specimen of Fe - 15% Ni alloy. The shear plates observed do not cross the gamma phase grain boundaries.

Although the masses of  $\alpha'$  are considered to be made up of shear plates, the individual plates are difficult to reveal by conventional etching techniques. The shear plates shown in figure 11 were revealed by a thermal grooving technique. Since this type of martensite is so different in microstructural appearance from the acicular forms of martensite, which consist of lenticular martensite plates embedded in a matrix of any retained parent phase, it is convenient to adopt the terms 'massive martensite' and 'acicular martensite' introduced by W.S. Owen<sup>(24)</sup> to distinguish between the two general forms of martensite.

Bell and Owen<sup>(137)</sup>, however, working on Fe-N alloys, found that the massive martensite structures often contained shear plates arranged in a Widmanstätten pattern suggesting that they had formed by shear on  $\{111\}_\gamma$  planes. Transmission electron microscopy revealed that the structure was made up of bundles of thin plates or laths. It was not possible to establish unambiguously that the individual laths correspond to the shear plates observed on prepolished surfaces of specimens transformed to massive martensite. The similarities in appearance and dimensions suggest that it is very probable they do correspond.

Alloy systems are known in which either massive ferrite or massive martensite can occur depending upon the composition of the parent phase, the annealing temperature, which determines the grain size of the parent phase, and the cooling rate. Very little undercooling is required for massive  $\alpha$  to occur in copper-gallium, iron-nickel,

iron-chromium or iron-silicon alloys. It has been shown<sup>(25)</sup> that the free energy change accompanying the transformation is only 20 - 80 cal/mole (84 - 335 J/g) compared with 300 cal/mole (1257 J/g) for the massive martensite transformation, so that the degree of supercooling below  $T_0$  before transformation takes place is very small. The massive alpha transformation is thermally activated and can often be suppressed by rapid cooling. This can be illustrated by reference to the example quoted by Owen and Wilson<sup>(30)</sup>. In the iron-nickel system between about 4-10% Ni either massive alpha or massive martensite can be obtained. Below 4% nickel the product is always massive alpha while above 10% the product is always massive martensite. Recent experiments have shown that the annealing temperature can influence the transformation, see figure 12 showing the transformation temperature of Fe - 10% Ni alloy as a function of the austenitising temperature. The alloy austenitised at any temperature between 700° and 1200°C and cooled at a rate of approximately 50°C per second transforms at about 530°C to massive alpha ( $\alpha$ ). When the experiment is repeated using a cooling rate of 300°C per second the specimens austenitised between 1050°C and 1200°C transformed martensitically to massive martensite ( $\alpha'$ ) at 450°C.

Owen and Wilson<sup>(30)</sup> state that, if it is assumed that the massive alpha is nucleated at the boundaries of the gamma grains, the effect of austenitising temperature may be due simply to the change in grain size. The increasing austenitising temperature produced an appreciable increase in the

size of the gamma grains thus decreasing the grain boundary area per unit volume available for nucleating purposes, so favouring the transformation to alpha martensite.

The change to massive alpha by short range diffusion is an isothermal one so that on continuous cooling a specimen may transform partially by the above mechanism, the transformation being completed, at some lower temperature, in a martensitic fashion.

In view of the similarity between the equilibrium diagrams of the Fe - Ni and Fe - Mn systems it is to be expected that both massive alpha and massive martensite structures will be found to form in alloys of low manganese content, in the Fe - Mn system, under similar conditions of heating and cooling. Very little cooling data appears to have been published on alloys of the Fe - Mn system. Perhaps one of the earliest works was that of Troiano and McGuire<sup>(31)</sup> who quenched specimens at rates of 450°, 3000°, and 9000°C per second and found that for any alloy containing more than about 3.2% Mn the transformation temperature was constant. Jones and Pumphrey<sup>(32)</sup> cooled Fe - Mn alloys at much slower rates lying between 2° and 150° per minute (0.033 - 2.5°C per second). They found that within this range the transformation temperature could not be depressed, and, on the basis of stabilisation phenomenon, they concluded that the transformation was diffusionless. Gomersall and Parr<sup>(33)</sup> carried out experiments to obtain cooling data for binary alloys containing up to 10% atomic Mn using cooling rates up to 40,000°C per second. They concluded that the transformation

temperatures of iron alloys with 1 - 10% atomic Mn are not depressed appreciably over wide ranges of cooling rate (see figure 13) eliminating the possibility of normal type diffusion controlled transformation. Thus the evidence favours conditions for the formation of either a massive or martensitic constituent. The following information was given:-

- (i) The transformed material arranges itself in blocks many of the sides of which appear straight and are similar to massive structures observed in other systems.
- (ii) The boundaries of the transformed blocks appear to cross the prior austenite boundaries, whereas martensite plates always terminate at the prior austenite grain boundaries.
- (iii) The curve of Mn content versus transformation temperature extrapolates to above the highest reported  $M_s$  temperature for pure iron. This evidence tends to support a diffusion-controlled transformation. Further the shape of the curve is very similar to that obtained by Owen for massive transformations in Fe - Ni system at cooling rates of  $5000^{\circ}\text{C}$  per second.

Gomersall and Parr's summary of the evidence would seem to be contradictory because in the first instance it would appear to be massive martensite that is being discussed whereas the later characteristics indicate massive ferrite.

Since this work Wilson and Bolton<sup>(138)</sup> have found both massive ferrite and massive martensite in iron-manganese alloys.

### 2.3.2. Epsilon-Martensite

The simplest type of martensite transformation is the transition from a high temperature f.c.c. phase to a low temperature h.c.p. phase. Such a change is found in pure cobalt, cobalt-rich alloys, iron-manganese alloys, and certain high alloy steels. The two structures are inter-related each being obtained by an appropriate stacking sequence of planar hexagonal sets of atoms. The lattices thus have a common plane which is the  $\{111\}$  plane of the f.c.c. structure or the (0001) plane of the h.c.p. structure.

On an atomic scale, the transformation from f.c.c. to h.c.p. may be accomplished automatically if a Shockley partial dislocation of Burgers vector  $\frac{a}{6} \langle 11\bar{2} \rangle$  moves through alternate atomic planes of a parallel set of  $\{111\}$  planes. This would produce a large shape deformation, and hence a large strain energy in the surrounding matrix when the transformation region is enclosed (Figure 14a).

A special feature of fcc - hcp transformations is that there are three equivalent shear directions in each  $\{111\}$  plane, the net effect of atomic displacement in any of these three directions being the same. This means that if the alternate atomic planes do not move relative to one another in a common direction but randomly in three equivalent  $\langle 11\bar{2} \rangle$  directions, there will be no macroscopic shape deformation and accompanying strain energy. If each lattice plane is separately nucleated, the stresses due to any net shear would certainly ensure that the three directions are utilised at random, giving a zero shape deformation. Thus the observation

of whether or not there is a macroscopic shape deformation in a spontaneous transformation gives important information about the growth mechanism.

Lysak and Nikolin<sup>(130)</sup> carried out a microscopic study of the surface relief formed as a result of the gamma to epsilon transformation on single crystals of steel, basically an Fe - Mn - C alloy. When the surface relief was studied no projections or hollows could be found such as would correspond to the formation of large epsilon phase lamellae. These were found to consist of finer lamellae which did not shift interferometric lines. It was concluded that the large  $\epsilon$  phase lamellae were the result of growth from a number of nuclei, and were not due to homogeneous shear from one nucleus (figure 14b). The magnitude of the homogeneous shear was not more than  $1000\text{\AA}$ , and considerably less than the size of the large lamellae ( $30 - 50\mu$ ) of the epsilon phase. This evidence partially supports the above theory of zero shape deformation resulting from the random operation of three equivalent  $\langle 11\bar{2} \rangle$  directions in that more than one nucleus is seen to operate to reduce the magnitude of the homogeneous shear in any large  $\epsilon$  lamella.

The hcp stacking across a fault of the fcc structure naturally suggests the possibility of this particular transformation beginning from single stacking faults, so that thermal nucleation may not be required. Christian, however, is of the opinion that the Bilby-Cottrell model for mechanical twinning offers a more acceptable physical picture for dislocation multiplication, which has been used to describe

the cobalt transformation by several authors<sup>(15,34-36)</sup>.

In essence it is proposed that the transformation occurs by the rotation of a Shockley partial dislocation about a  $\frac{2a}{3}$   $[111]$  pole which becomes a  $C[001]$  dislocation in the hexagonal structure. For each rotation of the partial dislocation about the pole, the hexagonal phase is thickened by two atomic planes. It is not obvious how the transformation is nucleated, and in particular whether the hexagonal phase can grow from a single fault. Seeger<sup>(38,39)</sup> proposed that the kinetic energy obtained by two partials after one revolution around the pole will be sufficient to overcome their mutual repulsion. Alternatively, Venables' mechanism for twinning which involves recombination after one revolution followed by cross glide could be adapted to the transformation. It seems more probable, however, that initially groups of stacking faults on neighbouring planes interact to give a small nucleus, which can grow by the pole mechanism. Whatever the growth mechanism, the resulting structure is highly faulted.

Several attempts have been made to determine the transformation mechanism using the electron microscope<sup>(40-42)</sup>. The hcp and fcc structures were observed to be profusely faulted, which the investigators claimed was proof that the transformation occurs by the motion of  $\frac{a}{6}\langle 112 \rangle$  partial dislocations. None of these studies revealed any clear evidence of pole dislocations or pole mechanisms.

Since the crystallographic structure of stacking faults in metals can resemble that of other phases, it has

often been suggested that faults in metals can nucleate and propagate martensitic transformations. An example often quoted is the formation of hcp epsilon-martensite in 18%Cr austenitic stainless steels containing between 8 and 10% Ni which has frequently been associated with stacking faults. Dash and Otte have reviewed this mechanism<sup>(43)</sup>. Otte<sup>(43)</sup> and Breedis<sup>(45)</sup> in their papers both concluded that the shear associated with the formation of alpha-martensite from austenite is sometimes relaxed by the nucleation of high densities of stacking faults in the surrounding austenite. The faults are believed to cluster in an ordered manner to generate the epsilon martensite. The presence of a strong  $(10\bar{1}0)$  reflection in selected area diffraction patterns of epsilon<sup>(43-45)</sup> indicates that epsilon is lightly faulted close packed hexagonal rather than a face-centred cubic structure containing a high density of randomly distributed faults<sup>(46)</sup>. It is now thought that epsilon-martensite is only present if the stacking fault energy of the austenite is low enough for wide stacking faults to form during deformation. A later study by Breedis<sup>(47)</sup> on a stainless steel with a higher stacking fault energy shows that similar deformation occurs adjacent to alpha-martensite needles except that it is accomplished by the slip of perfect dislocations.

Venables<sup>(44)</sup> has shown by electron microscopy that epsilon-martensite is formed initially in the absence of alpha-martensite by deforming 18 - 8 stainless steel small amounts above the  $M_s$  temperature. It, therefore, appears

that alpha-martensite is not necessary to nucleate epsilon. On further deformation at the same temperature alpha-martensite needles formed along the lines of intersection between the epsilon-martensite plates and it was concluded that under certain conditions  $\epsilon$  can nucleate  $\alpha'$ . The orientation relationships between the three phases were found to be

$$\begin{array}{ccc} (111)_{\gamma} \parallel (0001)_{\epsilon} \parallel (101)_{\alpha} \\ [\bar{1}\bar{1}0]_{\gamma} \parallel [\bar{1}\bar{2}10]_{\epsilon} \parallel [11\bar{1}]_{\alpha} \end{array}$$

which for the  $\alpha$  and  $\gamma$  is the Kurdjumov-Sachs relationship.

Kelly<sup>(48)</sup> investigated the  $\gamma \rightarrow \alpha$  transformation in two high alloy steels with low stacking fault energy using transmission electron microscopy. In a 12% Mn - 10% Cr - 4% Ni steel the  $\alpha$  martensite formed as laths, which were always contained within the  $\{111\}$  bands of almost perfect hexagonal  $\epsilon$ . The long direction of these laths was parallel to  $\langle 110 \rangle_{\gamma}$  and the habit plane was close to a  $(\bar{1}\bar{1}2)_{\gamma}$  plane. The orientation relationships between the three phases  $\alpha$ ,  $\epsilon$  and  $\gamma$  was found to be approximately that shown above. The transformation in a 17% Cr - 9% Ni steel was also examined and shown to be essentially similar to the transformation in the Mn-Cr-Ni steel.

Schumann<sup>(49,50)</sup> carried out a metallographic investigation of the reaction sequence  $\gamma \rightarrow \epsilon \rightarrow \alpha$  by means of the light microscope supported by dilatometry. By using the etchant sodium thiosulphate plus potassium meta bisulphite he was able to distinguish the three constituents under the

optical microscope in a series of iron-manganese steels. It was shown that the formation of epsilon-martensite first starts at the  $M_S^\epsilon$  - temperature followed by the formation of alpha-martensite at the lower  $M_S^\alpha$  - temperature. The difference between the two temperatures depends upon the chemical composition. For a 0.05w/oC and 12.75w/o Mn steel, during cooling, a few platelets of epsilon-martensite form in the octahedral planes of the austenite at  $M_S^\epsilon$  170°C. The epsilon platelets originate in the centre of the austenite grains, then grow until they meet obstacles, such as grain boundaries etc. At temperatures that are only 2 to 3°C lower, alpha-martensite needles form within the epsilon-martensite platelets. As Kelly<sup>(48)</sup> observed, the  $\alpha$  martensite needles may be orientated in twin positions resulting in a dark/light pattern. As the transformation temperatures  $M_S^\epsilon$  and  $M_S^\alpha$  are so close together it is difficult to separate them by thermal analyses<sup>(51)</sup>. The reason for this fact might be a potential coupling of the two transformations.

The  $\gamma \rightarrow \epsilon$  transformation produces a volume decrease resulting in a tensile stress within any grain while the  $\epsilon \rightarrow \alpha$  transformation causes compressive stress by volume increase. After small amounts of epsilon-martensite have formed in the austenite, the residual tensile stress state is reduced when part of this epsilon-martensite has transformed into alpha-martensite. Then the free energy of transformation does not have to do any mechanical work, as the residual tensile stresses are annulled by the expansion due to  $\gamma \rightarrow \alpha'$  transformation. This is demonstrated by the

dilatometric curves shown in figure 15. When a steel with 0.05w/o C and 12.75w/o Mn is heated, the  $\epsilon \rightarrow \gamma$  transformation occurs between 200 and 300°C and the  $\alpha \rightarrow \gamma$  transformation between 500 and 650°C (curve a). During cooling, an extension takes place at 150°C which could be recognised as overlapping of the  $\gamma \rightarrow \epsilon$  and  $\epsilon \rightarrow \alpha$  transformation. When cooling the sample from the austenite range (800°C) to just above 150°C, however, no increase in length is found (curve b). A subsequent heating again causes an extension due to the  $\epsilon \rightarrow \gamma$  transformation and a shortening due to the  $\alpha \rightarrow \gamma$  transformation, respectively. This means that during cooling down to just above 150°C epsilon and alpha-martensite are formed to such an extent that the volume change is balanced. Below 150°C a much greater extension due to the epsilon to alpha-martensite transformation dominates.

Schumann<sup>(49)</sup> states that cooling rates between 400°C per second and 0.001°C per second did not result in noticeable changes in structure. The epsilon-martensite particles which did not go over into alpha-martensite are thermally stable. Annealing for 1000 hours at 150 and 220°C, that is, just below  $\epsilon \rightarrow \gamma$  transition temperature did not result in further transformation of epsilon into alpha-martensite.

Considering the 0.05w/o C. 12.75w/o Mn steel, heating to 500°C converts the epsilon-martensite to gamma. Cooling from this temperature down to room temperature results again in the transformation  $\gamma \rightarrow \epsilon$  to the same extent as if no  $\alpha$  - martensite was present. The effect of time at

temperature would be of interest, as Parr<sup>(52)</sup> working with a 0.0055w/o C. 18.5% Mn iron alloy, was able to vary the amount of martensite present by tempering a quenched specimen at 450°C (above  $\epsilon \rightarrow \gamma$  change temperature) for varying lengths of time followed by water quenching. The epsilon-martensite concentration decreased with increasing time at temperature. The conflicting evidence probably results from the fact that whereas Schumann allowed sufficient time for equilibrium to be reached, Parr did not, which would seem to account for the decrease in epsilon-phase content with increasing tempering time.

### 2.3.3. Twinned Martensites

As already described, some martensites form in bands containing parallel arrays of relatively wide twins while many acicular martensites found in both ferrous and non-ferrous alloys contain twins on a very fine scale. The coherency strains are reduced if the twins are narrow which may be the situation in steels where widths of approximately 20Å have been observed and the transformation strain is large. In cases where the deformation of the lattice is small the energy of the coherent twin boundaries themselves may become important. It has been suggested that the energy can probably be minimised in such instances by having narrow twins at the interfaces broadening into much wider twins behind the interface. This can be inferred from photomicrographs of the interfaces in transforming single crystals of indium-thallium alloys<sup>(15)</sup>.

Warlimont<sup>(37)</sup> reported that twins in Fe - 30.9% Ni alloys are often confined to a band along the mid rib of the martensite plate and that outside this band the plate contains dislocations of increasing density. He suggested that the twin band delineates the 'mid rib' frequently observed in photo-micrographs, and represents that part of the martensite plate which formed first, the plate completing its growth by another mechanism involving a dislocation interface.

Shimizu<sup>(53)</sup> also reported twin plates crowded in the region of the mid rib in an Fe - 30.64% Ni alloy. The plane of the twin plates deviated from the  $\{112\}$  twinning plane by an angle of  $3-21^\circ$  the angle being almost constant in any one martensite crystal. It was suggested that this was due to periodic slipping within the twin plates, and some fine striations within the twins were visible. These observations suggest that the sub structure may be more complex than that predicted by simple theory.

Working with Fe - 29.8% Ni alloys, Patterson and Wayman<sup>(132)</sup> confirmed the opinion that the observed delineation of the mid rib was largely due to the fact that this is the region of greatest twin density. The evidence suggests, however, that the mid rib is something more than just the region of densest twinning since it is observed even in completely twinned plates. Furthermore, the contrast in the foils was often observed to change at the mid rib, implying a slight difference in lattice orientation at the mid rib<sup>(131)</sup>. The mid rib was also found to be visible in the surface relief of an unetched specimen, implying a difference in shape strain

at the mid rib. The reason for the uniqueness of the mid rib is not known at present but seems to be related to the fact that it is the initial portion of the plate to form.

Martensites which are not internally twinned have been found in low carbon stainless steels where they occur in conjunction with epsilon-martensite. The fine structure of massive martensite is of this form and consists of parallel slabs containing a high density of dislocations.

While acicular martensites with twinned sub-structures have been reported in high nickel iron alloys, it is found that in steels containing chromium or manganese the martensite plates are not internally twinned. Earlier suggestions by Kelly et al.<sup>(54)</sup> that martensite in low-carbon alloys and stainless steels forms as needles rather than plates now seems to have been discarded and it is believed instead that elongated plates are grouped together into sheets bounded by  $\{111\}$  planes<sup>(55,56)</sup>. Kelly made an analysis of the alpha-martensite formed in stainless steels and concluded that the elements of the lattice invariant shear are of the type  $\{111\} \langle 1\bar{2}1 \rangle$  in austenite or  $\{101\} \langle 10\bar{1} \rangle$  in martensite. These are different from those generally assumed for steels i.e.  $\{110\} \langle 1\bar{1}0 \rangle$  in austenite equivalent to  $\{112\} \langle 11\bar{1} \rangle$  martensite giving twinned products. The high-alloy steels in which untwinned martensites are observed are also those in which the stacking fault energy is low.

Yet another type of martensite characteristic of a low stacking fault energy in the product rather than the parent phase is to be found in the Cu-Al binary system. This results

in a sub structure in which there is a regular array of stacking faults presumably produced by a dislocation interface containing partial dislocations. If the stacking faults are very regularly spaced, the martensite plate may be regarded as an unfaulted single crystal of a larger unit cell<sup>(57,58)</sup>.

#### 2.4. Thermodynamics of Martensite Transformations

As no composition change accompanies the formation of martensite it is permissible to regard the reaction as a phase change in a single component system. The free energy-temperature relationships which might apply to the reaction are shown in figure 17. Gamma is the stable phase at high temperature and alpha is the stable phase at low temperature. The curves for alpha and gamma meet at temperature  $T_e$  the equilibrium temperature.  $\alpha'$  is the martensitic phase formed by a diffusionless change with a free energy greater than that of the stable structure at all temperatures. ' $T_0$ ' is the temperature below which it is thermodynamically possible to form  $\alpha'$  since  $\Delta G_{\alpha'-\gamma} = G_{\alpha'} - G_{\gamma}$  is negative and is the driving force for the martensite change.

Each martensite plate that forms generates considerable elastic strain due to shape change and the constraints of the surrounding matrix. The strain energy absorbs part of the free energy released by the transformation and the actual free energy released is a fraction of  $\Delta G$ . In addition the formation of each martensite nucleus involves the creation of a new interface with its associated energy. Surface and strain energies vary little with temperature whereas

$\Delta G_{\alpha'-\gamma}$  increases as the temperature decreases. Further cooling to a temperature below ' $T_0$ ' to a temperature  $M_S$  is necessary to provide sufficient driving force to initiate the change. The martensite start temperature ( $M_S$ ) is the highest temperature at which the martensite reaction can occur ( $T_e - M_S$ ) varies from a few degrees centigrade in pure alloys to several hundred degrees in complex alloy systems. The  $M_S$  temperature may be thought of as that temperature at which  $\Delta G_{\alpha'-\gamma}$  becomes equal to the opposing forces or the temperature at which the activation energy for nucleation becomes sufficiently small.

$T_0$  is related to the phase diagram as shown in figure 17. The stable phase in the Fe - Ni system is  $\gamma_{fcc}$  at high temperatures or a mixture of alpha and gamma at low temperatures depending on the composition as shown in figure 17a. In the bottom diagram figure 17e, the temperature is below  $T_0$  and the change from  $\gamma \rightarrow \alpha$  is accompanied by a decrease in free energy. If the alloy is quenched to  $T_1$  it may transform martensitically to  $\alpha'$  if  $\Delta G$  is greater than the opposing forces i.e. if  $T_1 < M_S$  : or alternatively to  $\alpha + \gamma$  by a diffusional change. The transformation that actually occurs is the one that leads to the most rapid reduction in free energy. At low temperatures the rate of a diffusional change is virtually zero whereas a martensite change permits the rapid production of  $\alpha'$ . At temperatures below  $T_S$  the equilibrium form is single phase  $\alpha$ . At this, and all other lower temperatures a diffusionless reaction produces the thermodynamically stable phase. If  $\alpha'$  is

formed at a temperature at which it is metastable, e.g.  $T_1$ , it will become stable on subsequent cooling to  $T_s$ .

$T_0$  and  $\Delta G$  may be evaluated provided the free energy-composition curves can be calculated theoretically or derived empirically from the phase diagram. Insufficient data are available for this approach to be used, and an alternative, but fundamentally less satisfactory method is necessary.

The free energy of  $\gamma$ , in an alloy A - B, of composition  $N_B$  is:-

$$G_\gamma = (1 - N_B) G_{A(\gamma)} + N_B G_{B(\gamma)} + G^M_\gamma \quad \dots (1)$$

where  $G_{A(\gamma)}$  and  $G_{B(\gamma)}$  are the free energies of the  $\gamma$  modification of pure A and pure B respectively and  $G^M_\gamma$  is the free energy of mixing of  $\gamma$  of composition  $N_B$ .

Similarly:

$$G_\alpha = (1 - N_B) G_{A(\alpha)} + N_B G_{B(\alpha)} + G^M_\alpha \quad \dots (2)$$

Subtracting (1) from (2) gives  $\Delta G_{\alpha-\gamma}$  the change in free energy accompanying the diffusionless transformation of  $\alpha$  from  $\gamma$ .

$$\Delta G_{\alpha-\gamma} = (1 - N_B) \Delta G_{A(\alpha-\gamma)} + N_B \Delta G_{B(\alpha-\gamma)} + \Delta G^M_{(\alpha-\gamma)} \quad (3)$$

where  $\Delta G_{A(\alpha-\gamma)}$  and  $\Delta G_{B(\alpha-\gamma)}$  are the differences in free energy between the  $\alpha$  and  $\gamma$  allotropes of pure A and pure B respectively and  $\Delta G^M_{(\alpha-\gamma)}$  is the difference between the free energies of mixing. When iron is the solvent:

$\gamma$ -iron is face centred cubic and  $\alpha$  iron is body centred cubic.  $\Delta G_{Fe(\alpha-\gamma)}$  has been calculated from specific heat data. In the case of Ni which is f.c.c. at all temperatures

$\Delta G_{Ni}(\alpha-\gamma)$  is an imaginary quantity.

$\Delta G^M(\alpha-\gamma)$  can be derived from activity measurements in  $\alpha$  and  $\gamma$  states. Where this data is not available models have to be assumed for the two solutions and these used as a basis for calculation. For the Fe - Ni system, if

$\Delta G_{Ni}(\alpha-\gamma)$  is assumed to be negligible it is found that  $\Delta G^M(\alpha-\gamma)$  at  $M_s$  is in the order of 300 cal/mole (1260 J/g).

In order to permit easy reference to American work on this subject, equation 3 may be written as:

$$\Delta F^{\alpha-\gamma} = (1 - x) \Delta F_{Fe}^{\alpha-\gamma} + X \Delta F_A^{\alpha-\gamma} + \Delta F_M^{\alpha-\gamma} \quad (4)$$

and for multi-component alloys as:

$$\Delta F^{\alpha-\gamma} = X_{Fe} \Delta F_{Fe}^{\alpha-\gamma} + \sum X_A \Delta F_A^{\alpha-\gamma} + \sum \Delta F_M^{\alpha-\gamma} \quad (5)$$

where  $F^\alpha$  = the free energy of the b.c.c. alpha phase,

$F^\gamma$  = the free energy of the f.c.c. gamma phase,

$\Delta F_{Fe}^{\alpha-\gamma}$  = the free energy change in pure iron on transference of 1 gramme mole from the gamma to alpha state,

$\Delta F^{\alpha-\gamma}$  = the driving force in cal/mol.,

$X_A$  = the atomic fraction of 'A',

$(1 - X)$  = the atomic fraction of iron,

$\Delta F_M^{\alpha-\gamma}$  = the difference in the free energies of mixing in the  $\alpha$  and  $\gamma$  state.

Ordinarily data concerning the free energy of mixing is not available and assumptions must be made to bridge the gap.

Zener<sup>(139)</sup> has derived the thermodynamic properties of

medium and alloy steels on the basis that the carbon and alloy concentrations are sufficiently dilute to allow the  $\alpha$  and  $\gamma$  phases to be regarded as ideal solutions. The mixing term  $\Delta F_M^{\alpha-\gamma}$  is then zero and  $\Delta F_A^{\alpha-\gamma} = RT \ln X_\alpha/X_\gamma$ . Since  $\Delta F_A^{\alpha-\gamma} = \Delta H_A^{\alpha-\gamma} - T\Delta S_A^{\alpha-\gamma}$ , the quantity  $RT \ln X_\alpha/X_\gamma$  is not generally constant, but Zener makes it so, implying the  $\Delta S_A^{\alpha-\gamma} = 0$ . In this case

$$\Delta H_A^{\alpha-\gamma} = RT \ln \frac{X_\alpha}{X_\gamma} = \Delta H_A^{\alpha'-\gamma} \quad \dots (6)$$

with the latter arising from the assumed ideality of the solutions.  $\Delta H_A^{\alpha'-\gamma}$  is the difference between the heats of solution of component 'A' in the  $\gamma$  and  $\alpha$  phases.

Equation (4) now simplifies to

$$\Delta F^{\alpha-\gamma} = (1 - X) \Delta F_{Fe}^{\alpha-\gamma} + X \Delta H_A^{\alpha'-\gamma} \quad \dots (7)$$

Comparing this equation with equation (4) it can be seen that

$$\Delta H_A^{\alpha'-\gamma} = \Delta F_A^{\alpha-\gamma} + \frac{\Delta F_M^{\alpha'-\gamma}}{X} \text{ cal/mole} \quad \dots (8)$$

Thus  $\Delta H_A^{\alpha'-\gamma}$  is not likely to be constant, as is assumed, because  $\Delta F_A^{\alpha-\gamma}$  depends on temperature and  $\Delta F_M^{\alpha-\gamma}$  depends upon both temperature and composition. In addition,  $\Delta H_A^{\alpha'-\gamma}$  may or may not have the same sign as  $\Delta F_A^{\alpha-\gamma}$  depending on the sign and magnitude of  $\Delta F_M^{\alpha'-\gamma}/X$ .

Jones and Pumphrey<sup>(32)</sup> utilised Zener's approach to derive the free energy changes for the Fe - Ni and Fe - Mn systems. However, in order to make  $\Delta H_{Ni}^{\alpha'-\gamma}$  and  $\Delta H_{Mn}^{\alpha'-\gamma}$  come out reasonably constant, it was necessary to multiply

$\Delta F_{Fe}^{\alpha-\gamma}$  by two different empirical constants. This indicates a basic deficiency in the thermodynamic treatment because

$\Delta F_{Fe}^{\alpha-\gamma}$  should be identical for all iron base systems.

The discrepancy arises from the fact that the austenitic and martensitic phases are not ideal over the range of composition involved, nor is  $\Delta H_{Ni}^{\alpha'-\gamma}$  or  $\Delta H_{Mn}^{\alpha'-\gamma}$  constant over the range of composition considered.

Fisher's<sup>(140)</sup> analysis of the thermodynamics of the martensite transformation in steels made the following assumptions (a)  $X \Delta F_A^{\alpha-\gamma}$  in equation (4) is negligible; (b)  $RT \ln f_A^\gamma / f_A^{\alpha'}$  is constant and  $f_{Fe}^{\alpha'} = f_{Fe}^\gamma = 1$  : ( $f_A^\gamma$  and  $f_A^{\alpha'}$  are the activity coefficients of component A in the austenitic and martensitic phases of the same composition). When the latter is true, it can be shown that  $XRT \ln f_A^\gamma / f_A^{\alpha'} = \Delta F_M^{\alpha'-\gamma}$  ; and (c)  $f_A^\gamma / f_A^\alpha$  is regarded as independent of concentration for a diffusionless transformation when  $\alpha$  and  $\gamma$  have the same concentration. In the case of carbon a temperature dependence is introduced for  $\Delta F_M^{\alpha'-\gamma}$  along with an order parameter  $\Delta F^*$  which takes into account the preferential arrangement of carbon in the b.c.t. lattice.

$$\Delta F^{\alpha'-\gamma} = X_{Fe} \Delta F_{Fe}^{\alpha-\gamma} + X_c (-10,500 + 3.425T) - \Delta F^* + \sum X_A RT \ln f_A^\gamma / f_A^\alpha \quad \text{cal/mole} \quad \dots (9)$$

Kaufman and Cohen adopted a more rigorous treatment for the Fe - Ni system. For the Fe - Ni system equation (4) becomes:-

$$\Delta F^{\alpha'-\gamma} = (1 - X) \Delta F_{Fe}^{\alpha-\gamma} + X \Delta F_{Ni}^{\alpha-\gamma} + \Delta F_M^{\alpha-\gamma} \quad \dots (10)$$

There was no information available concerning the free energy of mixing of the  $\alpha$  solid solution, therefore, the following assumptions were made concerning the  $\alpha$  and  $\gamma$  solid solutions.

- (a) Both the  $\alpha$  and  $\gamma$  solid solutions are regular solid solutions.
- (b) The specific heats of mixing of the  $\alpha$  and  $\gamma$  solid solutions are independent of temperature.

Applying the rule of common tangents mathematically they derived the equation:

$$\Delta F^{\alpha'-\gamma} = (1 - X) \Delta F_{Fe}^{\alpha-\gamma} - X \left[ RT \ln \frac{X_{\gamma}}{X_{\alpha}} + B(X - 2X_{\gamma} + X_{\gamma}^2) \right] + XA(X - 2X_{\alpha} + X_{\alpha}^2) \quad \dots (11)$$

where

$$A = d^{\alpha} + e^{\alpha}T(1 - \ln T) \quad \dots (12)$$

$$B = d^{\gamma} + e^{\gamma}T(1 - \ln T) \quad \dots (13)$$

and  $d^{\alpha}$ ,  $d^{\gamma}$ ,  $e^{\alpha}$  and  $e^{\gamma}$  are constants.

The value of A was found to be  $< 0.02$  at  $M_S$  and  $A_S$  for alloys up to 25a/o Ni and may be ignored in this composition range. Over the range of this approximation it was found that  $T_0 = \frac{1}{2}(M_S + A_S)$  and that  $\Delta F^{\alpha'-\gamma}_{l_{A_S}}$  was equal to  $\Delta F^{\gamma-\alpha}_{l_{M_S}}$ . Neglecting 'A' above 25a/o causes serious error in calculating  $T_0$ .

Assuming

$$\Delta F^{\alpha-\gamma}_{l_{A_S}} = \Delta F^{\gamma-\alpha}_{l_{M_S}} = - \Delta F^{\alpha'-\gamma}_{l_{M_S}} \quad \dots (14)$$

$$\Delta F^{\alpha'-\gamma}_{l_{M_S}} + \Delta F^{\alpha'-\gamma}_{l_{A_S}} = 0 \quad \dots (15)$$

the following equation was derived:-

$$\Delta F^{\alpha'-\gamma} = (1 - X) \Delta F_{Fe}^{\alpha-\gamma} + X(a_{Ni} + b_{Ni}T^2 + c_{Ni}T^3) + X(1 - X)(d + eT(1 - \ln T)) \quad \dots (16)$$

where  $d = d^{\gamma} + d^{\alpha}$  and  $e = e^{\gamma} - e^{\alpha}$ .

The constants were derived using existing data so that equation (16) becomes:

$$\Delta F^{\alpha'-\gamma} = (1 - X)(1202 - 2.63 \times 10^{-3}T^2 + 1.54 \times 10^{-6}T^3) + X(-3700 + 7.09 \times 10^{-4}T^2 + 3.91 \times 10^{-7}T^3) + X(1 - X)(3600 + 0.58T(1 - \ln T)) \text{ cal/mole} \quad \dots (17)$$

The thermodynamic properties calculated on the basis of this analysis were found to be in good agreement with the measured values.

Using similar reasoning to the above, Kaufman<sup>(141)</sup> derived equations for  $\Delta F^{\alpha-\gamma}$  and  $\Delta F^{\epsilon-\gamma}$  in the Fe - Ru system i.e.

$$\Delta F_{[T.X]}^{\alpha-\gamma} = (1 - X) \Delta F_{Fe}^{\alpha-\gamma} + X \Delta F_{Ru}^{\alpha-\gamma} - X(1 - X)(3800 - 2.5T) \text{ cal/mole} \quad \dots (18)$$

$$\Delta F_{[T.X]}^{\epsilon-\gamma} = (1 - X) \Delta F_{Fe}^{\epsilon-\gamma} + \Delta F_{Ru}^{\epsilon-\gamma} + X(1 - X) 1800 \text{ cal/mole} \quad \dots (19)$$

The driving force for the martensitic f.c.c.  $\rightarrow$  b.c.c. reaction was found to be temperature dependent and similar to that observed for Fe - Ni alloys. The driving force for the martensitic f.c.c.  $\rightarrow$  h.c.p. reaction was about 50 cal/mole (210 J/g) and, as expected from crystallographic considerations, was smaller than the corresponding f.c.c.  $\rightleftharpoons$  b.c.c. driving force.

#### 2.4.1. Magnetic Effect in the Martensite Transformation

Several gamma loop elements which raise  $T_0$  also lower  $M_S$ . To account for this anomaly Zener<sup>(70)</sup> has proposed a two parameter theory that recognises the role played by magnetic changes in iron-base alloys. The change in free energy  $\Delta F_{Fe}^{\alpha-\gamma}$  is treated as the sum of two components, one non-magnetic and the other magnetic.

$$\Delta F_{Fe}^{\alpha-\gamma} = \Delta F_{Fe}^{\alpha-\gamma} \text{ (NON-MAG)} + \Delta F_{Fe}^{\alpha-\gamma} \text{ (MAG)} \quad . . . (20)$$

The significance of this separation is shown in figure 18. The linear part of the curve below  $500^\circ\text{C}$  represents the free energy change in the absence of magnetic uncoupling, and the curve, A, deviating from the linear curve above  $500^\circ\text{C}$ , is the effect due to uncoupling. The free energy change actually occurring is the algebraic sum of these component curves. The extended curve, B, is regarded as the non-magnetic component of the free energy change, and represents the change in free energy associated with the transformation in the absence of magnetic uncoupling.

Zener<sup>(70)</sup> proposed that on addition of a solute atom, the magnetic and non-magnetic terms in equation (20) are affected independently, producing vertical shifts along the temperature axis proportional to the amount of solute added.

$\Delta T_{(NM)}$  and  $\Delta T_{(MAG)}$  are defined as the shifts produced in the non-magnetic and the magnetic components respectively, by the addition of 1% of solute. Thus he was able to show that the driving force at temperature T is:

$$\begin{aligned} \Delta F_{(T)}^{\alpha'-\gamma} &= -1.41(T_1 - T_2) + \Delta F_{Fe(MAG)}^{\alpha-\gamma} \cdot (T_2) + \Delta F_{Fe(NM)}^{\alpha-\gamma} \cdot (T_2) \\ &= -1.41(X)(\Delta T_{(MAG)} - \Delta M_s) + \Delta F_{Fe}^{\alpha-\gamma} \cdot (T_2) \quad \dots (21) \end{aligned}$$

where X is the weight per cent of solute added,

$$T_1 = (T - X \Delta T_{(NM)}) = (T - X \Delta M_s)$$

$$T_2 = (T - X \Delta T_{(MAG)})$$

and  $\Delta M_s$  is the change in martensite start temperature produced by the addition of 1.0% alloying element. The effect of the additional element is not easily explained in terms of physically measurable quantities. For example, the effect of the additional element on magnetic coupling can only be measured by its effect on the Curie temperature, which in this case shows no obvious correlation with the variation of calculated parameter  $\Delta T_{(MAG)}$ . Without verification of the parameter  $\Delta T_{(MAG)}$  the predicted values of  $\Delta F^{\alpha'-\gamma}$  cannot be used with confidence.

According to Zener<sup>(70)</sup>, the free energy change for the  $\gamma$  to  $\alpha$  transformation in the Fe - Cr system may be represented by the equation:

$$\Delta F^{\alpha-\gamma} = (1 - X) \Delta F_{Fe}^{\alpha-\gamma} + X \Delta H_{Cr} \quad \dots (22)$$

Assuming an ideal solution by definition the heat of mixing term  $\Delta F_M^{\alpha'-\gamma}$  of equation (4) becomes zero and

$$\Delta F_{Cr}^{\alpha-\gamma} = RT \ln \frac{X_\gamma}{X_\alpha} \quad \dots (23)$$

Substituting the values of  $X_\gamma$  and  $X_\alpha$  corresponding to the gamma loop maximum we obtain a value of  $\Delta H_{Cr}^{\alpha-\gamma} = 150$  cal/mole (630 J/g) and equation (22) becomes:

$$\Delta F^{\alpha'-\gamma} = (1 - X) \Delta F_{Fe}^{\alpha-\gamma} + 150X \text{ cal/mole} \quad \dots (24)$$

Fisher et al. (142) estimated  $\Delta H_{Cr}^{\alpha-\gamma}$  to be about -1200 cal/mole (5040 J/g) at about 600°K. As the addition of Cr causes the formation of a gamma loop, however, it is reasonable to assume that it increases 'T<sub>0</sub>' and the estimate would appear to have the wrong sign and the free energy change is estimated to be:

$$\Delta F^{\alpha-\gamma} = (1 - X) \Delta F_{Fe}^{\alpha-\gamma} + 1200 X \text{ cal/mole} \quad \dots (25)$$

Kaufman (128) derived an explicit expression for the free energy change in the iron-chromium system:

$$\begin{aligned} \Delta F^{\alpha-\gamma} &= (1 - X) \Delta F_{Fe}^{\alpha-\gamma} + X(460 + 1.0T) \\ &\quad + X(1 - X)(-2,800 + .75T) \text{ cal/mole} \quad \dots (26) \end{aligned}$$

In an attempt to rationalise the different estimates of  $\Delta H_{Cr}^{\alpha-\gamma}$  Kaufman wrote equations (26) in the same form as (24) and (25) so obtaining

$$\Delta H_{Cr}^{\alpha-\gamma} = (460 + 1.0T) + (-2,800 + .75T) \text{ cal/mole}(1 - X) \dots (27)$$

If the alloys are considered as being dilute (1 - X) is approximately equal to 1.

$$\Delta H_{Cr}^{\alpha-\gamma} = (460 + 1.0T) + (-2,800 + .75T) \text{ cal/mole} \quad \dots (28)$$

At 1,410°K, which is the gamma loop maximum, equation (28) gives  $\Delta H_{Cr}^{\alpha-\gamma}$  of 127 cal/mole (534 J/g) comparing favourably with Zener's ideal solution approximation when evaluated at the loop maximum. At 600°K however, equation (28) gives a  $\Delta H_{Cr}^{\alpha-\gamma}$  of -1290 cal/mole (5420 J/g) which compares well with the value of -1,200 cal/mole (5040 J/g) as obtained by Fisher et al.

Owing to the different assumptions made in the ideal

solution approximation and the regular solution approximation, it is difficult to substantiate this comparison as a rigorous thermodynamic analysis.

Although the assumptions made in Zener's ideal solution approximation are rather sweeping when considering anything but dilute solid solutions, it nevertheless provides a means of estimating the free energy change involved in martensitic reactions. The Kaufman regular solution approximation, however, allows explicit equations to be derived for the system under investigation, using known data to find values for the various constants introduced, thus permitting a closer estimate of  $\Delta F^{\alpha'-\gamma}$  to be obtained.

Kaufman's value of 50 cal/mole (210 J/g) for the driving force involved in the  $\epsilon - \gamma$  reaction in the Fe - Ru system, explains why this reaction is preferred in other systems e.g. Fe - Mn, where the  $\epsilon$  phase appears as a transitory state in the  $\gamma \rightarrow \epsilon \rightarrow \alpha$  transformation; the direct  $\gamma \rightarrow \alpha$  transition being less desirable on the grounds that the driving force required is some 200 plus cal/mole (838 J/g).

## 2.5. Kinetics of Martensite Transformations

For the martensite transformation to take place the parent phase has to be retained down to the  $M_S$  temperature. This requires cooling so as to exceed some critical rate the value of which depends upon composition, grain size, and previous thermal and mechanical history. Once the  $M_S$  temperature has been reached subsequent martensite transformation may occur athermally or isothermally.

### 2.5.1. Athermal Reactions

In most systems transformation occurs only during cooling and ceases if the temperature is held constant below  $M_S$ . The fraction transformed is a function of the temperature to which the specimen has been taken. The temperature at which transformation is complete is known as the  $M_F$  temperature. The needles grow at a very high speed, which is of the order of the speed of sound in the material and this high speed is maintained down to temperatures of liquid helium ( $4^{\circ}\text{K}$ ) (176). It follows that the activation energy for growth is virtually zero. Two types of athermal growth may be recognised. In the first, once a nucleus becomes active the interface advances rapidly until stopped by a grain boundary or some other structural obstacle in the parent crystal. The rate of transformation in this case is governed by the number of nuclei and size of the martensite plates. The above reaction is found in a system in which there is a large barrier to the formation of nuclei of the product phase. The  $M_S$  temperature is considerably below ' $T_0$ ' so that once a nucleus has formed there is sufficient free energy available to cause it to propagate at a fast rate. Such a system exhibits considerable hysteresis between  $M_S$  for the cooling reaction and  $A_S$  for the corresponding reverse reaction, e.g. for an Fe - 10% Mn alloy the gap is about  $500^{\circ}\text{C}$ .

The second type of athermal reaction involves the discontinuous growth of existing plates in addition to the nucleation of new ones as the temperature falls. In this case the barrier to nucleation is small and  $M_S$  is close to

' $T_0$ '. Thus there is little free energy available to overcome the elastic strain. At any temperature a plate grows rapidly at roughly the same speed as in the previous case until the strain energy builds up to a point at which it equals the driving force when growth abruptly ceases. Further cooling makes available additional free energy enabling rapid growth to proceed until either a new balance point is reached or a structural obstacle blocks the interface. An example of this type of reaction is found in the Au - Cd system: for an approximately equiatomic alloy the difference between  $M_S$  and  $A_S$  is  $16^\circ\text{C}$ .

### 2.5.2. Isothermal Martensite Reactions

The majority of martensite reactions are athermal although a number of isothermal reactions are known. In some systems the isothermal reaction follows the athermal reaction when cooling is stopped and the temperature held. Complete isothermal transformation is known to occur in a few alloys, and in these cases a C curve T.T.T. diagram results. The active temperature range is usually below room temperature as shown in figure 19 for an Fe - Ni - Mn alloy. Isothermal martensite is structurally indistinguishable from athermal martensite. The reaction rate is governed by the rate of nucleation and the size of the fully grown plate. Isothermal reactions show that growth can be thermally activated in some systems.

The isothermal reaction observed in the uranium-chromium alloys<sup>(59-62)</sup> is rather exceptional in that it proceeds largely by the slow growth of existing plates with

virtually no new nucleation. In isothermal reactions the driving force is constant and if growth is slow then the restraints must decrease with time. It has been suggested that the elastic stresses are reduced by thermally activated plastic deformation in the product or matrix or both. An alternative is that the complexity of the atom movement renders the interface relatively immobile and some small scale readjustment of the atoms at the interface has to occur to enable growth to proceed. If this is so, then the reaction should be classed with the massive reactions previously mentioned.

### 2.5.3. Autocatalytic Effects

The stresses generated around a martensite plate may induce the nucleation and growth of other plates nearby. This phenomenon is known as the autocatalytic effect and often gives rise to 'bursts' of transformation resulting in discontinuities in the fraction transformed-temperature graph. This phenomenon is particularly evident in Fe - Ni - C alloys, when it is associated with audible clicks and the liberation of heat.

### 2.5.4. Thermal Stabilisation

If cooling is interrupted above  $M_S$ , it is sometimes found that the  $M_S$  is depressed. Similarly if cooling is interrupted below  $M_S$  in an athermal reaction, transformation does not commence immediately when cooling is resumed. This phenomenon is known as thermal stabilisation. It was at one time, thought to be an essential characteristic of the

martensite transformation but there is now evidence to show that it only occurs in alloys containing interstitial solutes. It is thought likely that the interstitial atoms migrate to form Cottrell atmospheres making the matrix more resistant to atomic displacements involved in the martensite formation.

### 2.5.5. Nucleation of Martensite

An understanding of the kinetics of the martensite transformation depends upon a quantitative understanding of the rate of nucleation. Although several attempts have been made to compare calculated and measured rates no satisfactory theory is yet available. The general ideas of homogeneous nucleation and growth have been applied to martensitic reactions in steels, usually with the assumption that the original embryos and the succeeding nuclei are small discs or oblate spheroids. The conclusions cannot be reconciled with the existence of  $M_s$  temperatures and rapid rates of reaction at 4°K. It has also been shown that in some non-ferrous martensite changes the nucleation is heterogeneous. For these and other reasons the theory of homogeneous nucleation in martensitic changes has been discarded. The following discussion indicates the type of approach that has been used.

If the supposed embryos are in the form of oblate spheroids of radius  $r$  and thickness  $2c$  (figure 20) and if  $r$  is much greater than  $c$ , the volume is approximately  $\frac{4}{3}\pi r^2 c$  and the surface area  $2\pi r^2$ . The free energy of formation of one embryo  $\Delta G$  is:

$$\Delta G = \frac{4}{3}\pi r^2 c \Delta G_V + 2\pi r^2 \gamma + \frac{4}{3}\pi r^2 c \left( A \frac{c}{r} \right) \quad . . . (29)$$

where  $\Delta G_v$  is the change in free energy per unit volume of martensite,  $\gamma$  is the interfacial energy and 'A' is the elastic strain energy constant defined so that  $A_c/r$  is the energy per unit volume of the embryo. The activation energy W for the formation of a critical nucleus is the value for which  $\delta(\Delta G)/\delta c = \delta(\Delta G)/\delta r = 0$ .

Differentiating the above equation and applying these conditions:

$$r_c = \frac{4A\gamma}{(\Delta G_v)^2}$$

$$c_c = \frac{-2\gamma}{\Delta G_v}$$

$$W = \frac{32}{3} \pi \frac{A^2 \gamma^3}{\Delta G_v^4}$$

where  $r_c$  and  $c_c$  refer to the critical nucleus. Since the activation energy for growth is negligible it is reasonable to assume that the equilibrium distribution of embryos is maintained even down to the lowest temperatures. Further, it may be shown by means of the Volmer - Weber theory that the rate of nucleation is given by:

$$I = N \cdot v e^{-\frac{W}{KT}}$$

where N = the number of sites per unit volume at which embryos can form and v = the frequency of vibration of the atoms at the interface. The equation predicts a C curve dependence of I.

In this theory all martensitic reactions are essentially isothermal in nature. To account for athermal characteristics it is necessary to identify  $M_s$  as that temperature at which the isothermal nucleation rate becomes appreciable, say

1 nucleus per sec/cm<sup>3</sup>.  $\Delta G_v$  increases with undercooling and from the above equation it follows that I increases extremely rapidly as the temperature is decreased to the nose of the C - curve. At any temperature above  $M_s I \ll 1$  and an isothermal reaction is not observed. Similarly below  $M_s I \gg 1$  and an isothermal nucleation cannot be suppressed by the most rapid quench. Fisher applied this theory to the isothermal martensitic reaction in an Fe - Mn - Ni alloy<sup>(63)</sup>. In this theory the value of  $M_s$  for any alloy is that temperature at which  $\log I = 0$ , so that any alloy for which the nucleation frequency is less than unity should not transform athermally during cooling to 0°K. Thus the theory predicts that alloys containing more than 30.1% Ni should not transform. In fact, alloys up to 33% Ni transform isothermally.

Cohen<sup>(64)</sup> using a dislocation model of the interface, calculated for an Fe - 30% Ni alloy (with an  $M_s$  of - 40°C and  $\Delta G_v = 315$  cal/mole (1322 J/g) ) that the interfacial energy ( $\gamma$ ) was 200 ergs/cm<sup>2</sup>. The dimensions of the resulting embryo were found to be  $r_c = 490 \text{ \AA}$ ,  $c_c = 22 \text{ \AA}$  with an activation energy (W) of  $13 \times 10^7$  cal/mole ( $545 \times 10^6$  J/g). The chances of such a nucleus arising by thermal activation are negligible, and thus homogeneous nucleation is unlikely in this system.

#### 2.5.6. Heterogeneous Nucleation

The most straight forward clues that martensite nucleates at preferred sites rather than in a random fashion comes from metallographic studies. In instances where the martensite transformation can be reversed, as in the case of

beta brass<sup>(65)</sup>, the position and formation sequence of the plates on cooling are repeated precisely in the cooling cycle: after complete reversal of the transformation by heating between the cooling cycles. This behaviour certainly suggests that preferred nucleation sites exist in the parent phase. The martensite produced on cooling a single crystal of gold -47.5% cadmium<sup>(66)</sup> consists typically of many plates but if the single crystal is first annealed at a relatively high temperature in the austenite type phase the nucleation pattern on cooling is changed so that a single unit of martensite can be generated, with only one interface sweeping through the specimen. It is evident here that nucleation is not a random process.

Cech and Turnbull<sup>(67)</sup> carried out a series of experiments which have a bearing on this subject. They austenitised and quenched tiny particles of an iron-nickel alloy into the martensite range. It was found that the reaction started at widely different temperatures among the particles and some did not transform at all down to the lowest temperatures reached even though they were of the same composition. Some of the particles evidently contained fewer effective sites than others and hence supercooled further. It may be noted that although the particles were sufficiently small to disclose the heterogeneity of the process they were more than large enough to allow homogeneous nucleation to come into play had it been operative. Particles larger than 100 microns had  $M_s$  temperatures comparable to that of bulk specimens.

It is possible to assume that a number of sites exist in the parent phase having a spectrum of energy barriers.  $M_s$  is that temperature at which the driving force is sufficient to overcome the energy barrier of the most effective site. During cooling, the preferred sites are activated as the temperature drops with the larger embryos being consumed first and then the smaller ones requiring progressively more super-cooling. Unfortunately, when numerical comparisons are made disparities exist.

The strain nucleus theory is a special case of the heterogeneous nucleation theory. Cohen, Machlin and Paranjpe<sup>(68)</sup> introduced the idea that dislocation arrays or other lattice imperfections may provide 'strain embryos' which survive the usual austenitising treatment and produce centres of high energy suitable for the nucleation of martensite. This idea was carried further by Knapp and Dehlinger<sup>(69)</sup> and by Kaufman and Cohen<sup>(4)</sup>.

Using the Frank model of the austenite-martensite interface Knapp and Dehlinger assumed that the martensite embryo is a thin oblate spheroid bounded by loops of dislocations as shown in figure 20b. These loops consist mainly of screw dislocations with short edge components. Expansion of the loops causes growth in the  $\langle 110 \rangle$  and  $\langle 225 \rangle$  directions, whilst new loops must be added to produce growth in the  $\langle 554 \rangle$  direction. The treatment of Knapp and Dehlinger is unsatisfactory in that it does not explain why an embryo forms. In order to overcome this difficulty Kaufmann and Cohen retained the idea that embryos are concerned with dislocation arrays.

11

They regard the free energy of austenite as being increased by the presence of dislocations and the coalescence of these dislocations into an interface as lowering the strain energy sufficiently to permit the formation of a martensite embryo. At high temperatures above  $T_0$  the size of the critical embryo in the sense of the classical nucleation theory increases as the temperature falls (because  $\Delta G^{\alpha-\gamma}$  decreases) and so on cooling an austenitic specimen, the embryos tend to coalesce and this involves diffusion which may be so slow that the critical nucleus size is never attained. The catastrophic growth of the embryo into a martensite plate is, as in the treatment of Knapp and Dehlinger, regarded as occurring when the driving force becomes sufficient to expand existing dislocation loops, and to create new loops: this is regarded as occurring at a critical nucleus radius which can be calculated by assuming that the array of dislocations shown in figure 20b can be replaced by a dislocation loop lying in the  $\{225\}$  plane. If the energy of the loop is  $Wl$ , the relationship between  $Wl$  and  $\Delta W$  as functions of  $r$  are of the form shown in figure 20c.

As soon as the size of the embryo reaches  $r^*$  it may expand spontaneously, if the thermal fluctuations are sufficiently great, whereas, once the size of the nucleus reaches  $r_c$ ,  $Wl$  begins to decrease and  $\Delta W$  falls so rapidly that the expansion can occur catastrophically without thermal fluctuation. After a given austenitising treatment, the austenite will contain dislocation embryos of varying sizes and on cooling, the catastrophic martensite transformation

will begin when the largest embryo size is equal to  $r_c$  for the temperature concerned. It would be expected that the isothermal formation of martensite would be more common than is actually the case and that  $M_s$  would not be such a definite characteristic of a steel of a given composition.

There has been a tendency in recent years to think of twins as forming the austenite-martensite interface instead of dislocation interfaces, both may, however, be involved.

## 2.6. Effect of Applied Strain on the Martensite Transformation

The effect of applied strain on the martensite reaction in Fe - Ni alloys has been studied in some detail by Scheil<sup>(71)</sup>. Data are also available for lithium and lithium-magnesium alloys<sup>(72)</sup>, copper-zinc<sup>(65)</sup> and copper-aluminium alloys<sup>(73)</sup>, austenitic stainless steels<sup>(74-79)</sup> and manganese steels<sup>(80-82)</sup>. It was found that under certain conditions martensite formation can be induced isothermally even at temperatures above  $M_s$  by the mechanical deformation of the parent phase. When stress is applied to an alloy, such as during a cold working process, the mechanical energy interacts with the thermodynamics of the martensite reaction as shown by Patel and Cohen<sup>(83)</sup>. In figure 21  $F^\gamma$  and  $F^{\alpha'}$  (free energy of alpha martensite) represent the relative conditions in the unstressed system and  $F^{\gamma'}$  and  $F^{\alpha'}$  are the conditions in the strained system where  $F^\gamma$  and  $M_s$  are displaced by an amount  $\Delta G_E^{\gamma-\alpha'}$  the mechanical energy due to

the applied stress.

$$\Delta F^{\gamma - \alpha'}_{l_{M_S}} = \Delta G_E^{\gamma - \alpha'} + \Delta F^{\gamma - \alpha'}_{l_{M_S}} \quad . . . (30)$$

It can be seen that the  $M_S$  in the unstrained system can be moved to a higher temperature  $M_S$  because at this temperature the algebraic sum of the mechanical and thermodynamic energies is equal to  $\Delta F^{\gamma - \alpha'}_{l_{M_S}}$ , the critical cooling energy at  $M_S$ . Thus cold working at temperatures above  $M_S$  may result in the formation of martensite and the response to such treatment will depend upon the chemical analysis and also on the temperature of cold work. (Figures 22 and 23).

In the study of the mechanical properties of cold worked materials both the cold working process and the tensile testing itself must be regarded as cold working. When cold rolled materials are strained during tensile testing the amount of strain that can take place is controlled by the type of deformation that has taken place previously. In alloy compositions of the  $\gamma$  austenite type in which extensive slip has already occurred further slip to produce tensile elongation at room temperature will be limited. If the temperature of testing is lowered slip becomes more difficult and martensite formation is favoured; consequently, elongation values increase as the test temperature decreases.

Watson and Christian<sup>(84)</sup> showed this effect in cold worked stainless steels. They demonstrated that the ductility of standard grades in the cold worked condition increased as the temperature of testing decreased, although at very low temperatures the ductility reached a maximum then decreased.

This increase in ductility was shown to have been produced by the formation of martensite during tensile testing.

The influence of plastic strain is quite pronounced with respect to both the  $M_S$  point and the reaction rate. Schiel's results shown in figure 24 were obtained by compressing a series of samples at different temperatures. For a given temperature, the amount of transformation increases with the amount of cold work. When slip planes are produced in the parent phase, the  $M_S$  point on subsequent cooling is lowered apparently because of the introduction of extra barriers. Thus a parent phase with slips bands acts as if it were a fine grained material, with a lower  $M_S$  temperature.

Schiel also studied the effect of tension after previous compression. A specimen of Fe - 30% Ni alloy with an original  $M_S$  of  $5^{\circ}\text{C}$  was plastically deformed at  $100^{\circ}\text{C}$ . Its new  $M_S$  was  $-5^{\circ}\text{C}$ , the decrease being presumably due to the introduction of slip planes at the high temperature of deformation. Elastic stress changed the  $M_S$  as follows:

<u>Tensile Stress p.s.i.</u>	<u><math>M_S^{\circ}\text{C}</math></u>
1,760	-5
17,600	+5
35,200	+14

The phenomenon corresponds to a 'Bauschinger effect' in that the tensile stress tries to undo the effect of previous compression.

Considerable data are available on the effect of cold work on the  $\gamma - \alpha'$  transformation in stainless steels<sup>(74)</sup>. The usual 18% Ni - 8% Cr steel has an  $M_S$  point below room

temperature and can form ferrite by a martensite reaction as discussed above.

Llewellyn and Murray<sup>(85)</sup> studied the effect of alloying additions on the work hardening rate of stable austenitic structures. Alloying additions of 10% Co, 10% Mn, 10% Ni, and 4% Cu were made to a basic 18% Cr - 13% Ni alloy. Results of tests on the alloys in the solution treated condition are shown in figure 25. It can be seen that 10% Mn causes a very slight increase in work hardening whereas a similar addition of cobalt causes a considerable increase. They also show that C and Cr additions also increase the rate of work hardening. These effects are consistent with expected changes in the stacking fault energy of the austenitic structure. An alloying element such as cobalt readily undergoes transformation from cubic to a hexagonal structure and such a condition is recognised as being indicative of low-stacking fault energy. The association of the hexagonal structure and stacking faults arises out of the fact that a hexagonal structure would be formed by having stacking faults on alternate planes in a f.c.c. lattice. From the data it was concluded that nickel and copper raise the stacking fault energy and decrease the rate of work hardening of 18% Ni 8% Cr type steels, whereas the stacking fault energy and the rate of work hardening are respectively decreased and increased progressively by Mn, Cr and Co. Carbon is generally thought to lower the stacking fault energy but the marked effect on the rate of work hardening could be explained by dislocation atmosphere effects.

Dulieu and Nutting<sup>(133)</sup> studied the influence of solute additions on the stacking fault energies of austenites by measuring the radii of dissociated nodes, and by measuring the twin interface frequency per grain after a recrystallising anneal. On the assumption that there is a monotonic variation of stacking fault energy with atom per cent of solute over the range of the solute concentration used, the change in stacking fault energy per atom per cent of solute was calculated. A corresponding adjustment to the measured stacking fault energy was then made and the variation in stacking fault energy per atom per cent recalculated. See table 1 and figure 26. Further experiments showed that the addition of 5% Mn lowered the stacking fault energy by 3 ergs cm<sup>-2</sup>. The 18% Cr 10% Ni base material had a stacking fault energy of 10 ergs cm<sup>-2</sup>.

Considering Spreadborough's<sup>(134)</sup> treatment of the directed bonding theory of Altmann<sup>(135)</sup>, suggesting that it was possible to predict the relative stabilities of the three common structures, fcc, hcp and bcc by considering the electron contributions to the hybrid orbitals, Dulieu concluded that increasing the number of d-electrons available for bonding will favour the transition fcc → hcp → bcc. With a constant d-electron distribution an increase in s-electrons will favour the transition fcc → hcp or bcc. This implies changes in electron configuration will change the relative stabilities of fcc and hcp structures under conditions where the fcc structure is more stable and that this will become more apparent through a change in stacking fault

energy. Thus an increase in the number of bonding d-electrons, or of s-electrons, if the d-electron density remains constant, should be associated with decreasing stacking fault energy. Also, where the bcc structure is becoming more stable, there should be a decrease in stacking fault energy.

## 2.7. Strengthening Mechanisms in Martensite

Considerable progress has been made in recent years in gaining an understanding of the hardening mechanisms of martensite but the overall position is still rather confused.

The controversy has arisen from theories which attribute the strength of martensite in steels (a) to carbon atoms in solution and (b) to the fine twinning in the product. The evidence in favour of solid solution strengthening by carbon atoms is that the strength of carbon free martensite is not very high. The most convincing experiments were made by Winchell and Cohen<sup>(86-89)</sup>. Their experiments were conducted on a series of Fe - Ni - C alloys the compositions being adjusted to give a low  $M_s$  of about  $-40^\circ\text{C}$  to eliminate as far as possible the effects of auto-tempering. All the martensites examined were twinned. The flow stress was found to be a strong function of the carbon content, and the strengthening was independent of the test temperature except for ageing effects at higher temperatures. In the low carbon content region, the increase in flow stress measured was approximately  $2.3 \times 10^6 \text{ lb/in}^2/\text{W/oC}$  which compares with the values of about  $1.9 \times 10^6 \text{ lb/in}^2/\text{W/oC}$  determined by Wert<sup>(97)</sup> and  $0.6 - 0.75 \times 10^6 \text{ lb/in}^2/\text{W/oC}$  determined by other

workers.<sup>(90,91,177)</sup>

Stephenson<sup>(90)</sup>, and Cracknell and Petch<sup>(91)</sup> found the flow stress of ferrite to increase linearly with the carbon content, but other workers have reported that stress increases less rapidly than this. Winchell and Cohen obtained a straight line relationship when they plotted the flow stress against the cube root of the carbon concentration. More recent models according to Fleischer et al. assume that dislocations interact appreciably only with solute atoms close to the core. Mordike and Haasen<sup>(92)</sup> suggested a cube root dependence when considering the effect of interstitials on pure iron but this requires three dimensional bending and is improbable. If the dislocations are confined to slip planes and interaction is short range, the stress may vary with the square root of the atomic fraction. Winchell and Cohen's results, when plotted in this way (figure 27) give a straight line of slightly greater slope than that obtained from Wert's results for ferrite. This slope is approximately  $\mu/9$ , where  $\mu$  is the shear modulus, and corresponds to a slope of approximately  $\mu/18$  for the corresponding shear stress relationship: the equivalent value for ferrite is  $\mu/20$ <sup>(93)</sup>. This is a high rate of hardening but appreciably smaller than the theoretical value of  $0.4\mu$  obtained from Fleischer's<sup>(93)</sup> model of solid solution hardening.

In the case of Fe - Ni - C martensites, ageing has been found to occur at all temperatures above  $-60^{\circ}\text{C}$  and it is for this reason that there are no comparable results on martensite in plain carbon steel to compare directly with those

of Winchell and Cohen.

The suggestion that the twin substructure is responsible for much of the strength of martensite is due to Kelly and Nutting<sup>54,94,95</sup>). Kelly's theory attributed a considerable part of the increase in hardness with increasing carbon content to an increasing proportion of twinned plates, and a similar effect was suggested as part of the explanation for the increase in strength resulting from ausforming. Radcliffe and Schatz<sup>(96)</sup>, and Roberts determined the increase in hardness of Fe - Ni alloys with increasing nickel content. Up to about 5% Ni the hardness increases with increasing nickel and then remains nearly constant. Since the change from massive to acicular martensite (twinned) occurs at about 30% Ni it would appear that the substructure has little effect. The good agreement between hardening rates produced by carbon additions in ferrite and martensite (figure 27) together with the absence of a detectable substructure effect on strength, seems to suggest that hardening is predominantly due to carbon in solution. The main evidence that carbon is in solution and not clustered comes from Werts<sup>(97)</sup> and Stephenson's<sup>(90)</sup> comparable results on ferrite where internal friction methods were used, but the possibility of precipitation even here has been raised.

### Summary

Several types of transformation of a military or semi-military type have been found in both ferrous and non-ferrous alloy systems. These types may be categorised as follows:

- (i) massive transformations;

- (ii) massive martensite transformation
- (iii) acicular martensite;
- (iv)  $\epsilon$  - martensite.

### Massive Transformations

(i) No change in bulk composition occurs on quenching and in this sense the transformation may be regarded as diffusionless.

(ii) The interface between parent and product phases is incoherent and extremely rapid transfer of atoms must take place.

(iii) The free energy change is only 20 - 80 cal/mole compared with the 300 cal/mole for the martensite transformation.

(iv) The grains grow across pre-existing parent grain boundaries.

(v) Found in both substitutional and interstitial solid solution alloy systems.

### Massive Martensite

(i) Is a body centred cubic structure in iron alloys which gives very broad and diffuse X-ray reflections because of internal distortions.

(ii) The massive structure is regarded as being made up of sheared plates, or groups of laths, the irregular outline of the product being due to the impingement of plates at the grain boundary interface.

Special etching techniques have shown that the grains have a lath type substructure.

(iii) The massive slabs do not cross the boundaries of the pre-existing austenite grains.

(iv) Massive martensites have been shown to form by both athermal and isothermal processes.

(v) The habit plane in Fe - Ni alloys is  $\{111\}_\gamma$  since the shear plates form from and parallel to annealing twin interfaces which are  $\{111\}_\gamma$  planes. The shear direction of the laths is within a few degrees of  $[1\bar{1}0]_\gamma$  for the variant of the orientation relationship:

$$\begin{array}{l} (111)_\gamma \parallel (101)_\alpha \\ [1\bar{1}0]_\gamma \parallel [11\bar{1}]_\alpha \end{array}$$

Acicular Martensite

(i) Has a B.C.T. lattice above 0.6%C, which results from carbon atoms occupying the octahedral interstices of the B.C.C. lattice.

(ii) The crystallographic changes involved in the transition  $\gamma - \alpha'$  have been accounted for by a homogeneous shear followed by a macroscopic heterogeneous shear, which takes the form of fine slip, twinning or a mixture of both depending upon the composition.

Over the years a phenomenological theory has been developed to explain the diffusionless formation of martensite, which may be expressed in symbolic terms as:

Shape = Lattice x Lattice invariant

that is, the observed shape deformation occurring under experimental conditions may be expressed in terms of a lattice deformation followed by a lattice invariant

deformation, the former accounting for the surface tilting. The variations postulated by Bowles and Mackenzie, and by Wechsler, Lieberman and Read have been shown to be basically the same.

(iii) Acicular martensite has been found to form by both athermal and isothermal mechanisms.

(iv) The free energy change involved in the gamma to alpha martensite transformation is about 300 cal/mole (1256 J/g) for iron-carbon martensites but has been found to vary with the percentage of alloying element present.

(v) Both Kurdjumov-Sachs, and Nishiyama relationships have been observed in ferrous alloy systems, while the habit plane is either  $\{225\}$  or  $\{259\}$ . Sometimes, the two habits appear together the relative proportions of each changing with temperature of formation.

#### Epsilon-Martensite

(i) The  $\gamma \rightarrow \epsilon$  transformation is regarded as the simplest type of martensite transformation. It may be accomplished if a Shockley partial dislocation of Burgers vector  $\frac{a}{6} \langle 11\bar{2} \rangle$  moves through alternate planes of a parallel set of  $\{111\}$  planes.

(ii) There are three equivalent shear directions which are chosen at random, the effect of this is to reduce the homogeneous shear observed.

(iii) Epsilon-martensite is regarded by some authors as a metastable stage in the transition  $\gamma \rightarrow \epsilon \rightarrow \alpha'$ .

(iv) The transition to epsilon-martensite is preferred because the driving force required is lower than that for

transformation to alpha-martensite.

(v) The orientation relationship between the three phases has been found to be:-

$$\begin{array}{llll} (111)_{\gamma} \parallel (0001)_{\epsilon} \parallel (101)_{\alpha} & \text{For } \gamma \text{ and } \alpha \text{ this} \\ [1\bar{1}\bar{0}]_{\gamma} \parallel [1\bar{2}10]_{\epsilon} \parallel [11\bar{1}]_{\alpha} & \text{is the Kurdjumov-} \\ & \text{Sachs Relationship} \end{array}$$

### General Comments

#### (i) Effect of Applied Strain

- (a) The influence of plastic strain is quite pronounced with respect to both  $M_S$  point and the reaction.
- (b) For a given temperature the amount of transformation increases with the amount of cold work.
- (c) When slip planes are produced in the parent phase, the  $M_S$  point on subsequent cooling is lowered apparently because of the introduction of extra barriers.

#### (ii) Nucleation

- (a) The general ideas of homogeneous nucleation theory have been applied to martensitic reactions and have been found wanting, being discarded in favour of the heterogeneous theory of nucleation.
- (b) The reversibility of some of the martensite transformations suggests that preferred nucleation sites do exist.

(c) The strain nucleus theory postulates the existence of strain embryos which survive the usual austenitising treatment and produce centres of high energy suitable for the nucleation of martensite. Such centres have been observed in Fe - Ni alloys by transmission electron microscopy<sup>(143)</sup>.

### 3.0. Strengthening mechanisms in non-martensitic or partially martensitic structures

In addition to the strengthening effect of the martensite transformation various other factors are superimposed to give the observed mechanical behaviour under load.

In general polycrystalline metals have a much higher yield strength than single crystals due mainly to the high rates of strain brought about by the presence of grain boundaries.

Small angle boundaries may be described by a vertical wall of dislocations, which separate crystals with only a small difference in orientation. Generally, however, grain boundaries separate crystals which usually differ in orientation by relatively large angles. Such boundaries may still be described by an arrangement of dislocations, which is necessarily complex, the individual dislocations being not easy to recognise. As the orientation difference between grains on either side of the boundary decreases, the state of order of the boundary increases. Ordinary high angle boundaries have high surface energies somewhere in the region of

600 ergs/cm<sup>2</sup> while the twin boundary is only about 25 ergs/cm<sup>2</sup>. It is also usually found that there is a higher concentration of solute atoms in grain boundaries than present in the interior of the grain. This is because the different sized solute atoms are more easily accommodated at the distorted region of the boundaries. As a result of this the strain energy is lowered.

### 3.1. Strengthening Mechanism of Grain Boundaries

The strengthening effect of grain boundaries will depend upon the temperature of testing. It has been found that above approximately one half of the absolute melting point of the metal, that the grain boundaries are weaker than the interior of the grain. The temperatures considered in this investigation are in the region where grain boundaries may be expected to strengthen the metal.

There are two main mechanisms responsible for the strengthening effect of grain boundaries (a) the Barrier effect, (b) the complexity effect.

#### (a) The Barrier Effect

The grain boundary acts as a barrier to dislocation movement because it is a region of irregular lattice arrangement and the grains on either side are orientated at an angle to each other. This means that there is no continuity of slip planes across the boundaries. In metals with few slip systems the effect is greater. Thus the barrier effect is greater in h.c.p. than in b.c.c. or f.c.c. metals. As might be expected the effect is greater in fine grain metals than in coarse grain metals since the active length of slip plane

is smaller before pile-up at a grain boundary occurs. Subsequent dislocations pile-up behind the first until sufficient back stress is created to stop the source operating. Eshelby et al.<sup>(144)</sup> made a calculation relating slip displacement to grain size. The back stress exerted by a dislocation on its source varies inversely as the distance between the two. More dislocations are, therefore, needed near a grain boundary to offset the applied stress at the centre of a large grain than of a small grain. Their calculations showed that the number of dislocations  $n$  which can be compressed into the distance  $L$  between source and obstacle by a shear stress  $\tau$  is given by the equation:-

$$n = \frac{K \pi \tau L}{Gb} \dots \dots (31)$$

$K$  is equal to unity for screw dislocations and to  $(1 - \nu)$  where  $\nu$  is Poisson ratio, for edge dislocations.  $G$  is the shear modulus and  $b$  is the Burgers vector. The source will continue to produce dislocations because of the external stress  $\tau$  until the magnitude of the back stress  $\tau_b$  is equal to the applied stress less stress  $\tau_a$  necessary to activate the source.

$$\tau_b = \tau - \tau_a$$

The number of dislocations emitted by a source located at the centre of a grain of diameter  $d$  would be:-

$$n = \frac{K \pi \tau d}{4Gb} \dots \dots (32)$$

Petch<sup>(145)</sup> related yield stress and grain size supposing that yielding takes place when a critical stress ( $\sigma_c$ ), which is independent of grain size, is reached at the

head of a pile-up of dislocations at the grain boundary. Using the Eshelby, Frank and Nabarro relationship for an edge dislocation:-

$$n \sigma' = \frac{\pi \sigma'^2 d (1 - \nu)}{2Gb} = \sigma_0 \quad \dots \dots (33)$$

where n is the number of dislocations in the pile, and  $\sigma'$  is the effective applied stress thus:-

$$\sigma' = \sqrt{\frac{2Gb \sigma_0}{\pi d (1 - \nu)}} \quad \dots \dots (34)$$

The plots of yield stress versus  $d^{-\frac{1}{2}}$  when extrapolated back to  $d^{-\frac{1}{2}} = 0$ , indicated that a finite stress was still necessary for yielding. Petch assumed that an average internal stress  $\sigma_i$  has to be overcome by the applied stress  $\sigma$  so that  $\sigma' = \sigma - \sigma_i$ . Thus substituting in equation (34) and rearranging:-

$$\sigma = \sigma_i + \sqrt{\frac{2Gb \sigma_0}{\pi d (1 - \nu)}} \quad \dots \dots (35)$$

If the value of  $\sqrt{\frac{2Gb \sigma_0}{\pi (1 - \nu)}}$  is equated to a constant  $K_y$ , then the Petch relationship is established:-

$$\sigma_y = \sigma_i + K_y d^{-\frac{1}{2}} \quad \dots \dots (36)$$

The slope of the graph obtained when yield stress is plotted against  $d^{-\frac{1}{2}}$  is equal to  $K_y$  and the intercept at  $d^{-\frac{1}{2}} = 0$  is equal to  $\sigma_i$ .

The exact nature of the terms  $\sigma_i$  and  $K_y$  is subject to discussion, however. It is generally accepted that  $\sigma_i$  is a friction stress term indicating the resistance of the lattice to the passage of a dislocation.  $K_y$  may be regarded

as a term indicating the strength of dislocation locking, or the difficulty of nucleating slip in a neighbouring grain.

(b) Complexity Effect

Experimental observation has shown that cavities do not form at the grain boundaries, when a polycrystalline metal is deformed, until test temperatures of the order of half the absolute melting point are reached. Below this temperature it is, therefore, necessary for the polycrystalline aggregate to deform in a complex manner in order to maintain intergranular continuity. This effect is known as the complexity effect and accounts for a large proportion of the strengthening due to the presence of grain boundaries. G.I. Taylor has shown from theoretical considerations that for the grains to conform to each other's changing shape, individual crystals in a polycrystal must slip on at least five slip systems. This concept leads to two strengthening mechanisms: (a) When a stress below the yield stress is applied to a polycrystalline metal, it may be sufficient to cause yielding in certain grains which are favourably orientated. However, yielding is restrained until the applied stress is sufficient to activate slip in adjacent grains. Yielding is, therefore, delayed until the whole aggregate can deform together, thus resulting in an increased yield stress.

Because of the complexity effect, individual grains are forced to slip on several slip systems thus hardening by intersecting slip is more likely, Lomer-Cottrell locking and jog formation being mainly responsible.

The fact that multiple slip tends to be more marked

near grain boundaries in order to maintain intergranular cohesion means that strain hardening will be most rapid when the grain size is small enough for multiple slip to reach across each grain.

The degree to which any of the above mechanisms is operative in a particular metal is difficult to ascertain. As previously noted in section 2.6. it is also possible to bring about phase transformation, from  $\gamma \rightarrow \epsilon \rightarrow \alpha$  , by application of a certain strain which aids the chemical driving force involved. It has been observed experimentally that where transformation is preferred to slip that greater elongation values are obtained<sup>(84)</sup>. Presumably the more orderly arrangement of dislocations, produced by the transformation, provides fewer obstacles to further slip than when deformation is wholly slip in character.

### 3.2. Strengthening Effect of Alloying Elements

A number of mechanisms are believed to contribute to the strengthening effect of solute elements, although it is not known for certain which mechanism predominates in a particular system.

#### 3.2.1. Order or Fisher Hardening<sup>(146)</sup>

This hardening mechanism is believed to occur in alloys which are partly ordered on a local scale. This is presumably the case for most alloys since the solute-solvent bond energy is unlikely to be exactly halfway between that of a solvent-solvent and a solute-solute. The passage of a dislocation through a region of local order must diminish the degree of

order, which raises the internal energy and is reflected in a higher yield stress. The increase in yield stress is:

$$\tau = \frac{\gamma}{b} \dots \dots \dots (37)$$

where  $\gamma$  is the disordering energy per unit area of slip plane and  $b$  is the Burger's vector. This equation is based on the assumption that the passage of one dislocation completely destroys local order. The ordered nature of the structure will contribute to the locking term  $K\gamma$  and  $\sigma_i$  in the Petch equation as the structure will oppose movement of the dislocation which would leave a disordered structure in its wake.

### 3.2.2. Frictional Hardening Mechanisms

There are four possible frictional mechanisms whereby a solute introduces a resistance to the movement of a dislocation which is unaffected by strain, and may be regarded as a constant frictional force to be overcome during plastic deformation. This type of hardening mechanism will, therefore, contribute to the  $\sigma_i$  term of the Petch equation.

(a) Mott-Nabarro hardening<sup>(147,148)</sup> results from the strain created by the solute in the parent lattice, so that an extra force is needed to force the dislocations through the strained lattice. Various theoretical calculations have shown that the flow stress is given by the equation:

$$\tau = Gq^n c \dots \dots \dots (38)$$

where  $G$  is the shear modulus,  $q$  is the fractional change in lattice parameter per 100% solute (extrapolated) and  $c$  is the fractional atomic concentration.  $n$  may be regarded as 2 or

$4/3$  depending upon the criterion used for the length of dislocation which is bowed due to lattice distortion.

Experimentally determined values of the frictional force<sup>(149)</sup> (extrapolated to 100% solute) for Fe - Mn alloys give a shear stress of  $127 \text{ kg/mm}^2$ . Using  $n = 4/3$  in the above formula, a value of  $93 \text{ kg/mm}^2$  is obtained which is of the right order of magnitude for iron-manganese alloys. On this basis the flow stress is directly dependent on solute concentration and lattice distortion due to differing atomic diameters of solute and solvent.

(b) Strengthening by electrical interaction between dislocations and solute ions is due to the concentration of electrons into the expanded side of an edge dislocation and deprivation of electrons in the compressed side so that the dislocation becomes a line dipole, negatively charged on the expanded side.

The resultant binding energy has been calculated for some copper alloys and was found to be of the order of  $\frac{1}{8}$  to  $\frac{1}{4}$  ev. The alloys showed similar stress-strain curves at similar electron-atom ratios apparently indicating that this mechanism may be important in these alloys. However, it is thought more likely that this effect is due to the influence of the solute on the stacking fault energy.

(c) The Snoek effect<sup>(150)</sup> is believed to apply to carbon and nitrogen dissolved in alpha iron. Atoms of these elements take up preferred sites in the alpha lattice, these are the  $(\frac{1}{2} 00)$  positions, tending to produce both shear and dilational distortion. When a stress is applied, the unit

cube becomes elongated in one direction creating preferred sites for the solute atom where the stress produces the distortion their presence requires. A frictional force is produced on a dislocation as it moves past a carbon or nitrogen atom because these atoms tend to jump into the now favoured positions. This ordering dissipates energy and the dislocation finds itself in an energy well. Before a dislocation can be moved the state of local order must be destroyed and this leads to a higher yield stress.

(d) Cluster hardening<sup>(151)</sup>. This can be regarded as a type of precipitation hardening, although less effective, in which aggregates of solute atoms impede slip like a precipitate.

(e) Peierls-Nabarro force. A dislocation changes energy as it moves from one site to the next. For this movement to take place an applied stress, known as the Peierls-Nabarro stress, is needed to overcome this periodic change of energy. This stress must be very small, however, when the dislocation is wide, because the highly distorted region at the centre is then not sharply localised on any one single central crystal site.

The Peierls stress may then be regarded as the stress associated with the breaking of atomic bonds around the dislocation.

Theoretical estimates of the Peierls stress indicate that:

$$\tau_p \text{ the Peierls stress } \approx G \exp \left( \frac{2 \pi \omega}{b} \right) \dots (39)$$

where  $G$  is the shear modulus,  $\omega$  the width of the dislocation

and  $b$  the magnitude of the Burgers vector.

In general in close packed structures the dislocations are thought to be wide, of the order of 10 atom spacings, and in open structures e.g. b.c.c. and Ionic crystals, the dislocations are thought to be narrow, of the order of 1 atomic spacing. There are apparently no experimental results to verify this point. Hence it is thought that in close packed structures the contribution of the Peierls stress to the flow stress is small and in non-close packed structures the contribution is significant. The Peierls stress is very temperature dependent and it is well known that the flow stress of b.c.c. metals is very temperature dependent while the flow stress of f.c.c. and c.p.h. (153,154) metals is only slightly temperature dependent.

### 3.2.3. Influence of Solutes on Stacking Fault Energy

When slip occurs in f.c.c. metals, stacking faults are always created. The stacking sequence on the close packed planes of the undeformed region ABCABC changes to ABCBCABC when slip occurs.

For slip to occur, it is necessary for an  $\frac{a}{2}[10\bar{1}]$  slip dislocation to split up into two partials  $\frac{a}{6}[2\bar{1}\bar{1}] + \frac{a}{6}[11\bar{2}]$  this being energetically favourable, since the sum of the strain energy for the pair of partials is less than the strain energy of the single unit dislocation. The stacking fault energy is the algebraic sum of two factors:

- (a) The repulsion effect between the two partials;
- (b) The line tension effect tending to remove the

stacking fault layer. As a result of these two factors every alloy has a characteristic stacking fault energy which will result in a characteristic separation of the two partials. This will occur when the two above forces balance each other. For metals with a high stacking fault energy, the separation between the partials is small since repulsion between the partials is small compared with the line tension effect reducing the stacking fault.

Cross-slip is an important factor governing the rate of work hardening. Before cross-slip can occur in f.c.c. metals it is necessary for the partials to constrict into a single dislocation. The wider apart the partial dislocations the greater the force required to bring the partials together to enable cross-slip to occur. By coming together they acquire a common Burgers vector which permits cross-slip. Thermal activation will aid this constriction although it will be obviously more difficult in the case of metals with a low stacking fault energy where the separation of partials is greater.

Thus in the case of austenitic Fe-Mn alloys, or one predominantly  $\gamma$  in nature, with a low stacking fault energy, the work hardening rate should be high due to the difficulty with which cross-slip occurs.

#### 3.2.4. Dislocation Locking by Solute Atoms

Where both dislocations and solute atoms are present in a lattice interaction between them may occur to lower the strain energy of the system. So called "atmospheres" are formed which give rise to the sharp yield points shown by

some metals.

(a) Cottrell atmospheres<sup>(152)</sup>. These atmospheres are formed because, in the case of an edge dislocation, the region below the slip plane is dilated whilst above it the atoms are compressed. The strain energy of the lattice may be reduced if the lattice parameter of the compressed region is reduced or that of the dilated region is increased. This condition may be brought about by segregation of the larger solute atoms to the dilated region or smaller solute atoms to the compressed region. Thus there is created a binding energy between the solutes and the dislocations which are anchored or dragged at temperatures too low for rapid atomic diffusion.

(b) Suzuki locking. When a slip dislocation in f.c.c. metals dissociates into a pair of partial dislocations separated by a stacking fault, the fault itself represents a region in which the crystal structure is locally changed to c.p.h. From alloy chemistry and thermodynamic considerations it would be expected that when the solute atoms segregate to an extended dislocation of this kind, the concentration of solute atoms in the faulted layer will be different from that in the surrounding f.c.c. phase. Since the stacking fault energy varies with composition, after redistribution of the solute atoms the fault width may be expected to alter. It has been estimated that the effect of Suzuki locking is about one-tenth of that due to Cottrell locking. It differs from Cottrell locking in that it is independent of temperature so that it could be an important mechanism at temperatures where

Cottrell locking dies away, if the solute atom has a slow diffusion rate.

### 3.2.5. Effect of Precipitates

This effect is of only minor importance in the present investigation and will only be briefly dealt with.

Basically the problem is one of how the dislocations and precipitates interact. The precipitate particles lie across the slip planes along which the slip dislocations move. The dislocations can overcome these barriers to movement in one of two ways:

- (1) They can cut through the precipitate particles
- or (2) go around the particles.

It is thought that the first mechanism is operative in aged alloys where the precipitate is coherent i.e. up to the point of optimum hardness. The second mechanism is operative in over aged alloys containing semi-coherent or incoherent precipitates, which includes the so called dispersion hardened alloys e.g. NbC in steel,  $Al_2O_3$  or  $SiO_2$  in copper.

As a consequence of this reasoning, two theories have been advanced, one of which is based on coherent precipitates and dislocations passing through them (Mott and Nabarro) and one which is based on incoherent precipitates and dislocations moving between them (Orowan).

- (1) Internal strain hardening theory. This theory satisfactorily explains the increase in yield strength, hardness, etc. with ageing.

For a fine dispersion of coherent precipitate the

dislocation line is unable to go around the particles and may be regarded to exist as a straight line. Analysis of the situation gives the shear stress for pushing a dislocation through the precipitate as:-

$$\tau_o = 2G \Theta C_o \quad . . . . .(40)$$

where  $C_o$  is the volume of precipitate ( $\frac{4}{3}\pi r_o^3 N$  where  $r_o =$  radius of cluster and  $N =$  number of clusters per unit volume),

$\Theta$  is the mismatch function and  $G$  is the shear modulus of matrix.

On further ageing up to the optimum, local rearrangement of dislocations occurs since the particle spacing will increase. A net opposing force is created due to this local rearrangement of dislocations and is found to be a maximum when the particle spacing is  $50 - 100\overset{\circ}{\text{A}}$ .

(2) Dispersion hardening. In this case there is no continuity of lattice planes across the boundary between matrix and precipitates, i.e. the precipitate is incoherent. This incoherency necessitates that the moving dislocations pass around the precipitates. The shear stress involved is given by the equation

$$\tau_o = \frac{\alpha Gb}{R} \quad \text{or} \quad \tau_o = \frac{2\alpha Gb}{L} \quad . . . . .(41)$$

where  $\alpha$  is a constant equal approximately to a  $\frac{1}{2}$ ,  $G$  is the shear modulus,  $R$  is radius of dislocation line and  $L$  distance between precipitate particles.

It can be seen, therefore, that in order to get maximum hardening effect it is necessary to aim for:

- (a) optimum dispersion of particles, ( $50 - 100\overset{\circ}{\text{A}}$ )

- (b) a high concentration of particles,
- (c) a high mismatch between precipitate and matrix while still maintaining coherency.

### 3.3. The Influence of Temperature

In general a decrease in temperature results in an increased yield stress and an increased rate of work hardening. The behaviour of a metal can vary somewhat depending on the crystal structure and also the structural changes produced by the temperature, e.g. precipitation effects or order-disorder changes.

For f.c.c. metals, which show a gradual yield process the notable features are the small temperature dependence of the yield stress and the marked effect of temperature on strain hardening, figure 28. A notable feature of f.c.c. metals and alloys is their ductility at all temperatures: no ductile-brittle transition occurs unless rather special conditions of alloying are present e.g. in the case of Cu-Bi alloys.

Hexagonal close packed structures show marked differences in tensile properties depending on the modes of deformation and the amount and nature of interstitial impurities. In general the temperature dependence of yield stress is similar to that of f.c.c. metals, but the strain hardening exponents are smaller e.g. at room temperature  $n = 0.20$  for Ti and Zr in contrast to an average of 0.38 for f.c.c. metals. Practically all h.c.p. metals show a decrease in ductility with decrease in temperature. The nature of the ductile to

brittle transition behaviour depends on the metal concerned. Zinc shows a completely brittle behaviour with no ductility while magnesium shows a small amount of ductility.

In metals with a b.c.c. structure, which show a marked yield point, there is a strong temperature dependence of yield stress, figure 29. The major effect of decreasing temperature in b.c.c. metals is to cause a rise in the general level of the stress-strain curves due to an increase in the yield stress. The strain hardening exponent is little affected by temperature.

Petch<sup>(145)</sup> showed in his analysis that the value of  $K_y$  was independent of temperature and that the increase in yield stress with decrease in temperature was due principally to an increase in the friction stress  $\sigma_i$ . Figure 30 shows that  $K_y$  is constant for various temperatures whilst the intercept,  $\sigma_i$  increases. The value of  $\sigma_i$  is a measure of the stress needed to drive a dislocation against the resistance of impurities, lattice distortion, and grain boundaries and the Peierls-Nabarro force. It is thought that  $\sigma_i$  has two parts, a temperature independent factor  $\sigma_i^{**}$  and a temperature dependent factor  $\sigma_i'$ . The former is attributed to the resistance of random solute atoms and lattice defects to dislocation movement whilst the latter is attributed to the Peierls-Nabarro force (which is temperature dependent).

The above behaviour is modified by the unpinning of dislocations from their locking atmospheres, which is quite temperature sensitive.

The effect was neatly shown by Fisher (figure 31) using

pure iron containing 0.001%C. In the case of the furnace cooled specimens (curve ABCD), the solute atoms had sufficient time to diffuse to the dislocations locking them strongly, thus favouring the creation of new sources of dislocations rather than unpinning.  $K_y$  is, therefore, little affected by variation in temperature. However, in the case of the quenched specimens (curve ABE) minimum locking is achieved and the unpinning of dislocations becomes the favoured process above point B and  $K_y$  becomes sensitive to changes in temperature. Ageing quenched specimens (curve ABCF) allows the carbon and nitrogen interstitials to return to the dislocations so increasing the locking effect, thus the creation of sources is favoured to a higher temperature (point C) and thereafter unpinning is favoured,  $K_y$  becoming temperature sensitive.

The rate of work hardening is also affected by temperature. It is thought that the rate of work hardening is governed by the rate at which cross-slip occurs. This is in turn, governed by the stacking fault energy and temperature. Cross slip cannot take place until the dissociated slip dislocations are constricted. The lower the temperature the more difficult constriction becomes, making cross-slip more difficult, and the rate of work hardening increases. For maximum strength in f.c.c. materials it is thus desirable to choose alloying elements which lower the stacking fault energy, and so increase the rate of work hardening. The addition of manganese to iron produces such an effect.

### 3.3.1. Brittle Fracture

The brittle fracture problem is obviously one of great practical importance from the industrial point of view. Most uses of constructional materials demand a minimum ductility at room temperature which should be maintained or little reduced over the range of temperatures expected in service. This aspect is particularly important in b.c.c. ferrous systems where the material undergoes a so called ductile to brittle transition with a fall in temperature. Owing to its great importance, this problem has received considerable theoretical and experimental attention. The main considerations are outlined briefly below.

Theoretical calculations have shown that most materials break at stresses well below the predicted values, based on the stress required to pull apart two adjoining layers of atoms. Glass fibres and both metallic and non-metallic whiskers have strengths approaching the ideal values of  $E/10$ , but bulk metals rarely withstand stresses above  $E/100$ . Griffith<sup>(155)</sup> suggested that this behaviour was due to the presence of small cracks which propagate through the crystal. The Griffith theory deals with isotropic elastic materials, i.e. materials which behave in an elastic manner up to the point of fracture, no plastic deformation taking place. As a crack grows, each of the bonds in its path takes up the strain, and the work done in stretching and breaking these bonds becomes the surface energy of the fractured faces.

In calculations of the stress at the ends of a crack, it is usual to consider a flat plate with a crack of

elliptical cross-section in its middle. Figure 32 illustrates such a flaw. Using Orowan's approach to the crack theory Inglis<sup>(156)</sup> calculated that the stress at the end of the crack is:

$$S_{ne} = 2S_n \left(\frac{C}{p}\right)^{\frac{1}{2}} \dots (42)$$

where  $2c$  is the length of the major axis of the elliptical hole,  $S_n$  is the average applied stress, and  $p$  is the radius of curvature at the ends of the ellipse. If it is assumed that the radius of curvature at the ends of the crack is equal to 'a' the mean distance between atoms across the fracture plane, we may write equation (42) as:-

$$S_{ne} = 2S_n \left(\frac{C}{a}\right)^{\frac{1}{2}} \dots (43)$$

It may show that the maximum stress  $S_{nth}$  required to separate the rows of atoms is given by the following equation:-

$$S_{nth} = \left(2\sigma \frac{E}{a}\right)^{\frac{1}{2}} \dots (44)$$

where  $\sigma$  is the surface energy of the crack,  $E$  is Young's modulus and 'a' is the mean interatomic distance across the fracture plane at zero stress.

For the crack to propagate  $S_{ne}$  must be equal to  $S_{nth}$  and

$$2S_n \left(\frac{C}{a}\right)^{\frac{1}{2}} = \left(\frac{2\sigma E}{a}\right)^{\frac{1}{2}}$$

$$\therefore S_n = \left(\frac{\sigma E}{2C}\right)^{\frac{1}{2}} \dots (45)$$

As the crack length,  $2C$ , increases the stress required decreases which means that once the crack is moving it may accelerate to high velocities.

In general, calculations for other shapes in solids

have confirmed the relationship

$$S_n \propto \left(\frac{\sigma E}{2C}\right)^{\frac{1}{2}} \dots (46)$$

and it can be regarded as of general significance with regard to brittle fracture.

In the case of metals brittle failure by cleavage is accompanied by a certain amount of plastic deformation prior to fracture. This has been interpreted as evidence that metals do not fracture as the result of pre-existing cracks, but that cleavage cracks are nucleated by plastic deformation processes. Various models have been suggested for the formation of micro-cracks by Stroh<sup>(157)</sup>, Zener<sup>(158)</sup> and Cottrell<sup>(159)</sup>. It is postulated that the pile-up of dislocations against obstacles to their movement or the interaction of slip dislocations on intersecting planes results in the formation of microcracks. A ductile-brittle transition can be explained on the basis that a material is ductile at any temperature, if the yield stress at that temperature is smaller than the stress necessary for the continued growth of these microcracks, but if it is larger the material is brittle.

For b.c.c. metals, such as iron, the critical resolved shear stress for slip is very large, increasing almost eight fold in the temperature interval 20 to  $-196^{\circ}\text{C}$ . The high levels of stress needed to plastically deform iron at low temperatures thus favours the nucleation processes of cleavage and twinning. Thus it can be seen that the lattice friction term  $\sigma_i$ , dislocation term  $K_y$  and the grain size are all important from the brittle fracture aspect. The presence of grain boundaries makes the propagation of

microcracks more difficult, limiting their size to one grain or several grain diameters. An estimate of the average applied stress  $S_n$  required to propagate a crack may be obtained from equation (45), if the average microcrack length is regarded as equal to a grain diameter, and the surface energy term modified to include the energy of plastic deformation expended in forcing the crack through a polycrystalline aggregate.

This term is denoted  $\sigma_e$ . Thus equation (45) becomes:-

$$S_n = \left( \frac{\sigma_e E}{d} \right)^{\frac{1}{2}} \dots \dots \dots (47)$$

where  $\sigma_e$  is the effective specific surface energy,  $d$  the average grain,  $S_n$  the applied stress, and  $E$  Young's modulus. The relationship predicts that the strength of polycrystalline metals which fail by cleavage should vary as  $(d)^{-\frac{1}{2}}$ . An empirical relationship of this nature has been reported for iron by Greenwood et al. (160). As the diameter increases, a critical diameter is reached above which the stress to expand a microcrack becomes smaller than the stress to nucleate a crack in a grain. Thus, when the critical diameter is reached the first crack to form causes failure. Above the critical diameter the fracture stress is controlled by the stress required to nucleate cracks in crystals, and below it by the stress to propagate a crack through a polycrystalline mass. Gilman (161) summarised the above in the form of a diagram shown in figure 33.

In practice the tendency of a metal to brittle behaviour under impact loading may be measured by means of an empirical impact test. This test measures the energy absorbed in breaking a notched specimen of standard dimensions.

The ductile-brittle transition temperature is reported as the temperature at which a specific impact load is reached, e.g. 20 ft.lbs. or the temperature at which the average energy figure is obtained.

#### 4.0. The Structures of Alloys in the Iron-Manganese System

The equilibrium diagram of the iron-manganese system is of the open  $\gamma$  field type. It is of the same general type as the iron-nickel system apart from complications resulting from the occurrence of four different modifications of manganese (figure 1). Iron is freely soluble in  $\alpha$ -manganese and  $\beta$ -manganese and forms a complete range of solid solutions with the f.c.c.  $\gamma$ -manganese. Not only do the systems Fe - Mn and Fe - Ni resemble one another closely with regard to the general form of the equilibrium diagram but also in the way metastable phases are formed during the transformation (figure 2). In both alloy systems the  $\alpha$  and  $\gamma$  phases in equilibrium vary greatly in composition from one another and if transformation is to take place under equilibrium conditions considerable diffusion must take place. This means that diffusionless transformations are favoured. Figures 2 and 3 show the general characteristics of these alloys when heated or cooled under normal conditions.

The results of normal cooling in the iron-manganese system are complicated by the occurrence of a second martensitic transformation at higher Mn contents in which the austenite transforms to close packed hexagonal  $\epsilon$  solid solution. It has been reported that in the range 7.5 - 13% (at) Mn, these two martensitic changes overlap, alloys consisting of a

mixture of  $\alpha'$  and  $\epsilon$  phases being obtained. Between 13 - 30% (at) Mn the normal structure is composed of a mixture of  $\epsilon$  and  $\gamma$  solid solutions giving way to a completely  $\gamma$  structure above about 30% (at) Mn.

The temperatures recorded for the beginning of the  $\gamma \rightarrow \alpha'$  and  $\gamma \rightarrow \epsilon$  change reported by the various investigators differ and the curves shown in figure 2 may be regarded as a compromise on the data reported by the various investigators in this field<sup>(99-105)</sup>.

The temperature at which these structures start to transform athermally ( $M_s$ ) is independent of the rate of cooling<sup>(31,32)</sup>. On heating, the changes are reversible but considerable temperature hysteresis is observed particularly in the case of the  $\gamma \rightarrow \alpha'$  reaction where the hysteresis increases as the manganese content increases. Temperatures of the  $\gamma \rightleftharpoons \alpha'$  transformation have been determined in alloys up to approximately 13% Mn but Schmidt<sup>(106)</sup> has detected  $\alpha'$  in alloys up to 20% Mn. Thus, according to Schmidt, alloys in the range 7 - 20% Mn may consist of  $\alpha' + \epsilon$  as well as some retained  $\gamma$  phase. Later work by Schumann has shown, however, that  $\alpha'$  is confined to the range 7 - 16% Mn. The results reported are not consistent since impurities, especially carbon, and cold work have a considerable influence on the  $\epsilon$  transformation.

Ohman<sup>(108)</sup> observed that the lattice parameter of  $\alpha$  solid solution was not measurably different from that of iron. He also observed the presence of supersaturated  $\alpha$  which he unfortunately designated  $\alpha'$  to distinguish it from

equilibrium  $\alpha$ .

Troiano and McGuire<sup>(31)</sup> have presented direct evidence for the existence of two types of  $\alpha$  solid solution - equilibrium and supersaturated. Using precision lattice constant determinations they observed that for all temperatures, alloys containing 3 - 15% (at) Mn gave lines of supersaturated  $\alpha'$  under non-equilibrium conditions. They found for example, that an alloy containing 5.72% (at) Mn at 700°C formed approximately 40% equilibrium  $\alpha$  containing 2.5% (at) Mn and 60% equilibrium  $\gamma$  containing 8.4% Mn. On quenching to room temperature the  $\gamma$  transformed to supersaturated  $\alpha'$  of the same composition. Microscopic examination showed that specimens at equilibrium, quenched from the  $\alpha$  field, revealed polygonal grains characteristic of homogeneous solid solution. Where X-ray determinations revealed supersaturated  $\alpha'$  the structure resembled that of low carbon martensite.

Schmidt<sup>(106)</sup> first observed the  $\epsilon$  phase in Fe - Mn alloys. Using X-ray diffraction methods he showed that it was a hexagonal close packed structure existing over a range of composition 11.8 - 29% Mn and that the axial ratio was approximately a linear function of the manganese content. Later work confirmed the results of Schmidt<sup>(103,107,108,111)</sup>. Ohman<sup>(108)</sup> took X-ray photographs of suitable alloys at temperatures between 500 - 1000°C but in none of them was the  $\epsilon$ -phase, free or associated, detected. This discovery led him to suggest that the phase was only produced by quenching; that it was unstable, and that it was a transition phase occurring during the change from  $\delta \rightarrow \alpha$  solid solutions,

decomposing itself to reproduce  $\gamma$  or the b.c.c. phase  $\alpha'$  supersaturated in manganese.

Osawa<sup>(111)</sup> and Ishiwara<sup>(112)</sup> suggested that the  $\epsilon$ -phase was located about an intermetallic compound  $\text{Fe}_5\text{Mn}$  and this forms as a result of a peritectoid reaction occurring at about  $200^\circ\text{C}$  and at a composition of 20% Mn. The peritectoid reaction implies diffusion and cannot be considered seriously since at a temperature of  $200^\circ\text{C}$  this is not feasible. It has been observed for instance that at this temperature equilibrium is not attained even after two years.

Walters<sup>(113)</sup> and his co-workers<sup>(103,114)</sup> using purer materials than the earlier investigators confirmed the existence of the  $\epsilon$ -phase not only by X-ray and dilatometric measurements but also magnetically and microscopically. They recorded that  $\epsilon$  was produced in slowly cooled, as well as quenched, specimens. Walters concluded the  $\epsilon$ -phase might be produced by a peritectoid reaction, as an intermediary in the  $\gamma \rightarrow \alpha$  change, or as a transition phase.

Bain, Davenport and Waring<sup>(115)</sup> considered  $\epsilon$  to be a transition structure of the martensitic type. They suggested that the  $\gamma$ -solid solution for certain compositions decomposes to h.c.p. lattice instead of a b.c.c. Of the two modes of decomposition, that to h.c.p. requires less movement of atoms and is accompanied by a decrease in volume instead of an increase, therefore it is the favoured mode.

Parr<sup>(101)</sup> studied powders of 12.2%, 15.5% and 18.5% Mn alloys of high purity. He observed that there was no exact equality of interplanar spacing between the major

crystallographic planes in the  $\gamma$  and  $\epsilon$  phases. Therefore, it cannot be concluded that a simple  $\gamma \rightleftharpoons \epsilon$  transformation takes place. Thus the hypothesis of Bain, Davenport and Waring<sup>(115)</sup> and other workers, of a simple  $\gamma \rightleftharpoons \epsilon$  transformation is not substantiated as the change would involve the movement of all atoms. Some of Parr's other work is shown in Tables 2 - 4. Tempering quenched powders at temperatures up to 450°C brought about an initial increase in the amount of  $\epsilon$  at the expense of either or both of the cubic solid solutions, but continued treatment destroyed the  $\epsilon$ -phase and produced a stable b.c.c. phase. Parr thought the results of the quenching and tempering treatments could be best explained in terms of the theory of athermal nucleation put forward by Fisher, Holloman and Turnbull<sup>(116)</sup>. The theory argues that at temperatures between 750°C and 1350°C, when the alloy is in f.c.c. solid solution, there also exists embryos of a hexagonal phase which at the temperature of their environment are of a characteristic sub-critical size. When the alloy is quenched, however, the embryos remain at sensibly the same size, which at the reduced temperature is greater than critical, i.e. they are now stable nuclei and can grow. It seems significant that the lower limit of the quenching temperature range (750°C) which produces  $\epsilon$  coincides with the  $\alpha - \gamma$  Ac temperature. This indicates that the embryos of  $\epsilon$  can exist only in an environment of  $\gamma$  solid solution.

The microstructure of  $\epsilon$  is marked by its sharp definition as compared with the microstructures resulting

from the decomposition of  $\gamma$  to  $\alpha'$  and is characterised by a multiple twin-like structure arrayed in a Widmanstatten pattern.

#### 4.1. The Effect of Stress on the Formation of $\epsilon$ -phase

Gensamer, Ekel and Walters<sup>(107)</sup> in their X-ray investigation of iron-manganese alloys observed that a machined needle of a 20% Mn alloy contained only  $\epsilon$  whereas a ground and severely etched specimen was principally  $\alpha'$ . Bain, Davenport and Waring<sup>(115)</sup> found that cold work increased the amount of  $\epsilon$  and annealing aided its rapid destruction.

A more thorough study was made by Troiano and McGuire<sup>(31)</sup> who used powders and slivers of alloys in the composition range 10 - 20% Mn. Samples were quenched from the  $\gamma$  field and subsequently cold worked and X-rayed. The retained austenite in the 10% and 13% alloys transformed almost entirely to supersaturated  $\alpha'$  with only a trace of  $\epsilon$ . 15% and 17% alloys after quenching showed approximately equal amounts of  $\gamma$  and  $\epsilon$  but no  $\alpha$ : after deformations of 40 - 60% there was almost all  $\epsilon$  with a small amount of supersaturated  $\alpha'$ , but after severe deformation, supersaturated  $\alpha'$  predominated with a trace of  $\epsilon$ . Following this, all deformed specimens were annealed at 100 - 200°C for 1½ - 2 years. These temperatures are below the beginning of the  $\epsilon \rightarrow \gamma$  transformation and any decrease in the amount of  $\epsilon$  must therefore, result from the direct decomposition of  $\epsilon$  to  $\alpha'$ . All samples showed this e.g. a sliver of the 15% Mn alloy after moderate deformation (40 - 60%) contained a large amount of  $\epsilon$ , but after annealing for two years only

$\alpha$  was present. The position of the  $\alpha$  lines was nearly that of equilibrium. Lines of the  $\gamma$  phase normally expected as the result of compositional readjustments to attain equilibrium were not observed. This could be the result of a particle size effect (powders were used) since  $\gamma$  must precipitate from a matrix, either supersaturated  $\alpha$  or  $\epsilon$  or both.

Parr<sup>(101)</sup> carried out work on filings, his results are shown in table 5.

White and Honeycombe<sup>(119)</sup> investigated the work hardening behaviour of a wide range of Fe - Mn - C alloys. The structural changes resulting from heat treatment and deformation being studied by electron microscopy and X-ray diffraction. A summary of the structures found are shown in figure 34. Compositions close to the Hadfield's alloy (13% Mn 1.15%C) were shown to be stable under all experimental conditions. On lowering the carbon content both  $\alpha$  and  $\epsilon$  martensite are formed, the presence of the latter suggesting the stacking fault energy of the parent phase is low. The outstanding mechanical properties of Hadfield's steel are considered to arise from the presence of stacking faults and the interaction of the solute elements with them.

From figure 34, it can be seen that for the alloys containing no carbon, alpha martensite is reported to be present in the 18% Mn alloy thus confirming the work of Schmidt who reported alpha martensite to be present in alloys containing up to 20% Mn. The effect of carbon as a gamma stabiliser is also clearly shown, alloys containing as little as 8.0% Mn having an all gamma structure at 1.15%C.

Quenching to  $-196^{\circ}\text{C}$  and deformation at this temperature or at room temperature are depicted as causing the gamma phase to transform to either alpha or epsilon martensite depending upon the alloy composition.

Yershova et al.<sup>(120)</sup> investigated the phase transformations which take place during heat treatment and cold plastic deformation in manganese steels (table 6 and figure 35). The structure of a 0.06%C 19.7% Mn alloy in the quenched state consisted of  $\gamma + \epsilon$ . Determination of the amount of  $\epsilon$ -phase present at various quenching temperatures in the range  $400 - 1400^{\circ}\text{C}$  showed that the amount present did not depend upon the quenching temperature and was on average 50 - 60%. This is contrary to the findings of Parr<sup>(101)</sup> for an 18.5% Mn alloy, which showed the amount of phase present to depend upon the quenching temperature (table 2). The  $\gamma \rightarrow \epsilon$  transformation was also found to be apparently insensitive to quenching temperature and lay in the range  $90 - 100^{\circ}\text{C}$ . The effect of plastic deformation on the alloys is summarised in figure 35.

The effect of cold deformation on the 0.06%C 19.7% Mn steel (G20) is to bring about the transformation of gamma to epsilon phase. A maximum of 80% epsilon is reached at 37.0% deformation, further deformation causing a decrease in the amount of epsilon phase present, presumably it transforms to alpha martensite although this is not shown in figure 35.

The 0.29%C 23.1% Mn steel (30G23) is shown as having an all gamma structure before deformation instead of the gamma plus epsilon structure, which might have been expected

on the basis of manganese content alone. It would seem that 0.29%C exerts sufficient stabilising effect to give an all gamma structure. Deformation of this material results in the formation of epsilon phase at the expense of the gamma phase. The dotted curve is reputed to represent the effect of deformation on a sample of the above alloy after vacuum annealing at 850°C for three hours. Despite the fact that in the text it is reported that the initial alloy has an alpha content of 23% the curve is shown as originating at 0% alpha, casting a certain amount of doubt on the validity of the whole experiment.

Shklyer et al.<sup>(121)</sup> studied the nature and character of structural changes undergone by austenite in the process of repeated  $\gamma \rightleftharpoons \epsilon$  transformations and also the extent to which the different forms of imperfection were responsible for improving its stability in a Fe - Mn 19.1% steel (0.05%C). The behaviour of the phase composition and lattice parameter, probability of stacking faults in the austenite and the line width of the austenite and  $\epsilon$ -phase were studied by X-ray diffraction analysis as dependent on the number of  $\gamma \rightleftharpoons \epsilon$  transitions. The results of the investigations are summarised in figure 36. Phase transitions in the range  $400 \rightleftharpoons -196^\circ\text{C}$  had the greatest stabilising effect, the alloy having a completely austenitic structure after 12 cycles. The effect of stacking faults is demonstrated in figure 37. For  $400 \rightleftharpoons -196^\circ\text{C}$  cycle the probability of stacking faults rises considerably up to 6 cycles and then shows little change. From figures 36 and 37 it was concluded that both

the increase in the amount of  $\epsilon$ -phase in the first cycle and the rapid stabilisation of the austenite on subsequent ones are in a number of cases, accompanied by the decreased probability of stacking faults.

The cycling treatment would appear to destroy the centres for epsilon nucleation i.e. the stacking fault ribbons. At 400°C this alloy would be in the alpha plus gamma region of the equilibrium diagram so it is to be expected that alpha would be preferred on repeated cycling to this temperature. This is not so, which would seem to lead to the conclusion that the total time at 400°C is too short for equilibrium conditions to be established but sufficient time to allow constriction of the partials of the stacking faults resulting in their ultimate destruction.

#### 4.2. Mechanical Properties of Fe - Mn Alloys

There appears to be very little published information available on this subject. The book 'Manganese Steel',<sup>(124)</sup> summarises the mechanical properties obtainable in the austenitised at 1000°C and water quenched condition for manganese contents ranging from 0 - 26% Mn (see figures 38 and 39). Alloys of low carbon content ranging from 4 - 18% Mn are described as brittle, the tensile strength ranging from 30 - 40 t.s.i. Hadfield<sup>(125)</sup> found the alloys in the range 4 - 16% Mn extremely brittle. Walters, Kramer and Lorig<sup>(126)</sup> on the other hand, reported that far from being brittle, most iron-manganese alloys were more ductile than SAE steels of the same tensile strength and they suggested that the brittleness of Hadfield's alloys was probably due to

their high carbon and phosphorus contents. They studied the properties of relatively pure alloys in the range 3 - 14% Mn in the normalised condition. With increasing Mn content up to 10%, the strength increases but ductility decreases. Between 10 and 14% Mn both  $\alpha$  and  $\epsilon$  are formed by the decomposition of  $\gamma$  and the highest strength of the series of alloys is shown by those in this range. Above 14% Mn the  $\gamma$  only partly transformed to  $\epsilon$  and the alloys showed the low elastic limit and high ductility characteristic of austenitic alloys. Tempering for one hour at 540°C raised the ductility and lowered the tensile strength of alloys with less than 10% Mn, but both the ductility and strength of a 13% Mn alloy were increased by tempering. Walters, Kramer and Lorig show that the results would not have been materially different with other rates of cooling.

Uhlig<sup>(127)</sup> has correlated the effect of hydrogen on the reduction of area, elongation and tensile strength of Fe - Mn alloys in the range 3 - 22% Mn. However, at no stage is the hydrogen content kept constant, and it is difficult to understand how correlation of the results is obtained on this basis. Broadly speaking, the results do show that hydrogen in the contents investigated has an embrittling effect.

Summarising, in pure iron-manganese alloys the austenite transforms principally into  $\alpha$  and  $\epsilon$ -phases the proportions of which, together with any retained austenite, determine the observed mechanical properties.

#### 4.3. Fe - Mn - C Alloys

Although not of direct relevance to the present study, it is of interest to note the work being done on the carbon containing iron-manganese alloys.

Lysak and Vauk<sup>(109)</sup> reported that besides the well known martensite with a b.c.t. lattice ( $\alpha_t$ ), when steel is quenched, a K-phase with a body centred cubic lattice is also formed having a lattice parameter 2.874 KX, which remains constant in the range 0.52 - 1.25%C. Further investigations by Lysak and Vauk<sup>(110)</sup> on manganese steels (see table 7) revealed yet another new phase, called K' phase or K'-martensite is formed, having a b.c.t. lattice. This transforms on heating to K and  $\alpha_t$  phases.

Work by Lysak and Nikolin<sup>(123)</sup> on < 0.6%C. 8 - 18% Mn steels revealed the presence of a new martensitic phase which was designated  $\epsilon'$ -martensite. The  $\epsilon'$ -phase is seen to be produced from the austenite by the shear of every sixth layer bundle of (111) planes over a distance  $a/6$  in the [112] direction. On cooling to temperatures below that for the formation of the  $\epsilon'$ -phase, or on deformation of a specimen containing  $\gamma$  and  $\epsilon'$ -phases the latter is transformed into  $\epsilon$ -phase. The lattice of this phase may be represented as austenite in which there are stacking faults after each second (111) layer. Consequently, the  $\gamma \rightarrow \epsilon$  transformation can be represented as a gradual increase in the density of the periodic stacking faults in austenite.

Lysak and Nikolin<sup>(122)</sup> discussed the role of stacking faults in the formation of  $\epsilon'$  (multi-layered rhombohedral

lattice) and  $\epsilon$ -phase (c.p.h.) in Fe - Mn - C steels. On

$\gamma \rightarrow \epsilon'$  transformation the randomly arranged stacking faults also appear in the austenite, and are revealed by X-ray diffraction analysis as bands joining the  $\gamma$ ,  $\epsilon'$ , and  $\epsilon$ -martensite reflections. These defects appear together with the  $\epsilon'$  and  $\epsilon$  phases and disappear on heating together with the  $\epsilon$ -phase. On the basis of their results the authors proposed the whole process of martensitic transformation to be represented by the scheme shown in figure 40 with the following sequence:



The  $K'$  phase may be regarded as  $\alpha_t$  martensite with the stated c/a ratio.

The transformation from one phase to another is pictured as being due to successive shears on the (111) planes of the austenite.  $\epsilon'$  phase is the result of a shift of six layer bundles of planes;  $\epsilon$  phase results from a shift of bundles of two layers;  $K'$  martensite is produced from  $\epsilon$ -martensite as a result of atom displacements in the same planes and also a change in the structure of the layers themselves. Figure 41 shows the complete scheme of crystal lattice arrangement on the quenching of Fe - Mn - C steels.  $K'$  is highly unstable and even at temperatures below  $0^\circ\text{C}$  decomposes to K and  $\alpha_t$  phases.

Details of the phases reported in the literature are summarised below:-

PHASE	DESCRIPTION	COMMENTS
$\alpha_t$	b.c.t. martensite the tetragonality of which increases with carbon content according to the relationship. $\frac{c}{a} = 1.000 + 0.045 \text{ W/o C.}$	
$\alpha'$	b.c.c. massive martensite with a lattice parameter of $a = 2.86\text{\AA}$ .	A supersaturated b.c.c. solid solution which forms in the range 0-20% Mn in binary Fe-Mn system.
$\epsilon'$	Epsilon prime martensite with rhombohedral lattice parameters $a = 12.56\text{\AA}$ , $\alpha = 11^\circ 40'$ or in hexagonal axes $a = 2.53\text{\AA}$ , $c = 37.44\text{\AA}$ .	Reported to have been found by Lysak and Nikolin <sup>(123)</sup> in < 0.6% C 8-18% Mn steels. May be represented as a $\gamma$ structure with stacking faults every six layers apart.
$\epsilon$	Epsilon martensite c.p.h. lattice parameters $a = 2.53\text{\AA}$ , $c = 4.079\text{\AA}$	A supersaturated c.p.h. solid solution, which forms in the range 7-32% Mn in binary Fe - Mn alloy. Represented as a $\gamma$ structure with stacking faults two layers apart.
$\kappa'$	Kappa prime phase b.c.t. with lattice parameters $a = 2.883\text{\AA}$ , $c = 2.923\text{\AA}$ for a 0.72% C 8% Mn steel.	First reported by Lysak and Vauk <sup>(110)</sup> . Transforms at temperatures below 0°C to K and $\alpha_t$ phases. May be regarded as $\alpha_t$ martensite with the stated c/a ratio.
K	Kappa phase, b.c.c. lattice parameter $a = 2.880\text{\AA}$ over the range 0.52% - 1.25% C.	Reported by Lysak and Vauk <sup>(109)</sup> .

PHASE	DESCRIPTION	COMMENTS
$\gamma$	f.c.c. phase free from carbon with a lattice parameter $a = 3.5807 - 3.6237\overset{\circ}{\text{A}}$	Found in binary Fe - Mn system above 10% Mn.
$\gamma_c$	f.c.c. austenite containing carbon.	

Although some of the phases shown in the table have not been found in Fe - Mn alloys, it is possible they will be found in the more complex systems created when further alloy additions are made to selected Fe - Mn base compositions. The work is also of importance from the theoretical aspect in that it suggests the existence of more stages in the gamma  $\rightarrow$  alpha transition sequence.

## 5.0. Experimental Details

### 5.1. Preparation of Alloys

The impurity level in these alloys was kept as low as possible, Japanese iron and electrolytic manganese being used to make up the melts. The melting unit was a small high frequency furnace of about 10 lbs. capacity. The charge was air melted because due to the high vapour pressure of manganese considerable losses of this element would have occurred if melted under vacuum. This loss of manganese could have been reduced by melting under argon, but this would have required a special unit being built, so it was decided to air melt adding excess manganese to account for the melting losses.

- 100 -

The various melts were cast into  $1\frac{1}{2}$ " diameter x 6" long graphite pot moulds. These ingots were subsequently reheated and forged into lengths of  $\frac{3}{8}$ " diameter rod which formed the basic starting material for all the experiments in the series. Identification was maintained by stamping code numbers on the flattened ends of the bars.

The bars were inspected before further processing by cutting off samples from both ends. These samples were polished and etched and examined for piping. If any section taken from a bar was found to be piped, the respective bar was cut back until no piping was visible. This was confirmed by taking a further sample from the suspect end of the bar. Some of the samples examined revealed the presence of a negligible amount of inclusions, probably manganese silicate.

The analysis of the melts is given in appendix A1.0. It can be seen that as the manganese content increases, so does the value of the carbon and silicon figure although at no time do the values rise above 0.04% and 0.34% respectively. The values obtained for the other elements may be regarded as representing residual levels considering the starting materials employed in making up the melts.

The strip material used in the cold rolling experiments was produced by hot forging the  $\frac{3}{8}$ " diameter rod down to  $\frac{1}{8}$ " thick strip. The edges of this strip were then sheared parallel and the whole surface ground all over to remove scale and surface imperfections. The strip was further reduced by cold rolling to  $\frac{1}{16}$ " thick strip, then annealed at  $950^{\circ}\text{C}$  for  $1\frac{1}{2}$  hours in an argon atmosphere followed by air

cooling.

## 5.2. Testing Techniques

### 5.2.1. Mechanical Tests

#### 5.2.1.1. Tensile Tests

The tensile test pieces were machined from the  $\frac{3}{8}$ " diameter forged bar after it had been annealed at 950°C for 1½ hours in an argon atmosphere followed by air cooling. The tapered test pieces employed in the determination of true stress true strain curves is shown in figure 42.

The apparatus used for the tensile testing is shown in figure 43. For elevated temperature work the Hounsfield tensile machine was fitted with a small portable furnace, the temperature of which was capable of being controlled to  $\pm 5^{\circ}\text{C}$ . The specimen under test was surrounded by the furnace and connected to the machine by means of nimonic split grips and tie rods, which were connected in turn to the standard machine grips.

A similar set-up was used for the low temperature tests, the furnace being replaced by a cold chamber shown in section in figure 44. Again the specimen was connected to the standard grips via the nimonic split grips and tie rods. The specimen in the chamber was surrounded by a mixture of isopentane and liquid nitrogen at  $-100^{\circ}\text{C}$ . Before commencing a test the assembly was allowed to soak for 20-30 minutes in order to establish a uniform temperature in the specimen and grips. The temperature in the cold chamber was measured by means of a thermometer, small additions of liquid nitrogen

were made from time to time in order to maintain the correct temperature level.

In order to study the deformation characteristics at low temperatures ( $-100^{\circ}\text{C}$ ) and medium temperatures ( $300^{\circ}\text{C}$ ), the tapered tensile test pieces were pulled in tension to fracture, the reduction in area at different points along the test piece being used as a measure of the degree of strain. The true stress - true strain figures were obtained from the following relationships:-

$$\text{True strain } (\epsilon) = 2 \log e \left( \frac{D_i^0}{D_i} \right) \quad . . . . (48)$$

where  $D_i^0$  = original diameter at a point on the axis of the test piece, and  $D_i$  = final diameter in the same position.

$$\text{True stress } (\sigma) = \frac{P_{\max}}{A_i} \quad . . . . (49)$$

where  $P_{\max}$  = maximum load, and  $A_i$  = instantaneous cross-sectional area at a point on the axis of the tapered specimen after fracture.

### 5.2.2. Impact Tests

The Hounsfield balanced impact test was chosen because it required the least amount of material per test piece and preparation of the test pieces was comparatively simple. Starting with  $\frac{5}{16}$ " diameter x  $1\frac{3}{4}$ " long blanks, machined from the  $\frac{3}{8}$ " diameter forged rod, the notches were cut using the standard bench notching machine. The notches were checked with the standard gauge and found to be correct.

The low temperature specimens were soaked in a mixture of cardice and acetone for about 20-30 minutes prior to

testing. The temperature in the thermos bottle was checked by means of a thermometer. In order to minimise the pick up of heat, the specimen holder was swabbed with the freezing mixture at intervals prior to testing. The specimens were speedily transferred to the machine and tested immediately, thus reducing temperature change to a minimum.

The room temperature tests of course posed no particular problems.

The tests at 100°C were carried out by first raising the specimens to temperature by boiling them in water. The heat loss to the specimen holder was again minimised by swabbing with the boiling water prior to testing. The specimens were quickly transferred from the bath to the machine and tested immediately.

### 5.3. Metallography

#### 5.3.1. Optical Techniques

Sections were cut for microscopic examination using a hacksaw or small jeweller's saw. After mounting in a cold setting compound, the specimens were rubbed flat on a file prior to polishing down to a 600 grit finish on water lubricated emery papers. Initially the specimens were finish polished on rotating polishing pads impregnated with 6  $\mu$  and 1  $\mu$  diamond paste. The structures obtained on etching in 2% nital and other reagents were rather indistinct and it was concluded that mechanical polishing alone had failed to remove the distorted work hardened layers, so electro-polishing was resorted to. The mounted specimens were

drilled from the back to allow electrical contact with the specimen to be made. The specimens were electro-polished, after pregrinding to 600 grit, on an 'Electropol' machine using the A2 electrolyte under the following conditions:

Flow rate	3-4
Current	1.8 amps
Time (approx.)	10 seconds.

The above conditions refer to a  $1.0 \text{ cm}^2$  specimen.

The specimens were considered to be correctly polished when all the 600 grit scratches had been removed and the structure showed up clear and undistorted on etching.

The etching reagent employed consisted of saturated sodium thiosulphate + 10% potassium bisulphite. This stain etching reagent was first proposed by Schumann<sup>(50)</sup> as it preferentially etched the phases present in iron-manganese alloys. The  $\gamma$  phase is stained etched to a straw colour, the  $\alpha$  phase to a bluey-grey colour, while the  $\epsilon$  phase is outlined but not stained. The specimens need to be cleaned thoroughly before using this reagent, otherwise uneven staining results. A quick dip in one of the standard etching reagents, e.g. nital, prior to using the stain etch seems to give more uniform results.

### 5.3.2. X-ray Diffraction

Historically this work was started prior to finding the technique required for using the stain etching reagent successfully. In the first instant, X-ray diffraction was embarked upon as a means of identifying the phases present

in the alloys when difficulty was experienced with the optical techniques. Diffractometry was chosen because it was possible to use the as forged sections previously prepared for micro-examination; in any case it was known that deformation of any kind would lead to transformation of the original structure. Thus the use of the Debye-Scherrer technique using powder specimens was ruled out. In addition of course the diffractometer provided a direct record of the intensities of the various peaks, the intensity of which could be analysed by means of a planimeter. A molybdenum source was employed as this obtained the strongest response from the Fe - Mn alloys. A zirconium filter was used to remove  $K_{\beta}$  radiation.

The method used in the present series of experiments is based on comparing the integrated intensities of selected reflections of the phases present. The integrated intensity of a diffraction line is given by the following equation from reference (162):-

$$I_{(hkl)} = n^2 V m (LP) e^{-2m} (Ff)^2 \dots \dots (50)$$

where  $I_{(hkl)}$  = integrated intensity for a particular  
(hkl) reflection.

$n$  = number of cells in a cubic centimetre

$V$  = volume exposed to the X-ray beam

L.P. = Lorentz-Polarisation factor

$m$  = multiplicity of (hkl)

$e^{-2m}$  = Debye-Waller temperature factor

$F$  = structure factor

$f$  = atomic factor.

For  $n^2V$  in equation (50) we may substitute  $V/v^2$  (Ref. 163) in which 'v' is the volume of the unit cell.

If the ratio between the integrated intensities of the phases under comparison is denoted by P:-

$$P = \frac{I_x}{I_y} = \frac{V_x v_y^2 m_x (LP)_x e^{-2m(F_x f_x)^2}}{V_y v_x^2 m_y (LP)_y e^{-2m(F_y f_y)^2}} \dots (51)$$

Each of the above factors depend upon the reflection used.

A factor G is then calculated for each combination of peaks used so that:-

$$P = \frac{V_x}{V_y} \times G \dots (52)$$

If x and y are the only phases present,

$$V_x + V_y = 1 \dots (53)$$

Substituting (53) in (52) gives:-

$$V_y = \frac{1}{1 + P/G} \dots (54)$$

or  $V_x = \frac{1}{1 + G/P} \dots (55)$

The Philips PW 1011 diffractometer used for the analysis employs Bragg-Brentano focussing and the absorption factor is independent of the diffraction angle. The phases present result from diffusionless transformations and so they were regarded as being of the same composition. Therefore, no corrections were made for absorption differences.

Two methods were used for measuring the integrated intensity of the peaks observed:-

- (1) The area under the peak was measured by means of a planimeter, an average of at least five

readings being taken to give the intensity figure.

- (2) The integrated intensity was determined by subtracting the total scanned intensity from the means of the counts of the background on both sides of the peak.

A sample of N counts belongs to an infinite population of counts with a normal distribution. Thus in terms of small sample theory the confidence limits for the population mean can be represented by the equation

$$\bar{x} \pm t_c \frac{s}{\sqrt{N - 1}} \dots \dots \dots (56)$$

- where  $\bar{x}$  = the sample mean,  
 s = the standard deviation of the sample,  
 N = the total number of counts recorded,  
 $t_c$  = the confidence coefficient which depends upon sample size.

The standard deviation of the sample mean is given by the equation:-

$$\sqrt{\frac{\sum_{j=1}^N x_j^2}{N} - \left(\frac{\sum_{j=1}^N x_j}{N}\right)^2} \dots \dots \dots (57)$$

- where s = standard deviation of sample,  
 x = individual sample counts,  
 N = total number of sample counts.

The standard deviation of the intensity of the integrated peak ( $s_p$ ) is given by the equation:-

$$s_p = \sqrt{s_{p+b}^2 + s_b^2} \quad \dots (58)$$

$s_{p+b}$  = standard deviation of peak and background,

$s_b$  = standard deviation of mean background  
intensity of a particular peak,

where  $s_{b1}$  and  $s_{b2}$  are the standard deviations of the backgrounds on both sides of the peak.

A computer programme was devised to handle the data obtained and is given in appendix A.3.0.

The method proved to be most time consuming because it was necessary to reset the counting device manually as no automatic reset and print out device was fitted to the diffractometer.

Whenever possible the peaks were scanned at  $\frac{1}{4} 2\theta$  per minute for four minutes. Five counts were taken over each peak and five counts of four minutes duration on the background at both sides of the peaks. An average of the two background counts was taken as the background level for each particular peak.

The reflections  $(200)_\alpha$ ,  $(200)_\gamma$  and  $(10.1)_\epsilon$  were chosen for comparison purposes as they were free from serious interference by reflection from other planes. A typical trace for a duplex alloy is shown in appendix A.2.0. while table 8 shows the G values employed.

#### 5.4. Ageing of air cooled alloys

This experiment was done to find out if the alloys responded to ageing (tempering), which might bring about a

change in hardness due to precipitation hardening or cause a modification of the structure resulting from air cooling.

Small disc specimens  $\frac{1}{8}$ " diameter were cut from each of the  $\frac{5}{8}$ " diameter bars by means of a hacksaw and rubbed on a flat file to obtain smooth flat parallel faces. Each disc was identified by means of numbers stamped on lightly with small metal stamps. The samples were annealed at  $1050^{\circ}\text{C} \pm 5^{\circ}\text{C}$  for 24 hours in an argon atmosphere. This prolonged treatment produced a slightly oxidised and etched surface which was removed from the flat faces of the specimens by rubbing them on water lubricated emery laps. The sample discs were then divided into sections by electro spark machining so avoiding any work hardening or heating effects which might result from hacksawing. The sectors, suitably marked to maintain identification, were then aged in an electric furnace for periods of up to two hours. The cold samples were placed in the furnace held at the required temperature, aged for the desired time, then removed and allowed to air cool. The slight oxide film produced by this treatment was removed by polishing on fine emery paper prior to hardness testing.

The hardness tests were done on a standard Vicker's machine using a pyramidal diamond indenter. Each reported figure is an average of three or more tests taken at random position on the specimen.

### 5.5. Cold Rolling

The purpose of this experiment was threefold:-

- (1) To find out if the alloys could be cold worked

successfully.

- (2) To confirm that cold working causes transformation of  $\epsilon \rightarrow \alpha$  martensite.
- (3) To produce material suitable for the production of thin films for electron microscopy.

The thin strip used in this experiment was produced as described in Section 5.1. The samples of annealed strip were cold rolled in steps of 5% reduction in thickness, pieces being cut off at each stage for examination. This procedure was continued until the specimens showed signs of transverse cracking.

The series of specimens obtained were hardness tested on the Vicker's machine prior to being mounted in a cold setting resin for X-ray examination. The specimens were polished as described in Section 5.3.1. before being examined by the X-ray diffraction technique described in Section 5.3.2.

## 6.0. Results

### 6.1. Mechanical tests

A summary of the mechanical properties obtained is shown in figure 45. It can be seen that the properties depend very much upon composition which in turn determines the micro structure. The 12.5% Mn alloy, which consisted of about a 50:50 mixture of alpha and epsilon martensite, showed the highest strength and lowest elongation figures. The Hounsfield balanced impact value for this particular alloy indicates that the ductile to brittle transition value lies near room temperature. With increasing manganese content

alpha is firstly replaced by epsilon, and, as the percentage of retained austenite increases, the strength decreases and ductility increases.

The figures 46 a-e give the impact figures obtained by means of the Hounsfield balanced impact machine. Except for alloys containing about 12-13% Mn, fairly good impact values were obtained at  $-80^{\circ}\text{C}$ .

#### 6.1.1. True-stress v True-strain Curves

The alloys tested contained 15.6%, 28.25%, 32.5% and 37.0% Mn respectively. They were all of the austenitic gamma type except the 15.6% Mn alloy which in the  $950^{\circ}\text{C}$  normalised condition was composed of gamma and epsilon martensite.

The results of the experiment are shown in figures 47 a-d.

The change in shape of the true stress/true strain curves is due solely to a change in flow stress with temperature, providing the structure resulting from the deformation is the same.

Figures 48 a-e show that the mechanical properties have the usual temperature relationship for f.c.c. structures i.e. the ultimate tensile strength is more profoundly affected by change in temperature than either the yield strength or elastic limit.

### 6.2. Metallography

#### 6.2.1. Optical microscopy

In the region 0-10% Mn the gamma phase transforms

directly to alpha while between 10% and 15% Mn the uncompleted sequence  $\gamma \rightarrow \epsilon \rightarrow \alpha$  is followed. The alpha formed in this range is found sandwiched between pre-existing bands of epsilon phase which formed initially along the  $\{111\}$  planes of the parent gamma phase. This state of affairs is shown in figure 49 for a 12.5% Mn alloy at a magnification of X1600. The alpha phase is revealed as light grey lens shaped masses crossing light coloured epsilon bands. The similarity between the appearance of alpha in Fe - Mn alloys and that found in stainless steel of low stacking fault energy leads to the suggestion that the phase is likely to be in the form of laths and that a similar orientation relationship is likely to exist i.e.

$$\begin{array}{l} (111)_{\gamma} \parallel (0001)_{\epsilon} \parallel (101)_{\alpha} \\ [\bar{1}\bar{1}0]_{\gamma} \parallel [\bar{1}\bar{2}10]_{\epsilon} \parallel [11\bar{1}]_{\alpha} \end{array}$$

Alloys in the range 16-30% Mn are composed of varying percentages of gamma and epsilon phase. Figure 50 shows a typical microstructure for an 18.5% Mn alloy at X150. The structure has a pronounced widmanstatten pattern, the epsilon phase forming on the (111) planes of the parent structure.

Above 28% Mn the structure at room temperature consists of equiaxed gamma grains, a considerable number of which are twinned. This suggests a low stacking fault energy (see figure 51).

Representative samples of the specimens annealed at 950°C for 1½ hours followed by air cooling showed light and dark bands on stain etching in saturated sodium thiosulphate

plus potassium metabisulphite. The under-lying structure, however, appeared to be the same. A statistical hardness survey, using a Knoop penetrator with a 100 gramme load, of the light and dark areas showed that for a 95% confidence interval for Students  $t$  there was no significant difference in hardness. On the basis of the hardness survey it was therefore concluded that any residual segregation was insignificant. For details see appendix A.4.0.

In order to estimate the percentages of each phase present in the alloy a series of point counts were carried out using a grid with a 100 intersections. The magnification was adjusted to reveal the structural details present.

Figure 52 shows the structures resulting from annealing at  $950^{\circ}\text{C}$  for  $1\frac{1}{2}$  hours followed by air cooling. Each result shown is the average of five counts.

Samples annealed at  $1150^{\circ}\text{C}$  for 24 hours plus  $950^{\circ}\text{C}$  for  $1\frac{1}{2}$  hours gave a uniform appearance on etching showing no banding effect. The phases present on the basis of point counting are shown in figure 53, which is a plot of counts (number of intersections with epsilon phase) versus the manganese content of the alloy. The crosses indicate the actual values obtained while the ringed crosses indicate the middle value of a sample of five results. A similar count for the gamma phase is shown in figure 54. If the values for gamma and epsilon are added together, a number of intersections are unaccounted for, these are the bands of gamma criss-crossed by numerous laths of epsilon phase. Examination at a higher magnification revealed that these areas contained about 50%

of each phase in the case of alloys of higher manganese content (greater gamma content), while in the region of 15% Mn almost 100% epsilon is found (see figure 55). The dotted line indicates the revised counts based on the original count plus 50% of unallocated counts in the case of the higher manganese alloys, while in the case of the 15.6% Mn alloy, the original count plus 100% unallocated count is used as an estimate of the true value. Figure 56 shows a plot of percentage phase versus manganese content based on the above revised values.

The epsilon phase appears to reach a maximum of 85% at about 14% Mn. The gamma to alpha curve is very steep in this region which means that slight changes in composition would lead to considerable changes in microstructure.

Figure 57 shows the effect of etching time on the percentage of apparent epsilon phase counts present in a 15.6% Mn alloy. It can be seen that the longer the etching time the lower the apparent epsilon content. This is due to the fact that the reagent is also capable of staining the epsilon phase when the etching time is prolonged. Obviously this can be a source of error, therefore the minimum etching time which gave a uniform stain etch was used.

## 6.2.2. X-ray diffraction

### 6.2.2.1. Forged bar samples air cooled from 950°C

Figure 58(a) shows the results of an X-ray diffraction study carried out on a series of alloys air cooled from 950°C. On the whole the results were similar to those obtained by

Schumann for material heated to 1000°C and air cooled with the exception that the epsilon content appears to reach a maximum at about 15.0% Mn.

In view of the banding effect previously noted on etching, it was decided to extend the period of heat treatment in order to ensure homogeneity in the specimens examined. Therefore, samples were annealed at 1150°C for 24 hours plus 950°C for 1½ hours followed by air cooling. The sample showed no banding on stain etching. Figure 58(b) shows the results of this study. It can be seen that the epsilon content reaches a maximum at about 15% Mn then begins to decrease.

#### 6.2.2.2. Tapered tensile specimens

A diffractometer study was also made of sections cut from the tapered tensile test pieces pulled at various temperatures ranging from -100°C to 300°C. The results of this investigation are shown in figure 59. The alloys containing 32.5% Mn and 27.0% Mn respectively showed no phase change when pulled in tension and are therefore excluded from the figures. The 15.6% Mn alloy transforms completely to epsilon after about .06 strain. However, the degree of deformation achievable never reaches that required to cause the appearance of alpha martensite, even at the point of fracture. Nevertheless, if figure 59 is compared with figure 60(a) it can be seen that the same pattern is followed under both tensile and compressive stresses.

The figures do not compare quite so well for the

28.25% Mn alloy, (see figures 60(c) and 59). It should be borne in mind, however, that no attempt has been made to correct the percentage phase for orientation effects and to all intents and purposes the different modes of deformation achieve the same result. Deformation by rolling has, however, the advantage that large reductions can be achieved although it is difficult to control the actual deformation temperature. Large strains would, however, probably be achieved by machining the gauge length parallel when it begins to neck down. The disadvantage of this procedure is that the test has to be interrupted, which may affect the ultimate result.

#### 6.2.2.3. Cold rolling experiment

A diffractometer study was made of the phases present at each stage of reduction (see figures 60 a-c). No attempt was made to correct the results for preferred orientation, therefore, they may be regarded only as semi-quantitative. Nevertheless, they clearly indicate the effect of cold deformation on the phases present.

In the case of the 23.0% Mn alloy (initially gamma plus epsilon) the amount of gamma decreased with increasing deformation until at 50% reduction the structure consisted entirely of epsilon martensite.

The 15.6% Mn alloy showed somewhat different behaviour, the gamma phase disappearing at about 7.0% reduction. Greater amounts of reduction caused an increase in the alpha martensite phase with a corresponding decrease in epsilon. Micro-examination revealed that the alpha phase formed within the

epsilon phase plates formed on the  $\{111\}$  planes of the deformed structure figure 61.

### 6.3. Ageing experiments

From figures 62(a) and 62(b), representing alloys containing 12.5% and 12.86% Mn respectively, it can be seen that ageing at the lower temperature produces an initial increase of some 25-40 points Hv. followed by a very slight drop at extended times of ageing. At the ageing temperature of 600°C the initial increase was more rapid while at longer ageing times the hardness falls away rapidly to the initial level of 290 Hv. The ageing effect observed would appear to be due to the small residual content of interstitial elements. According to previous experiments by other workers at a temperature of 600°C the epsilon phase should have reverted to gamma phase while the alpha to gamma change might be partially or fully completed. This means that on cooling after ageing the gamma phase has transformed back again to a structure containing similar proportions of epsilon and alpha as evidenced by the hardness results. The small increase in hardness obtained on ageing would appear to be of no significance.

Figures 62 d-f for alloys containing 15.6% Mn, 18.5% Mn and 20.7% Mn shows a similar pattern of behaviour. Alloys containing between 23.0% Mn and 37.0% Mn showed little response to ageing, (figures 62 g-i). On the basis of the above evidence it was concluded that ageing would not benefit the general strength level to any large extent.

#### 6.4. Cold rolling

Alloys representative of the types of structure found in the range 10-40% Mn were selected for examination. The 15.6% Mn alloy represented a probable alpha plus epsilon plus gamma mixture while the 23% Mn alloy represented a gamma plus epsilon structure and the 28.25% Mn alloy an all gamma structure.

From the graph  $\Delta H_v$  versus percentage reduction in thickness (figure 63), it can be seen that the 28.25% Mn showed the greatest increase in hardness (300  $H_y$  at 50% reduction) being capable of 80% reduction before cracking.

#### 7.0. Discussion

From the experimental evidence it may be deduced that the mechanical properties of the alloys are dependant upon the combination of phases present in the metal structure and therefore upon the composition of the alloy in question. Alloys containing 10-15% Mn with alpha plus gamma structures were the strongest in the series of alloys examined but have a high ductile-to-brittle transition temperature under impact conditions. Above 15.0% Mn the ductile gamma phase appears in the structure, at the same time the alpha phase is eliminated, which leads to an improvement in ductility but a decrease in strength. Above 28% Mn all gamma phase structures are obtained at room temperature. Both mechanical tests and cold rolling experiments showed that all the alloys examined were capable of a considerable degree of cold work and should be comparatively easy to manufacture in the various wrought forms.

The fair level of strength combined with ductility shown by alloys with epsilon plus gamma structures suggests that they might form the basis for the development of a precipitation hardening alloy.

## 7.1. Properties of alloys examined

### 7.1.1. Phases present after standard heat treatment

Diffraction studies of the phases present in alloys containing from 10-37% Mn (in the air cooled condition) gave results similar to those obtained by Schumann. The structures found are confirmed by the optical microscopy survey although the quantitative values of the phases indicated are of limited value due to the difficulty of allocating areas composed of closely knit phases. Assuming a linear relationship between percentage phase and temperature an approximate expected percentage epsilon phase can be obtained which compares favourably with the experimental values obtained. An examination of figure 64, which shows the  $M_S$  temperatures determined by Schumann together with hypothetical  $M_F$  temperatures for the alloy series, tends to confirm the fact that the epsilon phase content reaches a maximum at about 15% Mn. The  $M_S^E$  lies at about 130°C and the  $M_F^E$  temperature would seem to be at about 20°C. Assuming an approximate linear relationship between percentage phase and temperature range above room temperature (although an s curve deviation is likely) an approximate expected percentage of epsilon phase can be obtained. This is shown as a dashed line in figure 58(b), which indicates that the estimated values conform favourably

with the determined values. At 28% Mn the  $M_S^\epsilon$  falls below room temperature so that an all gamma phase structure alloy is obtained.

The above results suggest that the temperature difference between  $M_S^\epsilon$  and  $M_F^\epsilon$  is approximately constant enabling a probable  $M_F^\epsilon$  to be predicted. This is shown as a dotted line in figure 64. A sample of material containing 28.25% Mn quenched from 950°C to -196°C failed to transform to epsilon phase suggesting that the  $M_S^\epsilon$  falls away steeply at this composition. Schumann studied the growth of epsilon phase platelets in a 26.12% Mn alloy, which contained a small amount of epsilon phase at room temperature. By cooling it to -196°C for five minutes he caused the existing plates to thicken after they intersected an obstacle such as a grain boundary. Transformation was incomplete suggesting that either the transformation was an isothermal one or that the  $M_F^\epsilon$  was much lower than predicted. Another possibility is that stabilisation may have occurred.

Applying similar reasoning to the  $\epsilon \rightarrow \alpha'$  transition temperatures enables a prediction of percentage alpha phase versus manganese content to be made. Again the predicted values fall quite close to those determined by diffractometry. A probable  $M_F^{\epsilon \rightarrow \alpha'}$  may also be predicted, see figure 64. The determination of the exact form of the  $M_F$  temperature curve could form the basis of a further study.

#### 7.1.2. Effect of temperature on properties

The properties of the alloys vary with the proportions of the various phases present. The alloys composed of

mixtures of alpha and epsilon phases (10-15% Mn) are the strongest in tension although unfortunately these alloys exhibited a ductile to brittle transition in impact at about room temperature. With increasing manganese content the ductile gamma phase appears resulting in a lower tensile strength but increased ductility. The ductile to brittle transition temperature is also lowered, an all gamma phase structure (37.0% Mn) realising an impact value of 48 ft.lbs. (Hounsfield Balanced Impact)  $\equiv$  to 115 ft.lbs. Izod at  $-100^{\circ}\text{C}$ .

Figure 45 summarizes the mechanical properties obtained. The figures are based on a strictly limited number of test pieces as the material was in limited supply, and it was desired to survey the whole field on as wide a front as possible. The fair level of strength obtained together with good ductility at room temperature and below suggests that the epsilon and gamma phase structures might form the basis for higher strength alloys. The mechanical properties show the usual temperature relationship, the ultimate tensile strength being more profoundly affected by change in temperature than either the estimated yield strength or elastic limit.

In general for f.c.c. metals temperature has a considerable effect on strain hardening, the stress/strain curves being appreciably steeper at  $-100^{\circ}\text{C}$  (figures 47a-d). In the presence of a c.p.h. phase ( $\epsilon$  martensite) the rate of strain hardening should increase particularly at temperatures below room temperature. This effect is shown in figures 65a-c in which the work hardening coefficient ( $d\sigma/d\epsilon$ ) is plotted against the degree of strain. It would seem that in the case

of the Fe-15.6% Mn alloy, which consisted almost entirely of c.p.h. epsilon martensite in addition to normal basal slip, the hard nonbasal slip planes are forced to operate in the polycrystalline mass in order to maintain coherence resulting in a high rate of work hardening. At higher temperatures more softer basal slip would be favoured and the rate of work hardening lowered. For the Fe-15.6% Mn alloy at 300°C this effect is most pronounced, the rate of work hardening being very low. For alloys with an all gamma f.c.c. structure the effect of temperature is not so pronounced. Figure 65(a) shows that the Fe-28.25% Mn alloy has a fairly high rate of work hardening at -100°C, which remains fairly constant up to 18% strain. Diffractometer studies have shown that up to about this strain the deformation process occurs mainly by a slip mechanism. The decreasing rate observed thereafter corresponds to the conversion of gamma phase to epsilon martensite.

At -100°C (figure 65(a) ) the Fe-32.5% Mn and the Fe-37.0% Mn alloy have similar work hardening rates although that for the former alloy decreases at the greater rate. At 10% and 35.5% strain the two alloys have the same work hardening coefficients. At room temperature (figure 65(b) ) the Fe-37.0% Mn alloy has the higher work hardening coefficient although after about 18% strain the work hardening is comparable to that of the Fe-32.5% Mn alloy. At 37% strain the work hardening ratios are the same. The probable explanation of the slightly higher rate of work hardening in the Fe-37.0% Mn alloy can be found in the effect of manganese

on the stacking fault energy. The addition of manganese is thought to lower the stacking fault energy which means that the alloy of higher manganese content should have the lower value. The effect of this would be to make cross-slip more difficult in the Fe-37.0% Mn alloy resulting in a higher rate of work hardening. At higher strains cross-slip is possible in both alloys and the rates of work hardening become similar. At 300°C (figure 65(c) ) the work hardening rates are practically the same, no doubt at this temperature cross-slip is thermally assisted to a greater degree, thus reducing the difference in the initial rates of work hardening.

#### 7.1.3. Diffraction study of sections cut from tapered test pieces

A diffraction study of sections cut from the tapered tensile test pieces, when compared with the results obtained from the cold rolled strip specimens, showed that the same pattern of deformation was followed under both tensile and compressive stress. The effect of stressing is either to produce deformation of the prior phases by slip or to bring about a change of phase, or both. Deformation of the gamma phase, for example, results firstly in the production of slip lines within the grains to be followed at greater degrees of deformation by the formation of epsilon phase within the slipped regions. At no time during the testing of the tapered test pieces, even at the point of fracture, was the alpha phase observed as a result of the deformation process. Lowering the temperature of deformation favours the

transformation to martensite, epsilon martensite in this case. It is well known that in the case of 18% Cr - 8% Ni stainless steels the degree of strain achieved before fracture is greater when it results in the formation of martensite rather than simple slip. If the formation of martensite can be delayed until the later stages of deformation in a tensile test, slip is replaced by transformation to martensite which increases the amount of elongation possible before necking and final failure of the specimen occurs. This effect was noted by Llewellyn and Murray<sup>(85)</sup> while working on austenitic stainless steels of varying stability. By lowering the temperature of testing they facilitated the formation of martensite through deformation. The elongation values were found to increase as the testing temperature was decreased, e.g. a 19% Cr - 10% Ni alloy previously cold worked at room temperature had a total elongation of about 5% at 20°C. This rose to 30% elongation at -196°C.

#### 7.1.4. Effect of deformation by cold rolling

The cold rolling experiments show that the alloys are capable of considerable reduction in thickness before they begin to crack. The greater ductility exhibited by the Fe-15.6% Mn alloy can be explained in terms of its preference to transform to martensite when deformed in rolling. A diffractometer study of the deformed strip showed that during rolling any gamma phase present transformed firstly to epsilon martensite, which on further deformation transformed to alpha martensite. As indicated in section 7.1.3. transformation to

martensite as opposed to deformation by the slip mechanism confers a greater degree of ductility on the material.

The Fe-23% Mn alloy showed a somewhat greater increase in hardness with reduction in thickness. Deformation in this alloy causes the gamma phase present to transform to epsilon martensite giving some degree of ductility. At the reductions achieved no transformation to alpha martensite was observed.

Although deformation of the Fe-28.25% Mn alloy resulted in a certain amount of transformation to epsilon martensite, the amount present was never more than about 36%. This means that deformation is predominantly slip in character accompanied by a certain amount of transformation to epsilon martensite resulting in the observed increased hardening effect.

Deformation is thus seen to provide the extra energy required to cause the  $\gamma \rightarrow \epsilon \rightarrow \alpha$  transformation to go to completion. The total driving force,  $\Delta G_{\gamma \rightarrow \text{martensite}}^{M_S}$  is seen to be made up of a mechanical energy factor and a thermodynamic one

$$\Delta G_{\gamma \rightarrow \text{martensite}}^{M_S} = \Delta G_E + \Delta G_{\gamma \rightarrow \text{martensite}}^{M_S} \quad (59)$$

The degree of strain developed in the tapered tensile specimens is, however, insufficient to cause transformation to alpha martensite.

## 7.2. Transformation thermodynamics

### 7.2.1. Thermodynamics of the $\gamma \rightarrow \alpha$ transformation

Assuming that iron and manganese form ideal binary solid solutions Jones and Pumphrey derived the following

equation for the free energy change involved in the gamma to alpha transformation:

$$\Delta G^{\gamma \rightarrow \alpha} = X \Delta H - \Delta (1 - X) G_{Fe}^{\gamma \rightarrow \alpha} \quad \dots (60)$$

where

$$\Delta G_{Fe}^{\gamma \rightarrow \alpha} = RT \ln \left( \frac{1 - X_{\alpha}}{1 - X_{\gamma}} \right) \quad \dots (61)$$

Using Schumann's<sup>(49)</sup> values for  $M_S$  temperatures and the Fe - Mn equilibrium diagram to obtain the concentrations of gamma and alpha in equilibrium at a specific temperature, the above formulae yielded the values plotted as in line (1) in figure 66. The driving force is seen to rise gradually until it reaches a plateau at 7% Mn corresponding to a driving force of about 250 calories per gramme atom (1050 J/g). A standard enthalpy of 2700 (11,310 J/g) calories was assumed for all alloys as this value gave the best agreement between the observed and calculated diagrams.

Values of  $\Delta G_{Fe}^{\gamma \rightarrow \alpha}$  calculated from the equilibrium diagram by means of equation (61) are generally lower than those determined by other workers in this field. Typical values of  $\Delta G_{Fe}^{\gamma \rightarrow \alpha}$  are shown in figure 67. It can be seen that the curve for the values of  $\Delta G_{Fe}^{\gamma \rightarrow \alpha}$  calculated from the equilibrium diagram has a very shallow gradient particularly at the lower temperature end. This shallow gradient is converted to a plateau in curve 1 figure 66, showing values of  $\Delta G^{\gamma \rightarrow \alpha}$  calculated according to equation (60). Apparently the values of  $X \Delta H_{Mn}^{\gamma \rightarrow \alpha}$  just compensate for any slight increase in  $\Delta G_{Fe}^{\gamma \rightarrow \alpha}$  producing the observed plateau.

Using Kaufman and Cohen's (hereafter referred to as

K and C) figures for  $\Delta G_{Fe}^{\gamma \rightarrow \alpha}$  and Zener's approximation formula

$$\Delta G^{\gamma \rightarrow \alpha} = (1 - X_B) \Delta G_{Fe}^{\gamma \rightarrow \alpha} + X_B \Delta H_{Mn}^{\gamma \rightarrow \alpha} \quad \dots (62)$$

where  $X_B$  equals the atomic fraction of manganese and

$\Delta H^{\gamma \rightarrow \alpha} = 2440$  cal/mole (10,210 J/g), the free energy change for the gamma to alpha transformation at 175°C for an Fe-10% Mn alloy is approximately -500 calories per gramme atom (2100 J/g). This figure is twice that given by the Jones and Pumphrey (hereafter referred to as J and P) approximation using values of  $\Delta G_{Fe}^{\gamma \rightarrow \alpha}$  calculated from the iron-manganese diagram.

It was noted in section 2.2.4. that the general approximation formula is:-

$$\Delta G^{\gamma \rightarrow \alpha} = (1 - X_B) \Delta G_{Fe}^{\gamma \rightarrow \alpha} + X_B \Delta G_B^{\gamma \rightarrow \alpha} \quad \dots (63)$$

where  $\Delta G_B^{\gamma \rightarrow \alpha}$  is the free energy difference between the gamma and alpha allotropes of element B, in this case manganese. Various ways of estimating  $\Delta G_B^{\gamma \rightarrow \alpha}$  have been suggested by Hillert<sup>(165)</sup>. Using the simple approximation formula:-

$$\Delta G_B^{\gamma \rightarrow \alpha} = RT \ln \frac{X^\gamma}{X^\alpha} \quad \dots (64)$$

and K and C's values of  $\Delta G_{Fe}^{\gamma \rightarrow \alpha}$ , gave values of  $\Delta G^{\gamma \rightarrow \alpha}$  similar to those of the Zener approximation (curve 3).

From equal free energy considerations Hillert<sup>(165)</sup> arrived at the approximation formula

$$\Delta G_B^{\alpha \rightarrow \gamma} \simeq - \frac{1 - X}{X} ( {}^\circ G_{Fe}^{\gamma} - {}^\circ G_{Fe}^{\alpha} )$$

or

$$\Delta G_B^{\gamma \rightarrow \alpha} \approx - \frac{1-X}{X} ({}^{\circ}G_{Fe}^{\alpha} - {}^{\circ}G_{Fe}^{\gamma}) \dots (65)$$

Using values of  $\Delta G_{Mn}^{\gamma \rightarrow \alpha}$  calculated from equation (65) and K and C's values of  $\Delta G_{Fe}^{\gamma \rightarrow \alpha}$ , gave the approximate values of  $\Delta G^{\gamma \rightarrow \alpha}$  shown in figure 66 curve 4. It can be seen that at 10% Mn the free energy change is similar to that obtained from the J and P approximation.

Considering the work of Zener<sup>(166)</sup>, Darken<sup>(167)</sup>, Kohlhaas and Brown<sup>(168)</sup> and others, Hillert<sup>(165)</sup> derived the expression:-

$$\Delta {}^{\circ}G_B^{\alpha \rightarrow \gamma} = \Delta {}^{\circ}H_B^{\alpha \rightarrow \gamma} - T \cdot \Delta {}^{\circ}S_B^{\alpha \rightarrow \gamma} - \frac{dTc}{dX} \cdot ({}^{\circ}S_{Fe}^{\alpha})_{mag.} \dots (66)$$

the free energy of alpha iron being divided into a magnetic and a non-magnetic term. Using values of  $\Delta G_{Mn}^{\gamma \rightarrow \alpha}$  taken from figure 6 of Hillerts<sup>(165)</sup> paper and K and C's values of  $\Delta G_{Fe}^{\gamma \rightarrow \alpha}$  the values plotted in figure 66 curve 5 were obtained.

There is little to choose between the various estimates of  $\Delta G^{\gamma \rightarrow \alpha}$  in the region of 500-800°C. Below 500°C curve 2 (Zener's approximation formula) and curve 3 (K and C  $\Delta G_{Fe}^{\gamma \rightarrow \alpha}$  and Hillerts estimate of  $\Delta G_{Mn}^{\gamma \rightarrow \alpha}$  equation (65) ) increase at about the same rate giving an estimate of  $\Delta G^{\gamma \rightarrow \alpha}$  of approximately 460-480 cal per mole (1930-2007 J/g) at an  $M_S$  temperature of 200°C. The plateau in curve 1 (J and P estimate) does not seem to be a true representation of the facts as logically it would seem more probable that the free energy change would continue to increase with decreasing  $M_S$  temperatures. Curve 5 (K and C  $\Delta G_{Fe}^{\gamma \rightarrow \alpha}$  and Hillerts

estimate of  $\Delta G_{Mn}^{\gamma \rightarrow \alpha}$  using equation (66)) gives an estimate of 280 calories per mole (1175 J/g) for  $\Delta G^{\gamma \rightarrow \alpha}$  at 200°C which is similar to previously reported values.

### 7.2.2. Thermodynamics of gamma to epsilon transformation

Above 10% Mn the gamma to epsilon reaction is preferred. In order to estimate the driving force for this reaction it was assumed that similar relationships existed for the gamma to epsilon change as for the gamma to alpha change, i.e.

$$\Delta G^{\gamma \rightarrow \epsilon} = X \Delta H - \Delta (1 - X) \cdot G_{Fe}^{\gamma \rightarrow \epsilon} \quad \dots (67)$$

No equilibrium diagram exists for the concentrations of gamma and epsilon in equilibrium so in order to obtain an estimate of the likely phase boundaries the following assumptions were made. The  $M_S^{\gamma \rightarrow \epsilon}$  was taken to represent the epsilon concentration in equilibrium with the gamma phase whose composition was represented by the extrapolated  $\gamma/\alpha$  phase boundary (figure 68). Using the hypothetical phase diagram it was then possible to calculate  $\Delta H$  and  $\Delta G_{Fe}^{\gamma \rightarrow \epsilon}$  using equations 68 and 69.

$$\Delta H^{\gamma \rightarrow \epsilon} = 4.57T \left[ \log_{10} X_{\gamma} - \log_{10} X_{\epsilon} \right] \quad \dots (68)$$

$$\Delta G_{Fe}^{\gamma \rightarrow \epsilon} = 4.57T \left[ \log_{10} (1 - X_{\epsilon}) - \log_{10} (1 - X_{\gamma}) \right] \quad (69)$$

The values obtained are given in table 9 and figure 66 curve 6. It can be seen that as the  $M_S^{\gamma \rightarrow \epsilon}$  decreases the free energy difference decreases reaching a value of 90 calories per mole (378 J/g) at 0°C. This  $M_S^{\gamma \rightarrow \epsilon}$  temperature corresponds to a manganese content of 28% and the beginning of the

all gamma field. Presumably the activation energy at this temperature is sufficiently high to prevent transformation to epsilon martensite.

Making similar assumptions concerning the compositions of the  $\alpha'$  phase and gamma phase in equilibrium with it, the figures given in table 10 and figure 66 were obtained. The free energy difference is seen to be somewhat higher for the gamma  $\rightarrow$  alpha transformation as might be expected from the relative positions of the  $M_S^{\gamma \rightarrow \epsilon}$  and  $M_S^{\gamma \rightarrow \alpha'}$  curves.

The validity of the assumptions made may obviously be challenged. However, the method may probably be justified on the grounds that it at least provides an estimate of the magnitude of the energy change involved.

7.2.3. Effect of mechanical energy on transformation thermodynamics

The cold rolling experiment has shown that the deformation of alloys with an entirely or partially gamma structure leads firstly to the formation of epsilon martensite followed at greater degrees of deformation by the formation of alpha martensite. Considering the schematic diagram shown in figure 69, it can be seen that the free energy of the gamma phase may be supposed to rise from  $\gamma \rightarrow \gamma'$  on deformation. Thus assuming that deformation is confined to the gamma phase,  $M_S^\epsilon$  is seen to be raised to  $M_S^{\epsilon'}$ , which is above room temperature, resulting in the formation of epsilon martensite. As deformation proceeds any residual austenite will become locked in between planes of epsilon phase from

- 101 -

prior deformation. At some stage deformation will be transferred to the epsilon phase raising its free energy level to  $\epsilon'$  (figure 70). Thus  $M_s^{\alpha'}$  is raised to  $M_s^{\alpha''}$ , which is above room temperature, causing alpha martensite to form at the expense of the epsilon phase. The cold rolling experiment indicates that some 80-100% epsilon phase must be present before alpha martensite forms as a result of deformation thus supporting the above argument. As shown in section 7.1.4. equation (30), the total driving force is seen to be made up of a mechanical energy factor and a thermodynamic one.

#### 8.0. Conclusions

- (1) Increasing the manganese content of iron alloys from 10-40% produces the following sequence of structures: 10-15% Mn  $\alpha + \epsilon$  mixtures; 15-28% Mn  $\gamma + \epsilon$  mixtures; 28-37% Mn all  $\gamma$  structures.
- (2) Alloys containing 10-15% Mn with  $\alpha + \epsilon$  structures are the strongest in the series but show a ductile to brittle transition under impact conditions at or around room temperature.
- (3) With the appearance of the gamma phase in the structures the alloys show increased ductility under impact conditions. This coincides with the disappearance of the alpha phase.
- (4) The fair level of strength obtained in the  $\epsilon + \gamma$  structures, together with good ductility under impact conditions at room temperature and below, suggests that these structures might form the basis for

precipitation hardenable alloys.

## 9.0. Future work

The effect of a few alloying elements has been previously studied with particular reference to austenitic manganese steels of high carbon content. This work, though limited in its scope, should nevertheless serve as a guide for future work in this field.

A logical division of potential alloying elements may be made on the basis of whether they favour the austenitic solid solution or undissolved carbides or intermetallic phases. Some solubility in both phases will, of course, normally exist.

### 9.1. Elements favouring solid solution

Nickel is completely soluble in the austenite of manganese steel in amounts up to 16%. It reduces strain hardening and fracture strength, improves ductility, and leaves yield strength unaffected<sup>(169,170)</sup>. The improved ductility is believed to be due to the slow rate of diffusion of nickel away from the grain boundaries, which, in turn, prevents the development of intergranular carbide films.

Silicon is not a particularly useful alloying element in austenitic manganese steels; it is reputed to increase the yield strength but causes embrittlement in amounts over 2%<sup>(169)</sup>.

Copper is generally detrimental to the properties of manganese steel in amounts over 1.0%. It appears to be prone to microsegregation promoting reduced ductility and hot

shortness.

Aluminium has been studied for solid solution effects and as an age hardening agent. Moderate hardening with loss of ductility has been found at 1-3% aluminium. The use of nickel-aluminium age hardening, so successful in stainless steels and nimonics does not appear feasible for manganese steel containing a high percentage of carbon as severe carbide embrittlement occurs at the ageing temperature required.

Chromium is a common additive to manganese steel. It gives increased yield strength but reduces ductility<sup>(169,170)</sup>. The increased yield strength is mainly a solid solution effect, but when chromium is used in conjunction with high carbon contents, some undissolved carbides result.

Nijhawan et al.<sup>(172)</sup> have shown that it is possible to produce austenitic Cr - Mn - N stainless steels on a commercial basis. In the solution treated condition, the steels have on average a tensile strength of 91 - 94 Kg/mm<sup>2</sup> (58-60 tons/in<sup>2</sup>) with an elongation of 50-55%. The nitrogen present is necessary to stabilise the austenite because above 15% Cr the all gamma structures cannot be obtained with manganese alone. As might be expected, the oxidation resistance is not as good as that of 18 - 8 Cr - Ni stainless steels. It is envisaged that the Cr - Mn - N steels will be used in place of 18 - 8 Cr - Ni stainless steels for applications such as hospital ware, dairy equipment, etc., particularly in countries with a plentiful supply of manganese, e.g. India or Russia.

- 15 -

In amounts up to 2.0%, molybdenum improves yield strength without impairing ductility<sup>(169,170)</sup>. Molybdenum also retards the decomposition of austenite during continuous cooling or isothermal exposure<sup>(171)</sup>.

### 9.2. Carbide dispersions

The usual heat treatment for 12.0% Mn, 1.0% C steel is to quench from a 1000°C to obtain a completely austenitic structure free from carbide particles. By varying the heat treatment and the addition of alloying elements it is possible to create various distributions of carbide.

Molybdenum, in conjunction with a relatively low austenitising temperature, yields a carbide dispersion leading to improved abrasion resistance<sup>(173)</sup>. Tungsten behaves in a similar manner but is not so effective<sup>(169)</sup>.

Vanadium is said to increase rapidly yield strength and to reduce ductility<sup>(14,169)</sup>. By austenitising at about 900°C some carbides are left undissolved resulting in an increased hardness level at a given strain.

Titanium and Zirconium additions create a fine dispersion of carbides, which are virtually insoluble. Yield strength is increased while ductility and fracture strength are sharply reduced<sup>(169)</sup>.

### 9.3. Transformation strengthening

Strain-induced martensite may be produced in manganese steel if the  $M_s$  is close to the deformation temperature and this may be achieved by adjustment of manganese and carbon contents<sup>(174)</sup>. The properties are inferior to those of

standard manganese steel, the high carbon, strain induced untempered martensite being too brittle to realise high levels of fracture strength.

#### 9.4. Age hardening

An experimental 12% Mn - Ni - Mo - V alloy showed a yield strength of 110,000 p.s.i. after ageing at 640°C. Low carbon levels were necessary to avoid embrittlement.

Work on high-purity austenitic steels<sup>(175)</sup>, based on 18/10 Cr - Ni and 35/15 Ni - Cr with additions of Ti, Nb and V, has shown that precipitation associated with stacking faults leads to a marked improvement in room temperature strength without a catastrophic fall in ductility. The strength can be further raised by (a) slight straining at room temperature prior to precipitation, (b) small additions of uranium (0.5%). Both these methods result in an increased density of stacking faults on ageing between 650° - 800°C. A similar mechanism may possibly work in the case of austenitic manganese steels of low stacking fault energy.

From the above information it might be concluded that carbon or nitrogen will serve as a useful hardening element provided it is in solution or dispersed in such a fashion that it has minimum effect on ductility while improving the strength of the alloy. Most of the above work was confined to alloys of high carbon content. It is, however, possible that alloys of lower carbon content might not be so sensitive to carbide precipitation as the total volume of precipitate would be less.

An addition of niobium might also be made so that the

carbon might be caused to precipitate as NbC at extended partial dislocations, created by heat treatment or prior cold working followed by ageing.

The addition of nickel on its own is not advantageous as it does not increase yield strength except in certain ranges where  $Ni_3Mn$  may form. However, together with aluminium it provides a standard age hardening system. If the carbon content is kept low the effects of carbide precipitation on ageing would be minimised. Titanium may also be a useful companion for nickel working on the assumption that intermetallic compounds of type  $Ni_3Ti$  might form and give a hardening effect similar to that found in nimonic alloys or  $NiTi$  as in maraging steels. Mn - Ti compounds might also form giving a further strengthening effect.

## 10.0. References

- (1) E.C. Bain, Trans. AIME. V. 70, p.25, 1924.
- (2) A.B. Greninger and A.R. Troiano, Trans. AIME, V.145, p.291; V.185, p.580, 1949.
- (3) J.S. Bowles and J.K. Mackenzie, Acta. Met. V.2, p.129.  
J.K. Mackenzie and J.S. Bowles, ibid. V.2, p.138, 1954.  
J.S. Bowles and J.K. Mackenzie, ibid, V.2, p.224, 1954.
- (4) L. Kaufman and M. Cohen, 'Progress in Metal Physics', V.7, Chapter 3, p.165, 1958.
- (5) D.G. Walker and D.W. Borland, J.Aust.Inst.of Met. V.5/2, p.75, 1960.
- (6) B.A. Bilby and J.W. Christian, Inst. of Metals Monograph and Report Series No. 18, p.121, 1955.
- (7) J.S. Bowles and C.S. Barrett, 'Progress in Metal Physics', V.3, Chapter 1, p.1.
- (8) J.S. Bowles and W.J. McG. Tegart, Acta.Met., V.3, p.90, 1955.
- (9) J.S. Bowles and J.W. Mackenzie, Acta.Met., V.2, p.224, 1954.
- (10) D.S. Lieberman, M.S. Wechsler and T.A. Read, J. Appl.Phys., V.26, p.473, 1955.
- (11) J.S. Bowles and R. Smith, Acta Met. V.8, p.405, 1960.
- (12) H.M. Otte and T.B. Massalski, Acta.Met., V.6, p.494, 1958.
- (13) F.C. Frank, N.P.L. Conference on the relation between structure and strength in metals and alloys, p.248, London, H.M.S.O. 1963.
- (14) J.S. Bowles and N. Kennon, J.Aust.Inst.Met. V.5/2, p.106, 1960.
- (15) Z.S. Basinski and J.W. Christian, Acta.Met., V.2, p.148, 1954.
- (16) L.C. Chang and T.A. Read, Trans. AIME. V.191, p.47-52, 1951.
- (17) H. Bibring et al., J.Inst.Metals, V.87, p.71-76, 1958-59.

- (18) S. Takeuchi and T. Honma: Sci.Rep.Inst. Tohoku University, V.A9, p.492-507, p.508-519, 1957.
- (19) P. Gaunt and J.W. Christian, Acta.Met., V.7, p.529-533, 1959.
- (20) Z.S. Basinski and J.W. Christian, J.Inst.Metals, V.80, p.659-666, 1951-52.
- (21) J. Lehmann and R.F. Hills, J.Nuclear Mat., V.2, p.261-268, 1960.
- (22) A.B. Greninger, Trans. AIME., V.133, p.204-227, 1939.
- (23) R.F. Mehl and D.W. Smith, Trans. AIME., V.113, p.203-210, 1934.
- (24) W.S. Owen et al., 'The Structure and Properties of quenched iron alloys', Second International Materials Symposium, University of California, 1964.
- (25) A. Gilbert and W.S. Owen, Acta.Met., V.10, p.45-54, 1962.
- (26) R.B.G. Yeo, Trans. AIME., V.224, p.1222-1227, 1962.
- (27) R.B.G. Yeo, Trans. ASM., V.57, p.48, 1964.
- (28) J.D. Bolton, E.R. Petty and G.B. Allen, J.I.S.I., p.1314-1318, October, 1969.
- (29) D. Hull and R.D. Garwood, J.Inst.Metals, V.86, p.485-492, 1957-58.
- (30) W.S. Owen and E.A. Wilson, Special Report 93, I.S.I., p.56, 1964.
- (31) A.R. Troiano and F.T. McGuire, Trans.ASM., V.31, p.340-359, 1943.
- (32) F.W. Jones and W.I. Pumphrey, JISI., V.163, p.121-131, 1949.
- (33) D.W. Gomersall and J. Gordon Parr. JISI., p.275-279, March, 1965.
- (34) A.B. Bilby, Phil Mag., V.44, p.782, 1953.
- (35) Z.S. Basinski and J.W. Christian, J.Inst.Metals, V.80, p.659, 1952.
- (36) Z.S. Basinski and J.W. Christian, Phil.Mag., V.44, p.791, 1953.

- 100 -
- (37) H. Warlimont, *Electron Microscopy*. (Pro. 5th Internl. Congr. Philadelphia) paper HH6. 1962 New York Academic Press.
  - (38) A. Seeger, *Z. Metall.*, V.44, p.247, 1953.
  - (39) A. Seeger, *Z. Metall.*, V.47, p.653, 1956.
  - (40) E. Votavo, *Acta. Met.* V.8, p.901, 1960.
  - (41) E. Votavo, *J.Inst.Metals*, V.90, p.129, 1961-62.
  - (42) W. Bollmann, *Acta.Met.*, V.9, p.972, 1961.
  - (43) J. Dash and H. Otte, *Acta.Met.*, V.11, p.1169, 1963.
  - (44) J.A. Venables, *Phil.Mag.*, V.7, p.35, 1962.
  - (45) J.F. Breedis, *ASM. Seminar on Thin Films*, Cleveland 1963.
  - (46) P.B. Hirsch, A. Kelly, J.W. Menter, *Proc.Phys.Soc.*, V.B68, p.1132, 1955.
  - (47) J.F. Breedis, *Franklin Institute Report*, Philadelphia. A. V.6, p.1840-3, 1963.
  - (48) P.M. Kelly, *Acta.Met.*, V.13, p.635, 1965.
  - (49) H. Schumann, *Archiv. Eisenh.* V.38/8, p.647, 1967.
  - (50) H. Schumann, *Prakt.Met.*, V.4/6, p.275, 1967.
  - (51) A.J. Goldman, W.D. Robertson and D.A. Koss, *Trans.Met Soc. AIME.*, V.230, p.240-241, 1964.
  - (52) J. Gordon Parr, *JISI.*, V.171, p.137-141, 1952.
  - (53) K. Shimizu, *J.Phys.Soc. Japan*, V.17, p.508-519, 1962.
  - (54) P.M. Kelly and J. Nutting, *JISI.*, V.197, p.199-211, 1961.
  - (55) R.P. Reed, *Acta.Met.*, V.10, p.865-877, 1962.
  - (56) P.M. Kelly, *ISI Special Report 86*, p.146-152, 1964.
  - (57) M. Wilkins and H. Warlimont, *Acta.Met.*, V.11, p.1099-1100, 1963.
  - (58) Z. Nishiyama and S. Kajiwara Japan, *J.Appl.Phys.*, V.2, p.478-486, 1963.
  - (59) A.N. Holden, *Acta.Met.*, V.1, p.617-623, 1953.

- (60) B.R. Butcher and A.H. Rowe, Symposium on the mechanism of phase transformations in metals. p.229-242, London, Institute of Metals, 1956.
- (61) B.R. Butcher, J.Nuclear Energy, V.4, p.273-278, 1957.
- (62) J. Burke and P. Dixon, J.Nuclear Mat., V.7, p.38-45, 1962.
- (63) J.C. Fisher, Trans. AIME., V.197, p.918, 1953: Acta.Met., V.1, p.32, 1953.
- (64) M. Cohen, Trans. AIME., V.212, p.171, 1958.
- (65) A.B. Greninger and V.C. Mooradian, Trans. AIMME., V.128, p.337, 1938.
- (66) L.C. Chang and T.A. Read, Trans. AIMME., V.189, p.47, 1951.
- (67) R.E. Cech and D. Turnbull, Trans. AIMME., V.206, p.124, 1956.
- (68) M. Cohen, E.S. Machlin, and V.J. Paranjpe, Thermodynamics in Physical Metallurgy. ASM., p.242, 1949.
- (69) H. Knapp and U. Dehlinger, Acta. Met., V.4, p.289, 1956.
- (70) C. Zener, Trans. AIMME., V.203, p.619, 1955.
- (71) E. Scheil, Zeitschrift fur anorganische und allegmaine Chemic., V.207, p.21-40, 1932.
- (72) C.S. Barrett and O.R. Trautz, Metals Technology, V.15, April 1948. Tech.Pub. No. 2346.
- (73) A.B. Greninger, Trans. AIMME, V.133, p.204-221, 1939.
- (74) K. Mathieu, Arch. Eisenh., V.16, p.215-218, 1942.
- (75) C.B. Post and W.S. Eberly, Trans. ASM., V.39, p.868-888, 1947.
- (76) D.J. McAdam et al., Journal of Research Nat. Bureau of Standards, V.40, p.375-392, 1948.
- (77) Z. Nishiyama, Sci.Rep.Tohoku Imp.Univ. (first series) V.25, p.94-103, 1936.
- (78) B. Cina. JISI., V.177, p.406-422, 1954.
- (79) H.C. Fiedler et al., Trans. ASM., V.47, p.267-285, 1955.
- (80) T. Saito, Trans. Jap.Inst.Met., V.6, p.179-186, 1965.

- (81) G. Collette et al., Rev.Met., V.LIV., p.433-486, 1957.
- (82) H. Schumann and K. Goodknecht, Prakt.Met., V.4, p.173-180, 1967.
- (83) J.R. Patel and M. Cohen, Acta.Met., V.1, p.531-538, 1953.
- (84) J.F. Watson and J.L. Christian, A.S.T.M. STP. (287), p.170-173, 1960.
- (85) D.T. Llewellyn and J.D. Murray, ISI. Special Report 86, p.197, 1964.
- (86) P.G. Winchell and M. Cohen. 'Electron microscopy and the strength of crystals'. p.995-1006: 1963. New York Interscience.
- (87) M. Cohen, Trans. ASM., V.224, p.638-656, 1962.
- (88) P.G. Winchell and M. Cohen, Trans. ASM., V.55, p.347-361, 1962.
- (89) M. Cohen, JISI., V.201, p.833-841, 1963.
- (90) E.T. Stephenson, Trans. ASM., V.55, p.624-639, 1962.
- (91) A. Cracknell and N.J. Petch, Acta.Met., V.3, p.186-189, 1955.
- (92) B.L. Mordike and P. Haasen, Phil.Mag., V.7, p.459-474, 1962.
- (93) R.L. Fleischer and W.R. Hibbard. Symposium on the relation between structure and strength in metals and alloys, p.261-297, 1963, London. H.M.S.O.
- (94) P.M. Kelly and J. Nutting, Proc.Roy.Soc., V.259A, p.45-58, 1960.
- (95) P.M. Kelly, Electron microscopy and the strength of crystals, p.917-932, 1962, New York, Interscience.
- (96) S.V. Radcliffe and M. Schatz, Nature, V.200, p.161-163, 1963.
- (97) C. Wert, Trans. AIME., V.188, p.1242-1244, 1950.
- (98) G.N. Lewis and M. Randall, Thermodynamics. McGraw-Hill, 1961.
- (99) A. Howie, Met.Rev., V.6, p.467-503, 1961.
- (100) R.F. Mehl and D.M. Van Winkle, Rev.Met., V.50, p.465, 1953.

- (101) J.G. Parr, JISI., V.171, p.137, 1952.
- (102) H. Scott, Trans. AIMME., V.95, p.284, 1931.
- (103) F.M. Walters and C. Wells, Trans. ASM., V.23, p.727, 1935.
- (104) E. Schiel, Arch. Eisen, V.3, p.293, 1929.
- (105) A.T. Grigorev and D.L. Kudryavtzev. Izvest.Sektora Fiz-Khim. Anal., V.16, P.70, 1946.
- (106) W. Schmidt, Arch. Eisen., V.3, p.293, 1929.
- (107) M. Gensamer, J.F. Eckel and F.M. Walters, Trans.Amer. Soc. Steel Treating, V.19, p.590, 1931-32.
- (108) E. Ohman, Z. Physik.Chem., V.8, p.81, 1930.
- (109) L.I. Lysak and Ya. N. Vauk, Fiz.Metal.Metalloved., V.19/5, p.699, 1965.
- (110) L.I. Lysak and Ya. N. Vauk, Fiz.Metal.Metalloved, V.20/4, p.540, 1965.
- (111) A. Osawa, Sci.Rep. Tohoku Imp.Univ., V.19, p.247, 1930.
- (112) T. Ishiwara, ibid., V.19, p.590, 1931-32.
- (113) F.M. Walters, Trans.Amer.Soc. Steel Treating, V.19, p.577, 1931-32.
- (114) V.N. Krivobok and C. Wells, ibid., V.21, p.807, 1933.
- (115) E.C. Bain, E.S. Davenport and W.S.N. Waring, Trans. AIMME., V.100, p.228, 1932.
- (116) J.C. Fisher, J.H. Holloman and D. Turnbull, J.Appl.Physics, V.19, p.775, 1948.
- (117) C. Wells and F.M. Walters, JISI., V.128, p.345, 1933.
- (118) C.R.Wohrman, Trans. AIMME., V.80, p.197, 1928.
- (119) C.H. White and R.W.K. Honeycombe, JISI., V.200, p.457-466, 1962.
- (120) L.S. Yershova, J.N. Bogachev and R.S. Shklyer, Fiz. Metal. Metalloved., V.12/5, p.670-677, 1961.
- (121) R.S. Shklyer, V.F. Yegolayev, L.D. Chumokova, L.S. Malinov and V.D. Solovey., Fiz.Met.Metalloved., V.21/2, p.235-241, 1966.
- (122) L.I. Lysak and B.J. Nikolin, Fiz.Metal. Metalloved., V.20/4, p.547-554, 1965.

- (123) L.I. Lysak and B.J. Nikolin, Dokl.Akad,Nauk.SSSR., V.153, p.812, 1963.
- (124) 'Manganese Steel' published for Hadfields Ltd., by Oliver and Boyd, London, 1956.
- (125) R.A. Hadfield, JISI., V.115, p.297, 1927.
- (126) F.M. Walters, J.R. Kramer, B.M. Lorig, Trans. AIMME., V.150, p.401, 1942.
- (127) H.H. Uhlig, Trans. AIMME., V:158, p.183, 1944.
- (128) L. Kaufman, Trans. AIME., V.215, p.218, 1959.
- (129) F.M. Walters and C. Wells, Trans. ASM., V.24, p.359, 1956.
- (130) L.I. Lysak and B.J. Nikolin, Fiz.Met.Metalloved., V.17/5, p.703-707 (p.59 English version), 1964.
- (131) R.L. Patterson and C.M. Wayman, Acta. Met., V.12, p.1306, 1964.
- (132) R.L. Patterson and C.M. Wayman, ibid., V.14, p.347, March 1966.
- (133) D. Dulieu and J. Nutting, ISI. Special Report 86, p.140, 1964.
- (134) J. Spreadborough, Acta.Cryst., V.13, p.603, 1960.
- (135) S.L. Altmann et al., Proc.Roy.Soc.A., V.240, p.145, 1950.
- (136) M.S. Wechsler, D.S. Lieberman and T.A. Read, Trans. AIMME, V.197, p.1503, 1953.
- (137) T. Bell and W.S. Owen, JISI., p.428, April 1967.
- (138) E.A. Wilson and J.D. Bolton, unpublished work.
- (139) C. Zener, Trans. AIMME., V.167, p.513, 1946.
- (140) J.C. Fisher, Trans. AIMME., V.185, p.688, 1949.
- (141) L. Kaufman, ISI., Special Report 93, p.48, 1965.
- (142) J.C. Fisher, J.H. Holloman, D. Turnbull, Trans. AIME., V.185, p.691, 1949.
- (143) M.H. Richman, M. Cohen, H.G.F. Wilsdorf, Acta. Met., V.7, p.819, 1959.
- (144) J.D. Eshelby, F.C. Frank and F.R. Nabarro, Phil. Mag. 42, 551, 1951.

- (145) N.J. Petch Fracture Ed. by Averbach.
- (146) J. Fisher, Acta. Met., 2, 9, 1954.
- (147) N.F. Mott and F.R.N. Nabarro, Conference on the strength of solids, Phys.Soc., p.1, 1948.
- (148) N.F. Mott, Imperfections in nearly perfect crystals, John Wiley and Sons, New York, p.173, 1952.
- (149) D. McLean, Mechanical Properties of Metals, John Wiley and Sons, 1962. Table 6.4., p.178.
- (150) G. Schoeck and A. Seeger, Acta.Met., 7, 469, 1959.
- (151) E.R. Parker and T.H. Hazlitt, Relation of properties to microstructure.
- (152) A.H. Cottrell, Report on the strength of solids, Phys.Soc., p.30, 1948.
- (153) R.P. Carreker and W.R. Hibbard, Acta. Met., 1, 654, 1953.
- (154) J. Garstone and R.W.K. Honeycombe, Dislocations and the mechanical properties of crystals, Lake Placid Conference, 1956, New York 1957, p.243.
- (155) A.A. Griffith, First International Conference, Appl. Mech., Delft (1924) 55A.
- (156) C.E. Inglis, Trans.Inst.Naval Arch., p.219, 1913.
- (157) A.N. Stroh, Advances in Phys., 6, p.418, 1957.
- (158) C. Zener, Fracturing of Metals. ASM. Symposium, p.3, 1948.
- (159) A.H. Cottrell, Trans. AIME., 212, p.192, 1958.
- (160) G.W. Greenwood and A.G. Quarrell, J.I.M. 82, p.551, 1954.
- (161) J.J. Gilman, Trans. AIME., 212, p.783, 1958.
- (162) B.L. Averbach and M. Cohen, Trans. AIMME. 176, p.401, 1948.
- (163) G.R. Speich, Trans. AIME. 227, 1426, 1963.
- (164) L. Kaufmann, Special Report 93, I.S.I., p.48, 1965.
- (165) M. Hillert, T. Wada and H. Wade, J.I.S.I., p.539, May 1967.

- (166) C. Zener, Trans. AIME., 167, 513, 1946.
- (167) L.S. Darken, Trans. AIME., 167, 546, 1946.
- (168) R. Kohlhaas and M. Braun, Arch. Eisenh. 34, 391, 1963.
- (169) H. Kroiner, Arch. Eisenh. 11, p.279, 1937.
- (170) H.S. Avery and H.J. Chapin, Welding. J., 33, p.459, May 1954.
- (171) F.J. Maratray and T.E. Norman Rev. de Met., p.489, June 1961.
- (172) B.R. Nijhawan et al., JISI. p.292, March 1967.
- (173) T.E. Norman et al. AFS. Trans., 68, p.287, 1960.
- (174) C.H. Shih, B.L. Averbach and M. Cohen, "Work hardening and martensite formation in austenitic manganese alloys". Private communication with E.R. Hall. Climax Molybdenum Company.
- (175) H.J. Harding and R.W.K. Honeycombe, JISI. 204, 259. March 1966.
- (176) Kulin and Cohen, Trans. AIME., 188, p.1139, 1950.
- (177) W. Hiller and Nacken: Arch. Eisenh. 31, p.723-730.

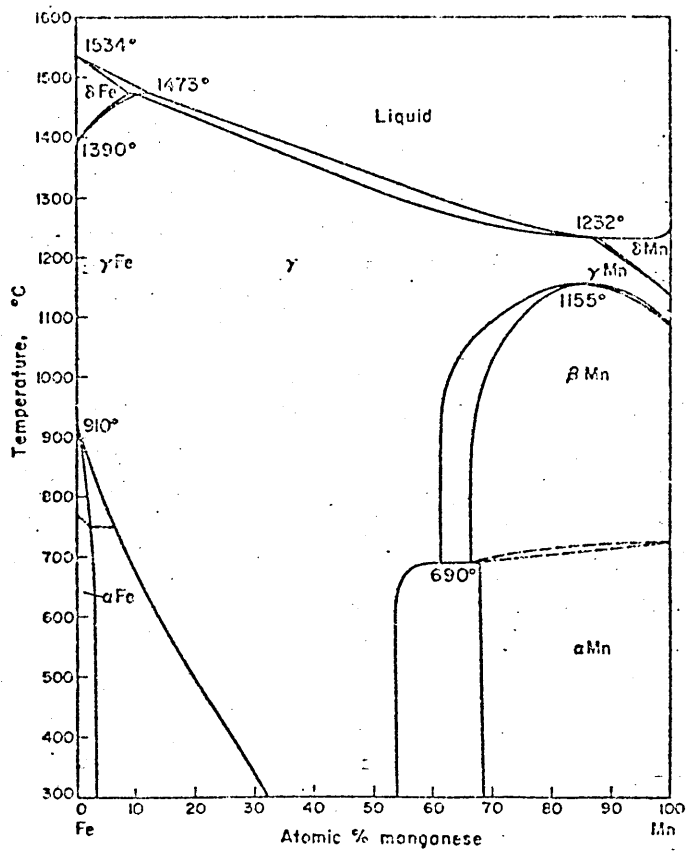


Figure 1 Equilibrium diagram of the system Fe-Mn.

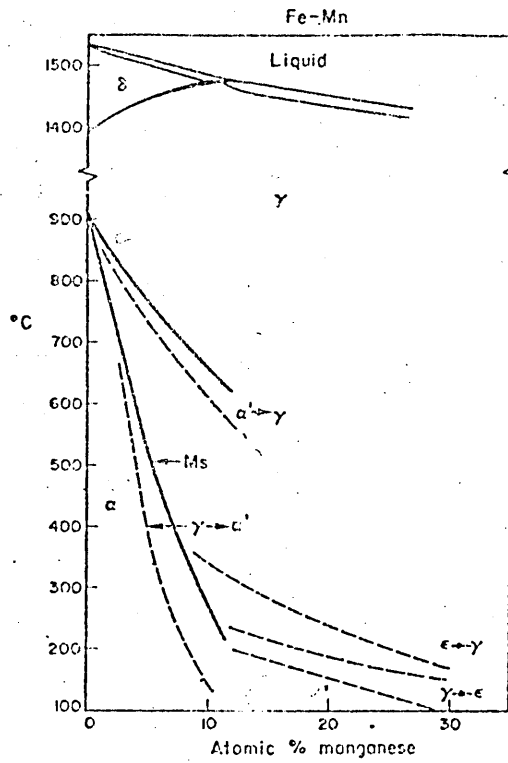


Figure 2 Transformation characteristics of Fe-Mn alloys.

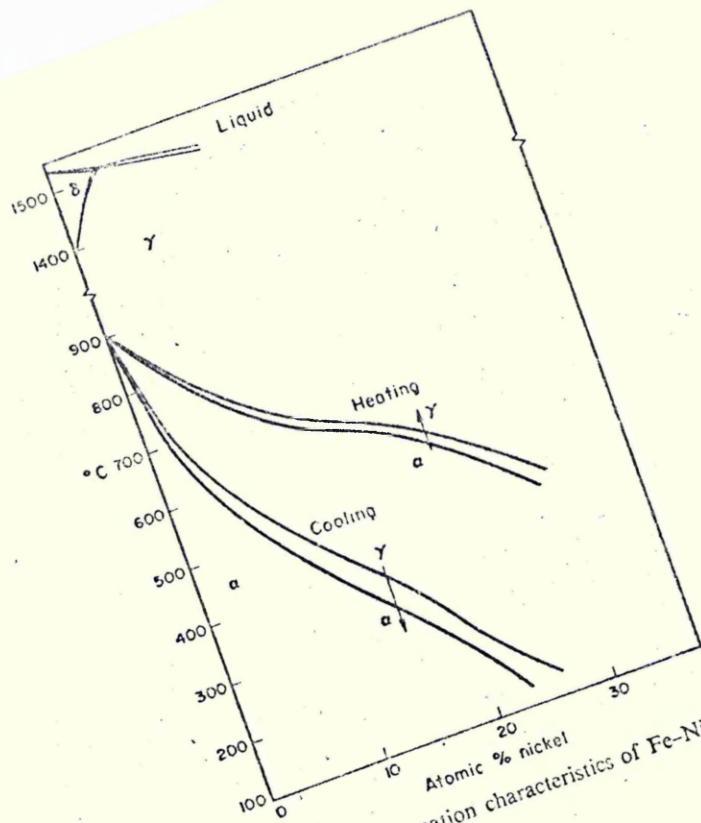


Figure 3. Transformation characteristics of Fe-Ni alloys.

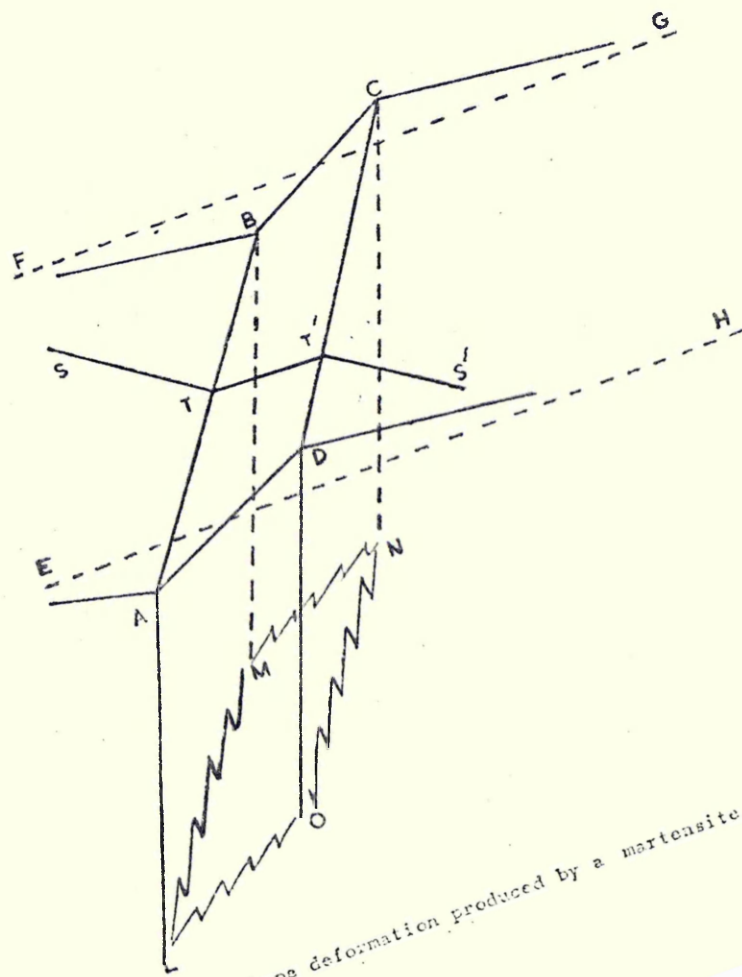


Figure 4. The shape deformation produced by a martensite plate

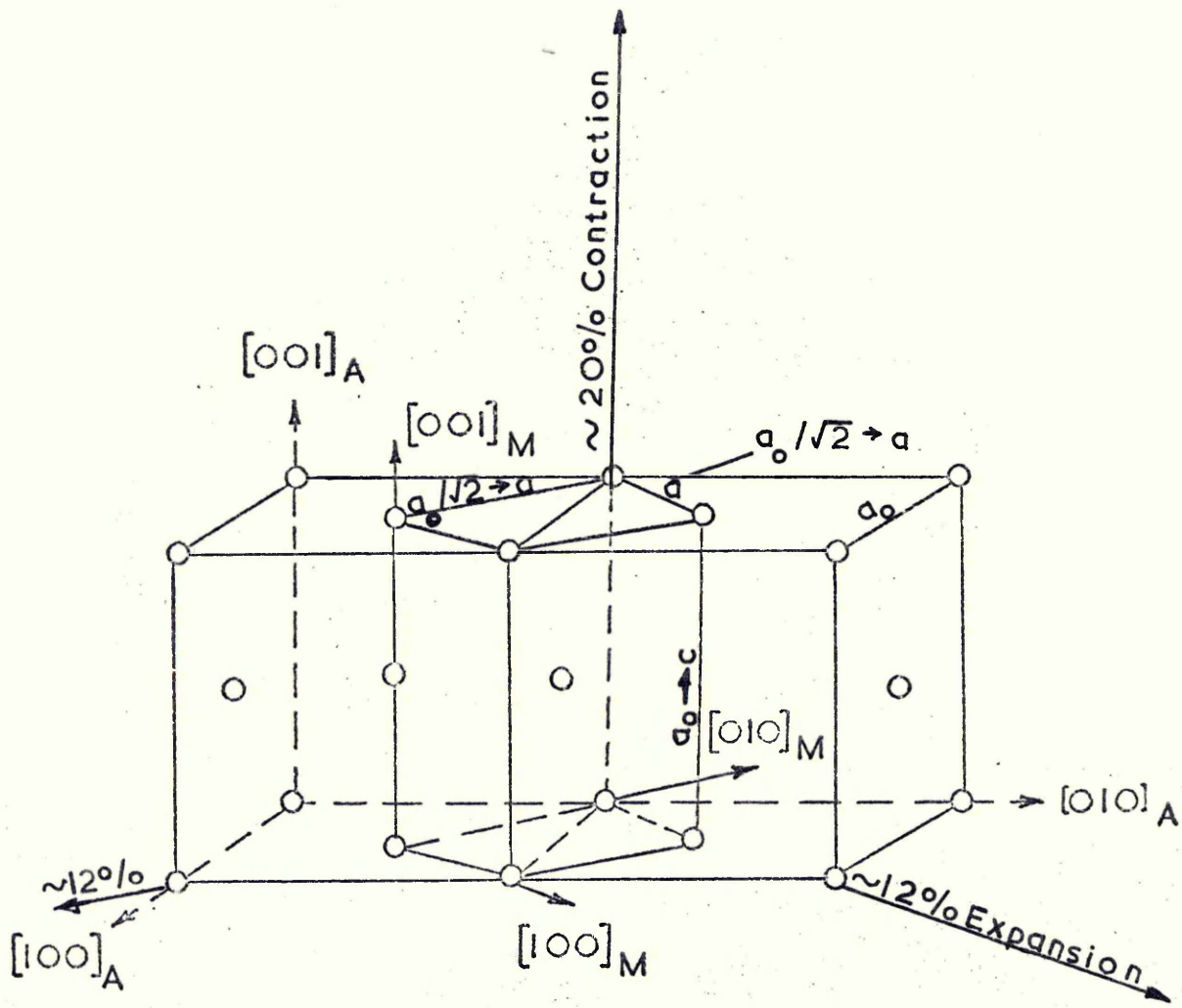


Figure 5 The lattice correspondence for martensite formation in steels ( $a_0$  is the austenite lattice parameter and the martensite parameters are 'a' and 'c'.)



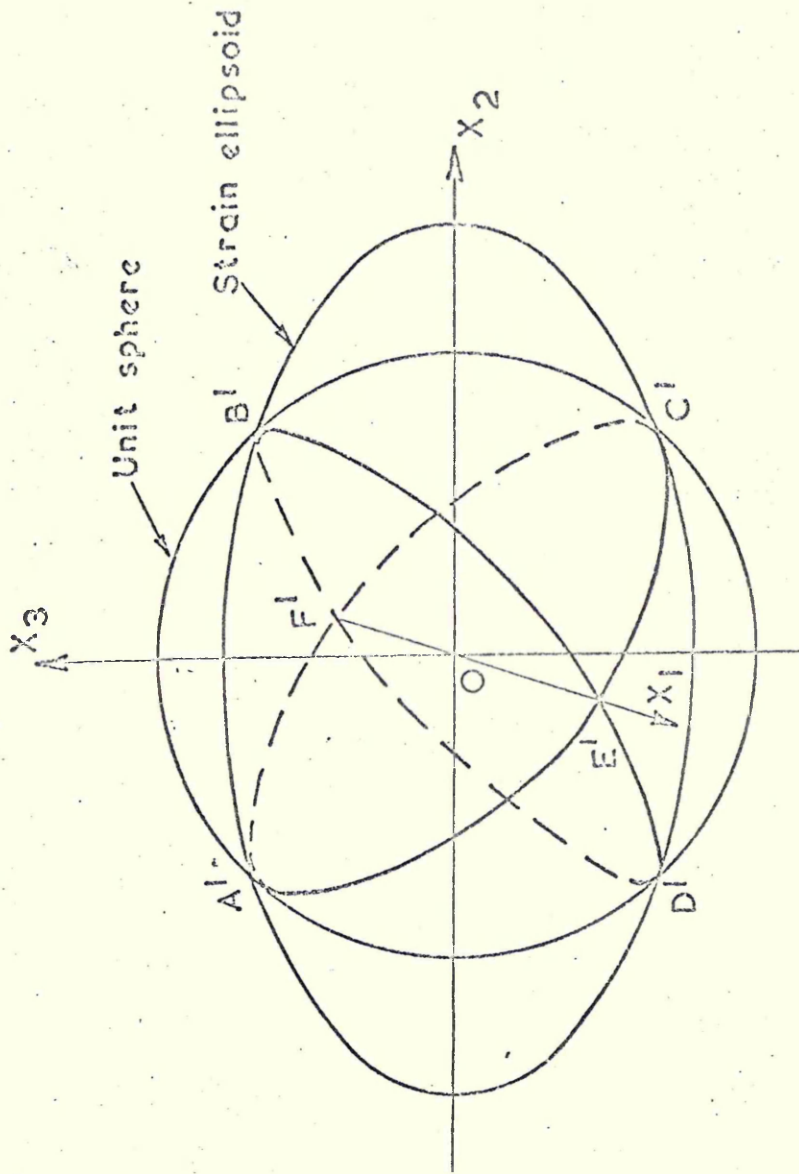


Figure 6b. An undistorted plane results when one of the principal strains is zero (along  $OX_1$ ) and the other two have opposite signs

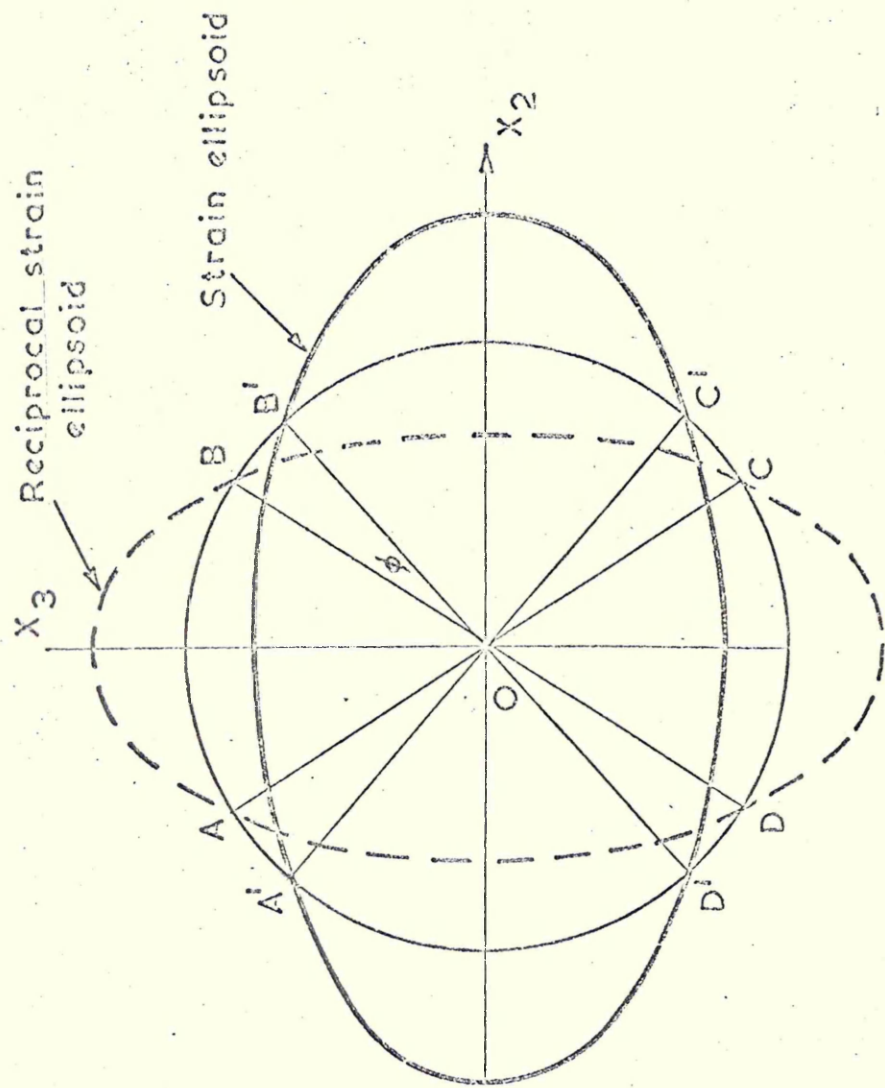


Figure 6c Section through  $X_2$ - $X_3$  plane

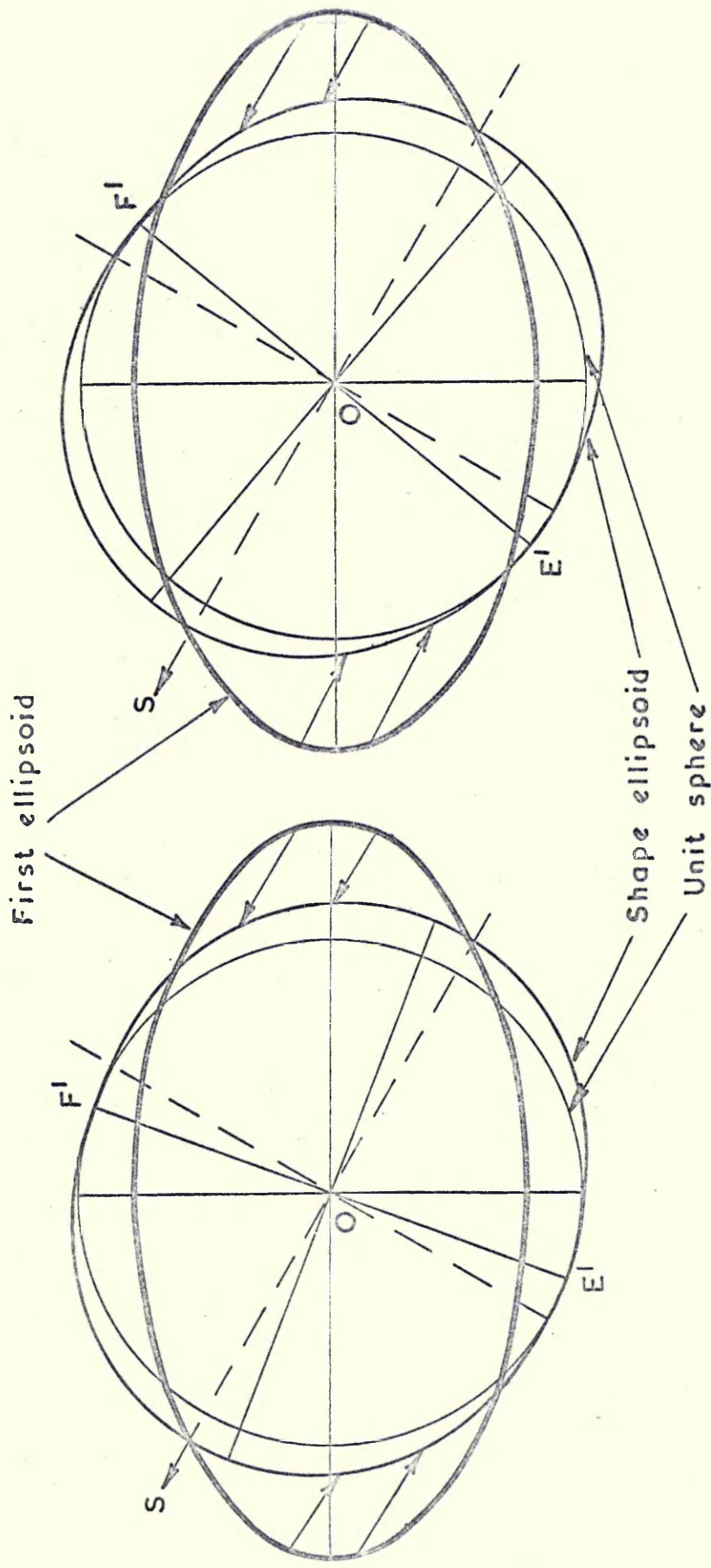
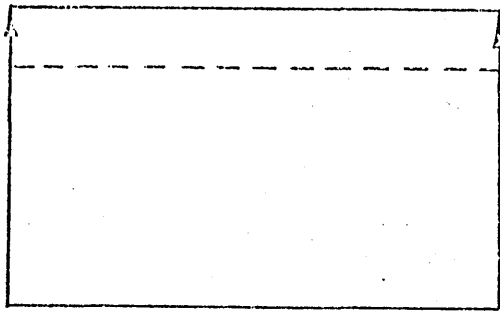
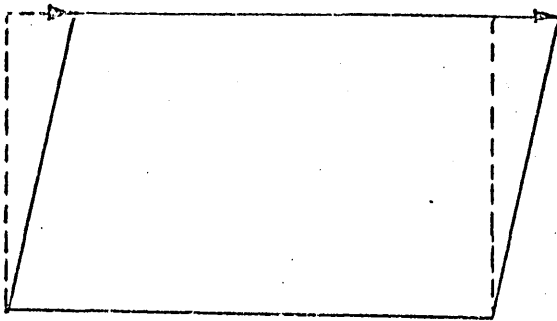


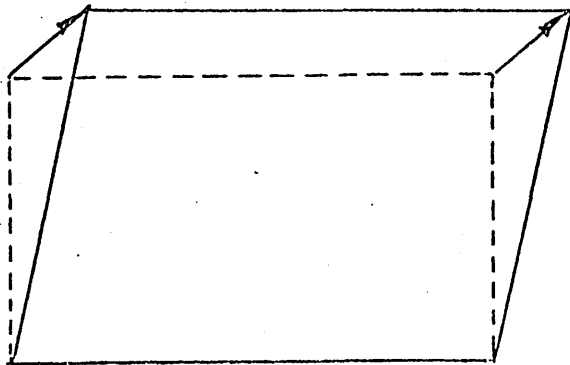
Figure 6d Shows the lattice invariant shear  $S$  required to distort the first ellipsoid to the shape ellipsoid



Simple Extension



Simple Shear



General invariant plane strain

Figure 7 Examples of invariant plane strains. In each case the dotted outline is deformed into the solid outline and the direction of motion common to all points is indicated by the arrow. The base of each figure represents the stationary invariant plane.

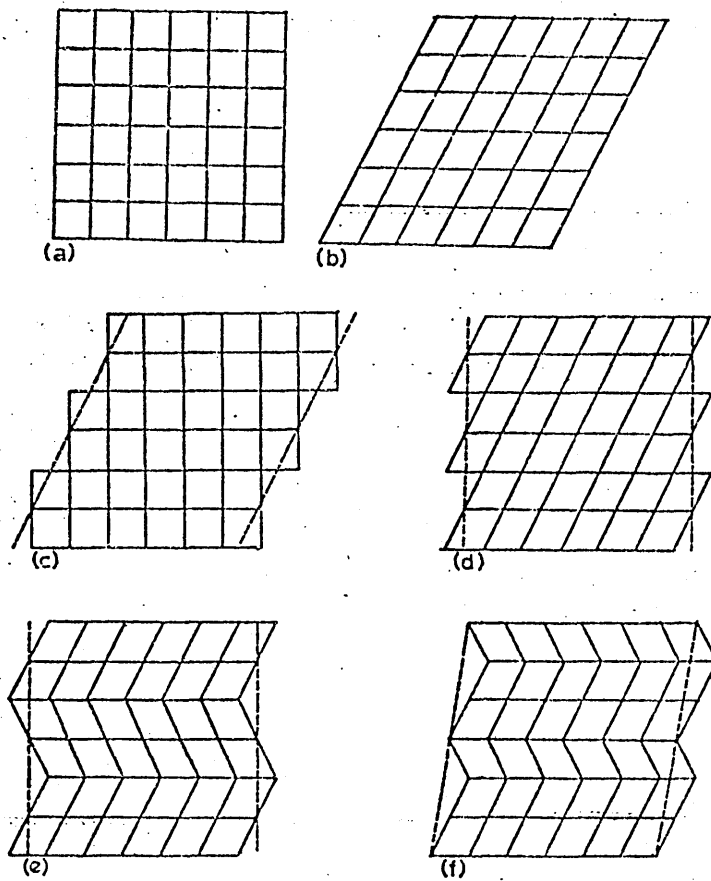


**Figure 8.** The crystallographic features of a martensitic reaction: (a) the original lattice, (b) the lattice after a homogeneous shear, (c) slip plus zero lattice deformation giving the same shape change as in (b), (d) lattice deformation plus slip giving zero shape change, (e) lattice deformation plus uniform twinning giving zero shape change, (f) lattice deformation plus non-uniform twinning giving a finite shape change. (After Bilby and Christian.)

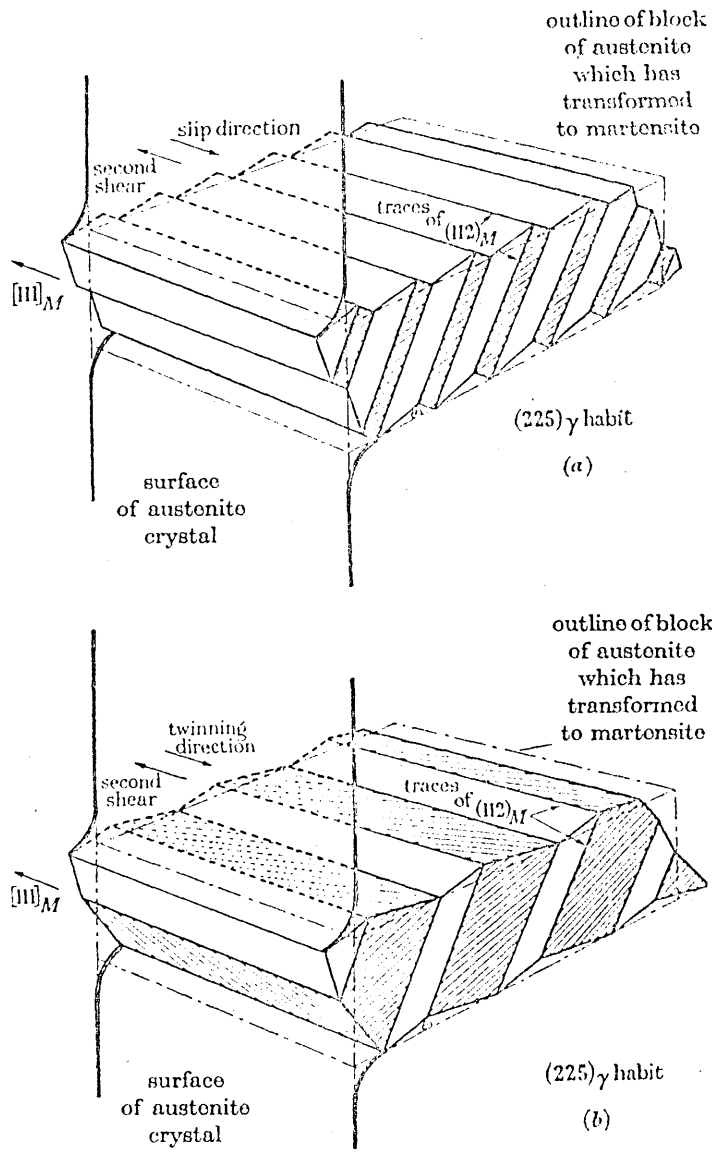


FIG. 9. To show how, in the formation of martensite, the second shear may be compensated by (a) slip, and (b) twinning. (After P. M. Kelly and J. Nutting.)

(Courtesy Royal Society)

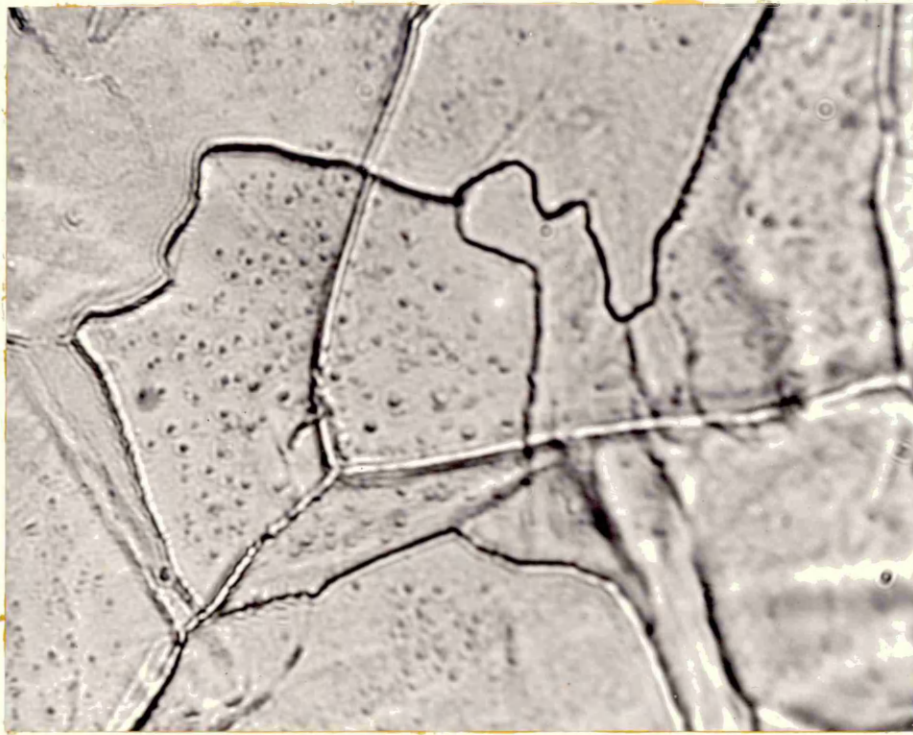


Figure 10 Massive ferrite in Fe-4.0%Ni (Mag. X1500)

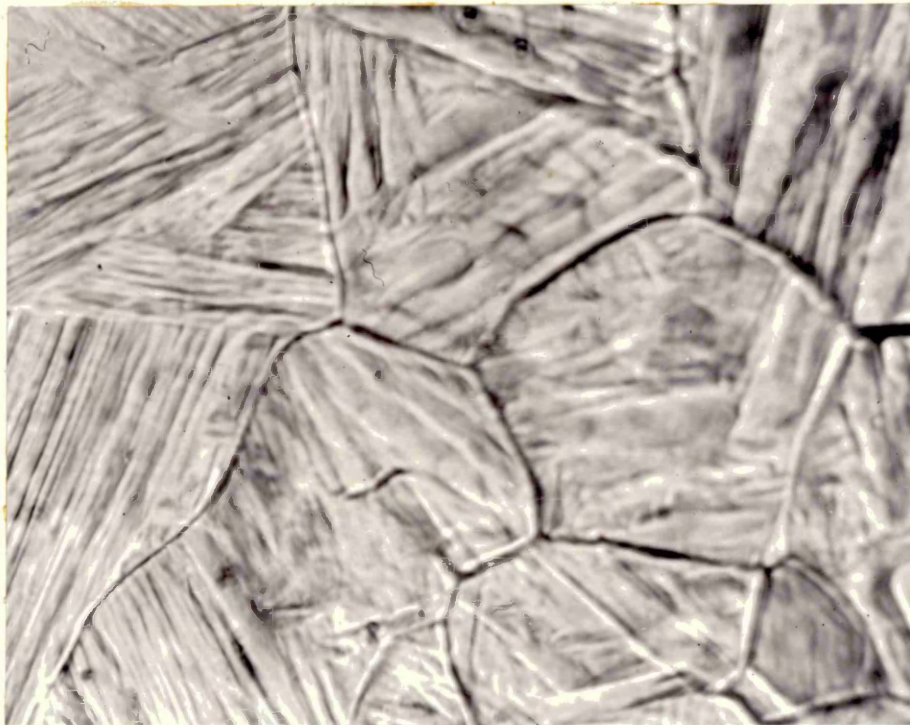


Figure 11 Surface shears on prepolished specimen of Fe-15.0%Ni alloy (Mag. X1000)

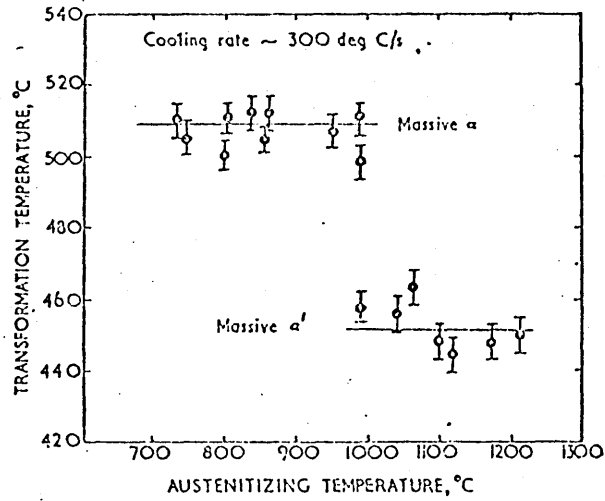
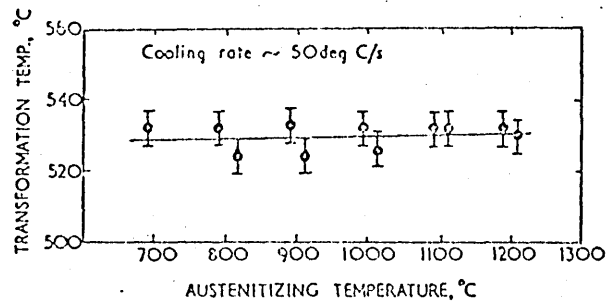


Figure 12. Transformation temperatures of an Fe-10%Ni alloy as a function of austenitizing temperature

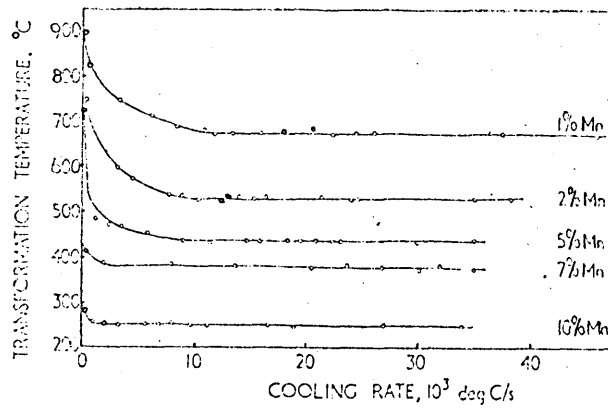


Figure 13 Transformation temperature v. cooling rate



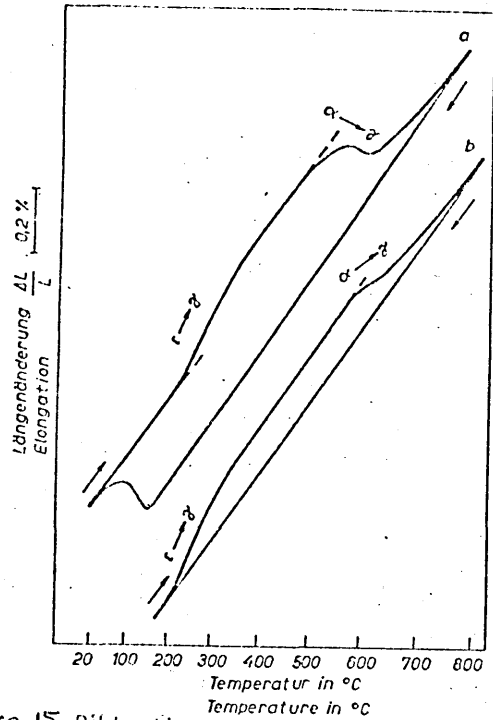


Figure 15 Dilatometric curves of a steel with 0,05 w/o C  
 1,1275 w/o Mn.  
 Curve a: 20° → 800° → 20°C  
 Curve b: 800° → 155° → 800°C

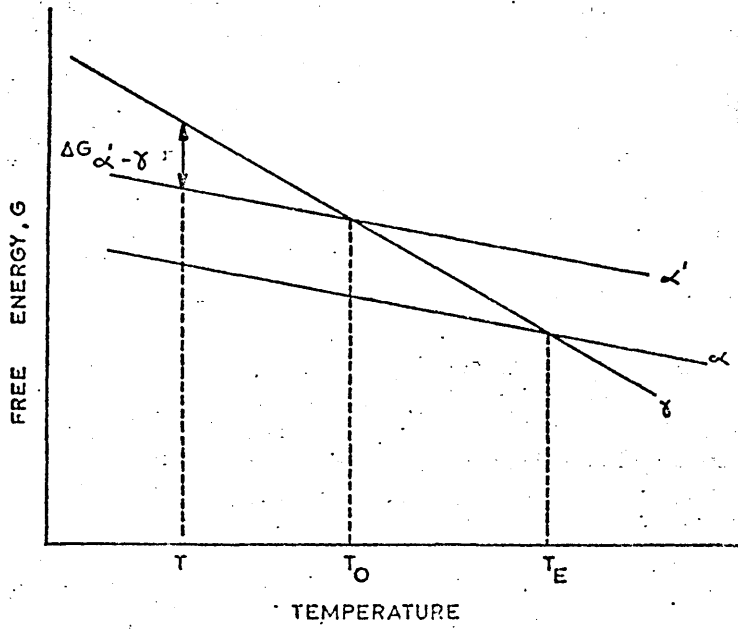


Figure 16. Schematic representation of the free energy as a function of temperature for a high temperature phase  $\gamma'$ , the phase stable at low temperature  $\alpha$  and the product of a martensitic change  $\alpha'$ .

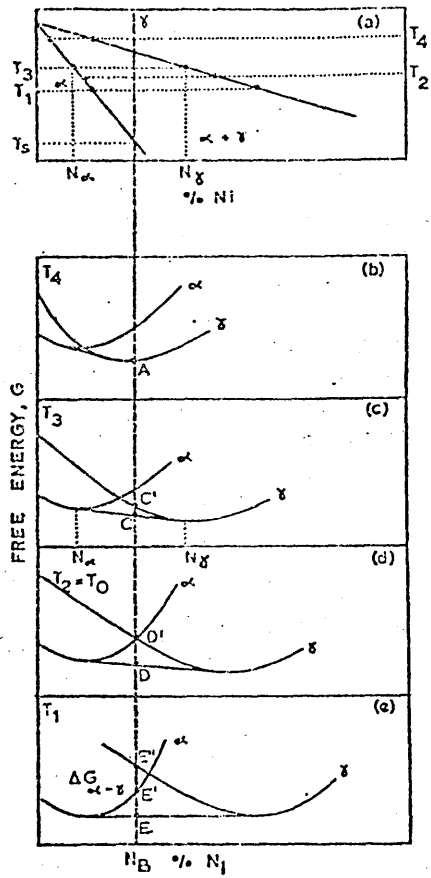


Figure 17 (a) Part of the Fe-Ni phase diagram. (b) (c) (d) and (e) are schematic free energy-composition diagrams for this system at four temperatures decreasing from top to bottom. (After Kaufman and Cohen.)

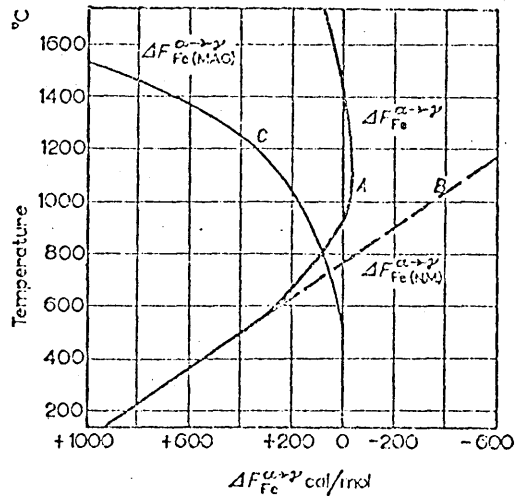


Figure 18 Separation of  $\Delta F^{\alpha \rightarrow \gamma}$  into magnetic and non-magnetic terms<sup>(60)</sup>

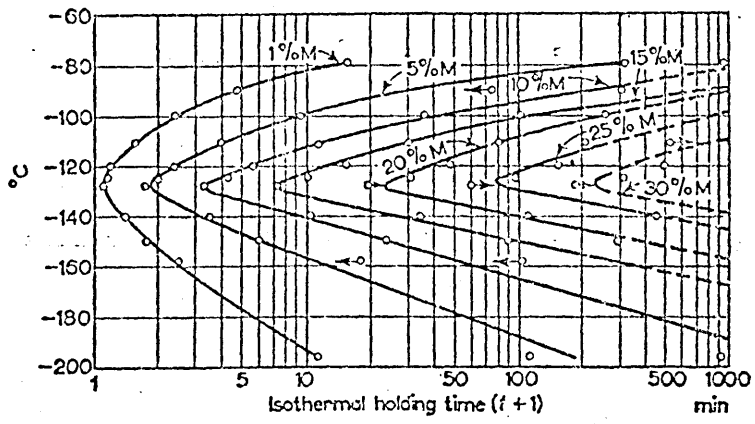


Figure 19. TTT diagram for  $\gamma$  isothermal martensite reaction in an Fe-Ni-Mn alloy. (After Cech and Hollman.)

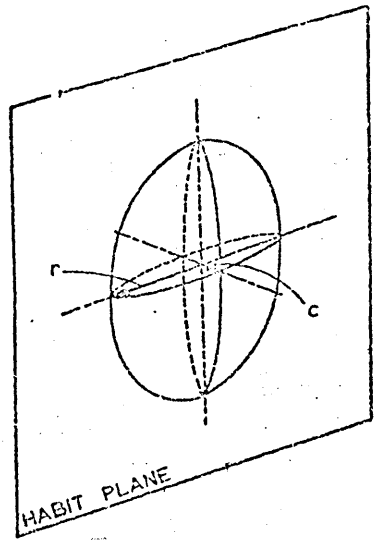


Figure 20a. Martensite embryo.

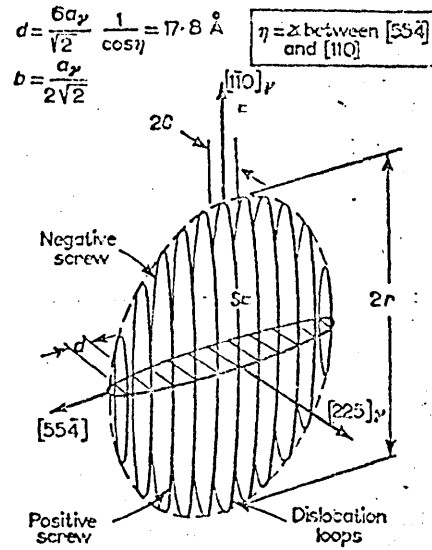


Figure 20b Knapp and Dehlinger's model of the martensite embryo.

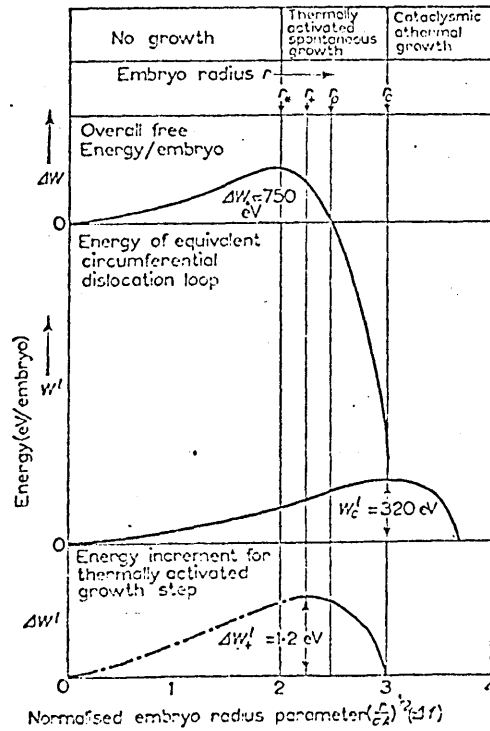


Figure 20c overall free energy ( $\Delta W$ ), energy of equivalent circumferential dislocation loop ( $W_c'$ ), and energy increment for each thermally activated growth step ( $\Delta W_t'$ ), shown as a function of the embryo radius parameter  $(r/\sigma A)^{1/2}(-\Delta f)$ , for ellipsoidal embryos. ( $-\Delta f$ ) is taken as  $3 \times 10^9$  erg/cm<sup>2</sup>, which is in the temperature range of an iron-nickel manganese alloy where isothermal transformation occurs

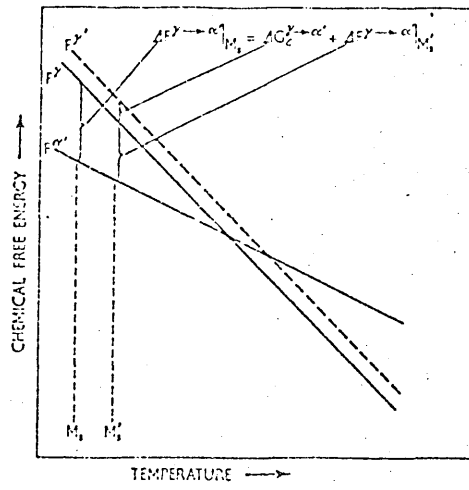


Figure 21 Effect of applied stress on the martensite reaction

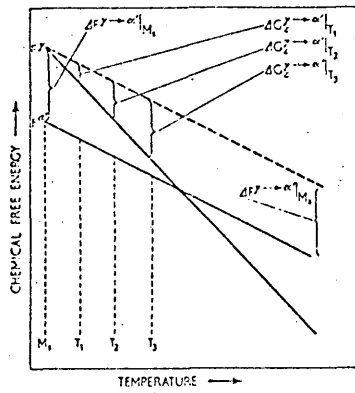


Figure 22 Various amounts of strain energy required to start the martensite reaction at various temperatures

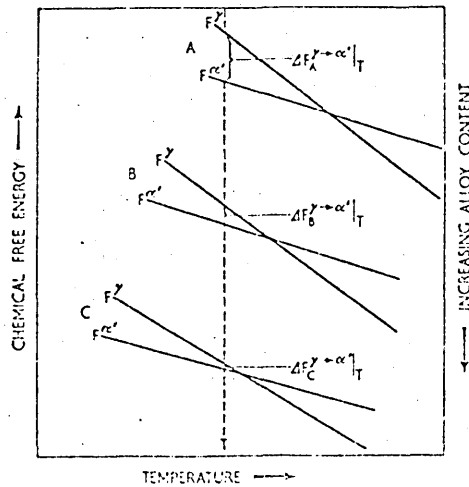


Figure 23 Available undercooling energy for the martensite reaction at temperature T for alloys A, B, and C

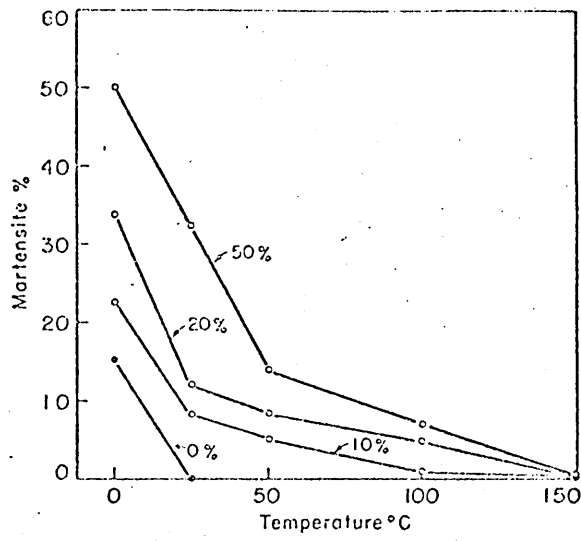


Figure 24. Effect of Testing Temperature and Degree of Deformation on Martensite Formation During Compression (70% Iron, 30% Nickel).

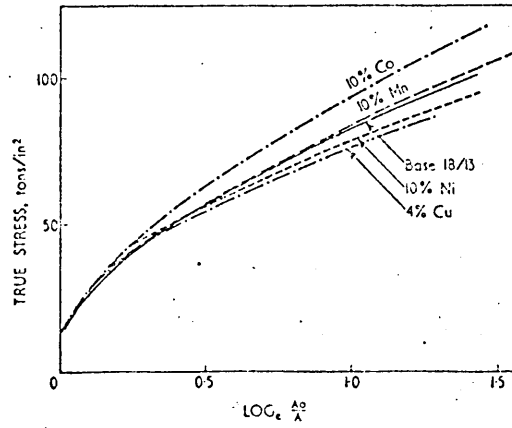


Figure 25 True stress-true strain in 18%Cr-13%Ni steel with alloy additions

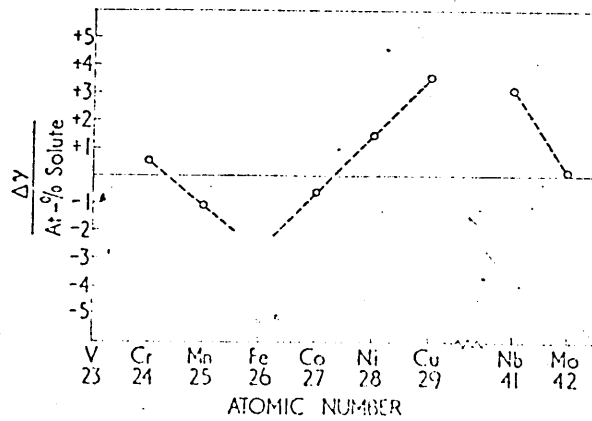


Figure 26. Stacking fault energy increment per at-% solute in 18%Cr-10%Ni base as a function of atomic number.

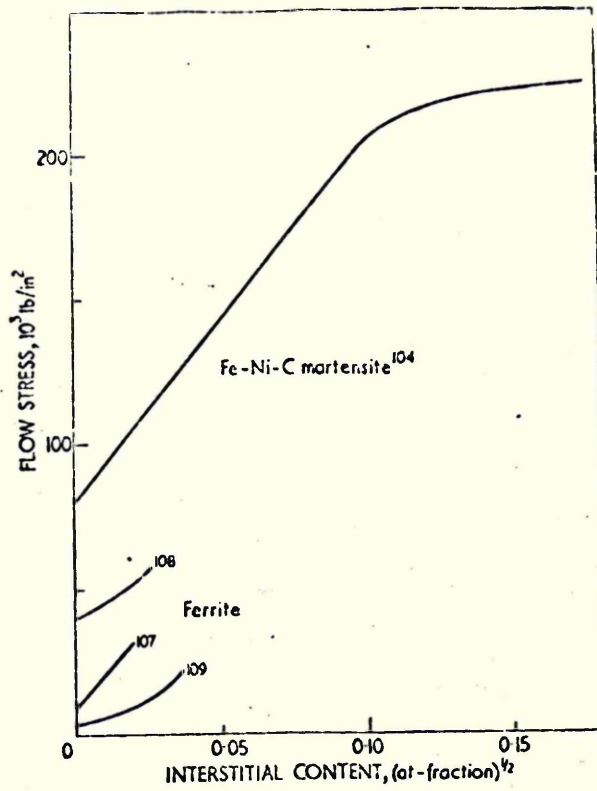


Figure 27 Comparison of hardening effects of interstitials (carbon and nitrogen) in solution in ferrite and in iron-nickel-carbon martensite

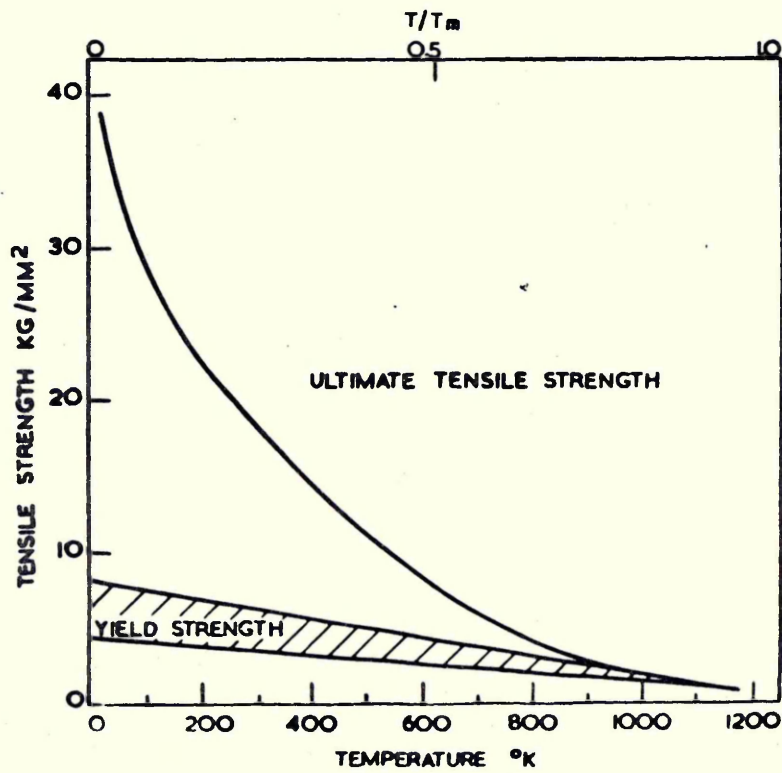


Figure 23 Tensile properties of silver as a function of temperature. (After Carreker, 1957.)

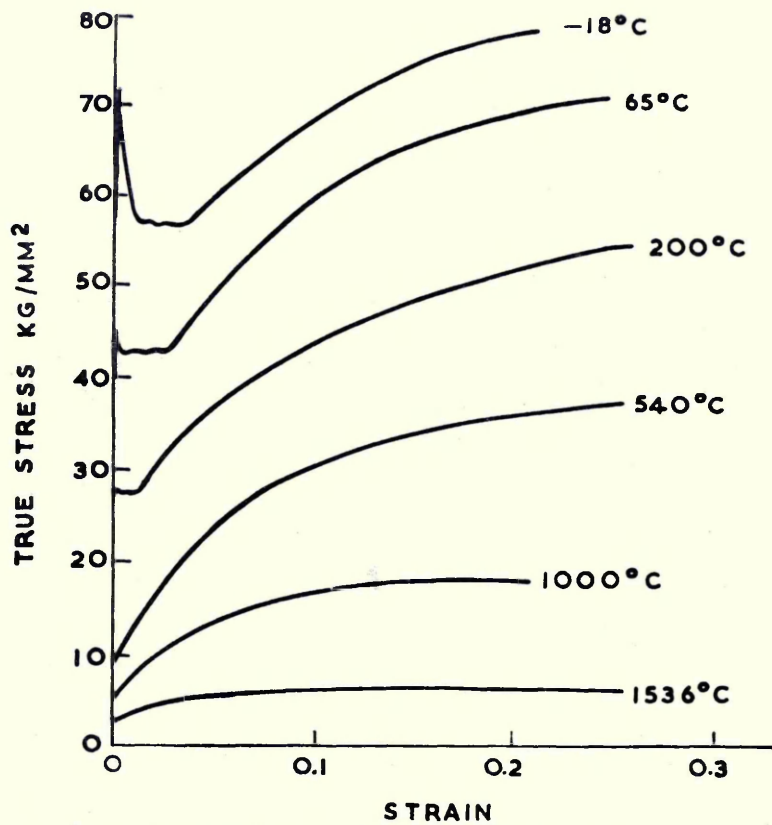


Figure 29 Stress-strain curves for molybdenum at various temperatures. (After Carreker and Guard, 1956.)

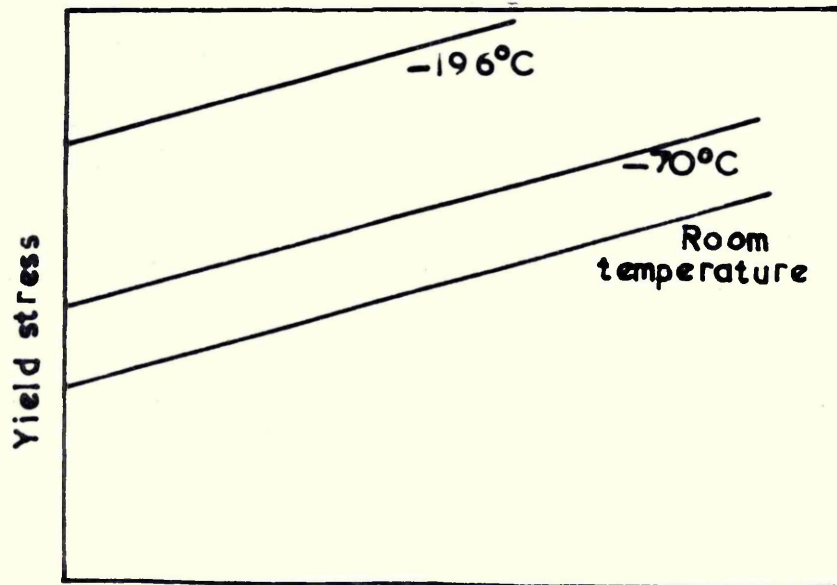


Figure 30 General influence of temperature on Petch analysis

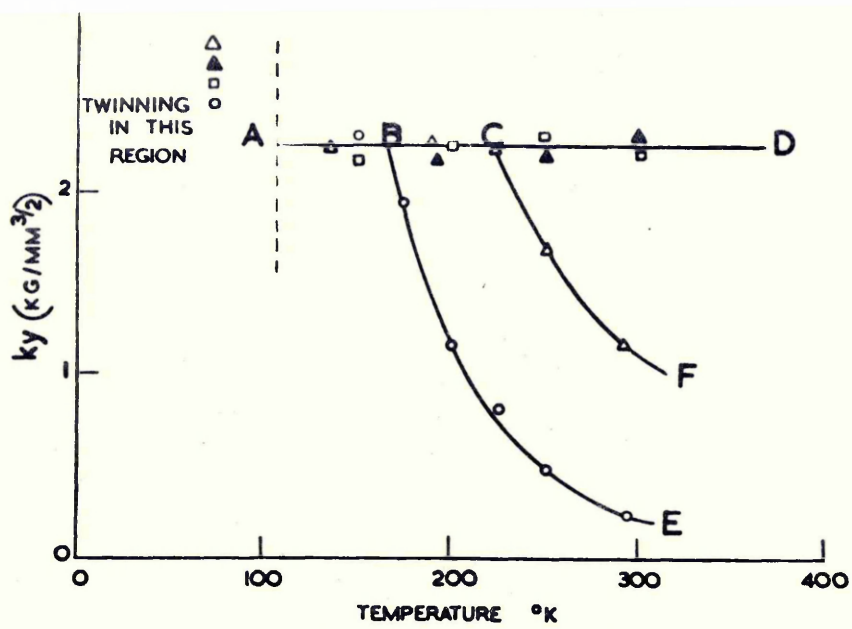


Figure 31 Dependence of  $k_y$  on temperature for iron containing 0.001% carbon and nitrogen after various quenching and ageing treatments (○ = as-quenched; △ = as-quenched + 1 hr at 140°C; □ = as-quenched + 12 hr at 140°C; ▲ = furnace cooled).

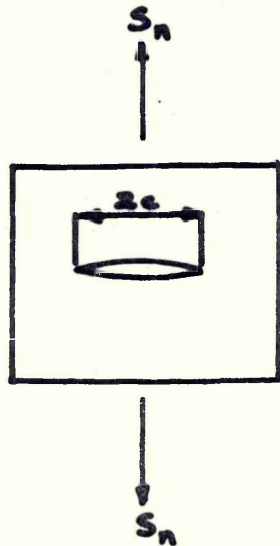


Figure 32 A Griffith crack

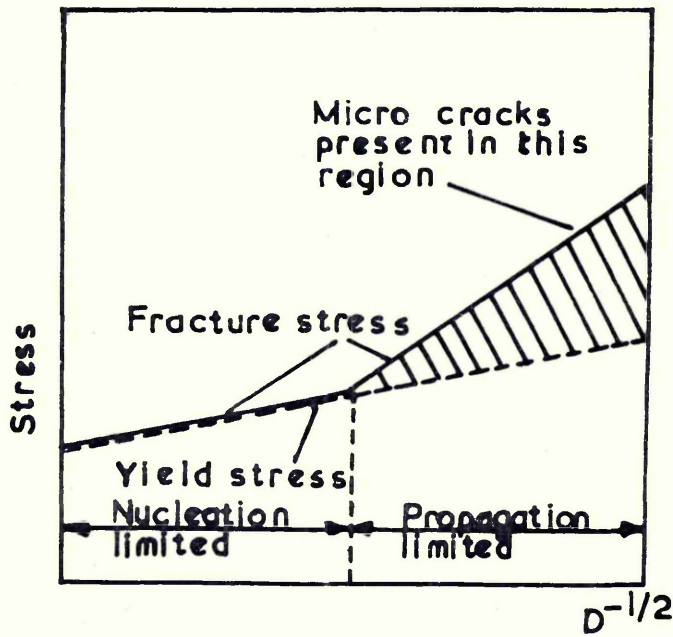


Figure 33 Effect of grain size on the yield and fracture stress of a polycrystalline metal

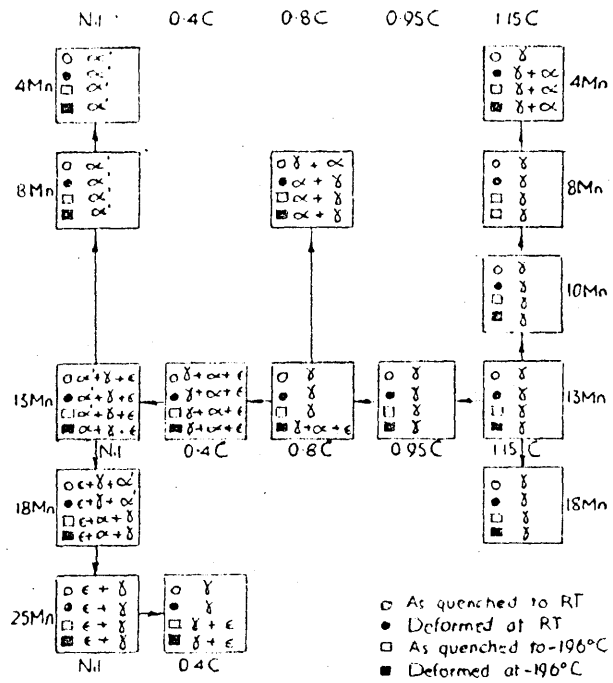


FIG. 34 Structures found in Fe-Mn-C alloys

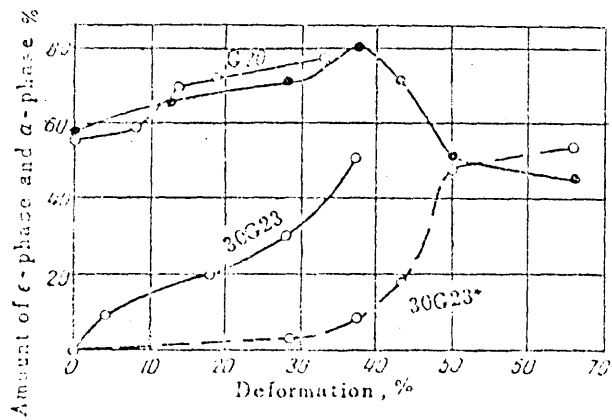


FIG. 35 Effect of plastic deformation on the amount of  $\epsilon$ -phase and  $\alpha$ -solid solution in manganese steels:

— amount of  $\epsilon$ -phase,  
 - - - amount of  $\alpha$ -phase.

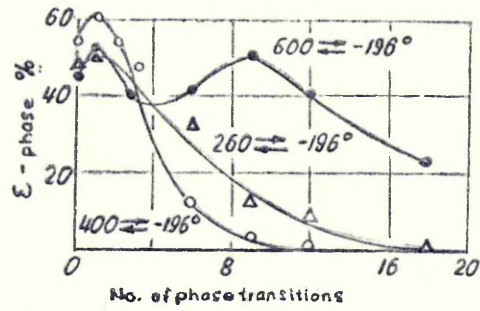


FIG. 36 Effect of  $\gamma \rightleftharpoons \epsilon$  phase transitions on the amount of  $\epsilon$ -phase in the alloy G19.

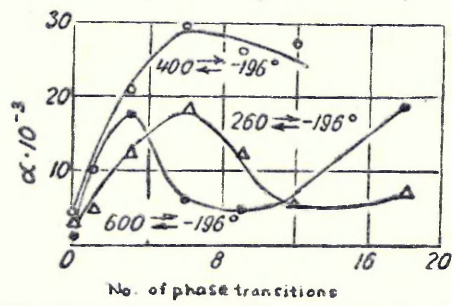


FIG. 37 Effect of  $\gamma \rightleftharpoons \epsilon$  phase transitions on the probability of stacking faults in G19.

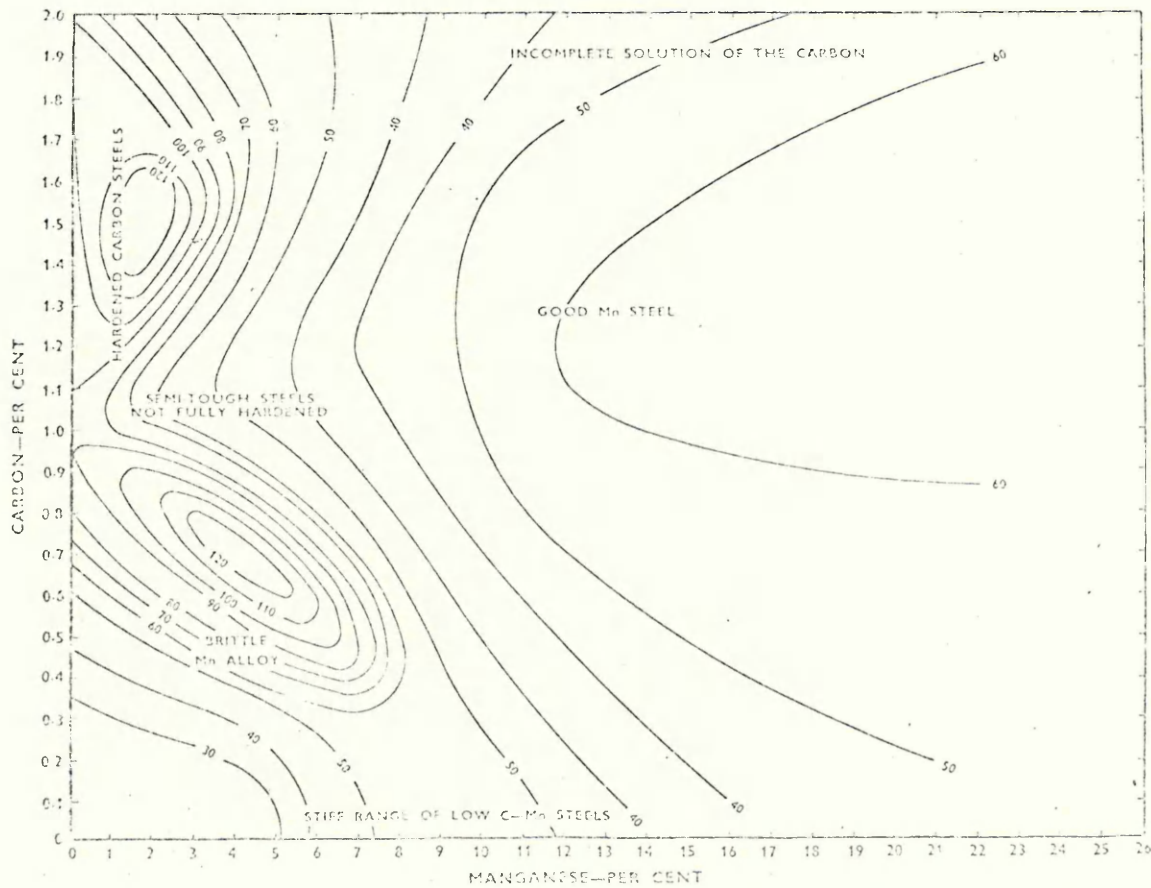


Figure 38 Tensile Strength of Carbon-Manganese Steels Treatment 1000°C Water

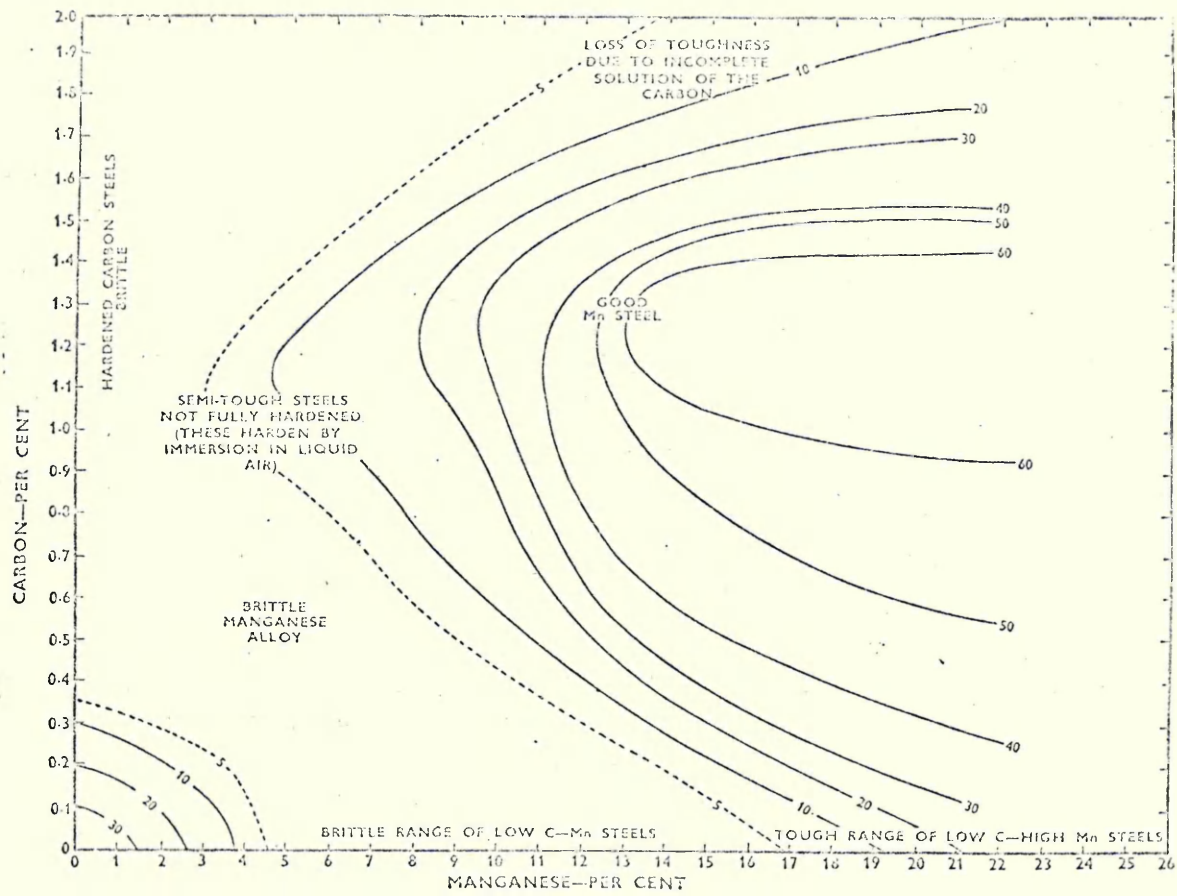


Fig. 39 Tensile Elongation of Carbon-Manganese Steels Treatment 1000°C Water

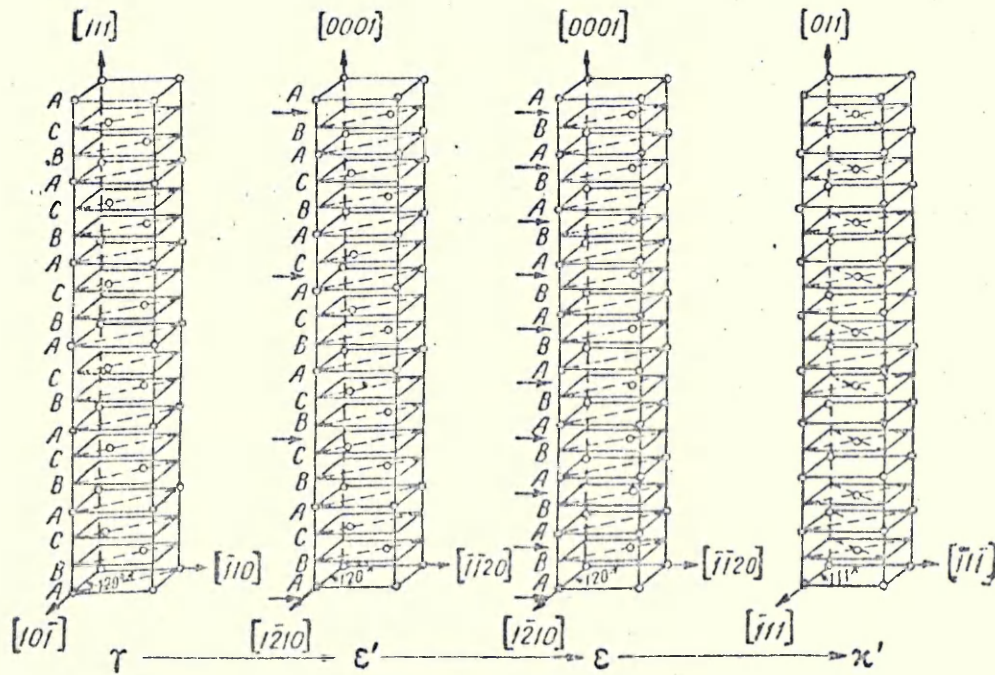


Figure 40 Gradual formation of martensitic phases by shears of the austenite (111) planes.

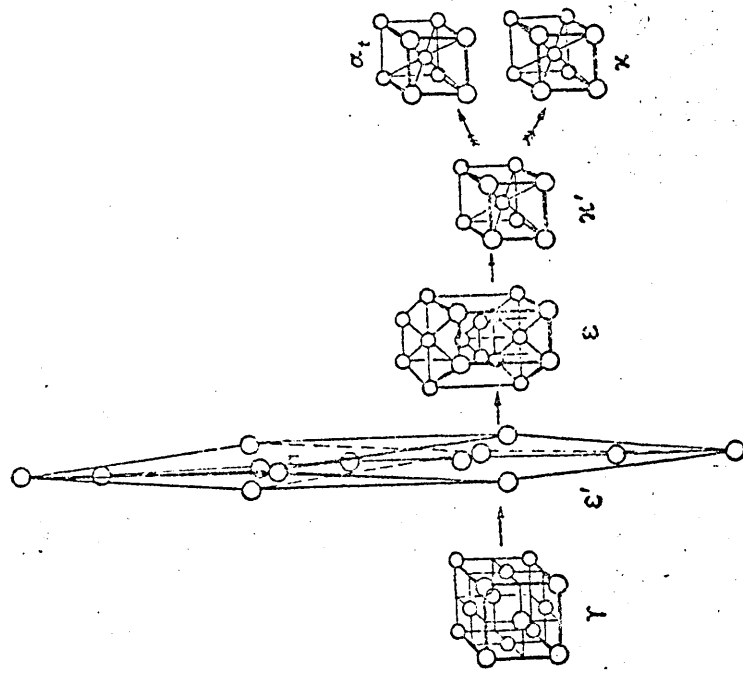


Figure 41 Alteration of crystal lattice on phase transformations in manganese-

containing steels:

$\rightarrow$  cooling;  $\dashrightarrow$  heating.

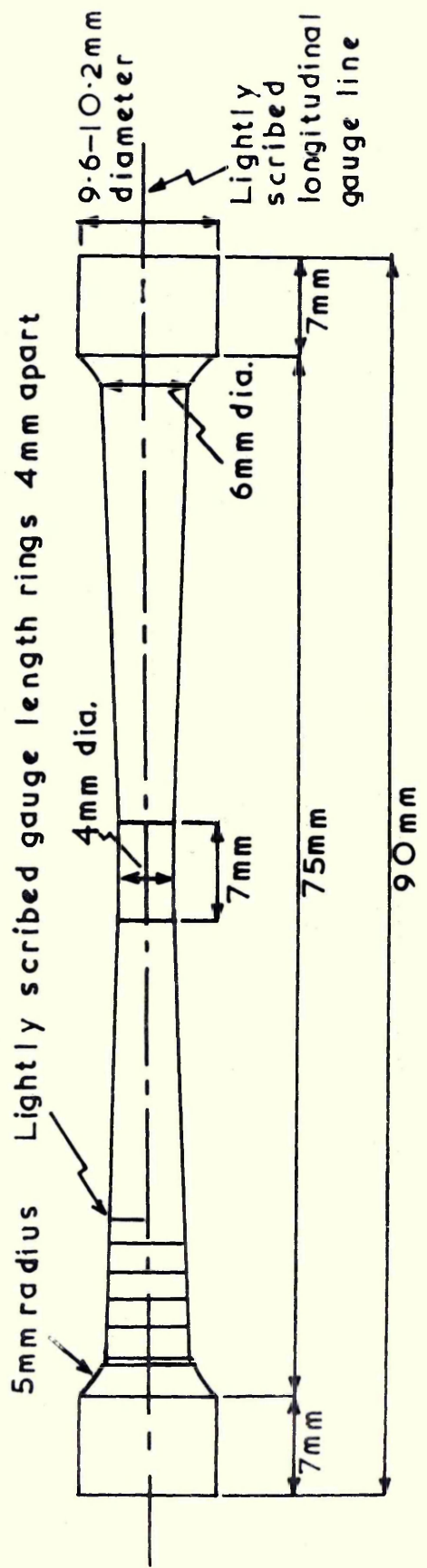


Figure 42 tapered tensile piece

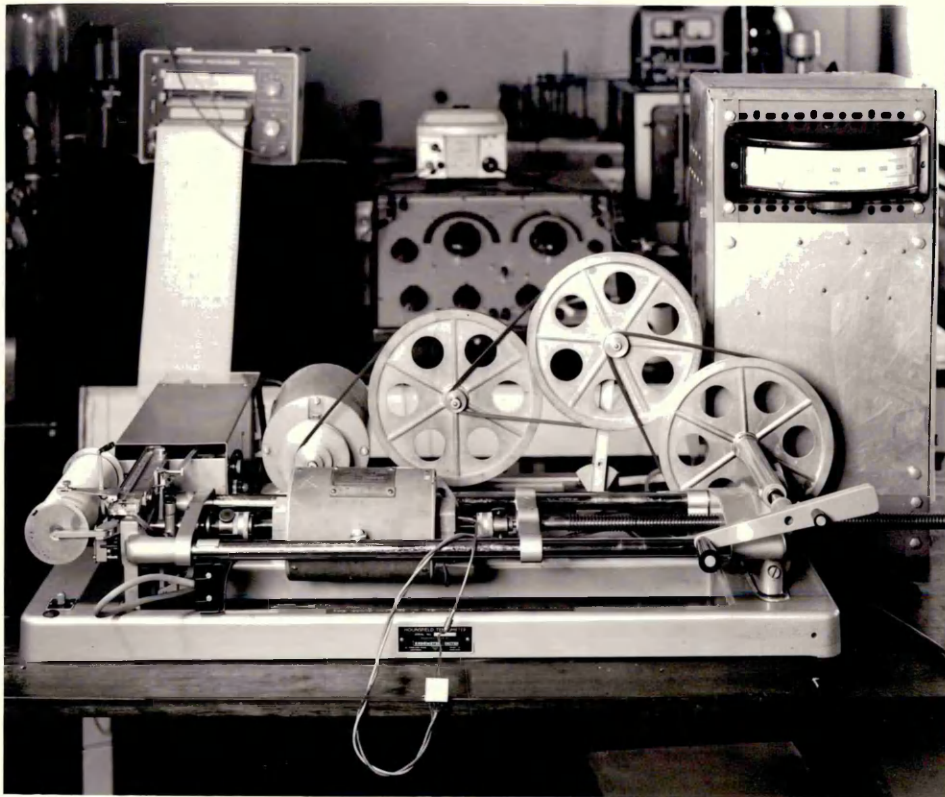
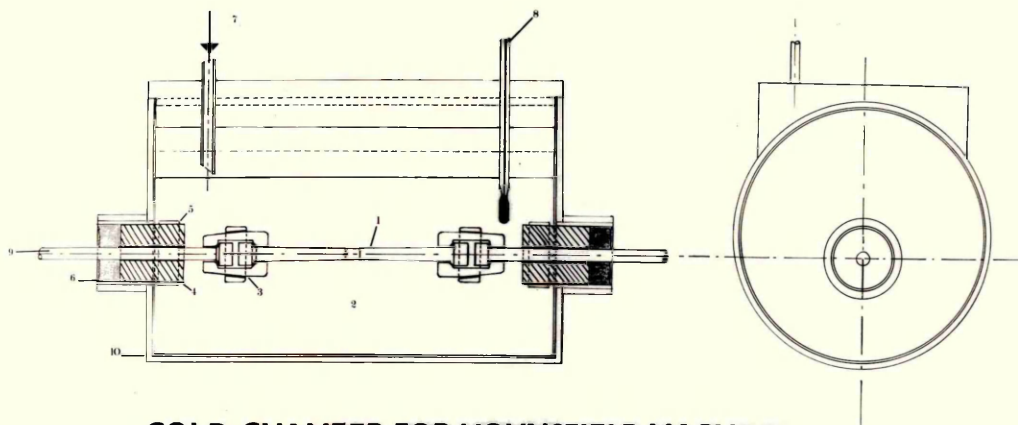


Figure 43 Apparatus for tensile testing at elevated temperature



**COLD CHAMBER FOR HOUNSFIELD MACHINE**

- 1. TAPERED TENSILE TEST PIECE
- 2. FREEZING MIXTURE
- 3. TAPERED SPLIT GRIPS
- 4. CORK SEAL
- 5. HOSE CLIP
- 6. SEALING COMPOUND
- 7. INLET FOR FREEZING MIXTURE
- 8. THERMOMETER
- 9. STIR ROD
- 10. THERMAL INSULATION

Figure 44 Cold chamber for Hounsfield machine

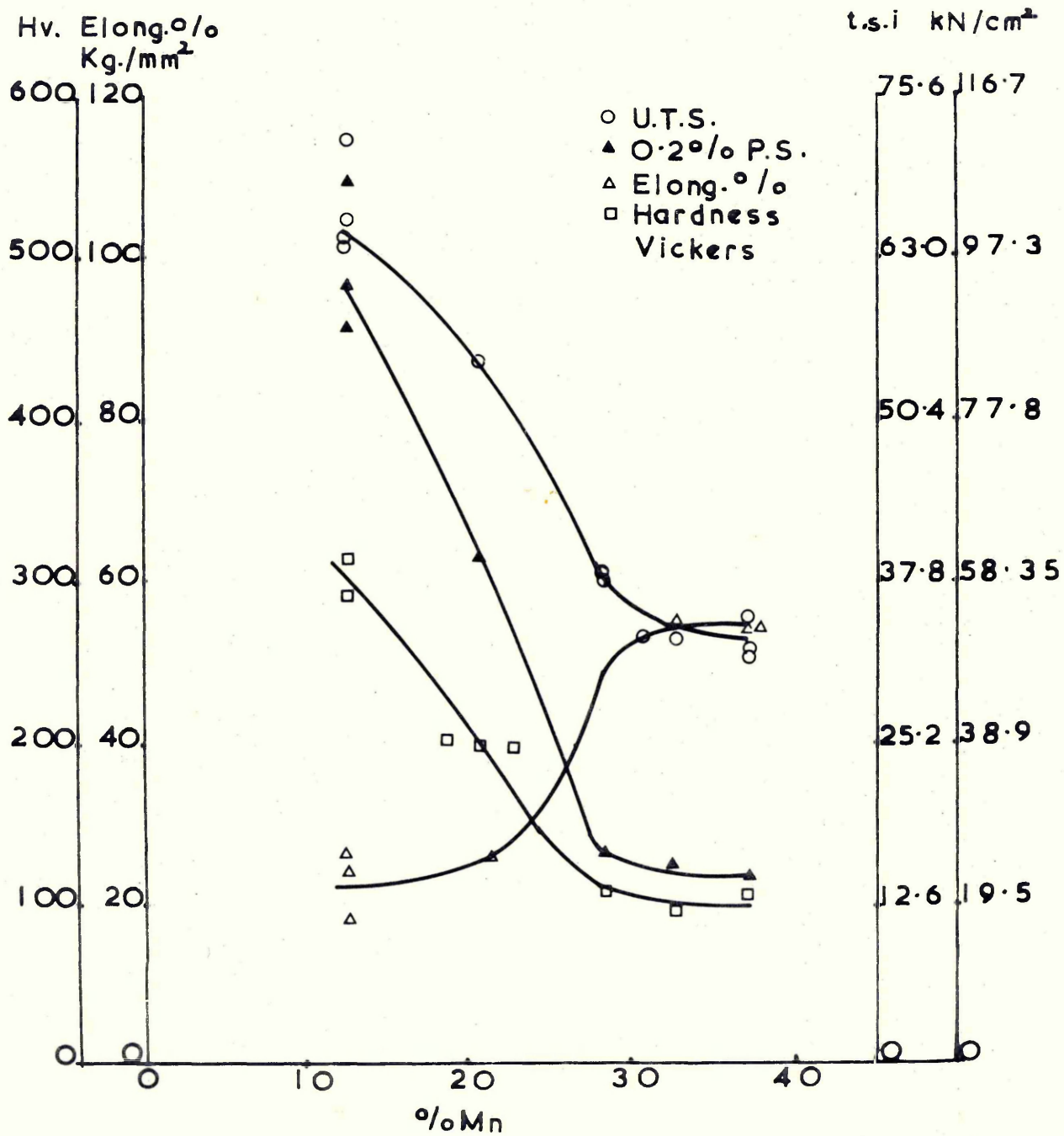


Figure 45 Mechanical properties V percent manganese



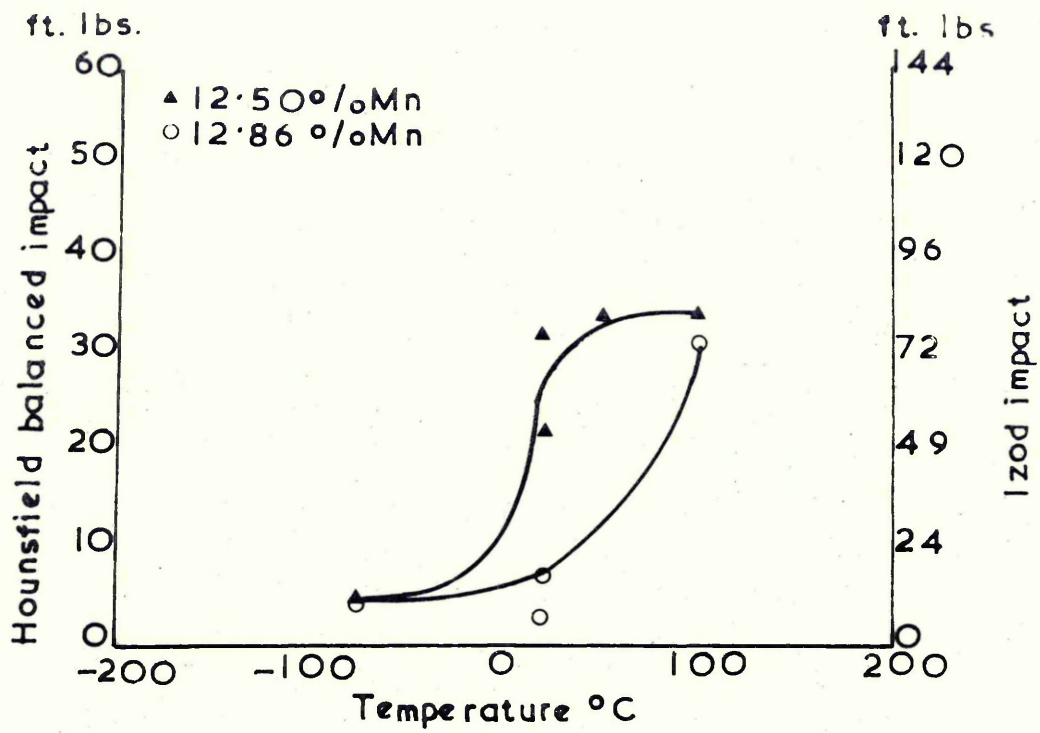


Figure 46a Hounsfield balanced impact ft. lbs. V temperature

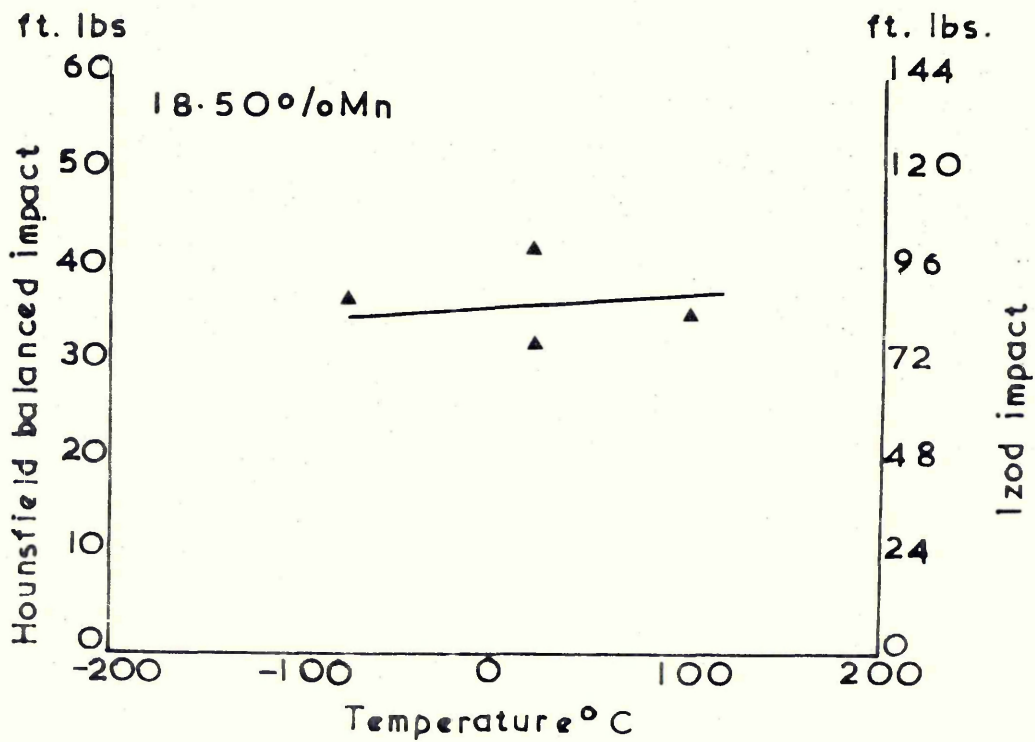


Figure 46b Hounsfield balanced impact ft. lbs. V temperature

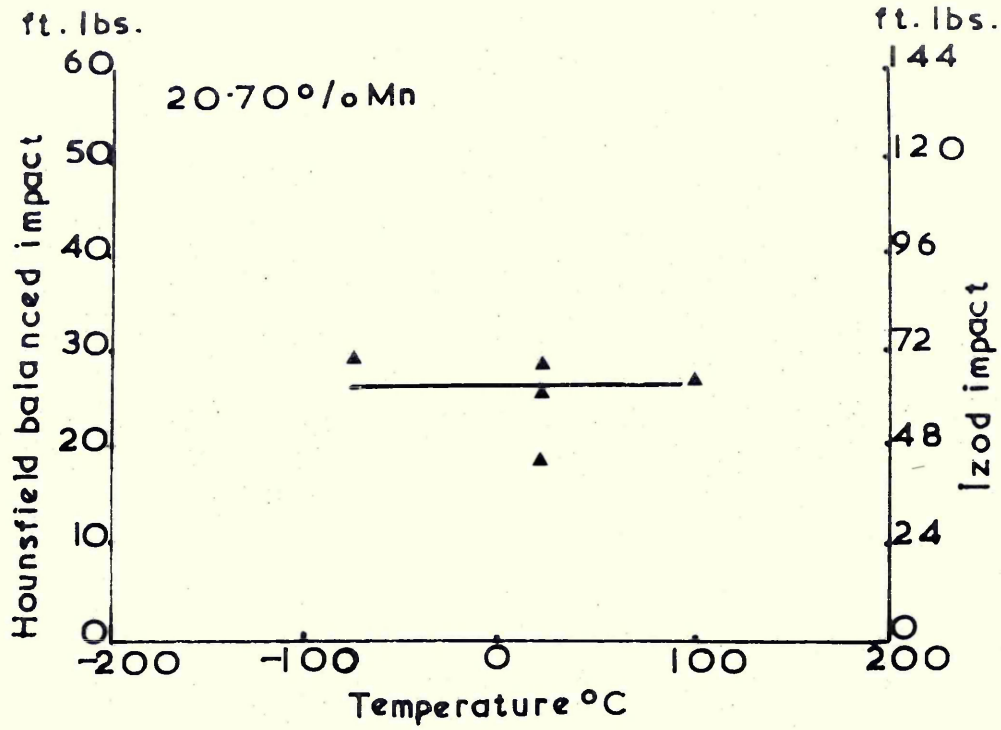


Figure 46c Hounsfield balanced impact ft. lbs.  
V temperature

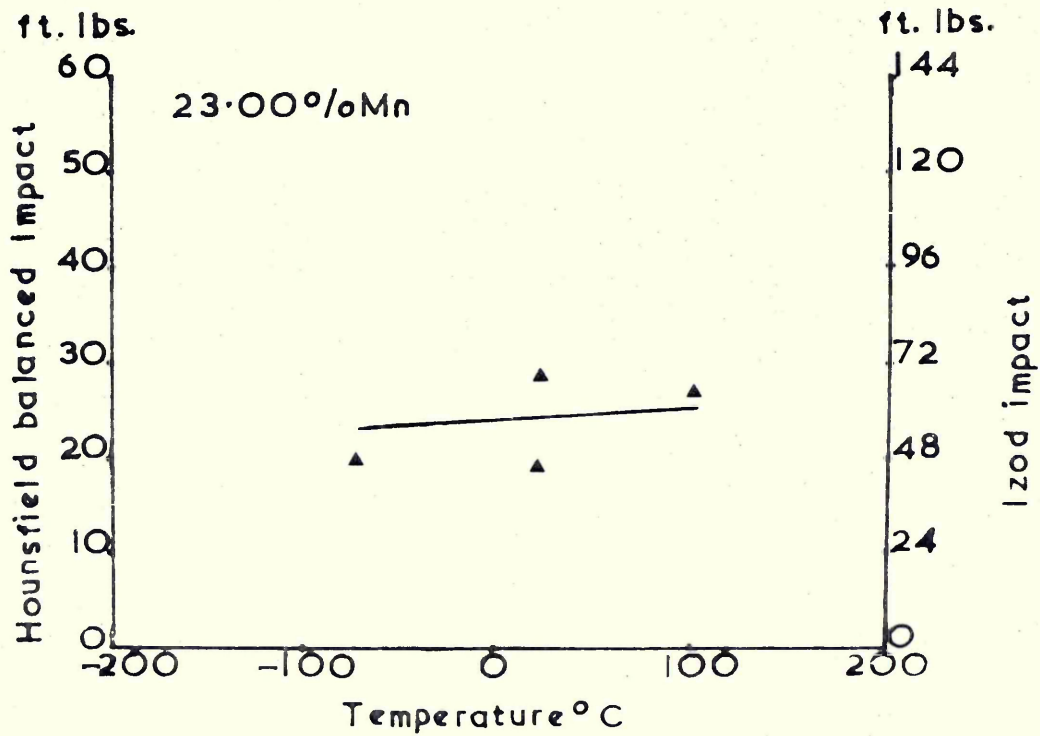


Figure 46d Hounsfield balanced impact ft. lbs.  
V temperature

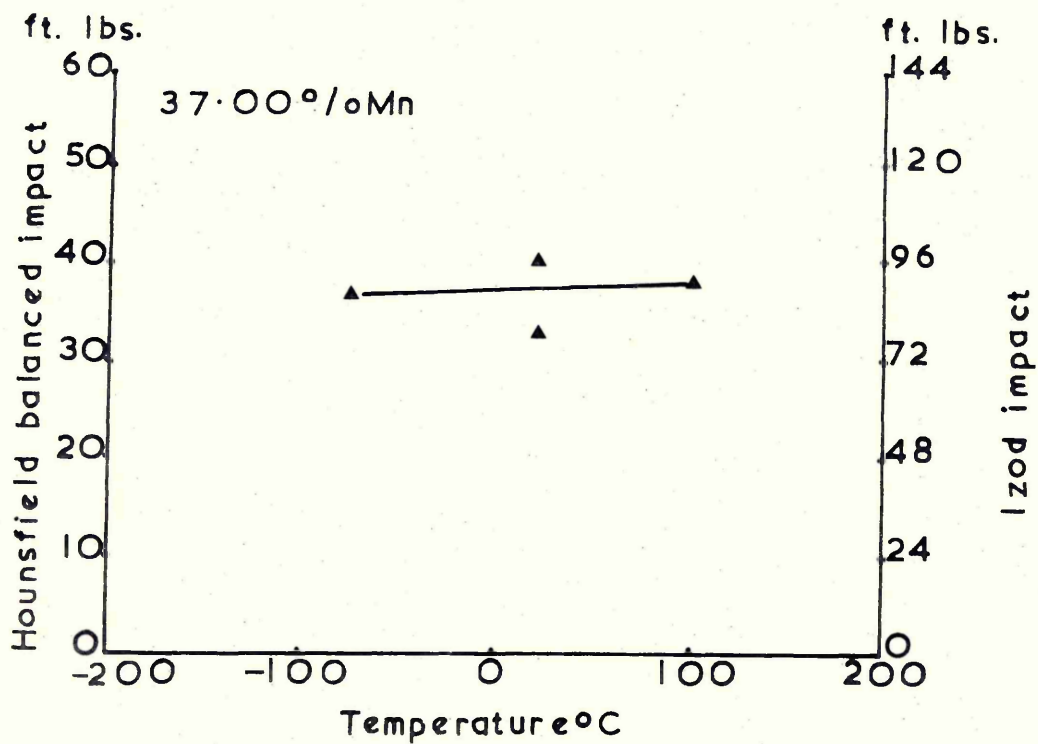


Figure 46e Hounsfield balanced impact ft. lbs.  
V temperature

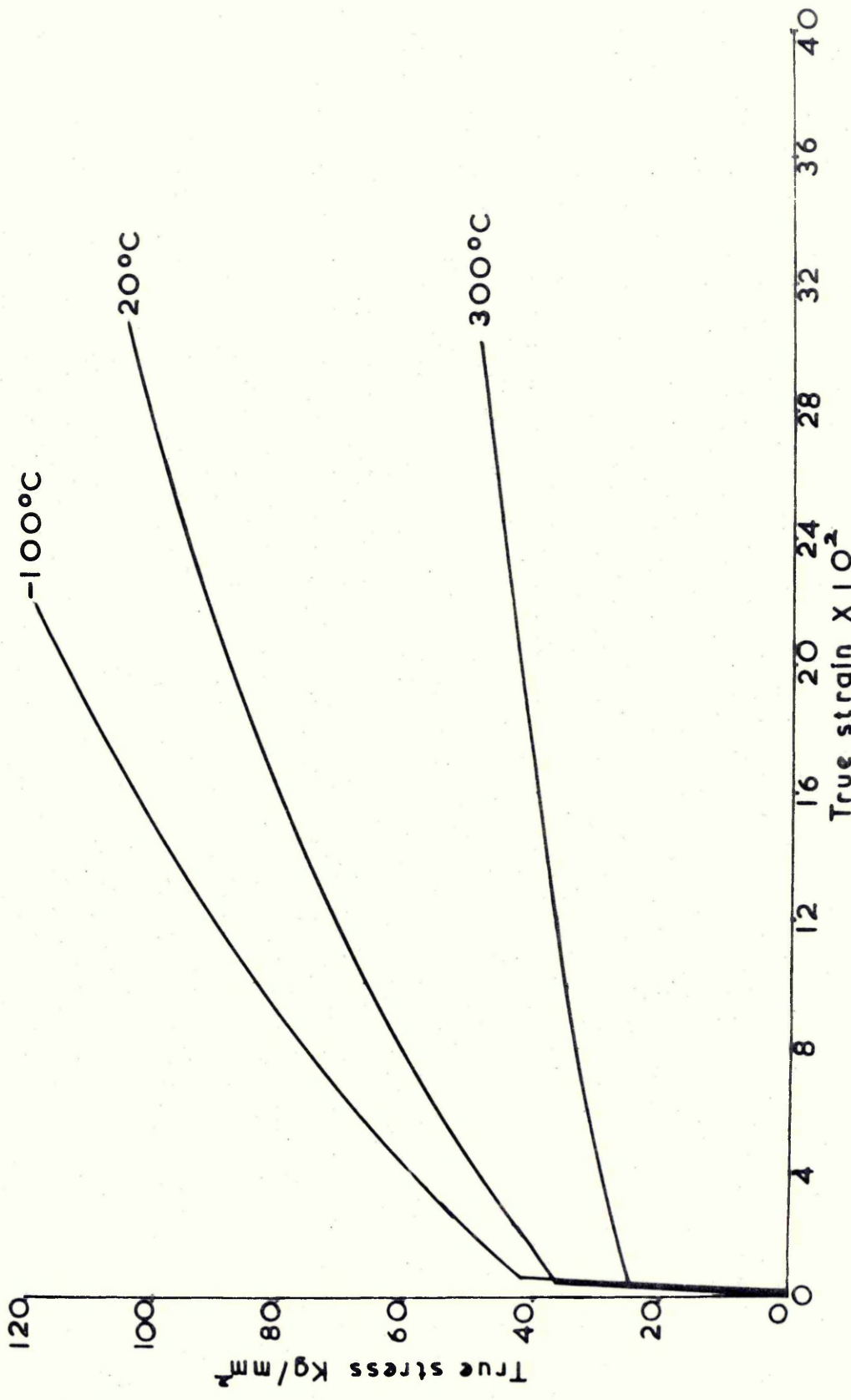


Figure 47a True-stress V True-strain curves Fe-15.6%Mn alloy

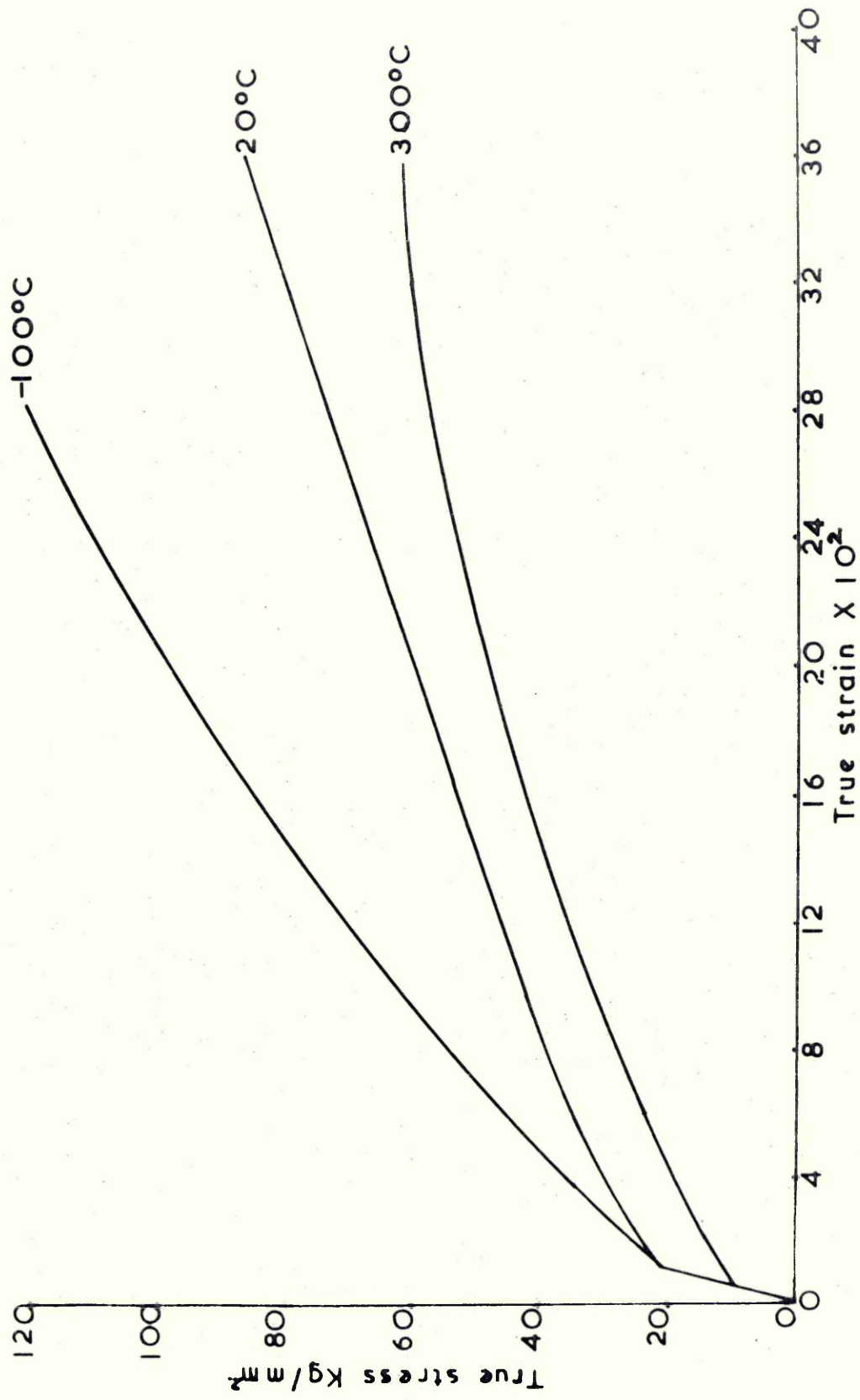


Figure 47b True-stress v True-strain curves Fe-28.25%Mn alloy

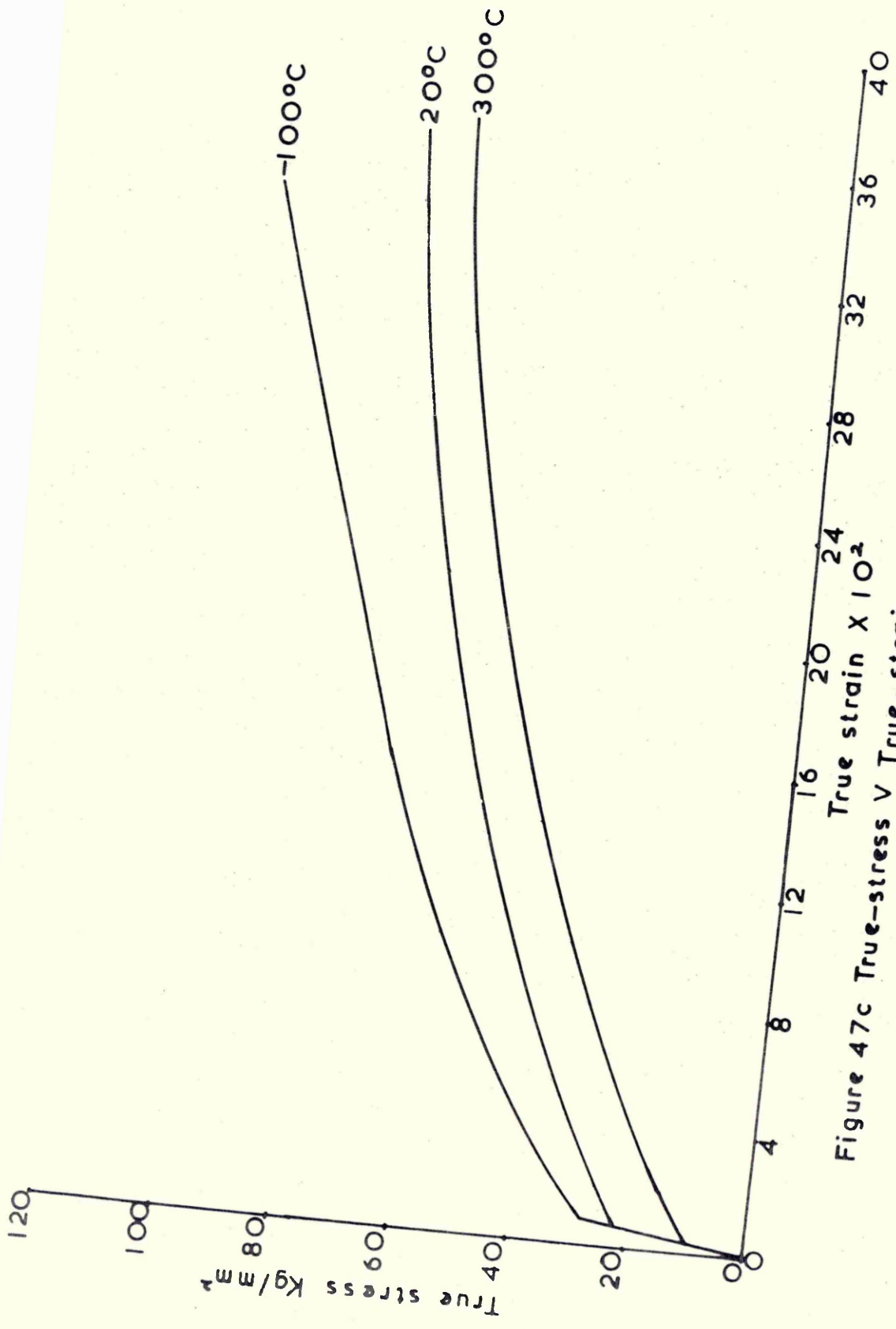


Figure 47c True-stress V True-strain curves Fe-32.50%Mn alloy

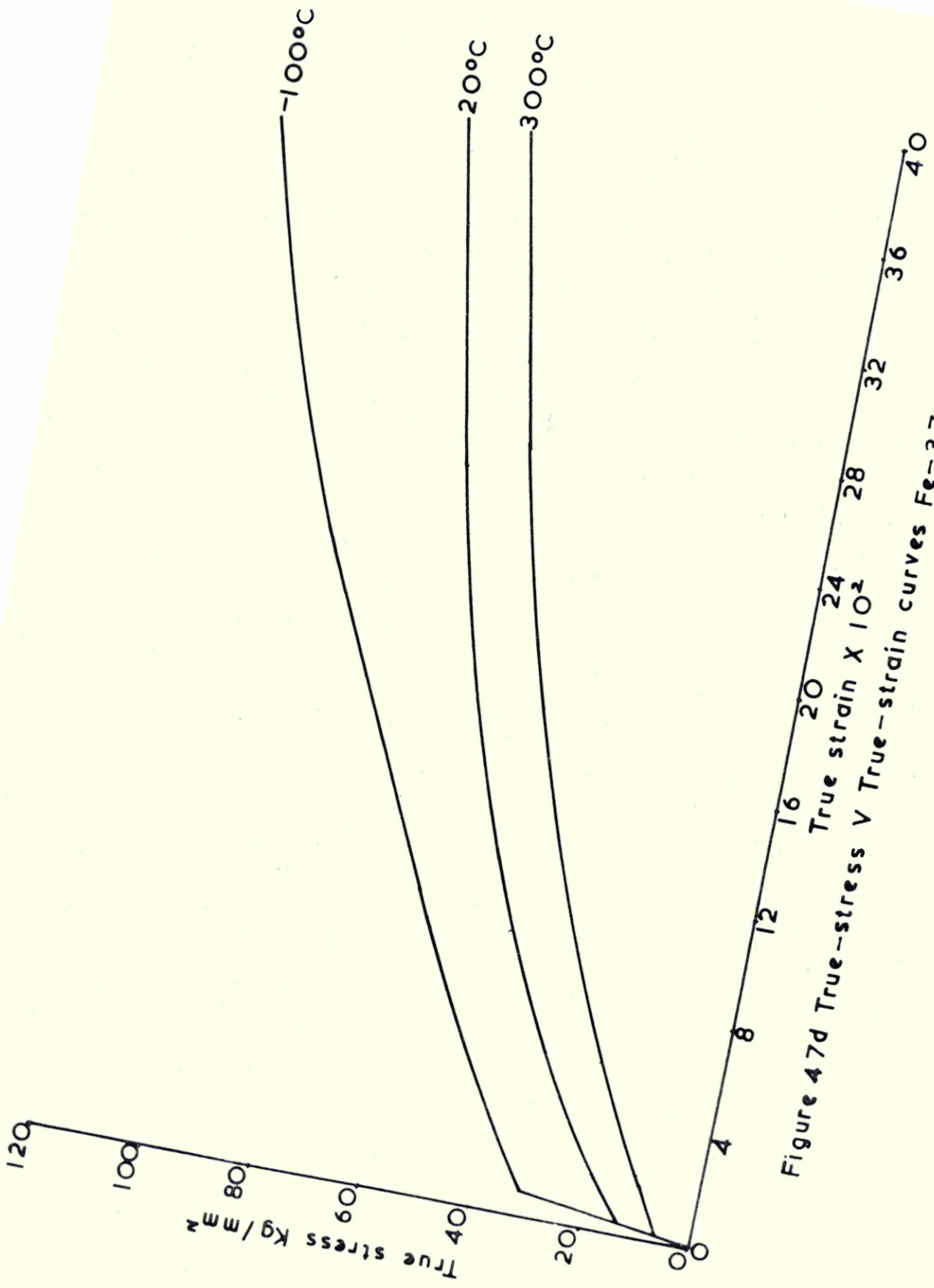


Figure 47d True-stress V True-strain curves Fe-37.00%Mn alloy

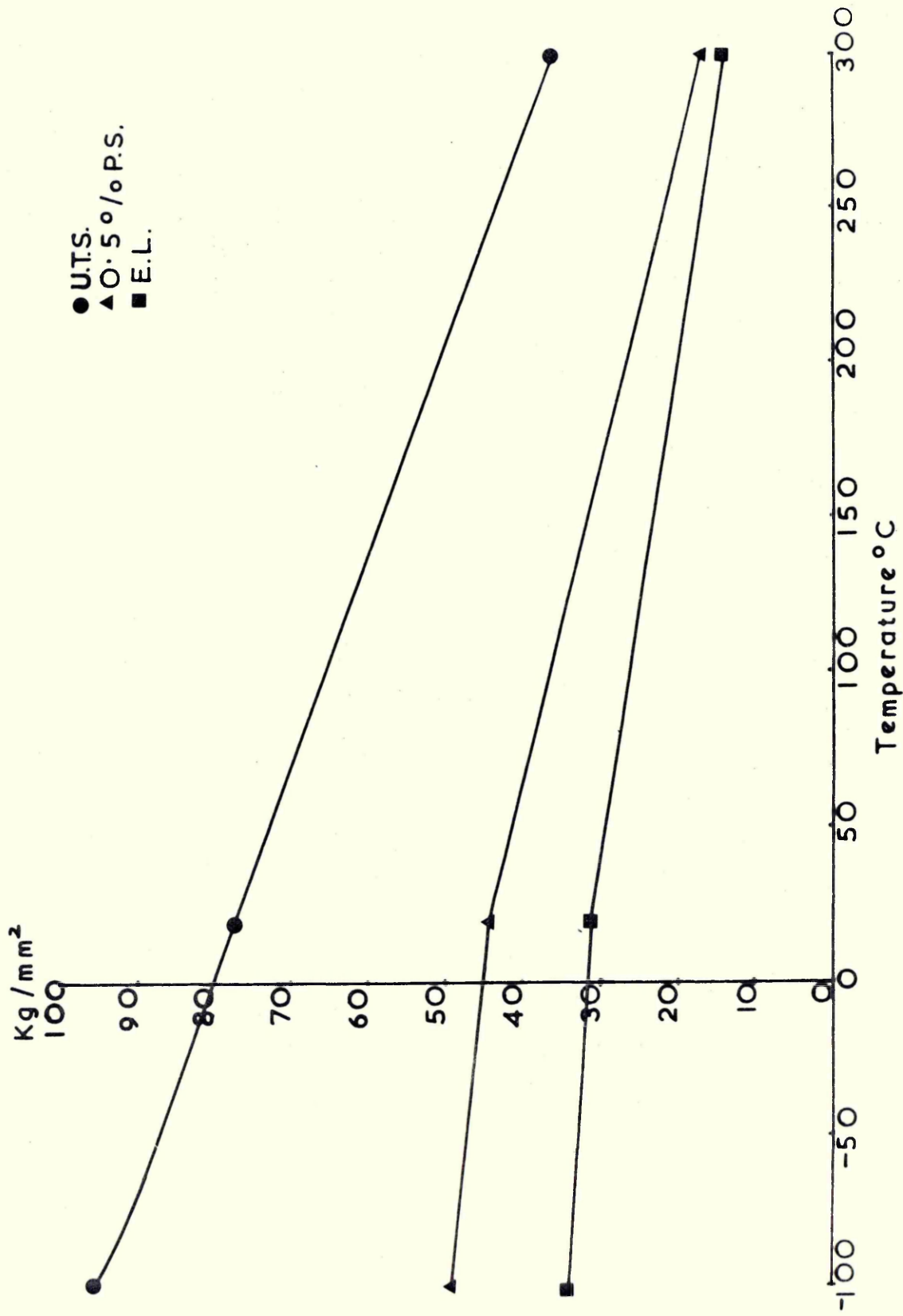
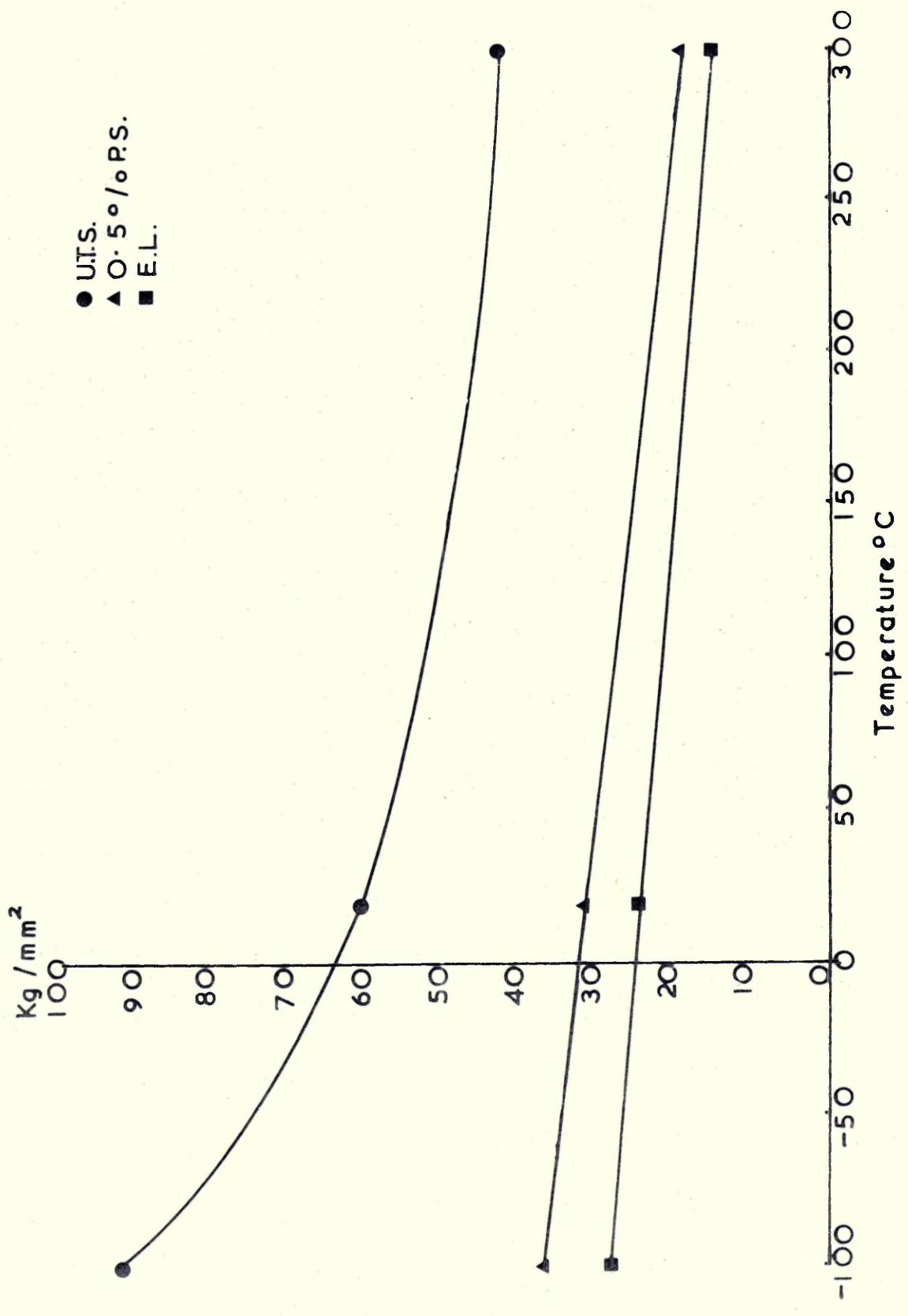
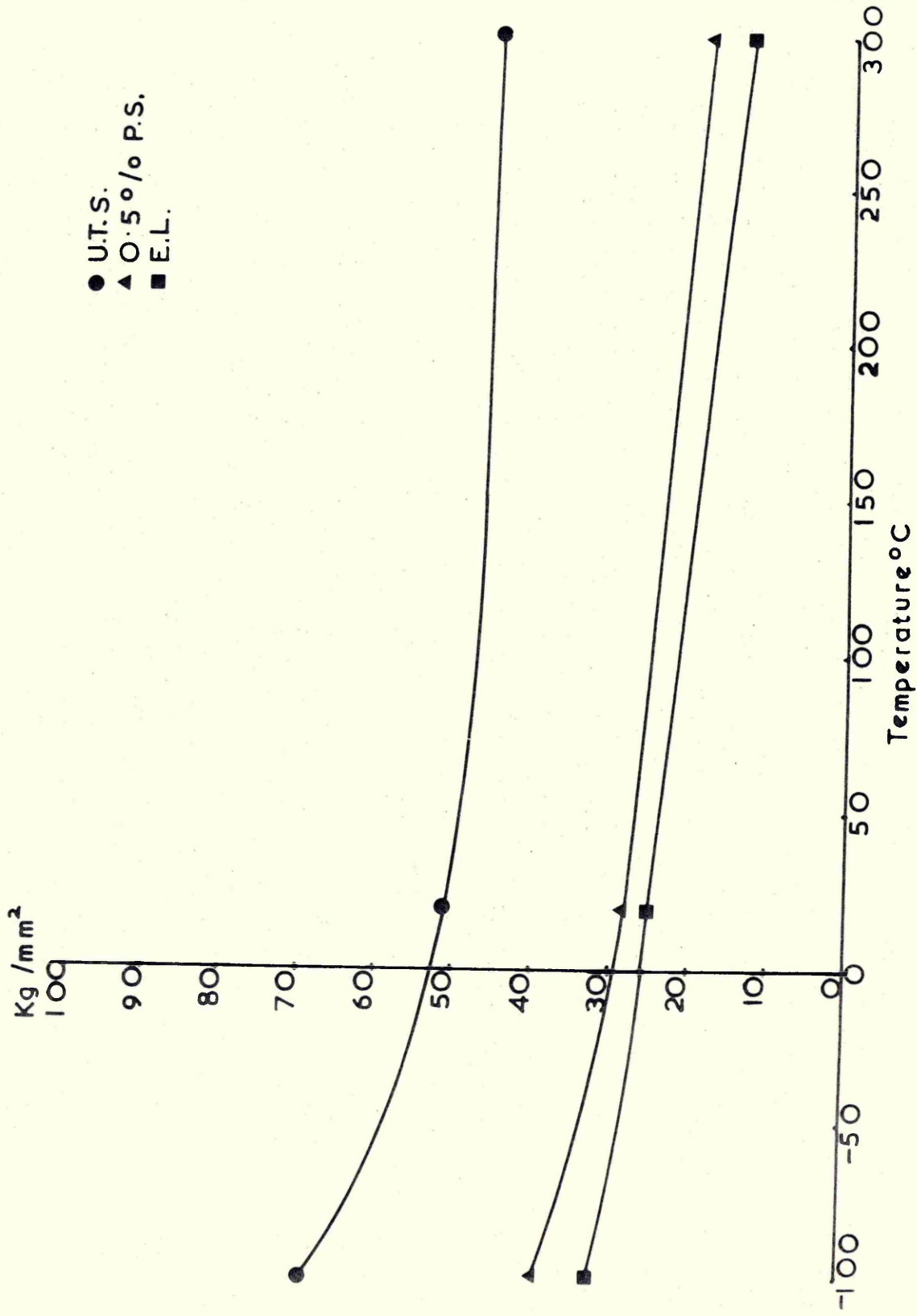


Figure 48a Mechanical properties V temperature Fe-15.60%Mn alloy



● U.T.S.  
 ▲ 0.5% P.S.  
 ■ E.L.

Figure 48b Mechanical properties V temperature Fe-28.25%Mn alloy



● U.T.S.  
 ▲ 0.5% P.S.  
 ■ E.L.

Figure 48c Mechanical properties V temperature Fe - 32.50%Mn alloy

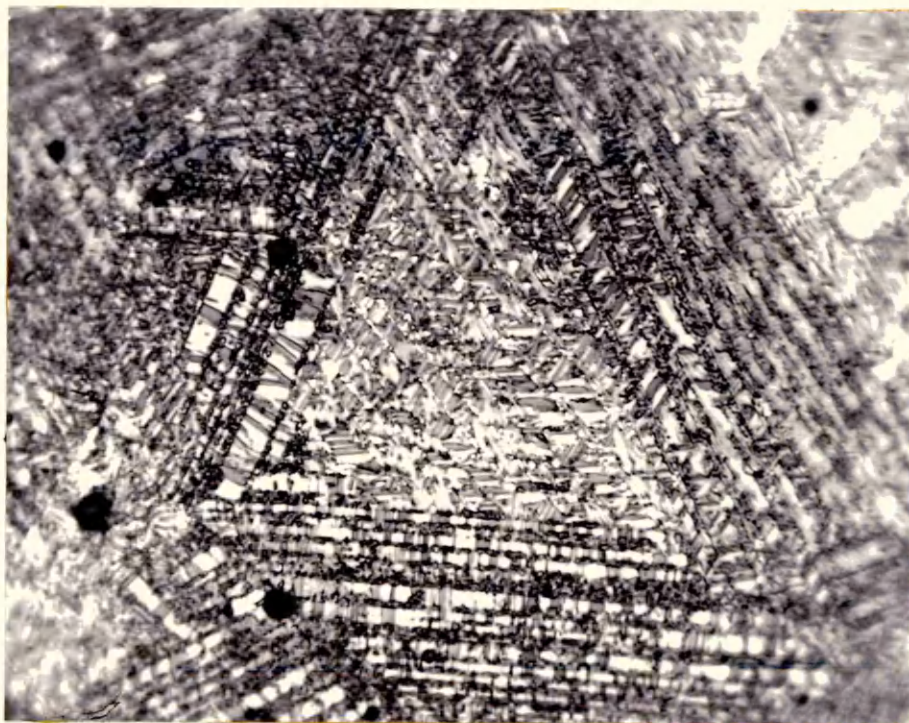


Figure 49 Fe-12.50%Mn alloy air cooled from gamma region (1150°C for 24hrs. + 950°C for 1.1/2hrs.)  
Mag. X1600

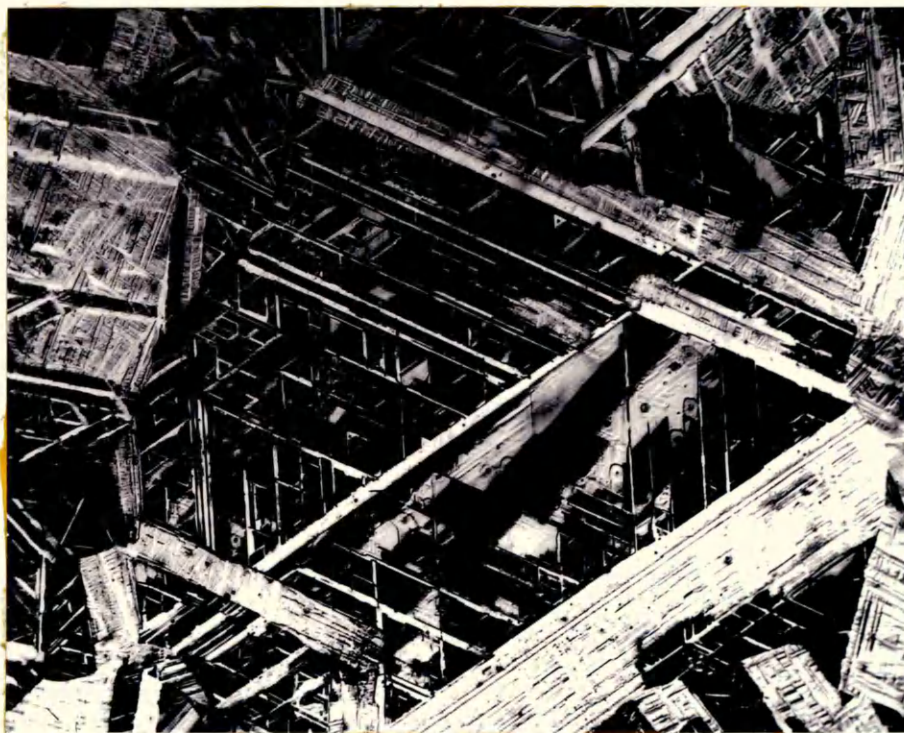


Figure 50 Fe-18.50%Mn alloy air cooled from gamma region (1150°C for 24hrs. + 950°C for 1.1/2hrs.)  
Mag. X150

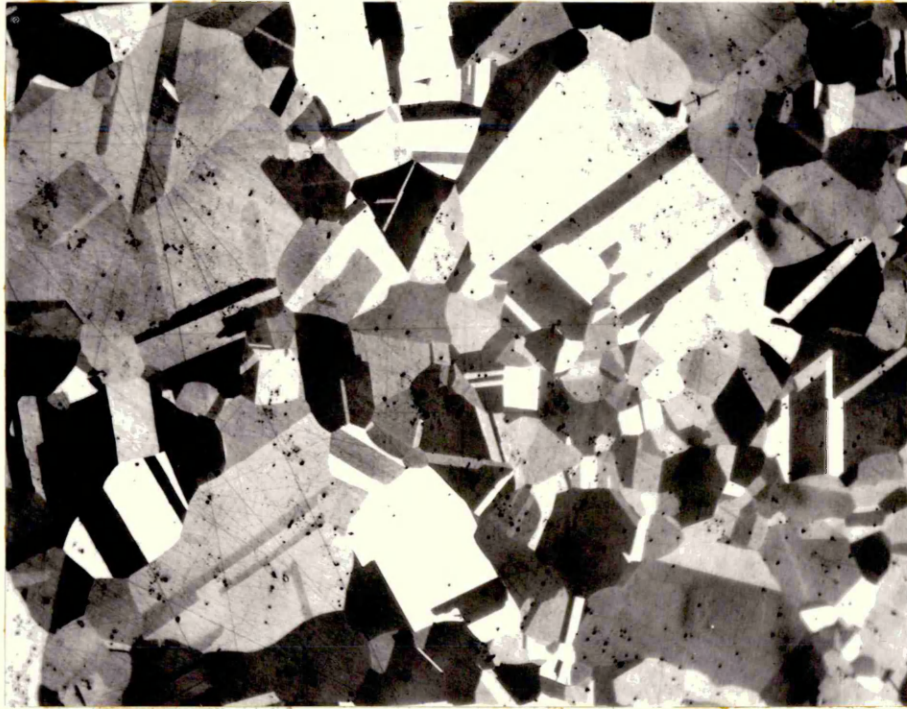


Figure 51 Fe-37.00%Mn alloy cooled from gamma region (1150°C for 24hrs. + 950°C for 1.1/2 hrs.) Mag. X 150

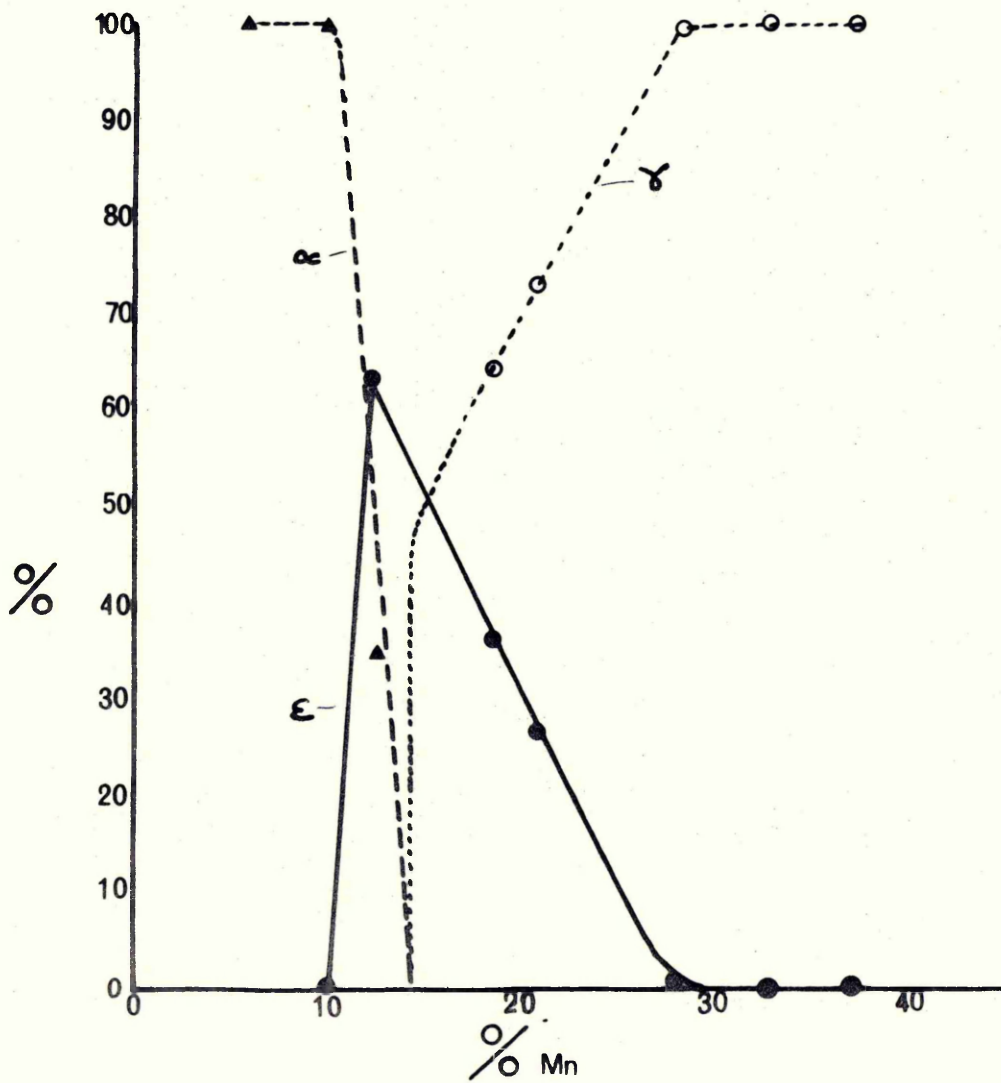


Figure 52 Percentage phase V composition based on point counting specimens annealed at 950°C air cooled.

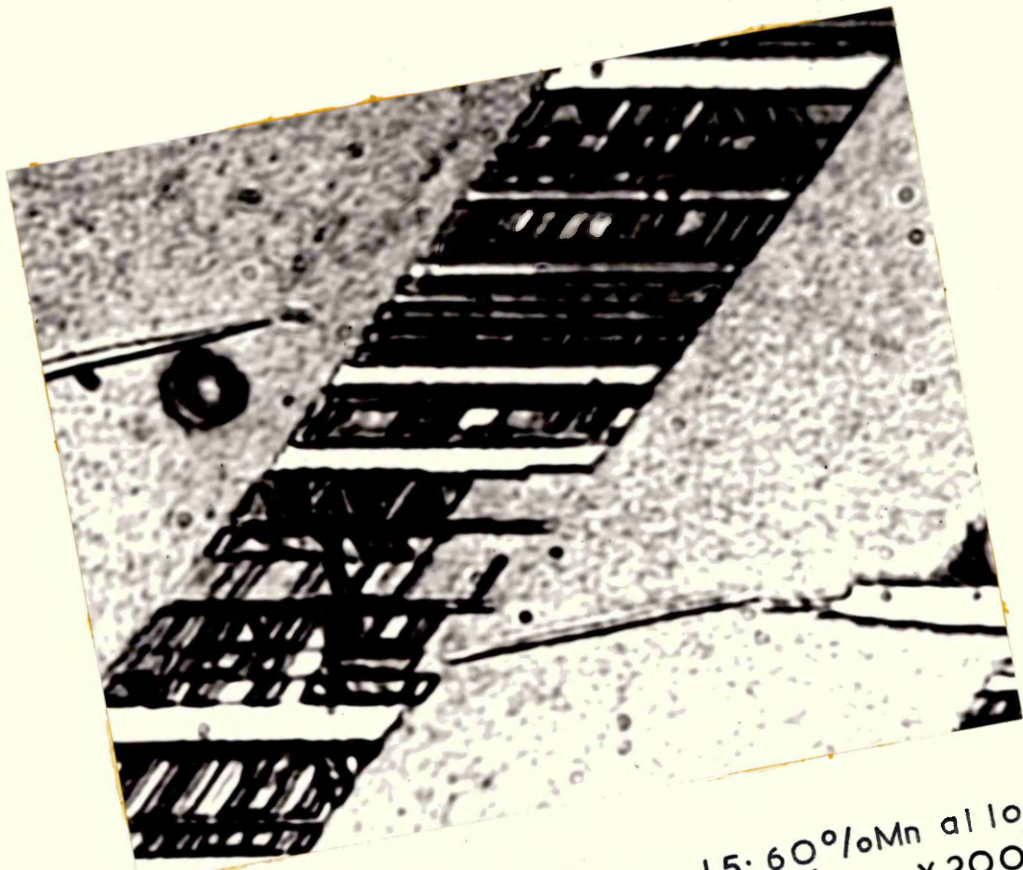


Figure 55 Unallocated area Fe-15.60%Mn alloy.  
(Mag. X2000)

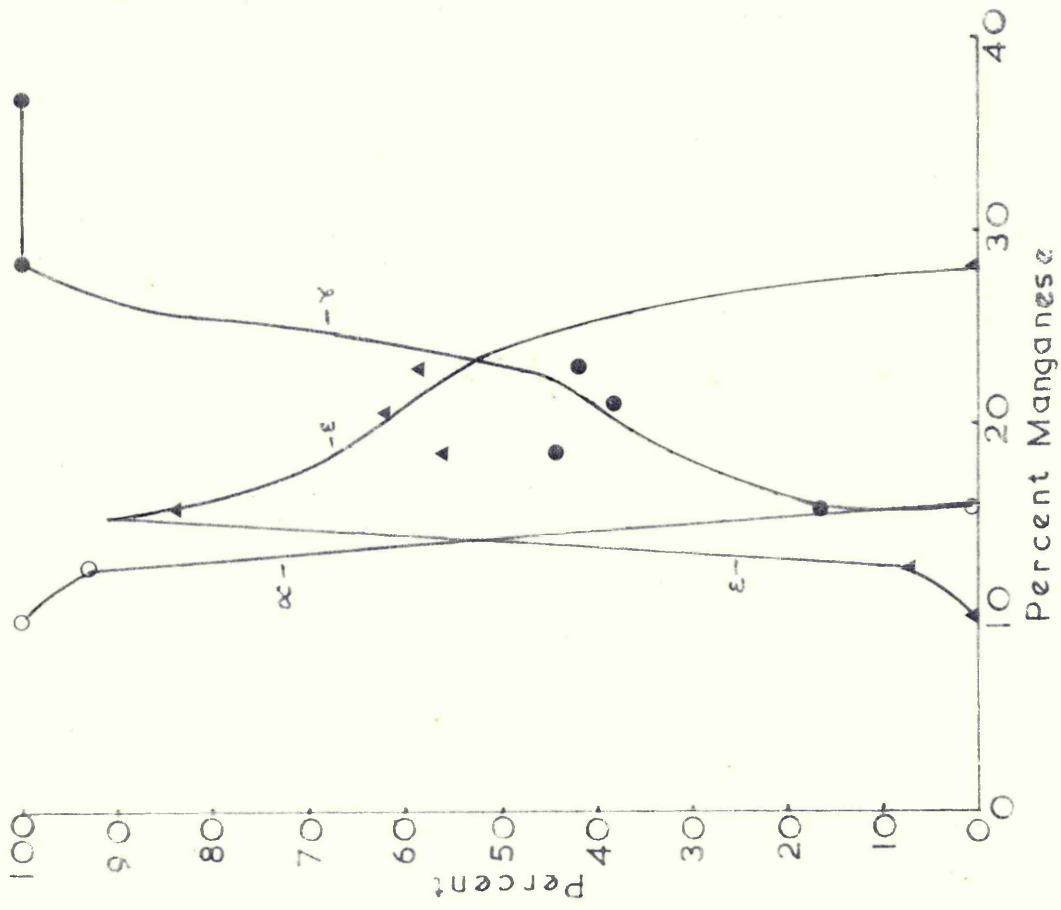


Figure 56 Revised estimate of phases based on point counting

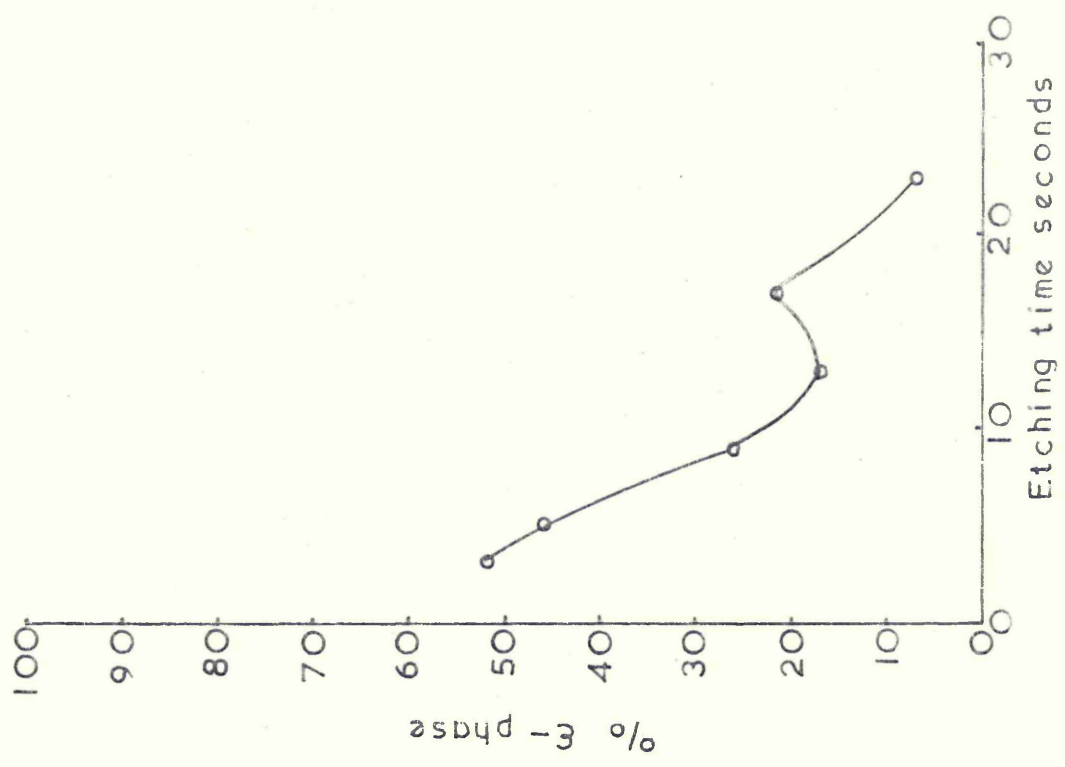
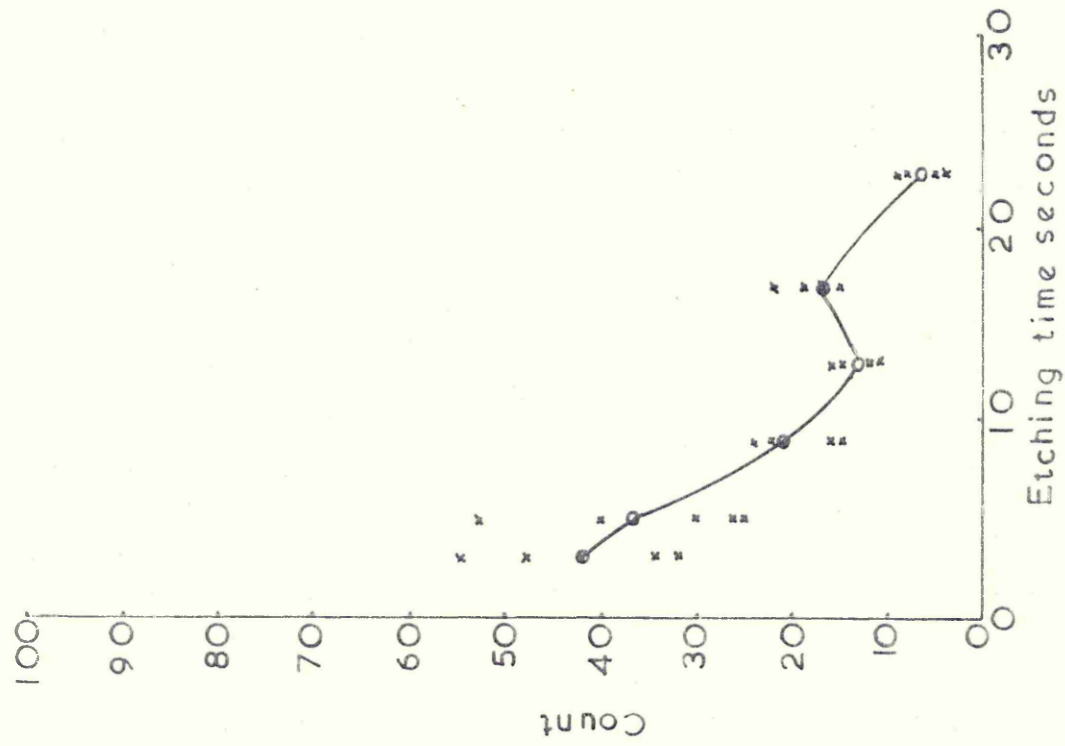
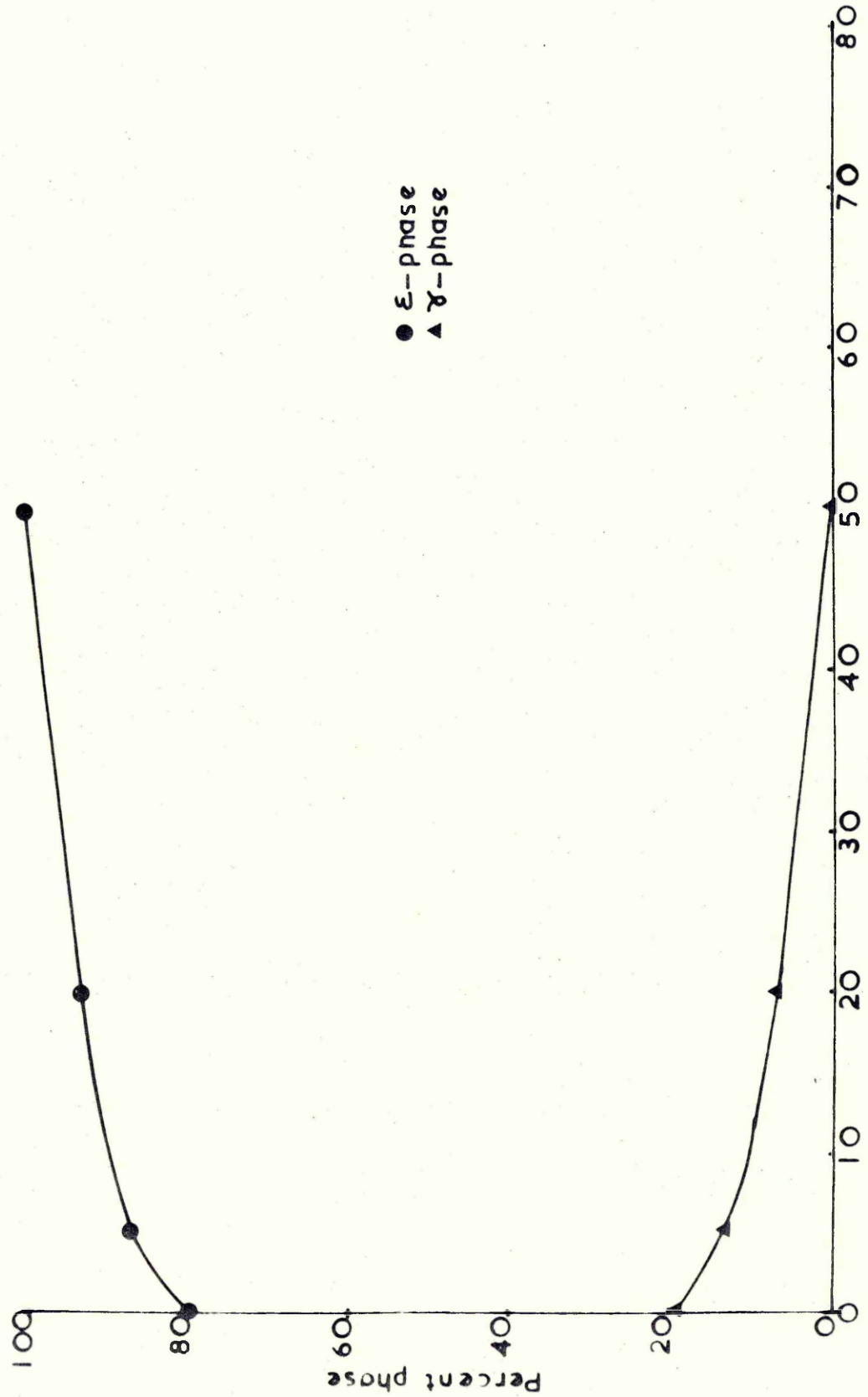


Figure 57 Effect of etching time on percent  $\epsilon$ -phase determined by point counting (reagent saturated Sodium thiosulphate + Potassium metabisulphite).



●  $\epsilon$ -phase  
 ▲  $\gamma$ -phase

Percent reduction in thickness

Figure 60b Percent phase V percent reduction in thickness Fe-23.00% Mn alloy

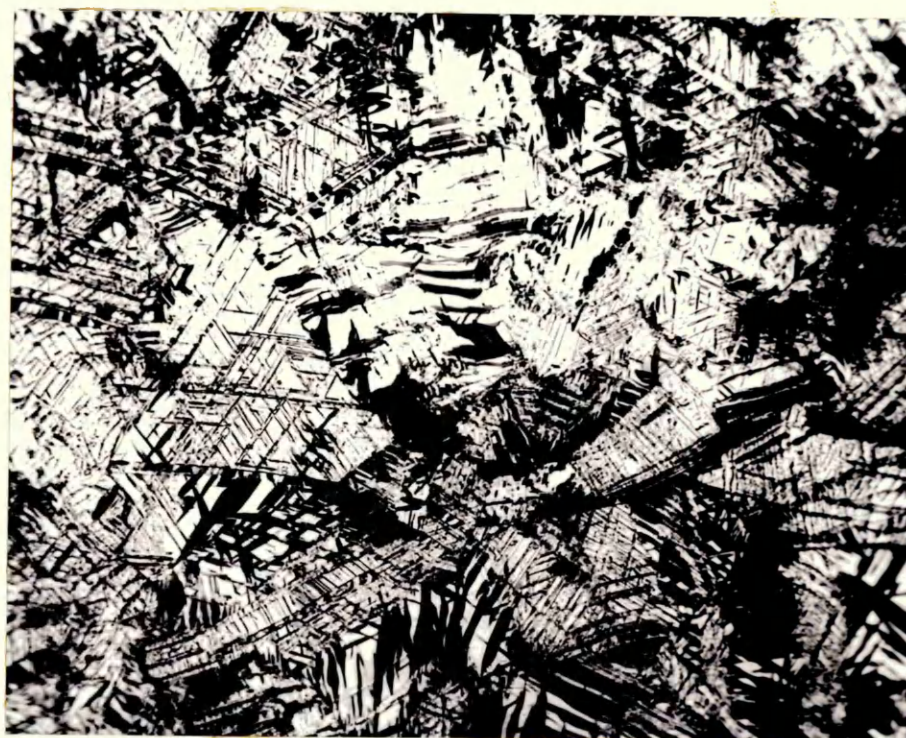


Figure 61 Fe-15.60%Mn alloy after 20% reduction  
(Mag. X 500)

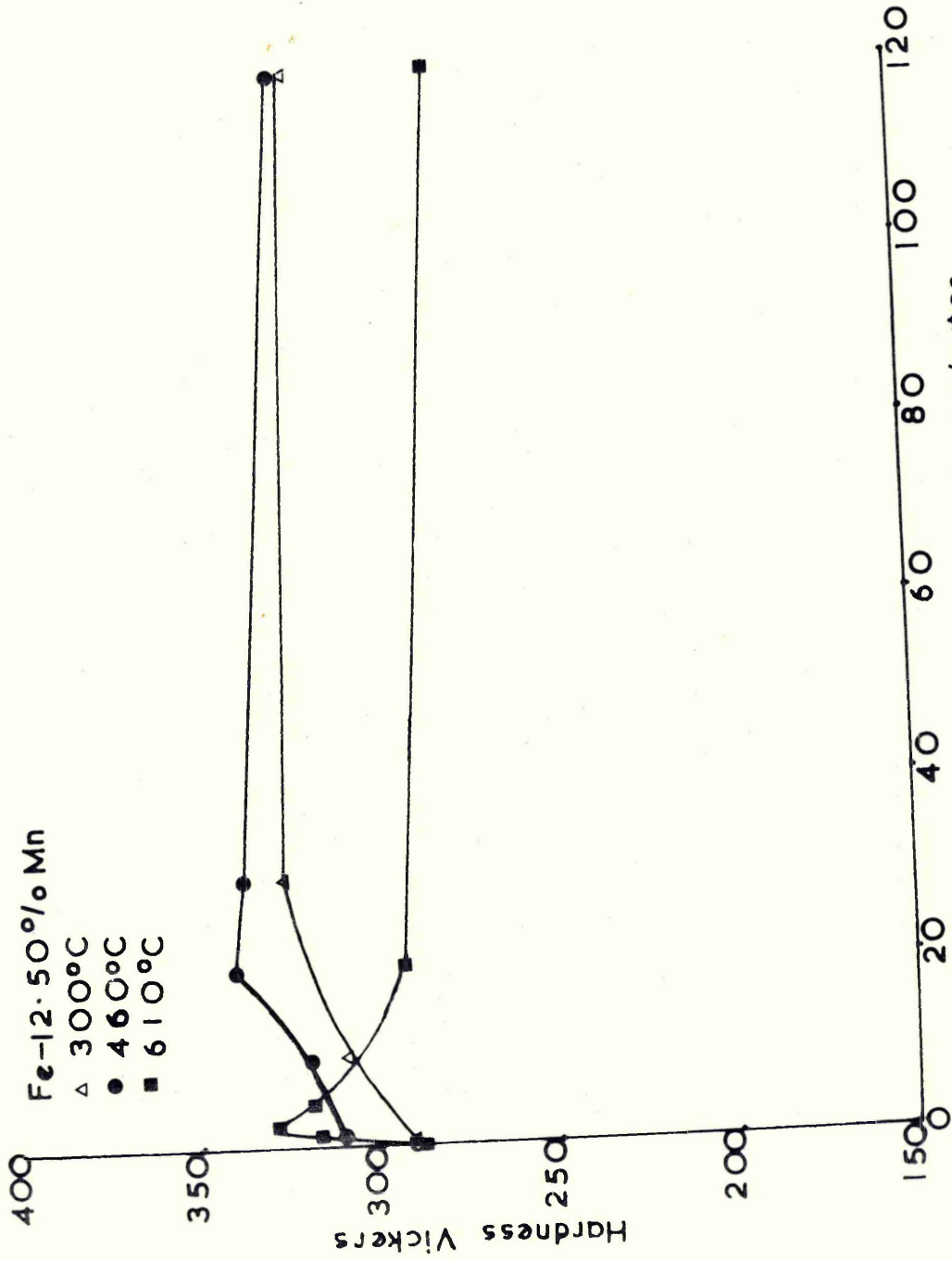


Figure 62a Ageing curves for Fe-12.50% Mn alloy

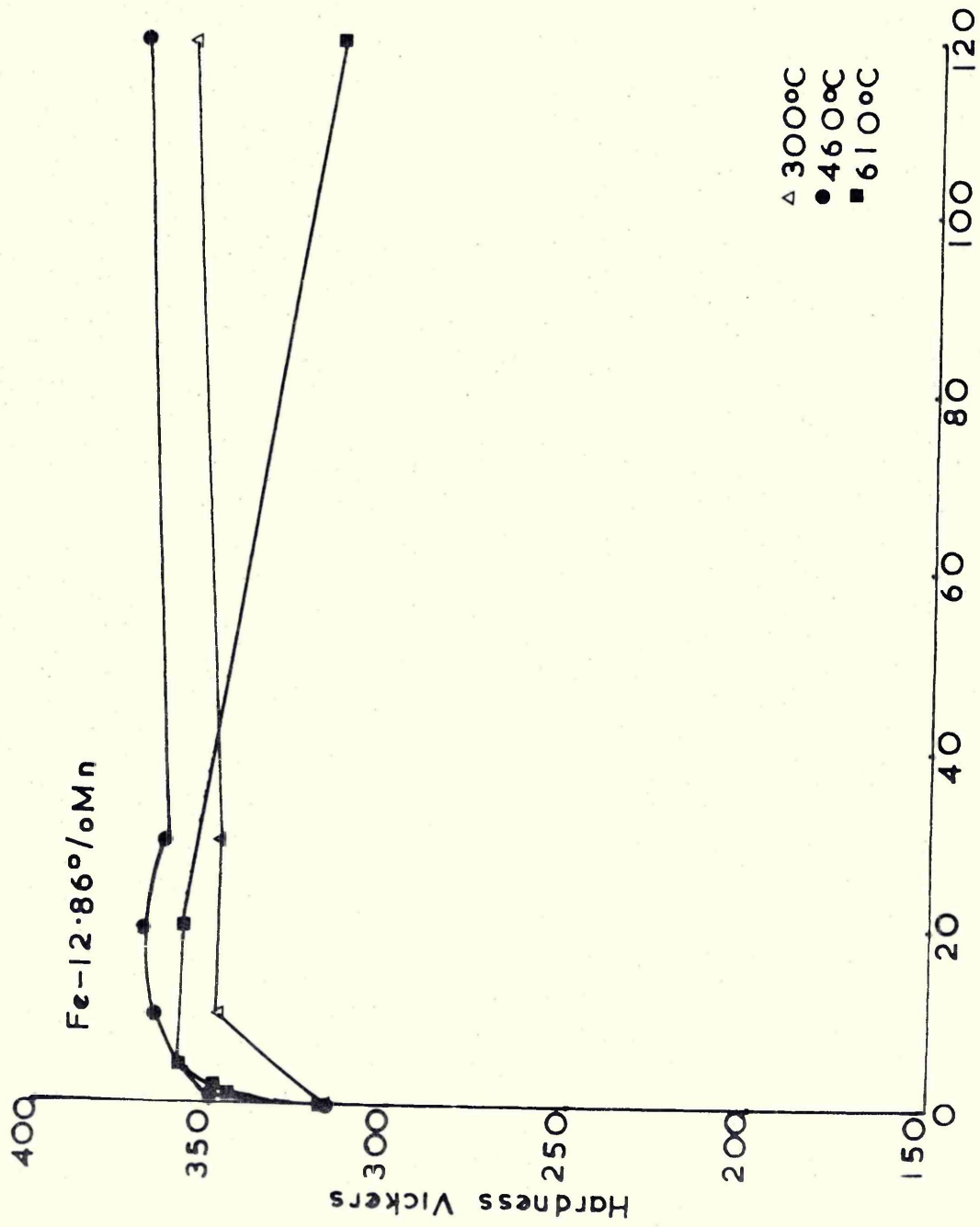


Figure 6.2b Ageing curves for Fe-12.86% Mn alloy

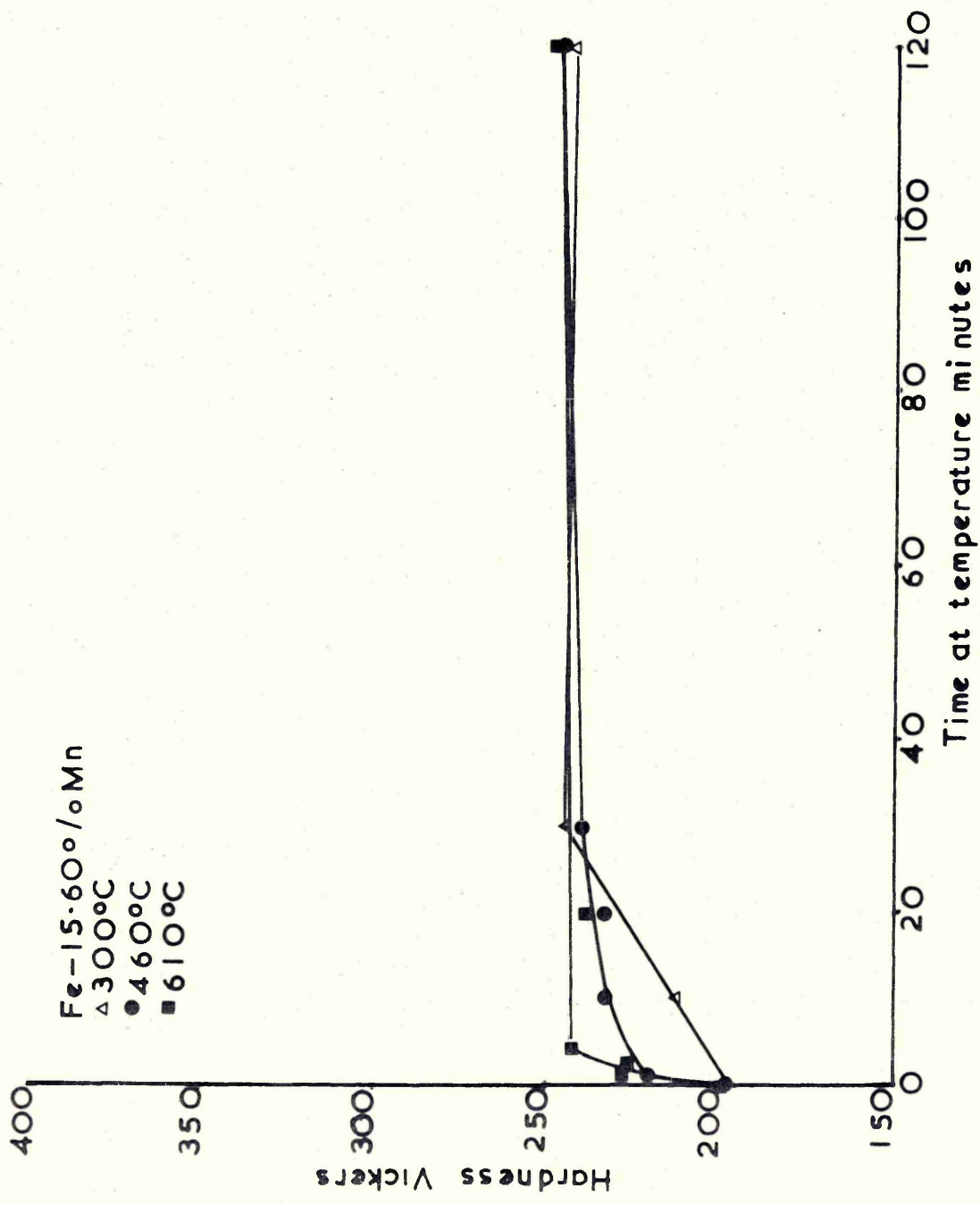


Figure 62c Ageing curves for Fe-15.60% Mn alloy

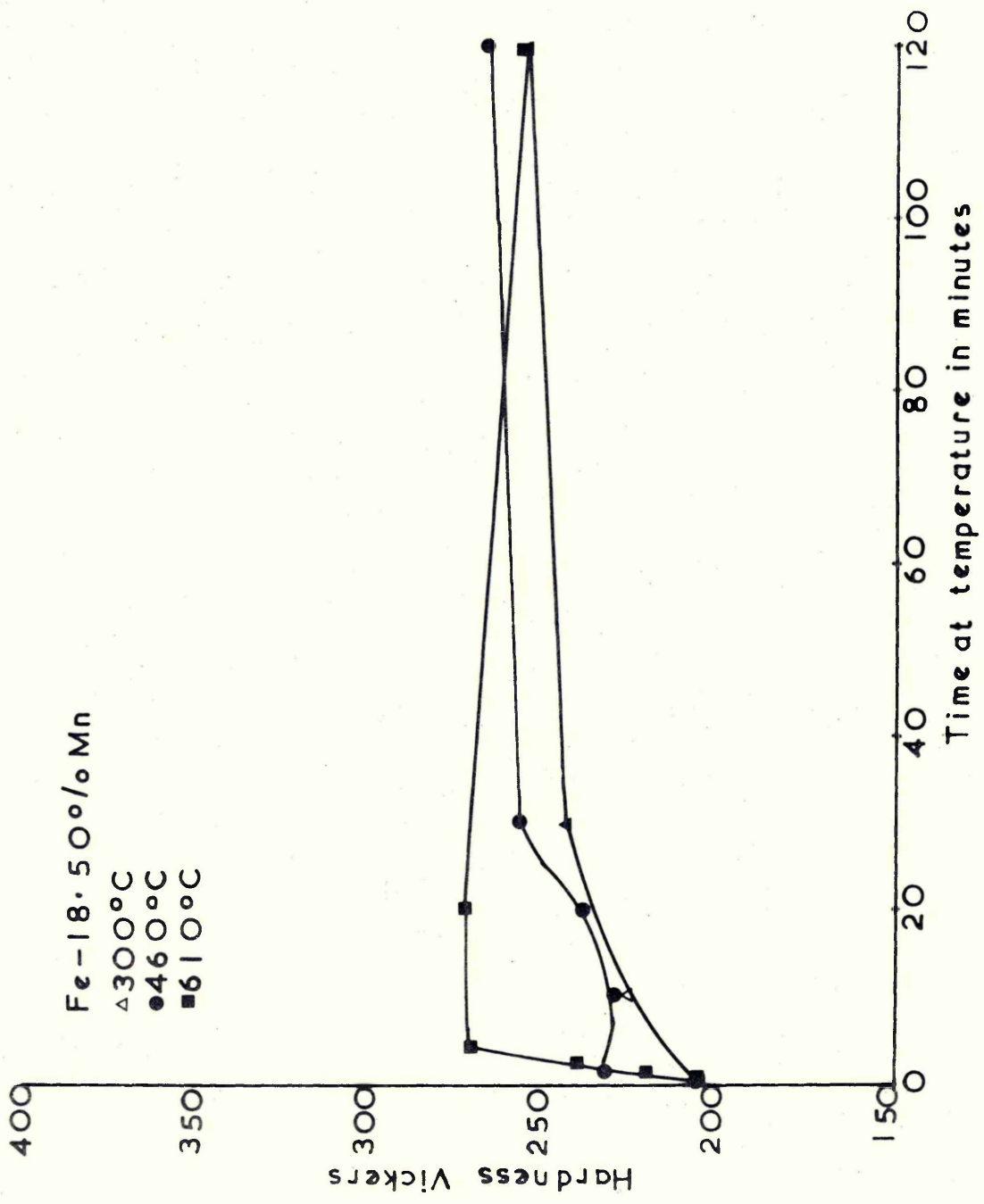


Figure 62d Ageing curves for Fe-18.50% Mn alloy

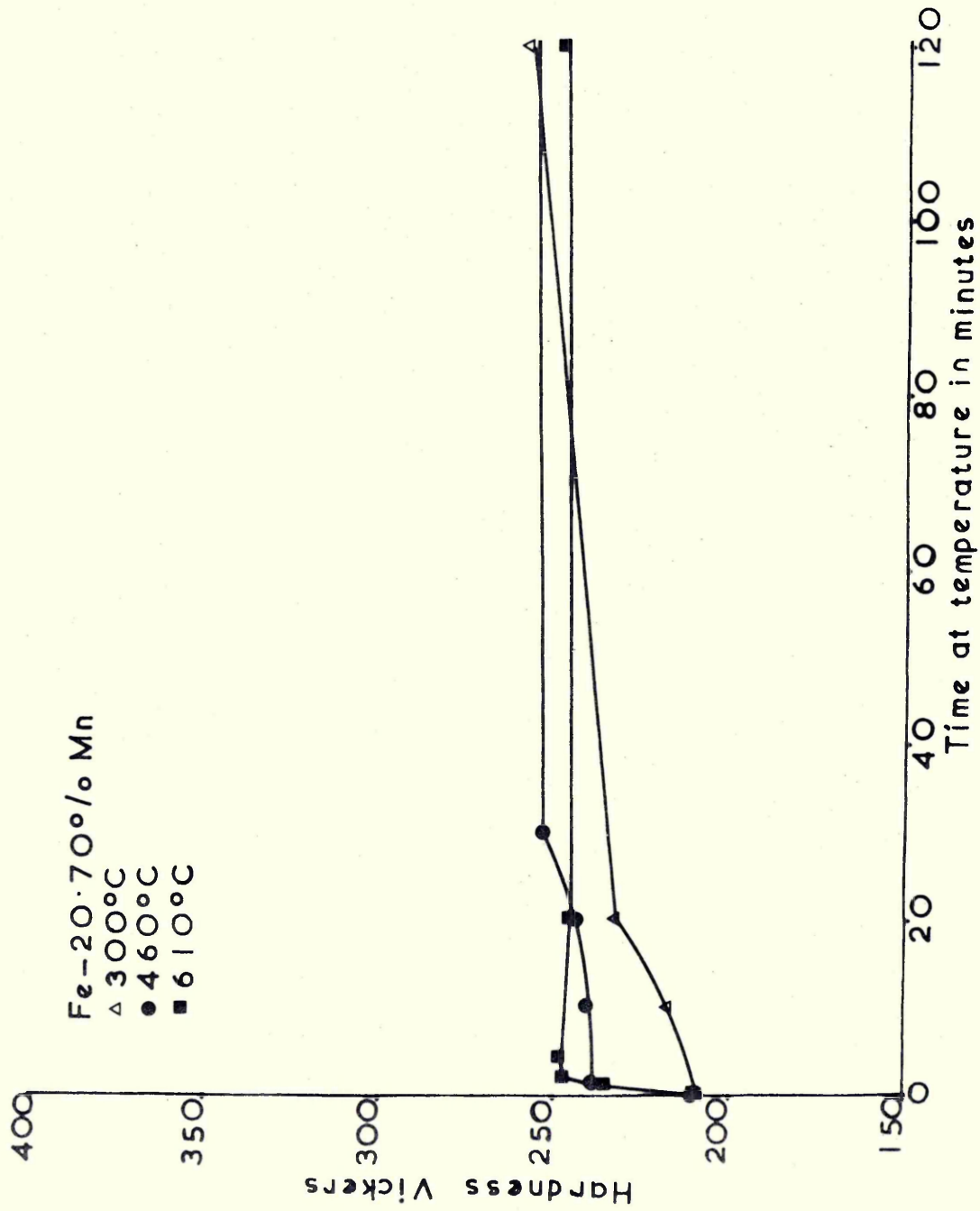


Figure 62e Ageing curves for Fe-20.70% Mn alloy

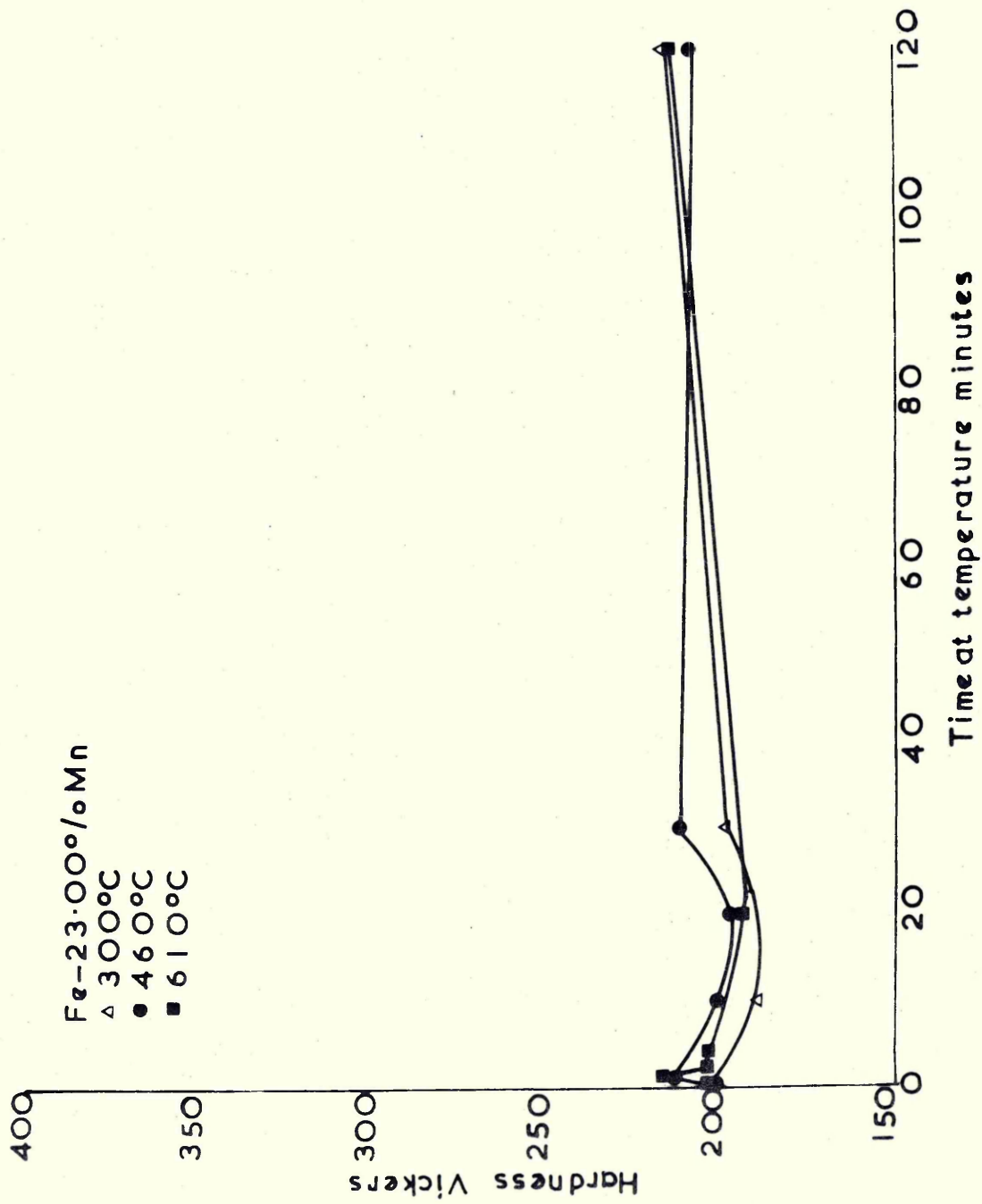
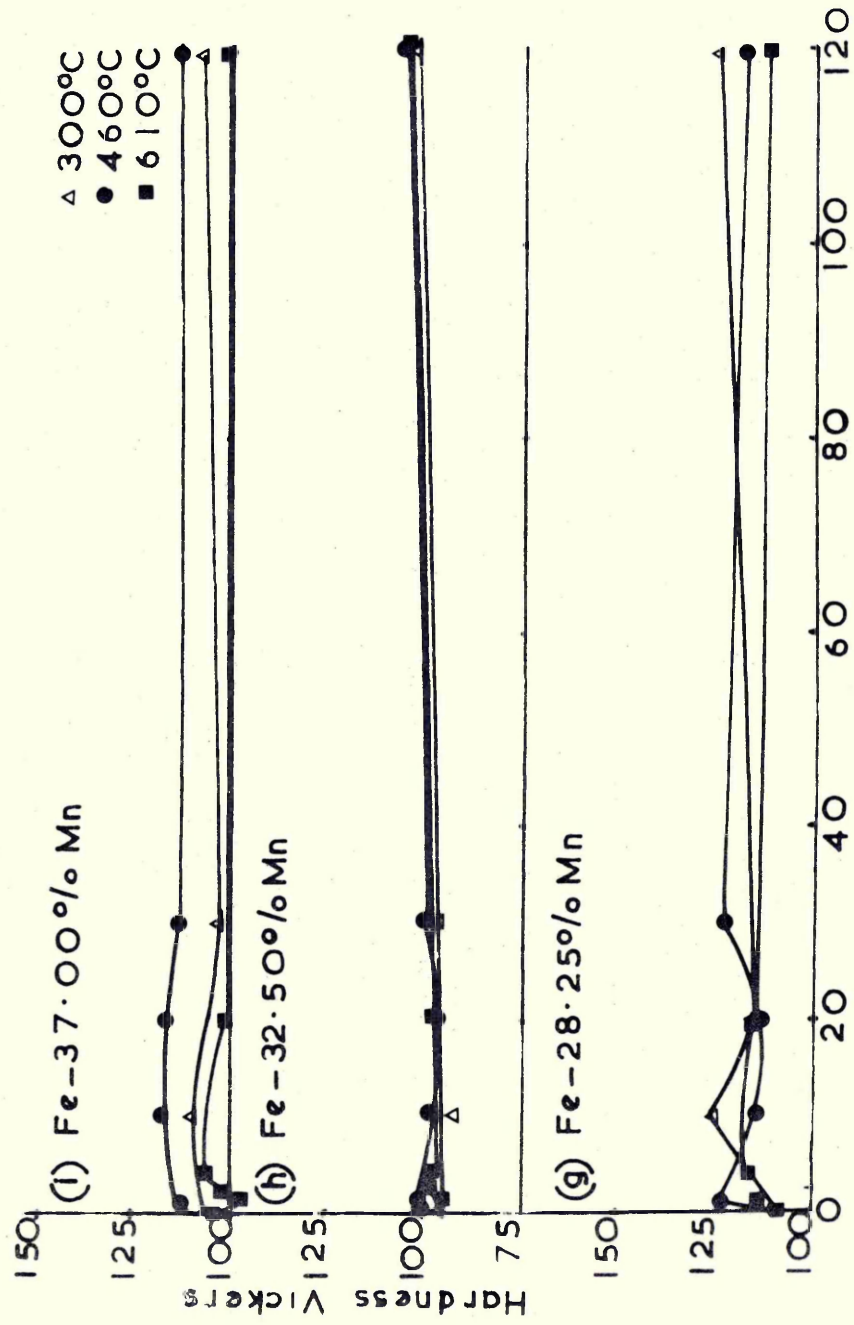


Figure 62f Ageing curves for Fe-23.00% Mn alloy



Figures 62g-i Ageing curves for Fe-Mn alloys air cooled from 1050°C.

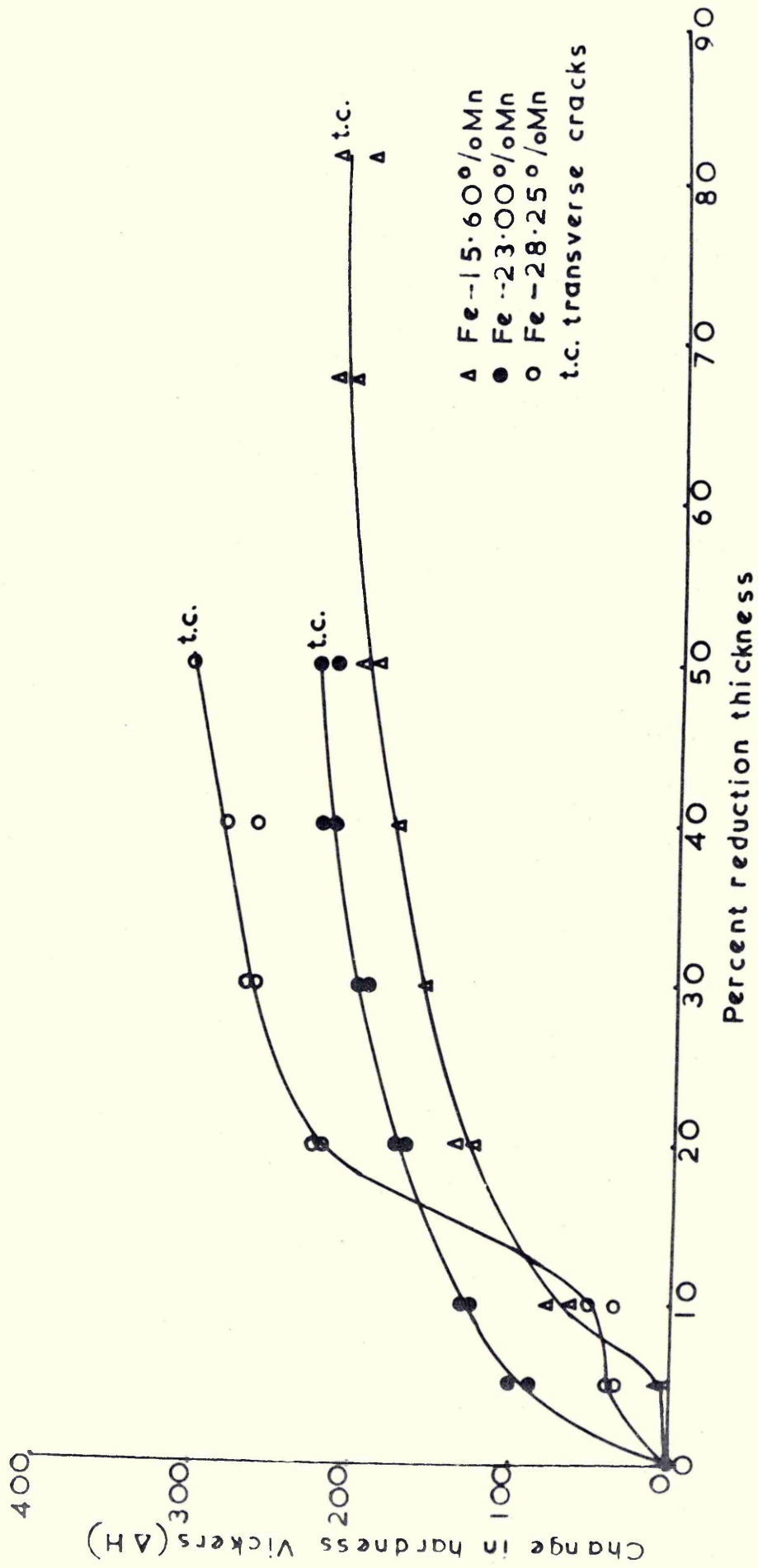


Figure 63 Change in hardness( $\Delta H$ ) V percent reduction in thickness

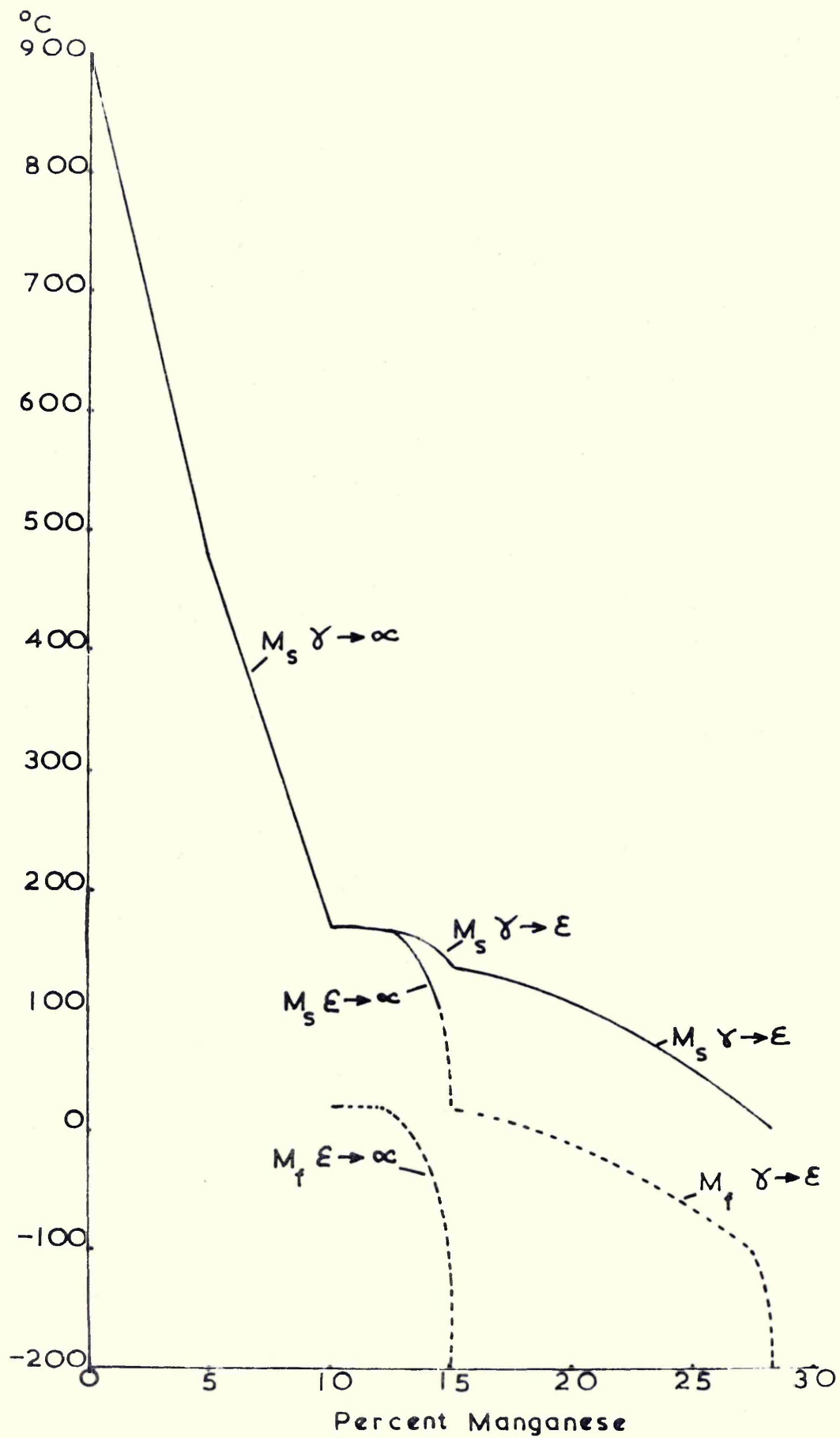


Figure 64  $M_s$  temperature V composition Fe-Mn system

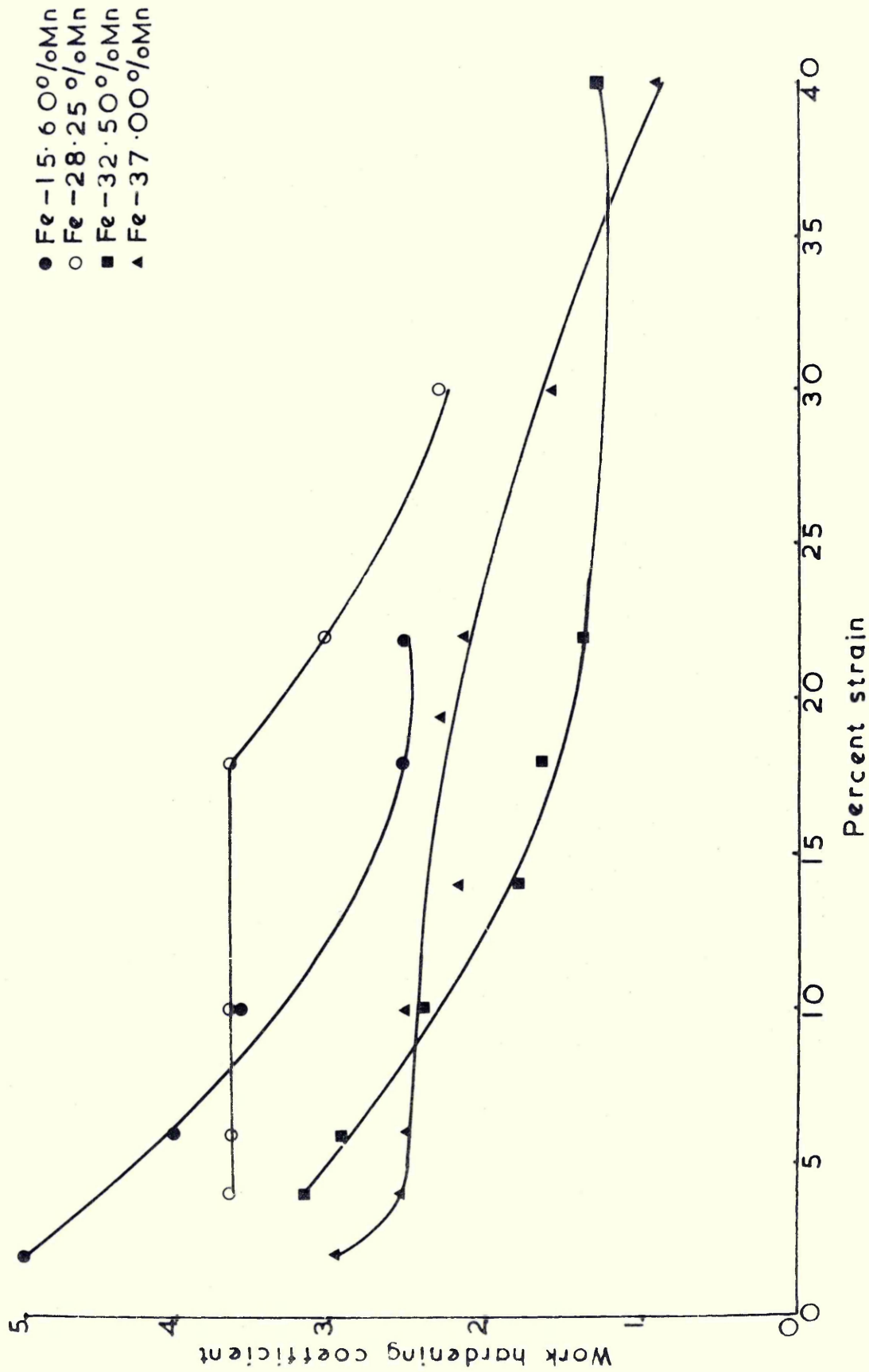


Figure 65a Work hardening coefficient V strain at 173°K

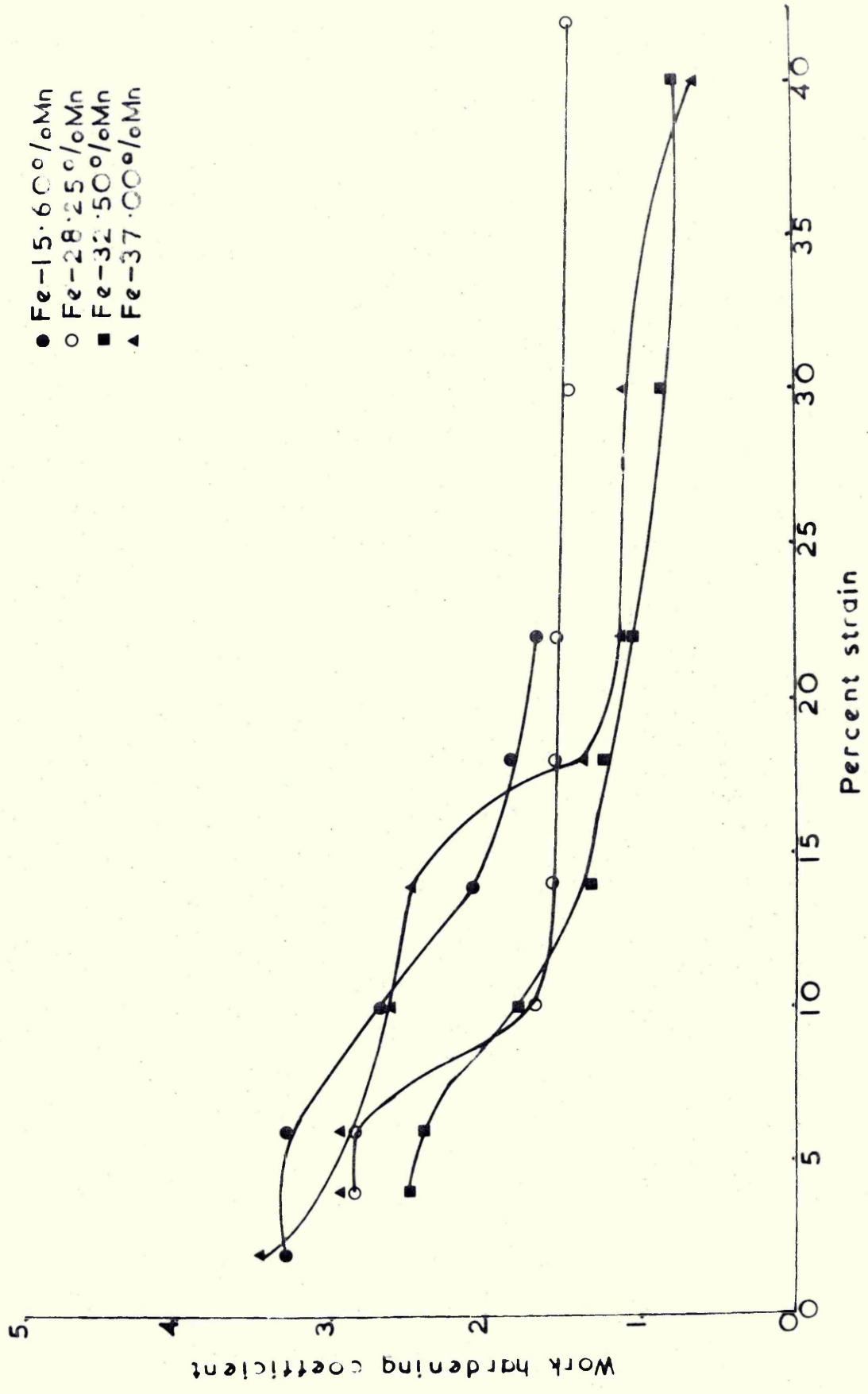


Figure 65b Work hardening coefficient V strain at 293°K

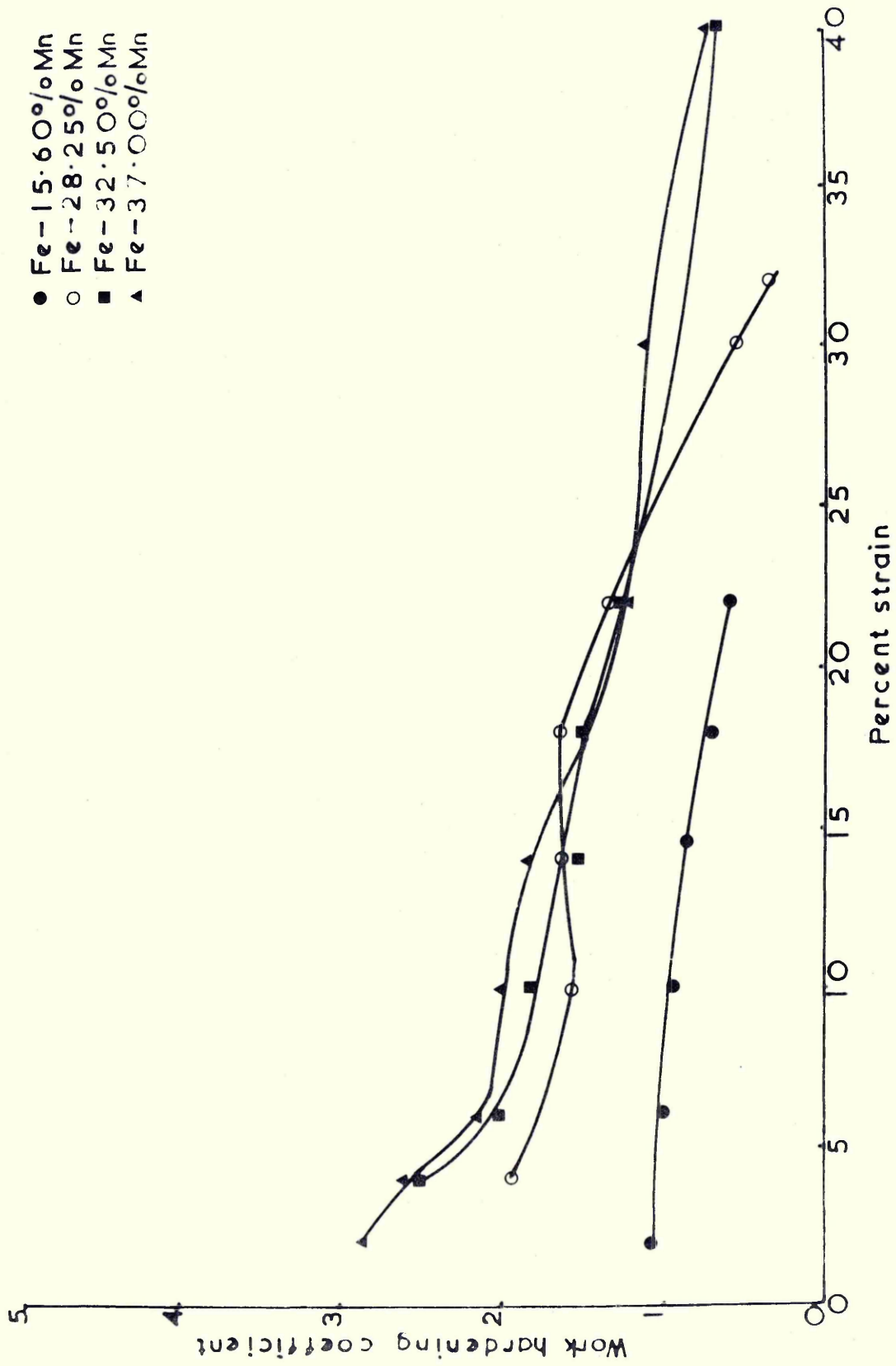


Figure 65c Work hardening coefficient V strain at 573°K

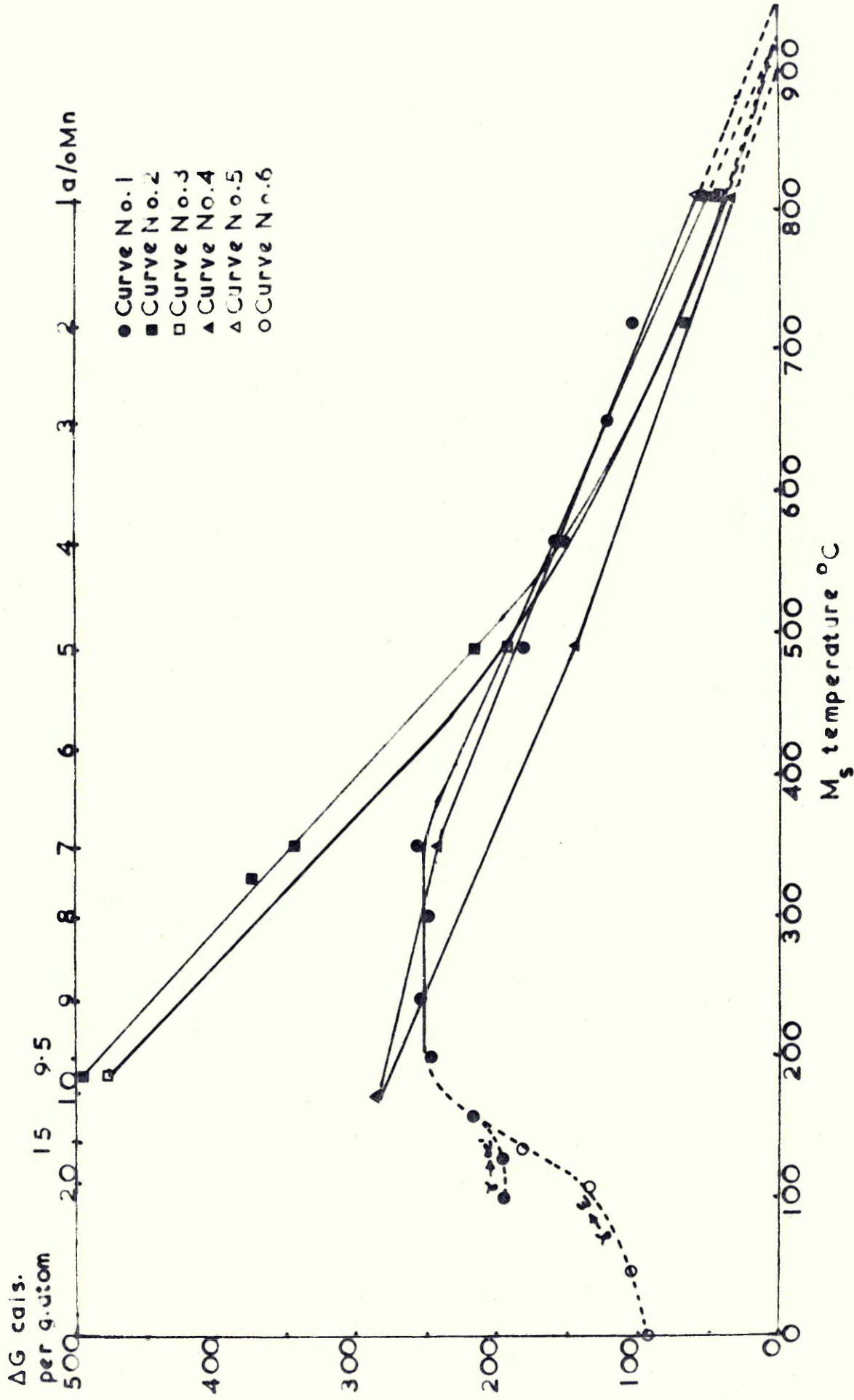


Figure 66 Estimated free energy change for martensite transformation Fe-Mn system

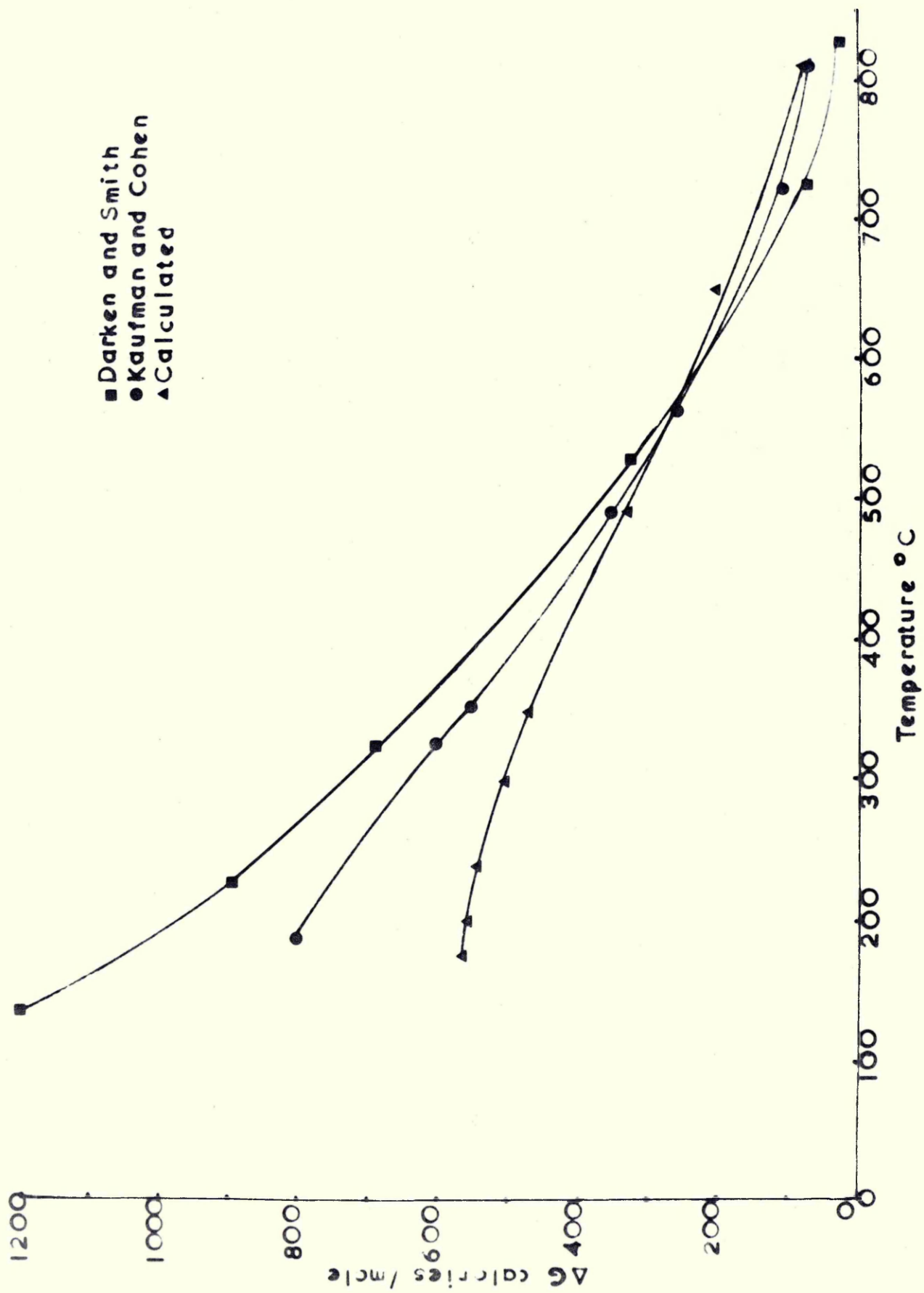


Figure 6.7 Free energy change for gamma to alpha transformation in iron

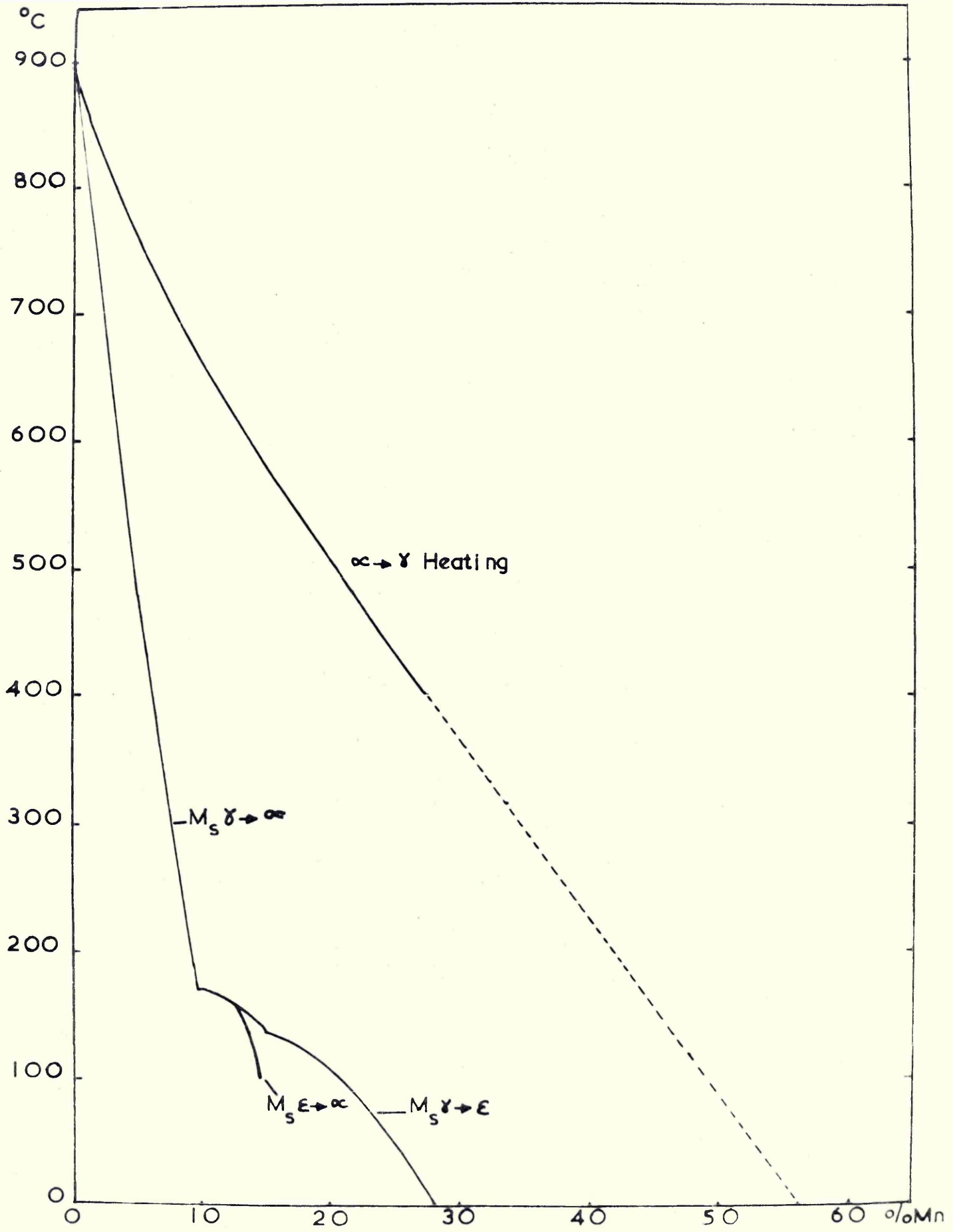


Figure 8B Hypothetical Fe-Mn equilibrium diagram